High-Precision Spectroscopy of Molecular Iodine: From Optical Frequency Standards to Global Descriptions of Hyperfine Interactions and Associated Electronic Structure

by

LISHENG CHEN

B.A., Beijing Polytechnic University, 1993

M.S., University of Colorado, 2002

A thesis submitted to the

Faculty of the Graduate School of the

University of Colorado in partial fulfillment

of the requirements for the degree of

Doctor of Philosophy

Department of Physics

LISHENG CHEN

2005

This thesis entitled:
High-Precision Spectroscopy of Molecular Iodine: From Optical Frequency Standards to Global Descriptions of Hyperfine Interactions and Associated Electronic Structure
written by LISHENG CHEN
has been approved for the Department of Physics

_____

Dr. Jun Ye

_____

Dr. John L. Hall

_____

Dr. David M. Jonas

Date _____

The final copy of this thesis has been examined by the signatories, and we find that both the content and the form meet acceptable presentation standards of scholarly work in the above mentioned discipline.

LISHENG CHEN (Ph.D., Physics)

High-Precision Spectroscopy of Molecular Iodine: From Optical Frequency Standards to Global Descriptions of Hyperfine Interactions and Associated Electronic Structure

Thesis directed by Associate Professor Dr. Jun Ye

A widely tunable and high-resolution spectrometer based on a frequency-doubled Ti:sapphire laser is used to explore sub-Doppler transitions of molecular iodine in the wavelength range $523 - 498$ nm. We investigate the natural width of the hyperfine components at various transitions and its wavelength dependence is mapped out in this region. The narrowest natural width observed is $\sim$52 kHz near 508 nm. The observed excellent signal-to-noise ratio should lead to high-quality optical frequency standards that are better than those of the popular 532-nm system. In addition, we employ a self-referenced femtosecond optical comb to measure the absolute frequency of the length standard at 514.67 nm, which is based on the a_3 hyperfine component of transition P(13) 43-0. This technique improves the precision of the frequency measurement by two orders of magnitude as compared with previous wavelength-based results.

The hyperfine spectra of $B \leftarrow X$ transitions in the wavelength range 500–517 nm are investigated systematically. Four effective hyperfine parameters, eqQ_B, C_B, d_B, and δ_B, are determined for an extensive number of rovibrational levels spanning the intermediate region $42 < \upsilon' < 70$ in the $B0_u^+(^3\Pi_u)$ state. Near vibrational levels $\upsilon' = 57 - 60$, the $1_g(^1\Pi_g)$ electronic state strongly perturbs the $B0_u^+(^3\Pi_u)$ state through rotational coincidence, leading to effects such as abnormal variations in the hyperfine parameters and strong u-g mixing recorded at the transition P(84) 60-0. Various perturbation effects in the $B0_u^+(^3\Pi_u)$ state identified so far are summarized.

We have also performed a high-resolution analysis of the six electronic states that share the same dissociation limit with the excited electronic state $B0_u^+(^3\Pi_u)$ in molecular iodine. These six states are coupled to the $B0_u^+(^3\Pi_u)$ state via hyperfine interactions. The four hyperfine parameters are calculated using available potential energy curves and wave functions constructed from the separated-atom basis set. We obtain a maximum separation of the respective contributions from all six electronic states and compare each individual contribution with high-precision spectroscopic data, allowing an independent verification of the relevant electronic structure.

Dedication

To my parents, for their inspiring and unconditional support.

Acknowledgements

This thesis is the outcome of several graduate projects that are related to precision laser spectroscopy. I wish to take this opportunity to acknowledge my debts to all those who have contributed to the work described in this thesis and apologize in advance to those whose names and efforts I failed to recognize.

First of all, my great gratitude goes to my thesis advisor Jun Ye, who ushered me into precision measurement and provided me with many research opportunities. He showed me how to search around in the laboratory to find the right optical elements, taught me how to lock diode lasers to cavities, and performed the magic in front of me that makes a scrambled Ti:sapphire laser work again in a few minutes. I had the freedom to explore various approaches and think independently and creatively in my experiments. He constantly encouraged me to broaden my research experience in the laboratory, to interact with other researchers, and to poke my head into other exciting experiments in the laboratory. His diligence, patience, exceptional high efficiency, and determination were the driving forces of my graduate study and will be a strong impetus to my future research. Without his mentorship, my graduate study would have gotten nowhere, and for this guidance I am forever indebted to him.

John Hall is more like my second advisor. On many occasions, he offered me help not merely for immediate "pain relief" but rather to stimulate a new round of inquiry. He carefully read several manuscripts related to this work and provided valuable comments. He shared with me his experience in the frequency control of

Ti:sapphire lasers. Many locking electronics he built years ago are still doing a wonderful job in our experiment. It is his hand drawings of circuits, and not the dazzling electronics on the market, that rekindled my old interests in circuit design.

Special thanks also go to Wang-Yau Cheng. We worked together on iodine spectroscopy for more than one year. Before I joined the project, Wang-Yau had already assembled the Ti:sapphire laser and the iodine spectrometer and had obtained some interesting hyperfine spectra of molecular iodine near the dissociation limit. He helped me quickly come up to speed with the necessary experimental skills on saturation spectroscopy. Without his hard work on the iodine spectrometer, I cannot imagine that the follow-up investigations on the hyperfine interactions would have come to fruition.

Contributions from Tai Hyun Yoon at an early stage of the iodine experiment are acknowledged. My understanding of the Franck-Condon principle and molecular symmetry is largely attributed to a one-semester course on molecular spectroscopy offered by David Jonas, whose wave-function picture of electronic transitions made a strong impression on me. I would also like to thank Wibe de Jong at Pacific Northwest National Laboratory for kindly sharing with us his *ab initio* potential energy curves of molecular iodine.

I owe my gratitude also to Mark Notcutt, from whom I have received considerable help and education. His finesse on vibration isolation, mechanical engineering, and various data collection and analysis methods in frequency domain has profoundly changed my way of doing research. The experiences I accumulated on laser frequency stabilization when I worked with Mark later turned out to be extremely helpful for the iodine spectroscopy.

I have benefited tremendously from doing research in the JILA laboratories, which retain a longstanding and rigorous investigation on the frequency stabilization of continuous-wave lasers and has extended this expertise to the frequency and

phase control of femtosecond laser frequency combs. I learned valuable lessons and sharpened my experimental skills through interactions with graduate students, postdocs, and visiting scientists in the laboratory. The absolute frequency measurement of molecular hyperfine transitions described in chapter 3 is the fruit of collaboration with Jason Jones and Kevin Holman, both of whom are experts on femtosecond laser frequency combs. In addition, Kevin helped me to understand the details of the femtosecond laser frequency comb, and Jason explained the mounting structure of the ultra-stable cavity used in his research on locking femtosecond pulses to stable cavities. I would also like to thank Seth Foreman for introducing to me his research on the synchronization of two femtosecond lasers, Eric Hudson and Heather Lewandowski for explaining their experiment on the collision properties of cold molecules and the related apparatus, and Long-Sheng Ma for sharing his experience in iodine spectroscopy.

I had also the pleasure of working with Joshua Zirbel and Kang-Kuen Ni from Carl Wieman's group on the photoassociation experiment of cold atoms. Josh generously offered me many projects closely related to the experiment and put up with the inconvenience caused by my busy research schedule.

During the period of my graduate study, I received valuable assistance from the supporting staff at JILA. The highly efficient and diligent work of Ed Holliness, Maryly Dole, Brain Lynch, Randall Holliness, and others in the purchasing office greatly accelerated the progress of the experiment. The numerous purchase orders they processed for a single experiment, including rush orders and instrumental trials, repairs, and returns, are a testimony to their indispensable contributions. Technical support from electronic shop is also highly appreciated. Far beyond the call of duty, Terry Brown taught me many informal lessons on circuit design with great patience and thoughtful ideas. James Fung-A-Fat repaired many electronic components for the experiment. Julie Phillips in the scientific report office contributed her editing

work, which not only expedited the publishing process but also improved the quality of the manuscript. I would like to thank Caroline Frazee, who helped to arrange my conference travel and who found me a desk and a book shelf in a quiet office despite the pressure of increasing demand for the office place. I had the fortune to be able to attend a course taught by Barb Tennis on spoken English. Barb also organized many seminars from which I began to learn the importance of academic communications. I would also like to thank everyone in the instrument and specialty shops. In particular, Hans Green taught me every detail about the operation of the tooling machines in the instrument shop, and the tricks he shared with me will be always treasured. Indeed, without help from so many warmhearted and hardworking people, the joy of discovery might have been a dream that never came true.

Finally, I must express my deepest thank to my parents, who have always been there for me. Their unconditional support and love are a constant inspiration for my personal development. I also thank my two brothers Linqi and Zongze for their support and for tolerating my long absence from family activities.

Contents

Chapter

Tables

Table

Figures

Figure

Chapter 1

INTRODUCTION

Precision spectroscopy provides an effective way to probe the internal structure of atoms and molecules. Moreover, rigorous spectroscopic investigations have in many ways refined and deepened our understanding of the fundamental laws of physics. The spectral measurement of black-body radiation in the late 19th century lifted the curtain on the quantum revolution. Precision measurement of Lamb shift in atomic hydrogen provided strong supporting evidence for quantum electrodynamics. A number of ongoing precision measurements, such as the detections of the time variation of the fine structure constant [1, 2, 3] and the particle intrinsic electric dipole moment (EDM) [4, 5, 6, 7], will put stringent constraints on various new theories beyond the standard model.

The narrow spectral lines of atoms and molecules are obscured or totally buried by three major broadening effects: the spectral impurity of the interrogating light, the broad Doppler profile due to the relentless thermal motions of atoms or molecules, and the limited interrogating time. With the advent of lasers, a number of sub-Doppler techniques have emerged that can effectively remove the Doppler broadening. Advances in laser frequency control and stabilization have greatly accelerated the improvement in spectral resolution. New methods and techniques in spectroscopy or related fields are continuously developed. Two distinct examples are the laser-cooling of atoms and ions [8, 9, 10, 11, 12] and the introduction of femtosecond laser frequency

combs [13, 14, 15] that have revolutionized the optical frequency measurement.

This thesis covers a systematic investigation of the hyperfine structure in molecular iodine. By using high-precision saturation spectroscopy, the hyperfine spectra of the $B \leftarrow X$ transitions in molecular iodine are measured for a large number of levels in the second excited electronic state B. In the following sections I will explain several key ingredients of our spectroscopic investigations such as the Doppler broadening that severely masks the hyperfine structure, how this broadening effect is circumvented by the saturation spectroscopy, energy levels in molecular iodine, and an effective hyperfine Hamiltonian developed by Broyer *et al.* [16] that is especially suitable for describing the hyperfine interactions in molecular iodine. The major tasks of this spectroscopic study are also discussed in this introduction. A thesis outline is given at the end of this chapter.

1.1 Sub-Doppler Saturation Spectroscopy

1.1.1 Doppler Broadening

Atomic or molecular transitions can be probed by passing an interrogating light through a gas sample. The spectral lines obtained in this way are usually much broad than what are expected from the natural widths of these transitions. This broadening effect prevents accurate and high-precision determination of the center of the spectral line. Furthermore, a broadened strong line can often skew or totally conceal the adjacent weak features from which valuable information might be extracted.

The spectral lines are broaden by the Doppler effect because atoms and molecules in a gas have different thermal velocities [17, 18]. A moving particle feels an increased or decreased frequency of the incoming light, depending on whether it is moving toward or receding from the incoming light. The first-order Doppler shift experienced by the particle is $-\mathbf{k} \cdot \mathbf{v}$ [18], where $\mathbf{k}$ is the wave vector of the inter-

rogating light and $\mathbf{v}$ is the velocity of the particle. As a result, if the particle has a sharp spectral feature at frequency ω_0 in its rest frame, then the frequency of the interrogating light has to be tuned to

$$\begin{aligned} \omega &= \omega_0 + \mathbf{k} \cdot \mathbf{v} \\ &= \omega_0 \left(1 + \frac{v_z}{c}\right) \end{aligned} \tag{1.1}$$

in order for the light to be in resonance with the the moving particle. Note that in arriving at the second equality in equation 1.1, we have assumed that the light propagates in the $+\mathbf{z}$ direction.

Gas particles move in all directions with different speeds. At thermal equilibrium and far from the quantum degeneracy, the probability distribution for each of the three velocity components is Maxwellian [19]:

$$w(v_x) = \frac{1}{\sqrt{\pi} v_p} \exp\left(-v_x^2/v_p^2\right), \tag{1.2}$$

where v_x is one of the three components of the velocity in Cartesian coordinate, $v_p = \sqrt{2k_B T/m}$ is the most probable velocity, m is the mass of the particle, k_B is the Boltzmann's constant, and T is the absolute temperature of the gas sample. Because of this velocity diffusion, the sharp resonances of the particle are spread out in the laboratory frame. The broadened line profile can be obtained by combining equations 1.1 and 1.2 [18]:

$$I(\omega) = I_0 \exp\left[-\frac{4 \ln 2 \left(\omega - \omega_0\right)^2}{\Delta\omega_D^2}\right], \tag{1.3}$$

where $\Delta\omega_D = 2\sqrt{\ln 2}\omega_0 \frac{v_p}{c}$ is the full spectral width at half maximum (FWHM). For iodine molecules at room temperature (300 K), the Doppler width at 514 nm is $\Delta\nu_D = \frac{\Delta\omega_D}{2\pi} = 454$ MHz. In contrast to this broad profile, the narrow lines of iodine molecules around 514 nm have natural widths of $\sim$ 100 kHz, and 15 or 21 such lines are clustered together with distance between two adjacent lines typically

ranging from 100 Hz to 100 MHz. These fine features are masked by the Doppler profile associated with each narrow line. In the case of detecting spectral lines with a broad natural width that is comparable to the Doppler width, the intensity profile for an isolated line is no longer Gaussian. Instead, it is a convolution of the Lorentzian and Doppler profiles, which is called a Voigt profile [18].

Since the Doppler width is scaled down in accordance with the square root of temperature, Doppler broadening is still prominent at low temperatures reached by cryogenic cooling or laser cooling. For instance, the $5^1S_0 - 5^3P_1$ transition (689 nm) in ^{88}Sr has a natural width of 7.6 kHz, but the associated Doppler width remains to be 33 kHz even if atoms are laser cooled to 1 μK. In this case, the information of the line center, the natural width, and the Doppler width can be extracted from a deconvolution of the experimentally determined Voigt profile [20]. However, this separation of the contributions of natural width and Doppler broadening becomes more difficult when the atomic transition is orders of magnitude narrower than that of the Doppler profile. Besides, the Doppler broadening prevents a real-time access to narrow atomic transitions in applications such as optical frequency standards. Consequently, without special countermeasures such as laser cooling and trapping atoms into the Lamb-Dicke regime [21, 17] the Doppler broadening can persist to be a limiting factor in the spectroscopy of some extremely narrow transitions in atoms or ions.

1.1.2 Sub-Doppler Techniques

To circumvent the resolution limit imposed by Doppler broadening, a direct approach is to reduce the term $-\mathbf{k} \cdot \mathbf{v}$ by collimating the atoms or molecules into a beam and probing all the particles in a direction that is perpendicular to the beam. Indeed, atomic or molecular beams were major tools for sub-Doppler spectroscopy before the era of lasers, and they are still widely used in spectroscopic studies.

The advent of lasers has completely changed the landscape of high-precision spectroscopy. With the development of various tunable lasers, such as dye lasers, semiconductor diode lasers, Ti:sapphire lasers, and fiber lasers, the spectral coverage of the intense laser radiation has been extended from visible spectrum to infrared and ultraviolet. On the other hand, the spectral purity of these tunable lasers has been greatly improved thanks to the advances in laser frequency stabilization [22, 23, 24, 25, 26]. By virtue of nonlinear effect, the intense radiation from a laser can exert strong influence on the gas sample. Based on this capability, a number of sub-Doppler techniques have emerged to remove the first-order Doppler effect. These sub-Doppler schemes can be classified as two major categories, namely, the saturation spectroscopy and the two-photon spectroscopy. In the first category, a subgroup of atoms or molecules with a narrow range of velocities in a particular direction is selected to interact with laser radiations, while in the second category all the atoms or molecules interact simultaneously with two counter-propagating laser beams via two-photon transition and the first-order Doppler shifts of the two beams are therefore cancelled. The following section gives a brief introduction of the saturation spectroscopy on which our investigation of the hyperfine spectrum of molecular iodine relies.

1.1.3 Saturation Spectroscopy

Rather than cooling the atoms or molecules to tame their thermal motions, saturation spectroscopy is based on the velocity-selective saturation of atomic or molecular transition [27]. The velocity-selective saturation was first observed [28, 29] as a Lamb dip [30] at the center of the Doppler-broadened absorption profile inside the cavity of a HeNe laser. The experimental implementation of saturated absorption spectroscopy was later refined by introducing the lock-in detection to remove the Doppler background [31, 32, 33]. Frequency-modulation (FM) technique has also been applied to the saturation spectroscopy [34, 35, 36]. This FM saturation spectroscopy,

combined with a high-finesse optical cavity for signal enhancement, has achieved high sensitivities in the detection of extremely weak molecular overtones [37, 38, 39].

Figure 1.1 (a) sketches the basic setup of the saturated absorption spectroscopy. The laser beam is divided by a beam splitter into two beams that counter propagate inside the gas sample. The strong pump beam selectively saturates the absorption of a subgroup of atoms or molecules with a very narrow velocity distribution in the direction of the pump beam. This saturation effect does not affect the absorption of the weak probe beam as long as the two beams are in resonance with different velocity groups. However, when the laser is tuned within a narrow bandwidth around ω_0, both beams are simultaneously in resonance with the same group of particles whose axial-velocity distribution is sharply centered around zero. Now the probe beam experiences an extra reduction of the loss because the available absorbers are depleted by the strong pump beam. As a result, the narrow spectral line is recovered as a sharp dip at the center of the Doppler-broadened absorption profile, as shown in figure 1.2. To remove the background signal arising from the Doppler-broadened absorption profile of the probe beam, the pump beam is chopped at frequencies ranging from several to a few tens of kilohertz. The background-free signal is then obtained with a lock-in amplifier.

FM sideband technique can be used to detect the changes both in the absorption and the dispersion, and to suppress the low frequency instrumental noise. Figure 1.1 (b) shows the setup for this detection scheme. The probe beam first passes a phase modulator to develop two FM sidebands with opposite phases. When the optical frequency is scanned across the resonance, changes in the absorption and the dispersion are converted to relative phase and amplitude variations among the two sidebands and the carrier. The line profile (either absorption or dispersion, or their combined effect) is recovered by a phase-sensitive detection at the modulation frequency with a fast photodetector and a RF mixer. By using a high modulation frequency, this

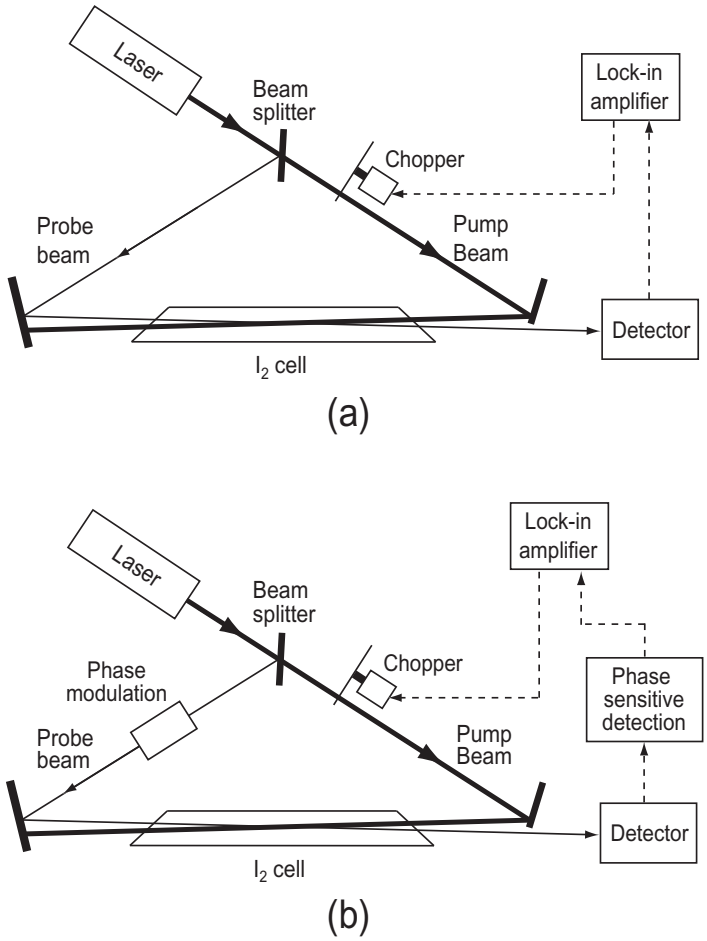

Figure 1.1: Experimental setup for sub-Doppler saturation spectroscopy. (a) Saturated absorption spectroscopy. (b) FM sideband spectroscopy.

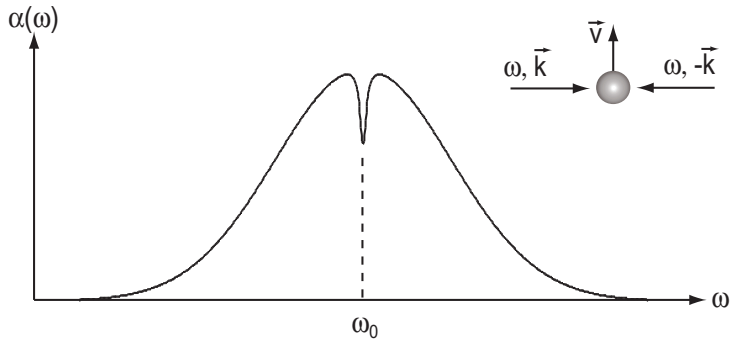

Figure 1.2: Lamb dip in the absorption profile. The frequency of two counter-propagating beams is tuned across the Doppler profile. For $\omega = \omega_0$ both waves are simultaneously in resonance with the same group of molecules that are moving perpendicularly to the laser beams, producing a sharp change of absorption around ω_0.

signal recovery scheme can effectively suppress the low-frequency instrumental noise. The line shape of sub-Doppler resonances recovered by FM sideband technique has been studied in reference [36].

1.2 Hyperfine Structure of Molecular Iodine

The saturation spectroscopy introduced in the previous section is particularly suitable for probing the gas sample around room temperatures. Using this sub-Doppler technique, narrow hyperfine lines of molecular iodine can be readily resolved. We move on now to highlight the central tasks of our spectroscopic investigation on the hyperfine spectrum of molecular iodine.

1.2.1 Hyperfine Structure as Frequency References

Figure 1.3 shows the simplified energy level diagram of molecular iodine. Plotted in this figure are several potential energy curves (PECs) converging to three different dissociation limits. Among these states are the ground state X, the second excited sate B, and a 1_g state converging with the B state to the second dissociation limit. Several rovibrational levels in the X and the B states are also shown in the figure. The thick vertical line in the figure indicates an electric dipole transition between two rovibrational levels (v'', J'') and (v', J') in the ground state X and the second excited state B, respectively. Because of hyperfine interactions, each rovibrational level is further split into hyperfine levels. Thus a rovibrational transition contains many hyperfine components.

High-precision measurement of hyperfine spectrum in molecular iodine over an extended range of rovibrational levels is valuable for selecting frequency references in the visible and in the near infrared. These frequency references can be used for frequency stabilization of lasers and for serving as wavelength standards. Among the wavelength standards recommended by Comité International des Poids et Mesures

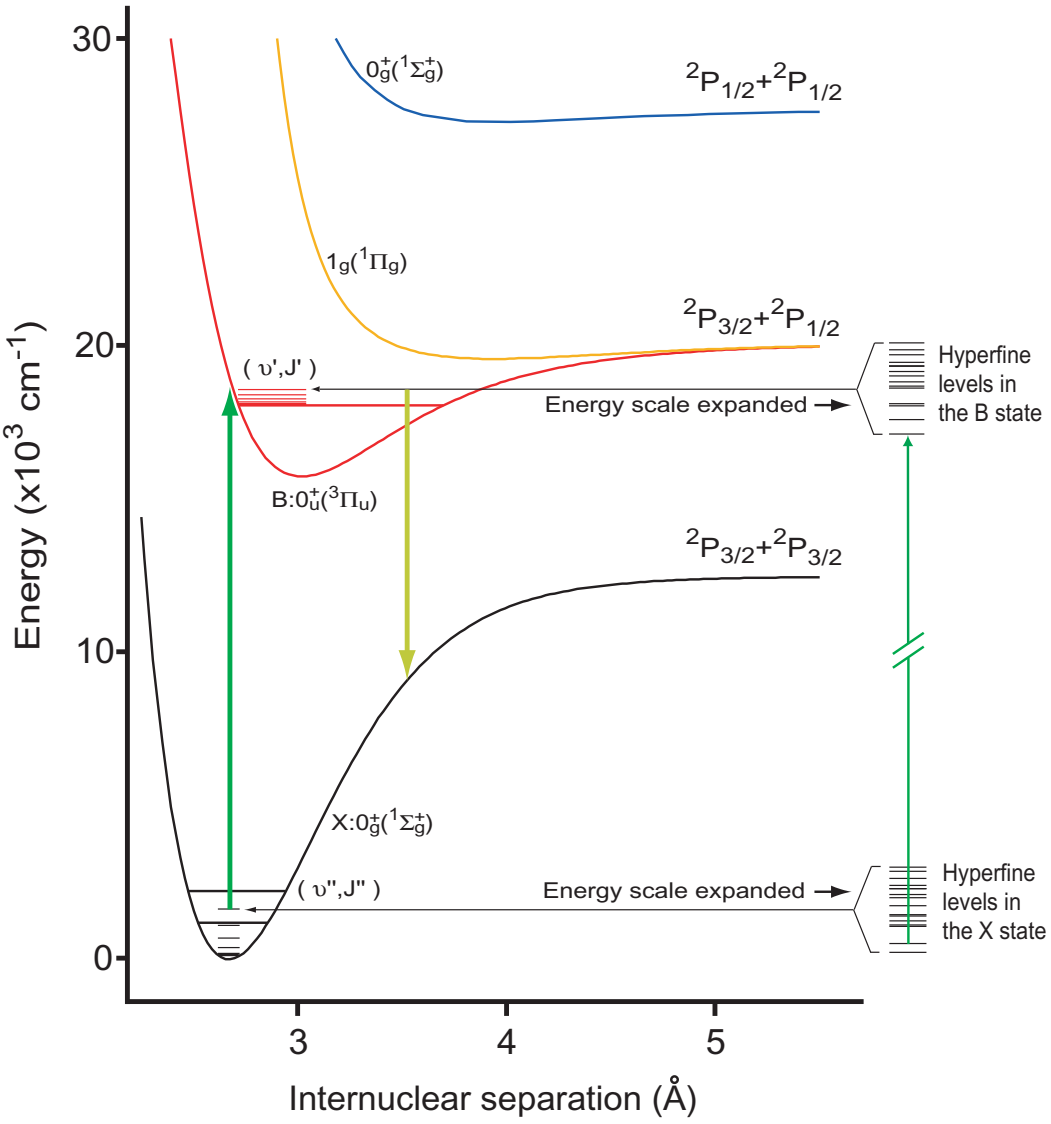

Figure 1.3: A simplified energy level diagram of molecular iodine. Several rovibrational levels in the X and the B states are shown. The thick vertical line on the left indicates a $B \leftarrow X$ rovibrational transition between two rovibrational levels (υ'', J'') and (υ', J') in the X and the B states, respectively. Each rovibrational level is further split into hyperfine sublevels. Thus one rovibrational transition contains many hyperfine components. Such a hyperfine component is indicated as a thin vertical line on the right.

(CIPM), molecular iodine (I_2) holds a unique position in that it offers five reference lines that have been widely used for metrological calibration [40]. The 633-nm HeNe laser stabilized by an iodine line is till widely used in the length metrology. Nd:YAG lasers stabilized by hyperfine lines at 532 nm are preferred to their companions at longer wavelengths because of their compact size, reliability, and high stability (with a fractional frequency instability of $< 5 \times 10^{-14}$ at 1 s) [41].

To reach higher frequency stability, it is useful to explore I_2 transitions at wavelengths below 532 nm, where the natural widths can decrease at a faster rate than that for the line strengths. Thus, it is of great interest to monitor the variation of the transition linewidth when iodine molecules approach the dissociation limit. We built a widely tunable and high-resolution I_2 spectrometer and measured the natural width of hyperfine components within the wavelength range $523 - 498$ nm. This investigation is described in chapter 2. In addition, to evaluate the potential of these hyperfine lines for serving as future frequency standards, we performed frequency measurements at 514.67 nm with the help of a femtosecond frequency comb and investigated the performance of our iodine-based laser system. Chapter 3 covers the details of this survey.

1.2.2 Systematic Study of Hyperfine Interactions

In order to accurately describe the hyperfine structure at wavelengths below 514 nm, where the perturbation effect becomes prominent, it is important to obtain a thorough understanding of hyperfine couplings between the B and the perturbing electronic states. Despite the dense spectroscopic data at longer wavelengths [42], precision measurement of hyperfine spectrum in the wavelength range $500 - 517$ nm ($42 < v' < 70$) is scarce, leaving the quantitative knowledge of the perturbation effects rather vague. In fact, previous study [43, 44, 45] of hyperfine interactions at vibrational levels $v' = 71 - 82$ in the B state has revealed a strong hyperfine perturba-

tion from a nearby electronic state, and the primary survey of the hyperfine spectrum described in chapter 2 shows that the hyperfine patterns in a much broad range of rovibrational levels are dramatically modified. Motivated by these observations, we performed a systematic investigation on the hyperfine spectrum of $B \longleftarrow X$ transition in the wavelength range $500 - 517$ nm. We measured the hyperfine spectra of a large number of rovibrational levels spanning the intermediate region ($42 < v' < 70$) in the B state. This investigation, which is detailed in chapter 4, provides rich information about the rotational and vibrational dependence of hyperfine interactions in molecular iodine.

An important theoretical tool that is heavily used in our spectroscopic investigation is an effective hyperfine Hamiltonian developed by Broyer *et al* [16]. This effective Hamiltonian, which contains several effective hyperfine parameters, is used to describe hyperfine interactions that can couple different electronic states. Through this effective hyperfine Hamiltonian, the seemingly intriguing patterns of the hyperfine spectrum, which can vary greatly even across neighboring rovibrational levels, can be described by a small number of hyperfine parameters whose variations across different levels are more predictable. It will be shown in chapter 4 that the hyperfine parameters determined from spectroscopic fits at a large number of rovibrational levels offer an effective way to examine the global evolution of hyperfine interactions in molecular iodine.

1.2.3 Probing the Electronic Structure Through Hyperfine Interactions

The hyperfine parameters introduced in the previous section serve as a bridge that connects spectroscopic data with the electronic structure of molecular iodine. On the experimental side, the introduction of these hyperfine parameters greatly simplifies the spectroscopic analysis of the hyperfine spectrum. On the other hand, these

hyperfine parameters can be dissected into pieces that correspond to the hyperfine couplings with various perturbing electronic states. Because these perturbing states are very close to the high-lying vibrational levels of the B sate, the hyperfine-coupling strength depends very sensitively on the electronic structure of the associated electronic states. Accordingly, the extensive and high-precision spectroscopic data on hyperfine spectrum permit a detailed study of electronic structure of the molecular iodine. This is especially feasible for the B state because vibrational wave functions in the B state samples a broad range of internuclear separations. In particular, experimentally determined hyperfine parameters over a large range of rovibrational levels allow a sensitive test of the relevant electronic wave functions and potential energy curves (PECs).

Hyperfine parameters have been calculated for several vibrational levels ($v' \sim 40 - 82$) in the B state [45, 46, 47, 48, 43]. The detailed information about the PECs of perturbing electronic states was largely unavailable when these calculations were performed, and hence the properties of the molecular wave function of the corresponding electronic state could not be independently inferred from these analyses. In our analysis, we take the advantage of the significant improvements in both experimental data and theoretical PECs. Thus a detailed calculation of the hyperfine parameters enables either the determination of the admixture of the basis wave functions in the separated-atom model or the verification of more-sophisticated molecular wave functions.

In chapter 5, we present a numerical analysis of the hyperfine parameters, using the related empirical/theoretical PECs and electronic wave functions derived from the separated-atom basis set. We divide the perturbing electronic states into several groups whose contributions to the hyperfine parameters can be separated and directly compared with the corresponding experimental data. With the help of this numerical analysis several interesting issues can be quantitatively addressed,

such as (1) to what extent the separated-atom model can be extrapolated to small internuclear separations, (2) the admixture of the basis wave functions at various internuclear separations, and (3) the susceptibilities of the hyperfine interactions to various adjustments of the relevant PECs.

1.3 Thesis Outline

Chapter 2 describes our investigation of the sub-Doppler transitions of iodine molecules in the wavelength range 523−498 nm. To explore various properties of these transitions, especially the variations of their natural widths, we developed a widely tunable and high-resolution spectrometer based on a frequency-doubled Ti:sapphire laser. The experimental details of the I_2 spectrometer are presented. An FM line shape analysis is used to extract the linewidth information from the sub-Doppler resonance. The results of this investigation include the linewidth dependence of the $B \leftarrow X$ transitions in the wavelength range $523 - 498$ nm, the strong modification of the hyperfine-resolved patterns near the B-state dissociation limit, and the potential performance of the iodine-cell-based frequency standard at wavelengths below 532 nm. The observed excellent signal-to-noise ration (S/N) at several transitions and a clear trend of the linewidth narrowing indicate that I_2 transitions in the wavelength range 532−501 nm hold great promise for the future development of optical frequency standards.

Chapter 3 reports the frequency measurement of the 514.67-nm length standard at a_3 hyperfine component of the P(13) 43-0 transition. The frequency measurement of such a transition in the interesting wavelength range $523 - 498$ nm provides first-hand information that can be used to evaluate the potential of iodine-cell-based systems serving as future frequency standards. A femtosecond frequency comb spanning an octave bandwidth is employed to check systematics and measure the absolute frequency of the optical transition. This chapter contains a brief introduction to fem-

tosecond lasers in the context of frequency metrology, the details of the experimental setup, the results of the frequency measurement of the length standard, and a characterization of the iodine spectrometer by a femtosecond frequency comb.

Chapter 4 presents a systematic investigation of $^{127}I_2$ hyperfine spectrum in the wavelength range $500-517$ nm. The precision measurement of hyperfine spectra over an extended range of rovibrational levels is valuable both for studying the molecular structure and for selecting references for laser frequency stabilization. This chapter begins with a brief overview of the hyperfine spectrum in molecular iodine. The experimental setup and data collection are then described. The hyperfine spectra at a large number of rovibrational levels are recorded and the four effective hyperfine parameters, eqQ_B, C_B, d_B, and δ_B, are extracted from the spectrum at each level. Spectroscopic data are presented and discussed in detail. This chapter also discusses the abnormal variations in eqQ_B, d_B, and δ_B observed at several vibrational levels. Various perturbation effects in the B state are summarized. In addition, the R-dependence of the four effective hyperfine parameters is obtained by removing the average effect of the molecular vibration.

Chapter 5 provides a detailed analysis of the excited electronic states converging to the second dissociation limit in molecular iodine. Comprehensive and high-precision measurements of the hyperfine spectrum in the $B \leftarrow X$ system of molecular iodine provide a unique opportunity for detailed examination of the global electronic structure relevant to the second dissociation limit, $^2P_{\frac{3}{2}} + {}^2P_{\frac{1}{2}}$. In this chapter, we extend previous calculations of hyperfine parameters to low vibrational levels and to rotational dependence at each vibrational level and compare these calculations with spectroscopic data. In doing so, we are able to perform a sensitive test of the associated electronic wave functions and potential energy curves.

Chapter 2

SUB-DOPPLER MOLECULAR-IODINE TRANSITIONS NEAR THE DISSOCIATION LIMIT (523–498 nm)

2.1 Introduction

Hyperfine-resolved optical transitions in molecular iodine (I_2) often provide stable references for precision spectroscopy [49, 50]. The narrow hyperfine components have been widely used in laser frequency stabilization, ever since the development of an early HeNe/$^{127}I_2$ system using intracavity saturated absorption in a red laser at 633 nm [51]. Other systems include HeNe/$^{127}I_2$ at 640, 612, 576, and 543 nm and Ar/$^{127}I_2$ at 515 nm as well as the $^{129}I_2$ variants. Most of these systems have wavelengths recommended for realization of the SI meter [40]. The I_2 lines near 532 nm are stronger than red transitions, have relatively narrower ($200-300$ kHz) linewidth, and are readily accessible by frequency-doubled solid-state Nd:YAG lasers [52, 53]. The 532-nm system has proved to be one of the best practical optical frequency standards because of its compact size, reliability, and demonstrated high stability ($< 5 \times 10^{-14}$ at 1 s) [41]. Recent development of wide-bandwidth optical combs shows that such I_2-based references can be useful not only for precision length metrology, but also for generation of highly stable time signals [54].

Our motivation for performing detailed studies of hyperfine transitions of I_2 in the wavelength range of $500 - 532$ nm is two-fold. First, the search for the best candidates of I_2-based optical frequency references requires a systematic study of the

linewidth and the strength of many transitions. To attain a higher frequency stability, it is useful to explore I_2 transitions at wavelengths below 532 nm where the natural linewidth may decrease at a faster rate than the line strengths as molecular iodine approaches its dissociation limit. In fact, coincidental overlaps between the I_2 transitions and corresponding Ar^+ laser lines at 515 and 501 nm have already revealed transition linewidth as small as $50-100$ kHz [half-width at half-maximum (HWHM)] at these wavelengths [55, 56]. It will be interesting to monitor variations in the transition linewidth when the I_2 molecules approach the dissociation limit. Second, a widely tunable laser system permits systematic studies of rotation-vibration dynamics and hyperfine interactions near the dissociation limit, providing rich information on molecular structure and dynamics. Specifically, a large range of rovibrational levels can be accessed, allowing a detailed parametric study of transition strengths, hyperfine interactions, and collision physics. We built such a widely tunable, yet high-resolution and high-sensitivity I_2 spectrometer and measured the linewidths of transitions within the range $523-498$ nm. Signals are recovered with an excellent signal-to-noise ratio (S/N). We observe a clear trend of linewidth narrowing with decreasing transition wavelength as molecular iodine approaches the dissociation limit. However, this tendency is complicated by variations in linewidth among different rotational or hyperfine components. The limit on lifetime imposed by predissociations and the associated broadening of the linewidth is studied. We also discover that the hyperfine patterns are dramatically influenced by the predissociation effect.

This chapter is outlined as follows. Section 2.2 covers the experimental details of the I_2 spectrometer based on a frequency-doubled Ti:sapphire laser. Discussions about single-mode selection in Ti:sapphire lasers, laser frequency stabilization and scanning, and saturated absorption spectroscopy are given in this section. Section 2.3 introduces the line shape analysis that is used to extract the linewidth from the sub-Doppler resonance in frequency modulation (FM) spectroscopy. Section 2.4

explains the processes used to remove the effects of power and pressure broadening from the measured linewidth. Section 2.5 gives experimental results on linewidth dependence of the transitions in the wavelength range $523 - 498$ nm, together with a discussion on the predissociation of the B state. The strong modification of the hyperfine spectrum near the dissociation limit is discussed in section 2.6. Section 2.7 discusses the potential performance of the iodine-cell based frequency standard at wavelengths below 532 nm. Section 2.8 summarizes the chapter.

2.2 Iodine Spectrometer

Figure 2.1 shows the experimental setup that implements precision scan and control of the laser frequency. Our single-mode Ti:sapphire laser is constructed in a ring-cavity configuration with a set of long-wavelength (1-μm) coating mirrors and is pumped by a commercial diode-pumped solid state laser at 532 nm. At a pump power of 8 W, the Ti:sapphire laser can be tuned from 1080 to 953 nm and provides 300 mW of useful output power from 1000 to 1034 nm, with a moderate power drop at the long-wavelength end. The mirror set consists of two curved mirrors (folding mirrors) and two flat mirrors. These four mirrors form the ring cavity with a beam waist (~ 0.4 mm) at the middle of two flat mirrors and a small beam waist (~ 0.03 mm) in the center of the two curved mirrors where the Ti:sapphire gain medium is placed. An optical diode is inserted into the beam path between the two flat mirrors to enforce unidirectional propagation of the laser radiation.

Three additional filtering components with decreasing bandwidth are placed inside the cavity to obtain single-mode operation. A birefringent filter with a bandwidth of ~ 1.5 THz is used for coarse wavelength adjustment. Single-mode operation is then achieved with the combination of a thin and a thick solid etalon. The thicknesses of the two etalons used in this system are 0.5 mm [free spectral range (FSR) ≈ 200 GHz] and 10 mm (FSR ≈ 10 GHz), respectively. Because each etalon has re-

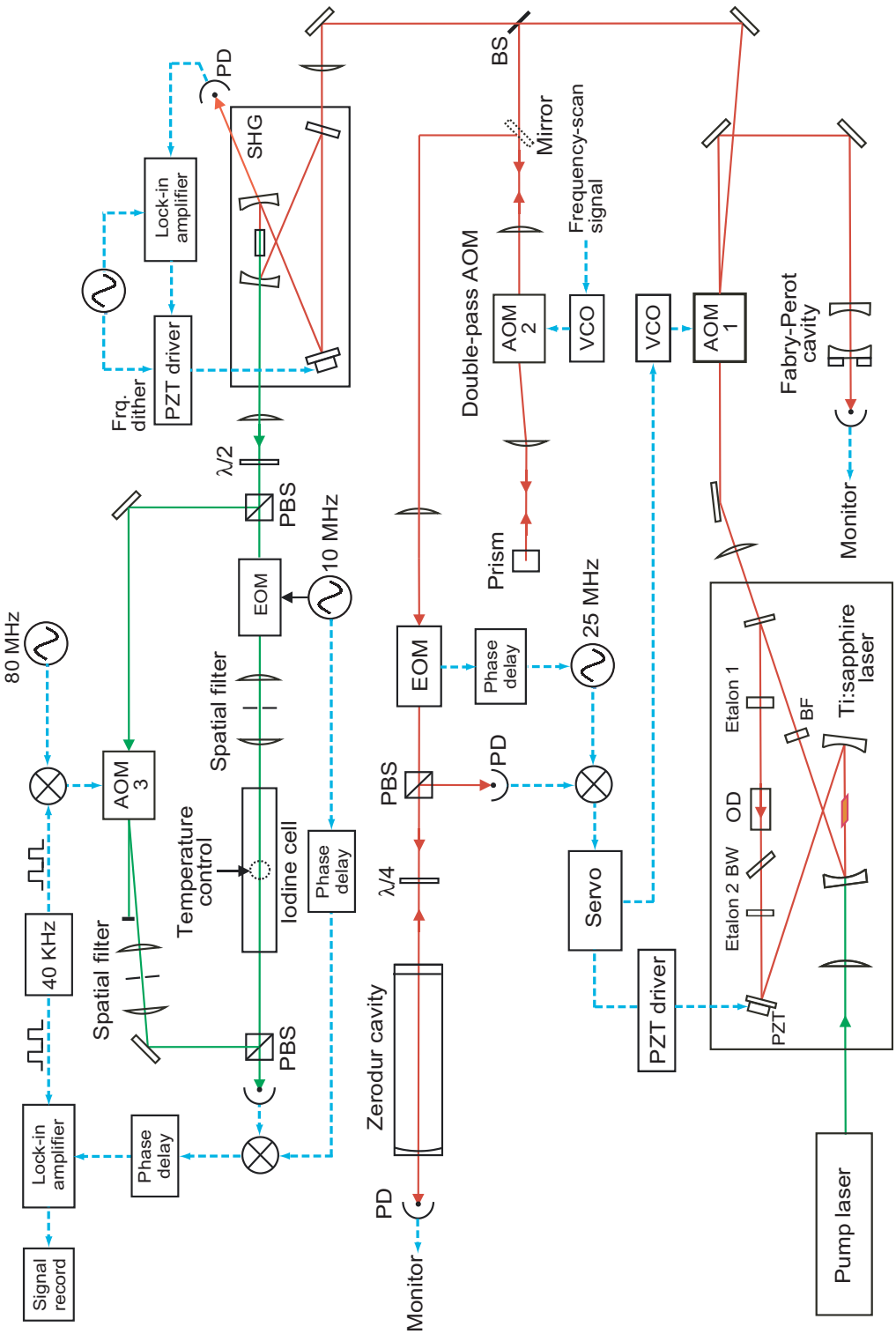

Figure 2.1: Experimental setup of I_2 spectrometer. AOMs, acousto-optic modulators; BF, birefringent filter; BW, Brewster window plate; EOM, electro-optic modulator; OD, optical diode; PBS, polarization beam splitter; PD, photodiode; SHG, second-harmonic generator; $\lambda/4$, quarter-wave plate.

peating transmission peaks, the FSR of the thin etalon is chosen so that it can select a single transmission peak of the thick etalon, which is narrower and in turn selects a single laser mode. This mode selection scheme is illustrated in figure 2.2. Because the lasing process is extremely sensitive to small variation of the net gain, a few percent of the loss provided by the etalon is sufficient to suppress the unwanted cavity modes and hence the etalons used for intracavity mode selection are not coated. The angles of the two solid etalons can be tuned by galvo scanners to select different laser modes.

To probe the narrow resonances of the $^{127}I_2$ transitions, we use a reference cavity with a fixed length to stabilize the frequency of the Ti:sapphire. A small portion of the fundamental power ($\sim$ 15 mW) is sent to this reference cavity for laser frequency stabilization. The cavity uses two highly reflective broadband mirrors (99%; a flat and a concave mirror with R = 1 m) and its FSR and finesse are approximately 234 MHz and 200, respectively. The Zerodur cavity spacer is suspended inside an evacuated aluminum chamber that is temperature controlled to within 20 mK. To effectively isolate the cavity from vibrations of different origins, we wrap the aluminum chamber with lead foils sandwiched by thermal insulation, and three stages of damping structure are cascaded between the chamber and the optical table. The laser is tightly locked to one of the cavity modes using the Pound-Drever-Hall method [22]. The laser frequency is corrected by two feedback transducers: One is a piezoelectric transducer (PZT) mounted on the back of a cavity mirror and the other is an acousto-optic modulator (AOM 1 in figure 2.1) that performs fast frequency correction. The operational laser linewidth is limited by the vibration noise and drift associated with the cavity. The linewidth of this cavity-stabilized Ti:sapphire laser is examined by heterodyne beating its infrared radiation against a free running Yb:YAG laser at 1031 nm. Figure 2.3 shows two beat notes obtained from the heterodyne measurement. The linewidth of the beat note is 23 kHz (FWHM) when the baseplate of the Yb:YAG laser is not temperature controlled, and it falls to 16 kHz

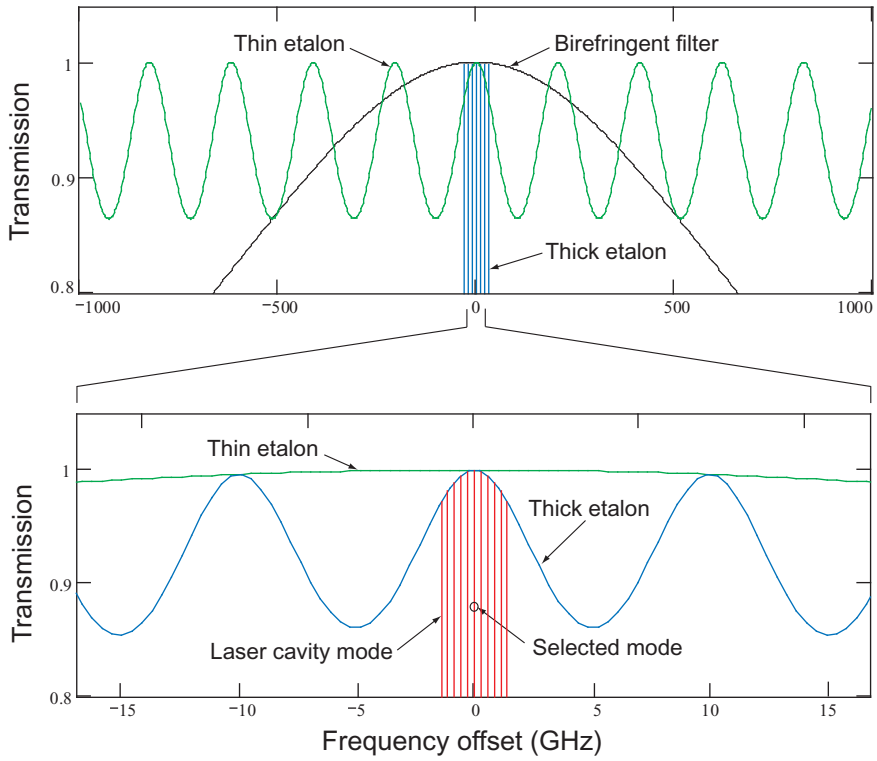

Figure 2.2: Single-mode selection using a birefringent filter and two solid etalons for a ring Ti:sapphire laser. The birefringent filter consists of three quartz plates whose thicknesses are related by integral multiples. The thicknesses of the thin and thick solid etalons are 0.5 mm and 10 mm, respectively. The etalons are uncoated.

(FWHM) once the laser is temperature controlled. This decrease in the linewidth implies that these measurements are probably limited by the free-running linewidth of the Yb:YAG laser.

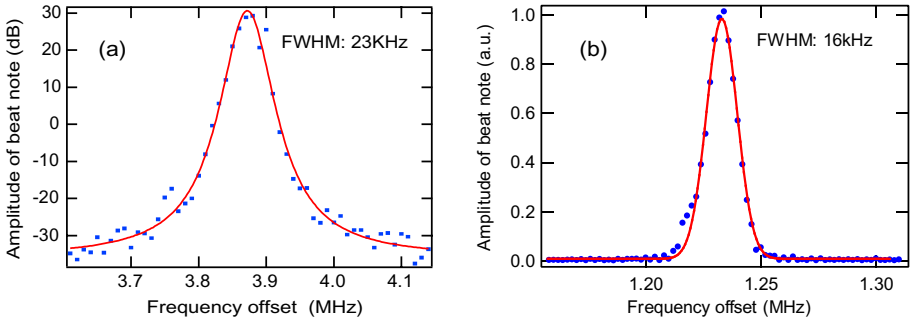

Figure 2.3: Beat signal between a cavity-stabilized Ti:sapphire laser and a free-running Yb:YAG laser at 1301 nm. (a) Yb:YAG laser without temperature control. (b) Yb:YAG laser temperature controlled.

Frequency scanning of the Ti:sapphire laser is accomplished with a double-passed AOM (AOM 2 in figure 2.1) that is located at the cavity input. With a fixed cavity length (aside from drift), changing of the drive frequency of AOM 2 will thus tune the stabilized laser frequency continuously over a 150-MHz range without losing the cavity lock. Because the cavity's FSR (mode spacing) is 244 MHz ($<$ 150 MHz$\times$2), this AOM-based laser tuning allows for continuous frequency scan over consecutive cavity modes, and is basically limited only by the single-mode tuning range of the laser itself.

For second-harmonic generation (SHG), a $KNbO_3$ crystal ($3 \times 5 \times 3$ mm; b cut) is placed inside a buildup cavity. The crystal temperature is varied from 172°C to 71°C to achieve noncritical phase matching at wavelengths ranging from 523 to 498 nm. At 502 nm, SHG yields a roughly 30-mW output power with 190-mW fundamental input. One of the transmission peaks of the buildup cavity is dither-locked to the fundamental laser frequency (see figure 2.1). In this locking scheme, the cavity length is dithered by applying a sinusoidal signal ($10 - 100$ kHz) to the PZT

mounted on the back of a flat cavity mirror. A photodiode receives the cavity leakage at the back of a curved mirror. This signal is then sent to a lock-in servo amplifier that generates error signal by phase-sensitive detection at the dither frequency and its harmonics. The cavity-length correction signal is combined with the dither signal at the high-voltage PZT driver.

Sub-Doppler saturated absorption spectroscopy of I_2 hyperfine components is mainly performed with the FM saturation spectroscopy [35]. The I_2 spectrometer shown in figure 2.1 is similar to that described in reference [41] but has the added flexibility of using either FM spectroscopy (FMS) or modulation-transfer spectroscopy (MTS) for appropriate recovery of a saturated-absorption signal. The light from the frequency-doubling cavity is divided by a polarization beam splitter into two beams that counter propagate inside the iodine cell. The strong pump beam selectively saturates a group of molecules with a very narrow velocity distribution along the direction of the pump beam, while the weak beam probes this group of molecules. The probe beam is phase modulated by a EOM to develop two FM sidebands with opposite phases. When the optical frequency is scanned across the molecular resonance, changes in both absorption and dispersion are converted to the relative phase and amplitude variations among the two sidebands and the carrier. The line shape information is recovered by a phase-sensitive detection at the modulation frequency with a fast photodetector and a radio frequency (RF) mixer. By using high modulation frequencies, this signal recovery scheme can effectively suppress the low frequency instrumental noise. To allow for a lock-in detection of the resonance signal, the pump beam is chopped at 40 kHz by an 80-MHz AOM (AOM 3 in figure 2.1).

The high-purity I_2 cell was prepared by the Bureau International des Poids et Measures and is 8-cm long, with a Brewster window at each end. The I_2 pressure is controlled by the temperature stabilization of the cell's cold finger. Figure 2.4 sketches the two-stage cooling of the cell cold finger. With this two-stage cooling, the

cold-finger temperature can be varied from 15°C to −22°C to access vapor pressures ranging from 18 to 0.37 Pa. The temperature of the copper tube enclosing the cold finger is stabilized and is monitored by a thermistor inside the base of the copper tube. A thermistor with a small bead size and of a different type is placed in contact with the glass wall of the cold finger to verify the accuracy of temperature measurement.

2.3 Sub-Doppler Line Shape Analysis

Using the I_2 spectrometer described in section 2.2, we investigate sub-Doppler transitions of iodine molecules in the wavelength range $523 - 498$ nm. To search for the best candidate for an I_2-based optical-frequency reference requires systematic studies of the linewidth and strength of many transitions in this wavelength region. For each hyperfine component selected, the Ti:sapphire laser is scanned across this component with a typical range of ~ 10 MHz (in green light) and the probe beam is modulated at a frequency of 6 MHz. For a majority of the transitions investigated, the collimated pump and probe beams are of $\sim$ 3-mm diameter and typical pump powers are $1 - 8$ mW. The power of the probe beam is kept an order of magnitude smaller than the pump power.

We fit the sub-Doppler resonance to the line shape derived by Hall *et al.* [36]. The linewidth and the center of the sub-Doppler resonance are extracted from the fit. With the introduction of the two profile functions

$$L^j = \frac{\nu^2}{\Gamma^2 + (\nu^j - \nu_0)^2}, \text{ and } D^j = \frac{\Gamma(\nu^j - \nu_0)}{\Gamma^2 + (\nu^j - \nu_0)^2}, \tag{2.1}$$

the signal obtained from phase-sensitive detection at modulation frequency f_m can be expressed as

$$I_{FM}(\nu) = \alpha[\left(L^- - L^+\right)\sin\phi + \left(D^+ - 2D^0 + D^-\right)\cos\phi]. \tag{2.2}$$

In equations 2.1 and 2.2, ν represents the optical frequency, ν_0 is the center frequency of the optical resonance, superscripts $j = +$, 0, and $-$ label three FM components

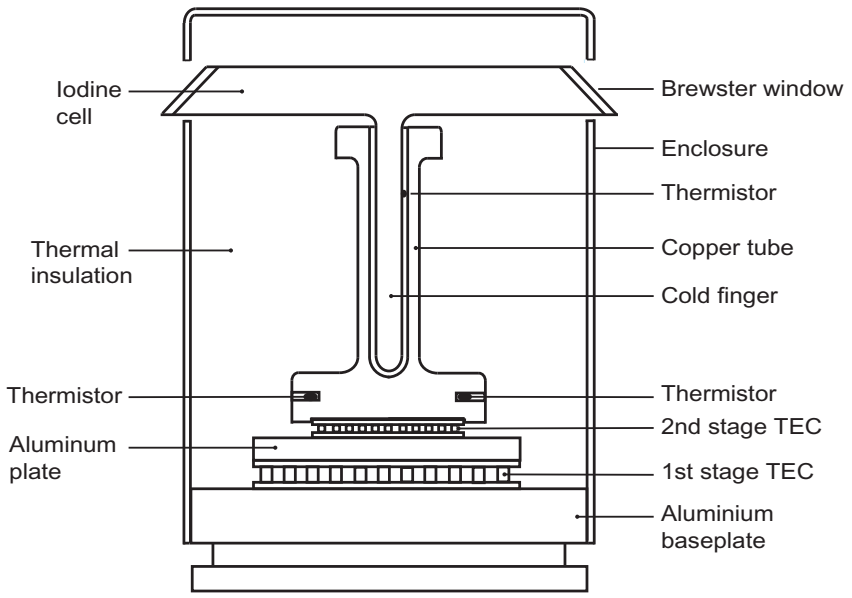

Figure 2.4: Temperature control of the iodine-cell cold finger. The small gap between the glass wall of the cold finger and the copper tube is filled with thermal grease. TEC, thermoelectric cooler.

$\nu^j = \nu + \frac{f_m}{2}$, ν, and $\nu - \frac{f_m}{2}$ [1] , respectively, and Γ is the linewidth (HWHM) of the resonance. In equation 2.2, α is a scaling factor, ϕ is a phase shift that can be adjusted with a delay line inserted between the local oscillator and the mixer used in the phase-sensitive detection. Note that in equation 2.2, we only consider the contributions from the carrier and the two first-order FM sidebands. The modulation spectrum contains mainly these three components because the phase modulation index is always below 1 in our measurements.

Figure 2.5 shows a typical resonance signal recorded for the a_3 hyperfine component at rovibrational transition P(13) 43-0. The resonance signal is obtained with 1.425-Pa vapor pressure, 3.7-mW pump power, and 6-MHz modulation frequency. The fit (solid line) gives a linewidth of 365.9(3.7) kHz. The residual error of the fit is plotted at the bottom of the figure. To reduce the influence of the slow and unidirectional drift of the external cavity, a scan across the resonance is followed immediately by a reverse scan, and the averaged linewidth is adopted.

2.4 Power and Pressure Broadening

To obtain the zero-power, zero-pressure linewidth of a particular line, we typically vary the I_2 cell's pressure from 0.4 to 4 Pa. At each pressure we measure the light-power dependence of the linewidth and determine its zero-power value. We then fit the zero-power linewidth versus pressure to find the zero-pressure linewidth. Near each wavelength we usually measure and compare a few lines that either have different rovibrational quantum numbers in the excited state or are different hyperfine components within the same transition.

The light-power dependence of the linewidth is determined by measuring the resonance linewidth at several power levels. The data points are then fitted to the

[1] The frequencies of the pump and the probe beams are simultaneously tuned, but only the probe beam is frequency modulated. This configuration results in an extra factor of $\frac{1}{2}$ for the modulation frequency f_m [36].

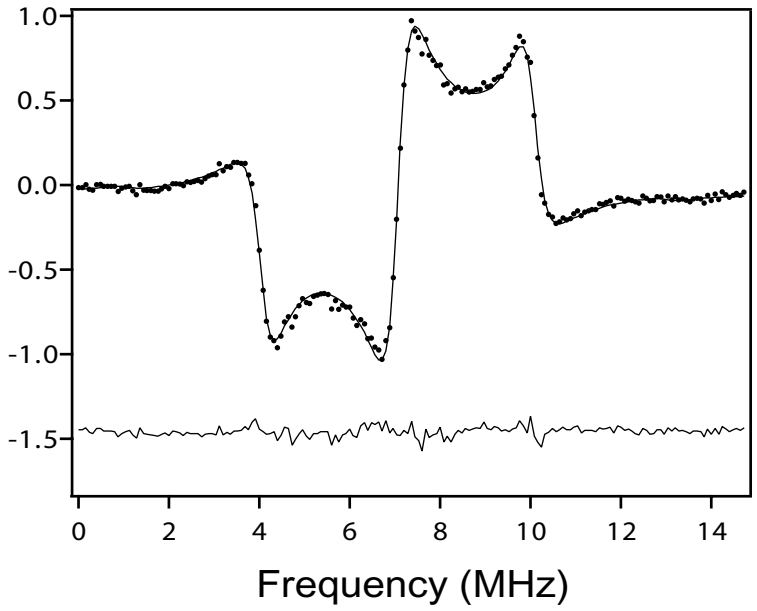

Figure 2.5: Sub-Doppler FM line shape recorded at the a_3 hyperfine component of the P(13) 43-0 transition. The fit (solid line) gives a linewidth of 365.9(3.7) kHz. The bottom curve is the residual error of the fit. The modulation frequency is 6 MHz, the vapor pressure is 1.425 Pa, and the pump power is 3.7 mW.

power-broadening relation

$$\Gamma\left(P,I\right)=\frac{\Gamma\left(P\right)}{2}\left(1+\sqrt{1+I/I_s}\right), \tag{2.3}$$

where I is the power of the pump beam, P is the vapor pressure, and I_s is a pressure-dependent saturation power. Note that this relation applies to our experimental condition in which only the strong pump bean can saturate the I_2 molecules. Figure 2.6 shows the power fit at several vapor pressures for the a_3 hyperfine component at the P(13) 43-0 transition. Each panel in figure 2.6 is the power fit at a certain vapor pressure. At each vapor pressure, power broadening is removed by extrapolating the linewidth to zero power.

Once the effect of the power broadening is removed, the zero-power linewidths at different pressures are fitted to a quadratic pressure dependence

$$\Gamma\left(P\right)=\Gamma+aP+bP^2. \tag{2.4}$$

Such a pressure fit at the a_1 hyperfine component of the P(17) 54-0 transition is shown in figure 2.7. In this case, two fits are performed. The first includes all the data points. As can be seen in the figure, a data point with a vapor of ~ 2 Pa has a relatively large residual error. This point is excluded in the second fit, which produces an 8-kHz difference in the fitted zero-pressure linewidth. The 1-σ uncertainties of the fitted zero-pressure linewidth are also given in the figure. As another example, figure 2.8 shows three pressure fits with the corresponding hyperfine components indicated in the figure. We notice that, even at nearly the same wavelength, natural linewidths of transitions with vastly different rotational quantum numbers can differ by as much as 40 kHz and exhibit quite different collision broadening coefficients.

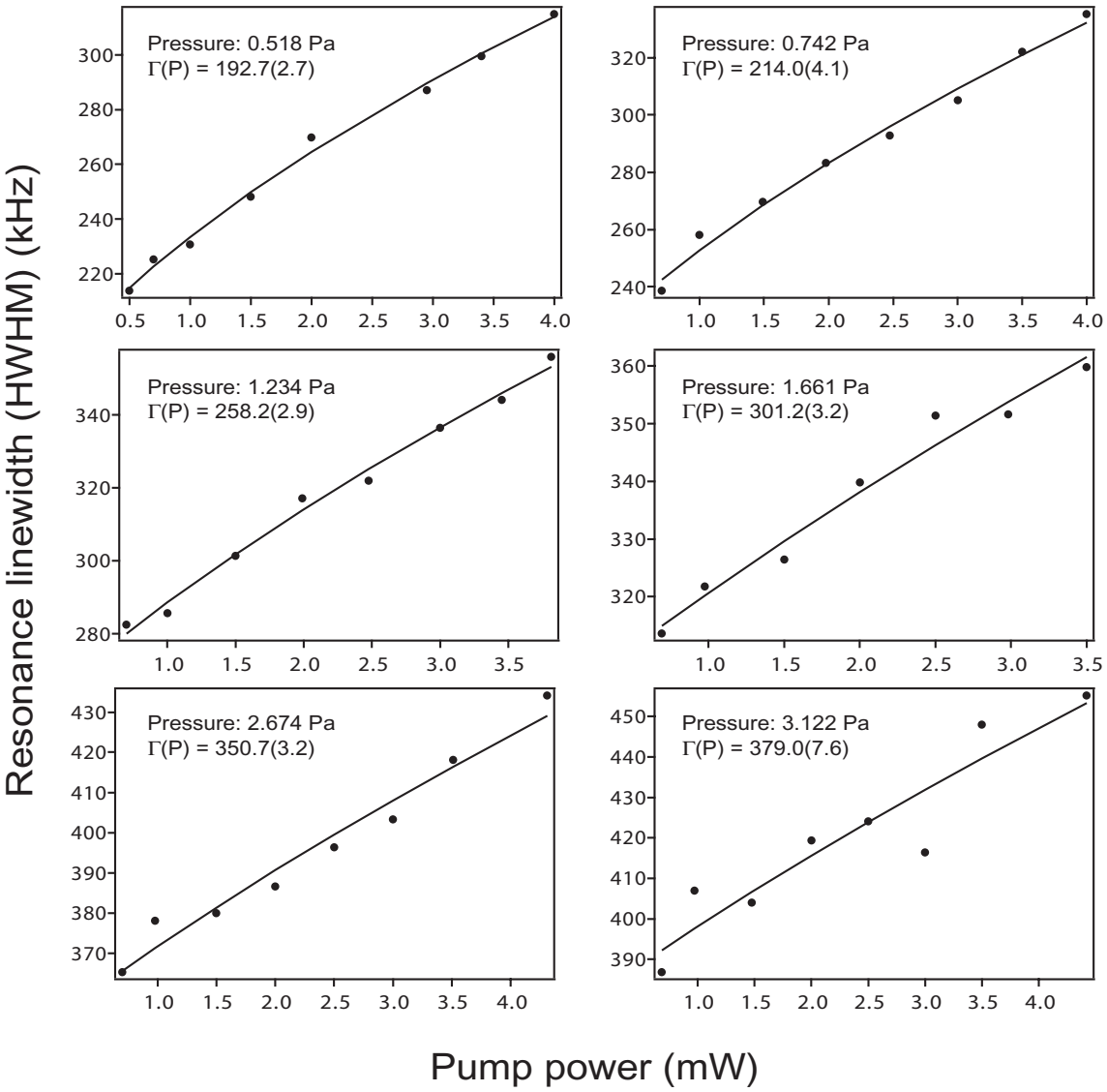

Figure 2.6: Power broadening at the a_3 hyperfine component of the P(13) 43-0 transition. Each panel shows the power broadening at a certain vapor pressure. Solid lines are the fit to the power dependence describing two counter propagating beams among which only the strong pump beam has a saturation effect. At each pressure, power broadening is removed by extrapolating the linewidth to zero power.

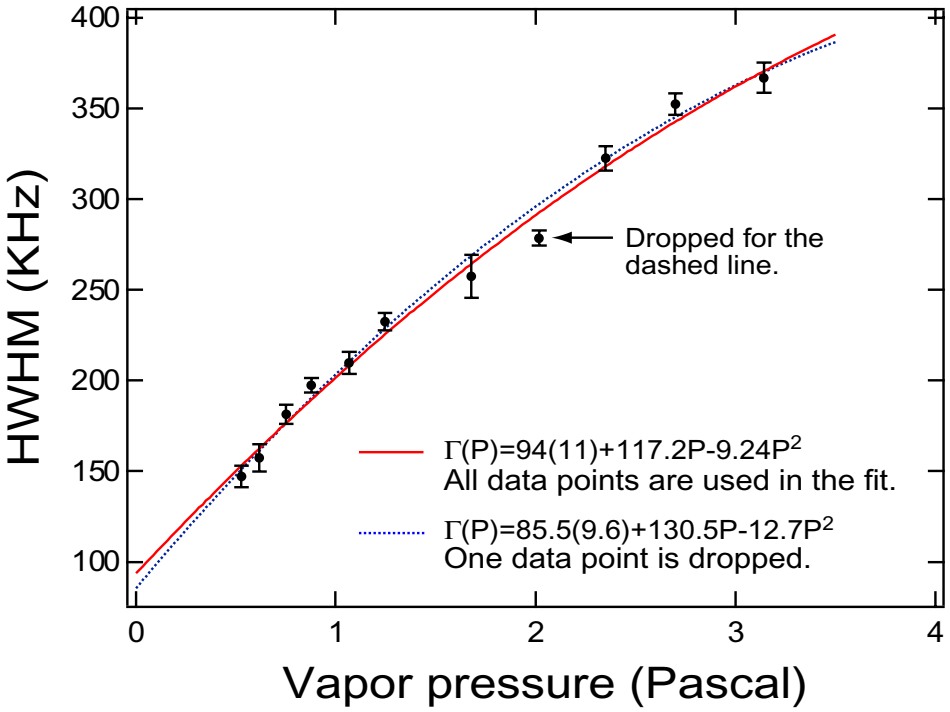

Figure 2.7: Pressure broadening at the a_1 component of the P(17) 54-0 transition. The power broadening at each pressure has already been removed.

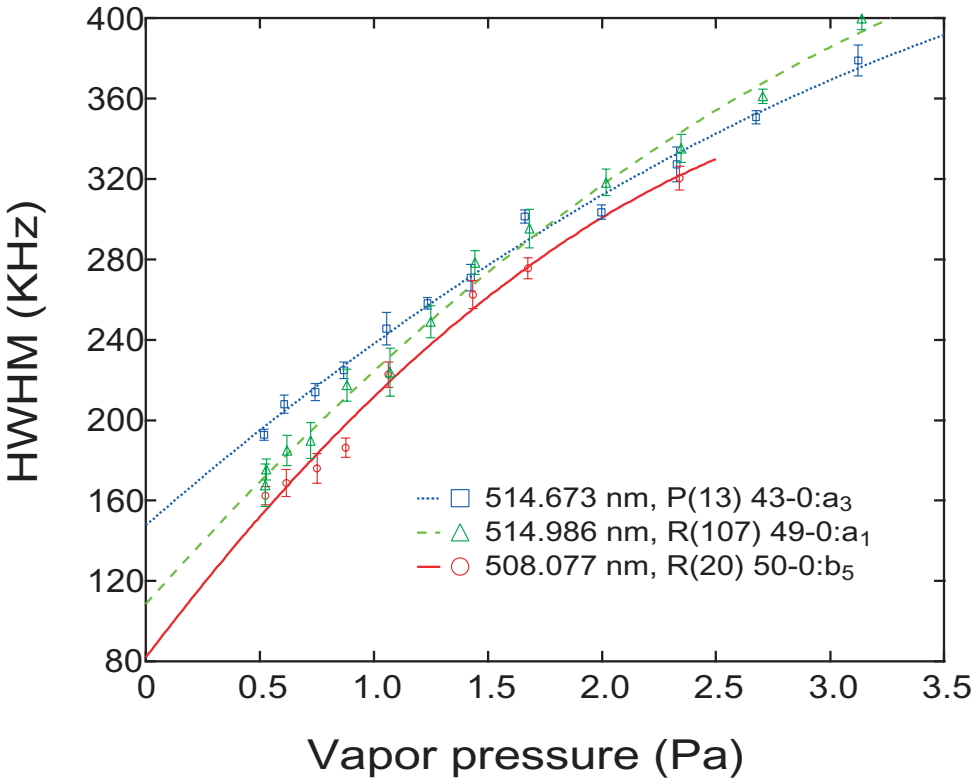

Figure 2.8: Half-width versus pressure of three iodine transitions. The power broadening at each pressure has already been removed.

2.5 Hyperfine-Transition Linewidth near the B-State Dissociation Limit

In this section we investigate various broadening effects encountered in the linewidth measurement. Their estimated values and corresponding uncertainties are summarized in table 2.1. At the a_3 hyperfine component of the P(13) 43-0 transition, we compare our result with that obtained by two-photon resonant scattering technique in a previous experiment [57]. Figure 2.9 shows the comparison. In both cases, various broadening effects, such as transit-time, power, pressure, and laser linewidth, have been removed.

Table 2.1: Estimation of various linewidth broadening effects.

Broadening effect	Dependence (HWHM)	Value	Uncertainty
Transit time $\Delta\nu_{tt}$ [18]	$\frac{1}{2\pi}\sqrt{2\ln 2}\sqrt{\frac{\pi kT}{2M}}\frac{1}{w(z)}$	15 kHz	2.0 kHz
Wave-front curvature [58]	$\Delta\nu_{tt}\left(\frac{\pi w(z)^2}{R(z)\lambda}\right)^2$	1.8 kHz	1.0 kHz
Recoil doublet [18]	$\frac{1}{2}\frac{h\nu^2}{Mc^2}$	3.0 kHz	–
Laser linewidth	$\frac{\Delta\nu_{beat}(\mathrm{HWHM})}{2}$	8 kHz	4.6 kHz
Pressure broadening	$\Gamma(P) = \Gamma + aP + bP^2$	–	10 kHz
Total		28 kHz	12 kHz

Figure 2.10 displays a number of measured zero-pressure linewidths. For comparison, the 543-nm (reference [60]) and 532-nm data points are also included. The dashed line (28 kHz) at the bottom of the figure represents the remediable technical limit to the measured linewidth, including contributions from wave-front curvature and transit time (17 kHz), laser linewidth (in the green, 8 kHz), and recoil doublet (3.0 kHz). The narrowest natural width that we have found so far is $\sim$ 52 kHz (HWHM) for the b_5 component at the R(20) 50-0 transition (508.077 nm). As

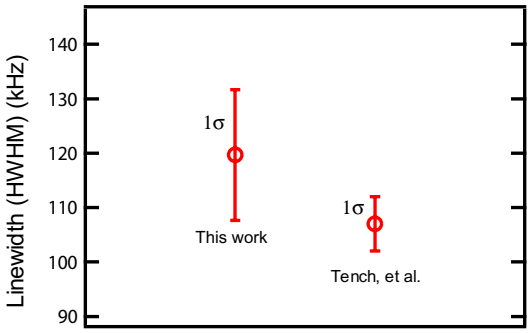

Figure 2.9: Comparision of linewidth measurement at the a_3 hyperfine component of the P(13) 43-0 transition. The data on the right is from reference [59]. In both results, various broadening effects, such as transit-time, power, pressure, and laser linewidth, have been removed.

shown in figure 2.10, we observe a clear trend of linewidth narrowing with decreasing transition wavelength.

This linewidth narrowing at shorter wavelength can be explained by the decreasing $B \rightarrow X$ transition probability when the levels in the B state approach the dissociation limit [61]. For a vibrational level close to the dissociation limit, a molecule spends most of its time around the outer classical turning point where it can be viewed as two separated atoms. With this separated-atom model in mind and considering that the B and the X sates dissociate respectively into $^2\mathrm{P}_{\frac{3}{2}} + {}^2\mathrm{P}_{\frac{1}{2}}$ and $^2\mathrm{P}_{\frac{3}{2}} + {}^2\mathrm{P}_{\frac{3}{2}}$ atomic states, a $B \rightarrow X$ transition at large internuclear separations requires an atomic $^2\mathrm{P}_{\frac{1}{2}} \rightarrow {}^2\mathrm{P}_{\frac{3}{2}}$ transition, which is an electric dipole forbidden transition.

In an attempt to quantitatively analyze the linewidth narrowing, we perform the calculations of the radiative decay rate from B to X. The radiative decay rates from a level (υ', J') in the B state to all possible levels (including energy continuum) in the X state amount to [62]

$$\begin{aligned} A\left(\upsilon' J'\right) &= \frac{1}{4\pi\varepsilon_0}\frac{64\pi^4}{3hc^3}\sum_{\upsilon''}\sum_{J''=J'\pm 1}\frac{S_{J'J''}}{2J'+1}\nu^3\left|\left\langle \upsilon' J'\right|\mu_e\left(R\right)\left|\upsilon'' J''\right\rangle\right|^2 \\ &= \frac{1}{4\pi\varepsilon_0}\frac{64\pi^4}{3hc^3}\sum_{\upsilon''}\nu^3\left|\left\langle \upsilon' J'\right|\mu_e\left(R\right)\left|\upsilon'' J'\right\rangle\right|^2, \end{aligned} \tag{2.5}$$

where $S_{J'J''}$ is the Hönl-London rotational intensity factor ($S_{J'J''} = J'$ for R branch and $S_{J'J''} = J'+1$ for P branch), ν is the frequency of the transition $(\upsilon' J') \rightarrow (\upsilon'' J'')$, R is the internuclear separation, and $\mu_e\left(R\right)$ is the transition dipole moment. The squared matrix element in equation 2.5 is often evaluated by employing the R-centroid approximation:

$$\left|\left\langle \upsilon' J'\right|\mu_e\left(R\right)\left|\upsilon'' J''\right\rangle\right|^2 \approx \left|\mu_e\left(R_c\right)\right|^2\left|\left\langle \upsilon' J'\right|\upsilon'' J''\right\rangle\right|^2, \tag{2.6}$$

where the R-centroid is defined as

$$R_c = \frac{\left\langle \upsilon' J'\right|R\left|\upsilon'' J''\right\rangle}{\left\langle \upsilon' J'\right|\upsilon'' J''\rangle}. \tag{2.7}$$

The radiative decay rates of the B-state levels in the wavelength range $500-540$ nm are calculated according to equation 2.5. In the first calculation we choose a transition dipole moment obtained by Tellinghuisen [63] from an empirical fit of radiative decay rates measured at various rovibrational levels in the B state [61]:

$$\mu_e(R)^2 = c_1 \exp\left[-c_2 (R-c_3)^2\right] R^{-2}, \tag{2.8}$$

where $c_1 = 21.5(2.1)$ Debye^{2}Å^2, $c_2 = 1.73(37)$ Å^{-2}, and $c_3 = 3.49(12)$ Å. The unit Debye is defined as 1 Debye $= (10^{-21}/c) = 3.33564095 \times 10^{-30}$ Cm [64], where c is the speed of light in m/s. In the second calculation we adopt the transition dipole moment obtained by Lamrini *et al.* [62]. Lamrini *et al.* determined the transition dipole moment by selectively exciting molecules to a B-state level and measuring the intensity spectrum of the florescence. Because only relative values are available in their measurement, the experimental determined radiative rate at $v' = 43$ [65] was used to calibrate the absolute scale of the transition dipole moment. This transition dipole moment is given in the R-centroid approximation:

$$\log_{10}\frac{|\mu_e(R_c)|^2}{1\ \text{Debye}^2} = \begin{cases} -134.0416 + 166.1989R_c - 75.81764R_c^2 & \\ +15.12918R_c^3 - 1.12537R_c^4 & (2.633\ \text{Å} \leqslant R_c \leqslant 3.9\ \text{Å}) \\ & \\ 2.6642 - 1.1635R_c & (3.9\ \text{Å} < R_c \leqslant 6.035\ \text{Å}) \end{cases} \tag{2.9}$$

with a standard deviation

$$\sigma(|\mu_e|^2) = \begin{cases} 0.150\,|\mu_e(R_c)|^2 & (2.633\ \text{Å} \leqslant R_c \leqslant 3.9\ \text{Å}) \\ 0.545\,|\mu_e(R_c)|^2 & (3.9\ \text{Å} < R_c \leqslant 6.035\ \text{Å}). \end{cases} \tag{2.10}$$

The radiative decay rates are calculated after a global shift of the right-hand side of equation 2.9 by an amount of 0.30103 to allow agreement with the radiative decay rate $\Gamma_{rad} = (31.4 \pm 1.8) \times 10^4$ s^{-1} measured directly at $v' = 43$ [65].

The calculated radiative decay rates are divided by a factor of 2 for HWHM and then are plotted as solid curves in figure 2.10. Both two calculations show a

decreasing trend consisting with the measurement. However, this tendency is complicated by variations in linewidth among various rotational or hyperfine components even at the same wavelength. Besides the radiative decay, the gyroscopic and the hyperfine predissociations through the $B''1_u(^1\Pi)$ state provide another depopulating channel that increases the B-state natural width. The predissociation rates not only depend on the rovibrational levels but are also different for hyperfine sublevels within one rovibrational level [66]. For example, the predissociations contribute $5 - 61$ kHz (FWHM) [57] to the natural widths of various hyperfine components belonging to the P(13) 43-0 and the R(15) 43-0 transitions. As the B-state level approaches the dissociation threshold, the limit on lifetime imposed by predissociations will need to be taken into consideration [66, 67, 61]. Last, we point out that both calculations overestimate the radiative decay rates compared with the experimentally determined natural widths, which are due to radiative decay and predissociations. The calculation can be improved by calibrating the absolute scale of the dipole moment, such as that given in equation 2.9, with radiative decay rates measured at more hyperfine levels in the wavelength range $500 - 550$ nm.

2.6 Hyperfine Spectra near the B-State Dissociation Limit

Figure 2.11 shows some typical saturation spectra of I_2 transitions from 523 to 500 nm. These spectra were obtained with a vapor pressure of 4.12 Pa. The I_2 transitions are identified by the CNRS I_2 spectral atlas [68]. However, spectra obtained below 500.53 nm are out of the range of the I_2 atlas. Our I_2 spectrometer is found to have a constant noise floor throughout the wavelength range of interest. Strong transitions (with strengths comparable to those of 532-nm lines) are relatively common in the range from 530 to 510 nm, as shown in figure 2.11. Near the dissociation limit (499.5 nm) [69], the line strengths and associated S/Ns decrease substantially.

With such a widely tunable spectrometer, a large range of rovibrational quan-

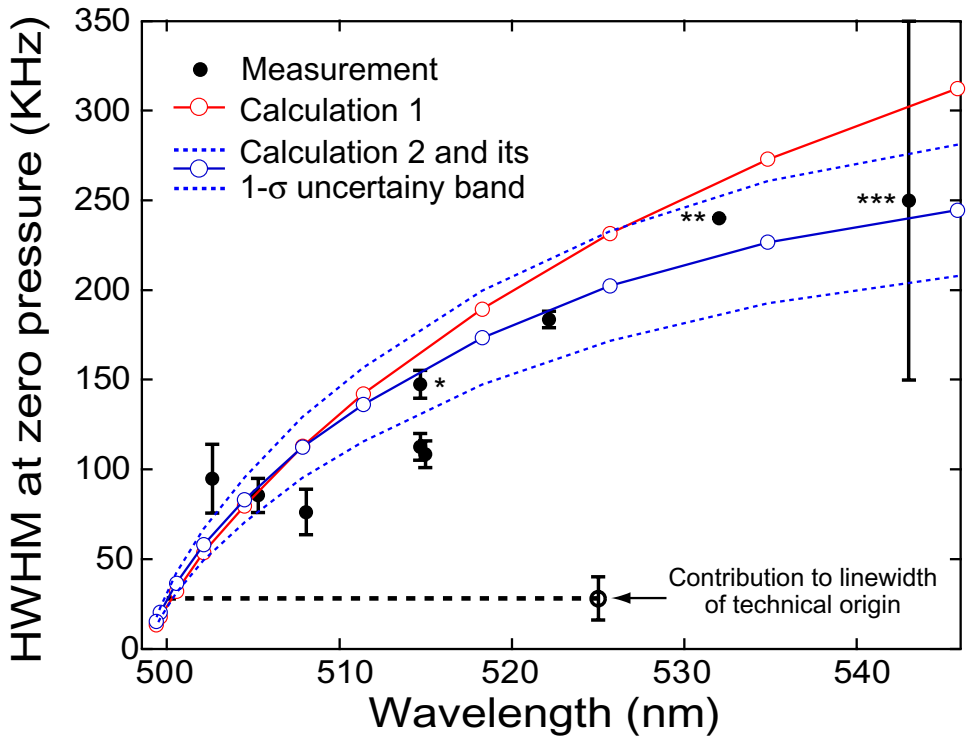

Figure 2.10: Wavelength dependency of linewidth. Solid circles are measurement results with the collision-induced broadening removed. These results include the broadening effects such as transit time, laser linewidth, and recoil splitting, whose accumulated contribution is represented by the dashed line. The solid curves with open circles are calculated widths due to electric dipole transition $B \longrightarrow X$. Calculations 1 and 2 adopt transition moment functions obtained by Tellinghuisen [63] and Lamrini *et al.* [62], respectively. Gyroscopic and hyperfine quenching of the B-state levels through a $B''1_u(^1\Pi_u)$ state also broadens the upper levels, which may prevent the fast decreasing trend indicated by the calculation near and below 500 nm. *, wavelength standard P(13) 43-0, a_3 at 514.673 nm [40]; **, measured by Nd:YAG laser; ***, measured by HeNe laser [60].

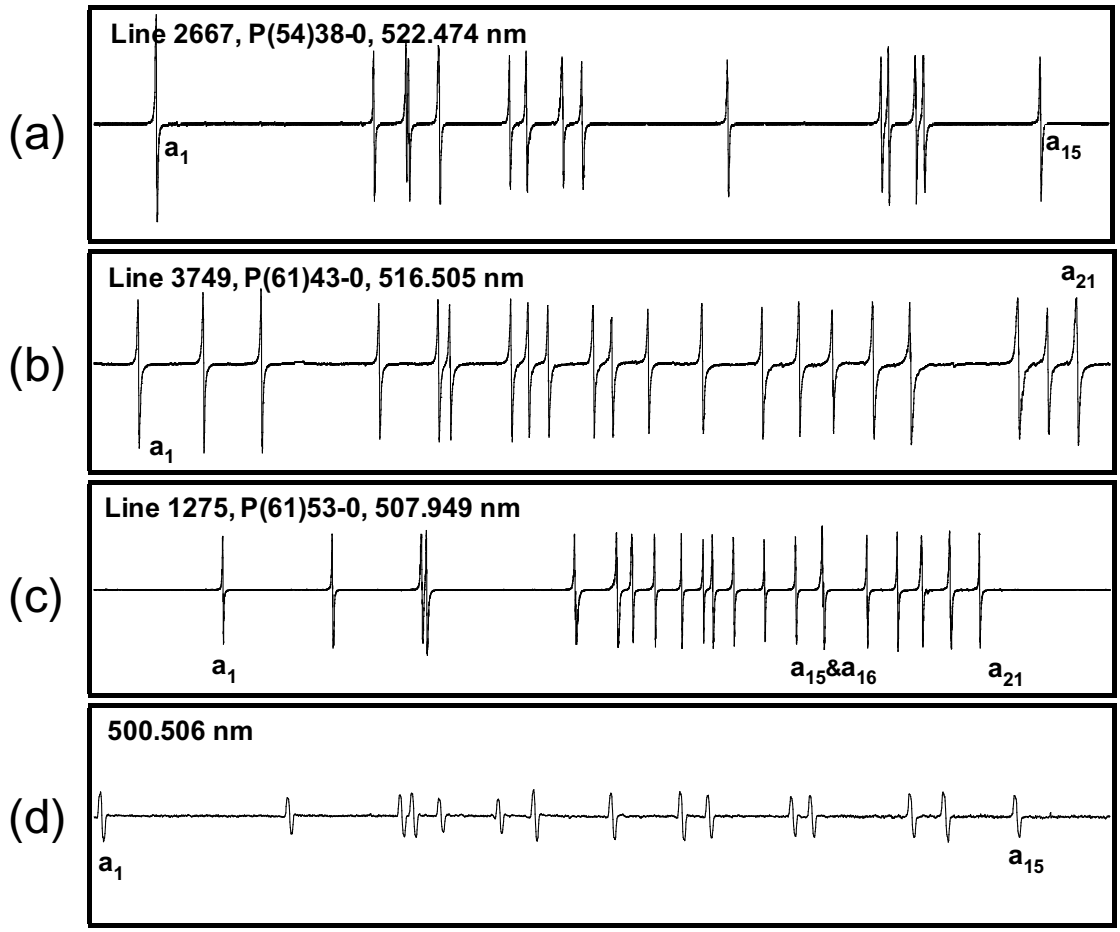

Figure 2.11: Typical spectra of I_2 hyperfine transitions from 523 to 500 nm. (a), (b), (c) MTS, 273-kHz modulation frequency; (d) FMS, 6-MHz modulation frequency. The quoted [68] line strengths are (a) 80, (b) 79, and (c) 55. The time constant is 5 ms for (a)–(c) and 100 ms for (d). Length of I_2 cell, 8 cm; vapor pressure, 4.12 Pa.

tum numbers can be addressed, allowing a detailed parametric study of transition strengths, hyperfine interactions, and collision physics. For example, figure 2.11 (a) shows that the spectrum of P(54) 38-0 at 522.474 nm (even rotational quantum number J'') follows the usual 15-line hyperfine pattern (1–4–4–1–4–1), whereas the spectrum of P(61) 43-0 at 516.505 nm (odd rotational number J''), shown in figure 2.11 (b), displays the typical 21 hyperfine components (3–4–4–3–4–3). However, as the transition wavelength approaches the predissociation region, e.g., line P(61) 53-0 at 507.949 nm [figure 2.11 (c)], the pattern of hyperfine splittings starts to change. When the wavelength approaches the dissociation limit, as at 500.506 nm, the 15-line pattern is completely modified [figure 2.11 (d)]. Similar observations are made for other lines near 500 nm. Clearly the hyperfine interactions are dramatically influenced by the dissociation effect and other nearby electronic states converging with the B state toward the second dissociation limit.

2.7 System Performance

In this section, we explore the potential performance of an iodine-cell-based frequency standard operating at wavelengths below 532 nm. The Ti:sapphire laser is locked on a hyperfine component of molecular iodine. We send the resonance signal extracted from FM saturation spectroscopy to a JILA loop filter to generate a frequency correction signal. This correction signal is dispatched to a voltage control oscillator (VCO), which in turn adjusts the frequency shift of the double-passed AOM between the external cavity and the Ti:sapphire laser (AOM 2 in figure 2.1). This second feedback loop basically suppresses the drift and low-frequency noise from the external cavity. The transition selected for this evaluation is one of the hyperfine components of R(86) 57-0 at 508.060 nm. Figure 2.12 shows the resonance signal of the selected hyperfine component recovered with FM saturation spectroscopy. The modulation frequency and the time constant used in the FM saturation spectroscopy

are 6 MHz and 1 ms, respectively. The cold finger temperature of the I_2 cell is $-15°C$, corresponding to a vapor pressure of 0.79 Pa.

The projected frequency noise of a laser locked to the center of a hyperfine component can be estimated from the discrimination slope and the rms noise at the baseline of the FM resonance signal. For the signal shown in figure 2.12, the estimated frequency noise is 3 kHz, corresponding to a fractional noise of 5×10^{-12} at 1 ms or 1.6×10^{-13} at 1 s, with an 8-cm-long cell. The best (in)stability reported in an I_2-stabilized laser system is 5×10^{-14} at 1 s with a 120-cm long I_2 cell, also at $-15°C$ [41]. Therefore the performance of the new system, if it is scaled to the same I_2 cell length, would have an (in)stability of 1×10^{-14} at 1 s. Placing the I_2 cell inside a multipass cavity will further improve system performance.

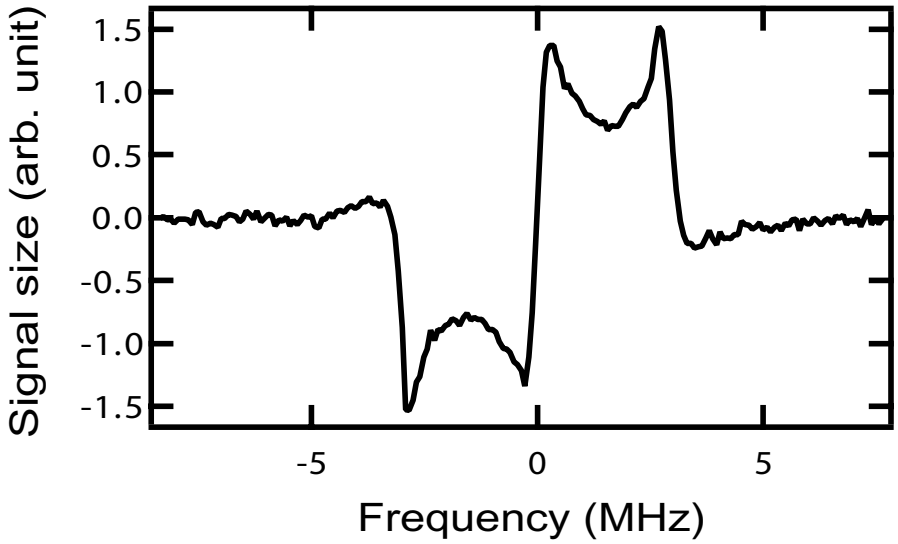

Figure 2.12: Typical FM signal recorded for a hyperfine component of R(86) 57-0 at 508.060 nm. Laser frequency stabilization with the discrimination slope at the line center will lead to a projected (in)stability of 1.6×10^{-13} at 1 s, or 1×10^{-14} at 1 s for a 120-cm-long I_2 cell.

2.8 Summary

A widely tunable and high-resolution spectrometer based on a frequency-doubled Ti:sapphire laser is used to explore sub-Doppler transitions of iodine molecules in the wavelength range $523 - 498$ nm. The wavelength dependence of the hyperfine transition linewidth of iodine is mapped out in this region, and the narrowest linewidth is ~ 52 kHz near 508 nm. The observed excellent S/N for the recovered resonance signal indicates that I_2 transitions in the wavelength range $532 - 501$ nm hold a great promise for future development of optical frequency standards, especially when coupled with the all-solid-state Yb:YAG laser. In addition, the hyperfine-resolved patterns are found to be largely modified toward the dissociation limit.

Frequency-based measurements of hyperfine spectra across a large number vibrational levels will reveal important information on the variations of charge distribution and molecular configuration. Based on this observation, we perform an extensive investigation of the hyperfine spectrum in the wavelength range $517 - 500$ nm. The details of this investigation will be covered in chapter 4.

Chapter 3

OPTICAL FREQUENCY MEASUREMENT OF MOLECULAR IODINE HYPERFINE TRANSITIONS

3.1 Introduction

Our knowledge of the precise values of physical quantities in many branches of metrology is ultimately tied to frequency measurement. The definition of the unit of length and its practical realization are based on the adopted value for the speed of light, $c = 299\ 792\ 458$ m/s, and the frequency of an optical transition. Thus, length measurements are based on the unit of time. This notion is reflected by the fact that twelve optical transitions in the infrared and visible regions are recommended by the Comité International des Poids et Mesures (CIPM) [40] for the realization of meter, the SI unit of length. Among the listed optical frequencies recommended by CIPM, molecular iodine (I_2) holds a unique position in that it offers five reference lines that have been widely used for metrological calibration.

Nd:YAG lasers, frequency doubled and stabilized by I_2 hyperfine transitions near 532 nm, have demonstrated a remarkably high stability of 5×10^{-14} at 1 s [41]. Near 515 nm, frequency-doubled all-solid-state Yb:YAG lasers with compact size and high output power also exhibit low intrinsic frequency noise. Moreover, our work discussed in the previous chapter showed that below 532 nm, the natural widths may decrease at a faster rate than line strengths. Therefore, to attain a higher frequency stability, it is useful to explore the performance of I_2-stabilized

laser systems below 532 nm. Absolute frequency measurements performed in this wavelength region are an effective way to evaluate the potential of these systems for serving as future frequency standards. Although the system at 514.67 nm promises to be one of the better-quality standards based on I_2, historically it has been probed only with cumbersome Ar^+ laser systems and the transition frequency determined only through wavelength interferometry. The recommended 514.67-nm length standard was based on such measurements of the hyperfine component a_3 at transition P(13) 43-0 of $^{127}I_2$. The adopted value by the CIPM in 1997 is 582 490 603.37 MHz, with a standard uncertainty of 0.15 MHz (2.5×10^{-10}), for an iodine-cell cold-finger temperature set at $-5°C$ [40].

The accepted primary frequency standard thus far is based on a hyperfine transition in atomic cesium, with the transition frequency of 9.1926317700×10^9 Hz. Prior to the introduction of femtosecond lasers, the optical frequency measurement was done by complex frequency chains (harmonic-synthesis frequency chains or optical-frequency interval-divider chains) [70, 71, 72, 73, 74, 75, 76, 77] to bridge the enormous frequency gap that separates the radio and optical frequencies. Since the introduction of Kerr-lens mode-locked femtosecond lasers for optical frequency metrology [13, 14], wide bandwidth optical combs have revolutionized optical frequency measurements, impacting a wide range of optical frequency standards based on transitions of atoms, ions, or molecules [78, 79, 80, 81]. Femtosecond laser combs serve the same purpose as frequency chains in measuring absolute optical frequencies, but do so in just one step with access to a broad optical spectrum and with a greatly simplified system setup. Basically, mode-locked lasers can generate a femtosecond-pulse train with precise periodicity. In the frequency domain, this pulse train corresponds to a comb of narrow and equidistant frequency components spanning a bandwidth ranging from several tens of terahertz to about one hundred terahertz. The frequency structure of the comb can be characterized by a surprisingly small set of parameters [82, 15]:

$\nu_m = mf_{rep} + f_{ceo}$, where m is the mode order ($\sim 10^5 - 10^6$), f_{rep} is the repetition rate of the pulse train or, equivalently, the mode spacing of the frequency comb, and f_{ceo} is the carrier-envelope offset frequency [83]. Both f_{rep} and f_{ceo} are radio frequencies (RF). Through this relationship, the optical frequencies are linked directly to the RF frequencies, and vice versa. In a typical frequency measurement, the repetition rate, f_{rep} (or mode spacing of the comb), of the femtosecond laser is phase-coherently locked to the Cs microwave frequency standard. The other degree of freedom associated with the femtosecond comb, i.e., the carrier-envelope offset frequency, f_{ceo}, can also be measured or stabilized with the same RF reference using a self-referencing approach [79] or another known optical standard. This drastically simplified frequency-measurement scheme can be realized with a reliable and compact table-top system. The measurement reliability and accuracy of the optical comb system have been carefully studied [80, 81]. The I_2-based 532-nm laser system has been used to stabilize an entire octave-bandwidth-spanning optical frequency comb based on a mode-locked Ti:sapphire laser, thus establishing an new concept of optical atomic clock in which the RF signal is phase-coherently derived from the I_2 optical transition [54].

This chapter reports the first absolute frequency determination of the 514.67-nm length standard at the a_3 hyperfine component of the P(13) 43-0 transition in $^{127}I_2$. Our absolute frequency measurement employs a phase-coherent optical frequency comb linked to the Cs primary clock, which is the current realization of the unit of time. This measurement produces a 100-fold improvement in the precision over previous wavelength-based results. In section 3.2, I will give a brief introduction of the principles and operations of femtosecond laser frequency combs in the context of frequency metrology. Section 3.3 covers the details of the experimental setup and measurement results. The frequency comb used in this experiment is described. The experimental details of the iodine spectrometer have already been discussed in the

previous chapter. Therefore only the modifications made for this experiment are explained in this section. The remainder of the section presents the results of the short- and long- term optical-frequency measurements, along with a characterization of the iodine spectrometer by the femtosecond laser comb.

3.2 Optical Frequency Comb Based on Femtosecond Lasers

3.2.1 Kerr-Lens Mode-Locked Ti:Sapphire Laser

The Kerr-lens mode-locked Ti:sapphire laser [84, 85] plays a central role in our optical frequency measurement. Figure 3.1 shows schematics of two typical Kerr-lens mode-locked Ti:Sapphire lasers with prism-based [86] and prismless ring-cavity [84] configurations. The Ti:sapphire crystal in the laser cavity is pumped by 532-nm green light from a diode-pumped solid-state (DPSS) laser that provides a reliable single mode operation. The Ti:sapphire crystal serves both as the gain medium and the saturable absorber for passive mode locking. A pair of prisms is added to the cavity to compensate for the group-velocity dispersion (GVD) of the Ti:sapphire crystal in the standing-wave configuration [87], while the same dispersion management is performed by a set of chirped mirrors in the ring-cavity configuration [88].

In sharp contrast to the singe-mode continuous-wave (CW) operation described in previous chapter, a large number of cavity modes ($\sim 10^5 - 10^6$) within the Ti:sapphire gain bandwidth ($700 - 1000$ nm) are active and are synchronized in phase in a mode-locked Ti:sapphire laser, resulting in a train of femtosecond pulses with precise periodicity and stable pulse shape. This soliton-like propagation of the optical pulse in the cavity is a consequence of the nonlinear interaction between the optical pulses and the Ti:sapphire gain medium. Most optical material exhibits a field-induced change in the refractive index, which is referred to as the optical Kerr

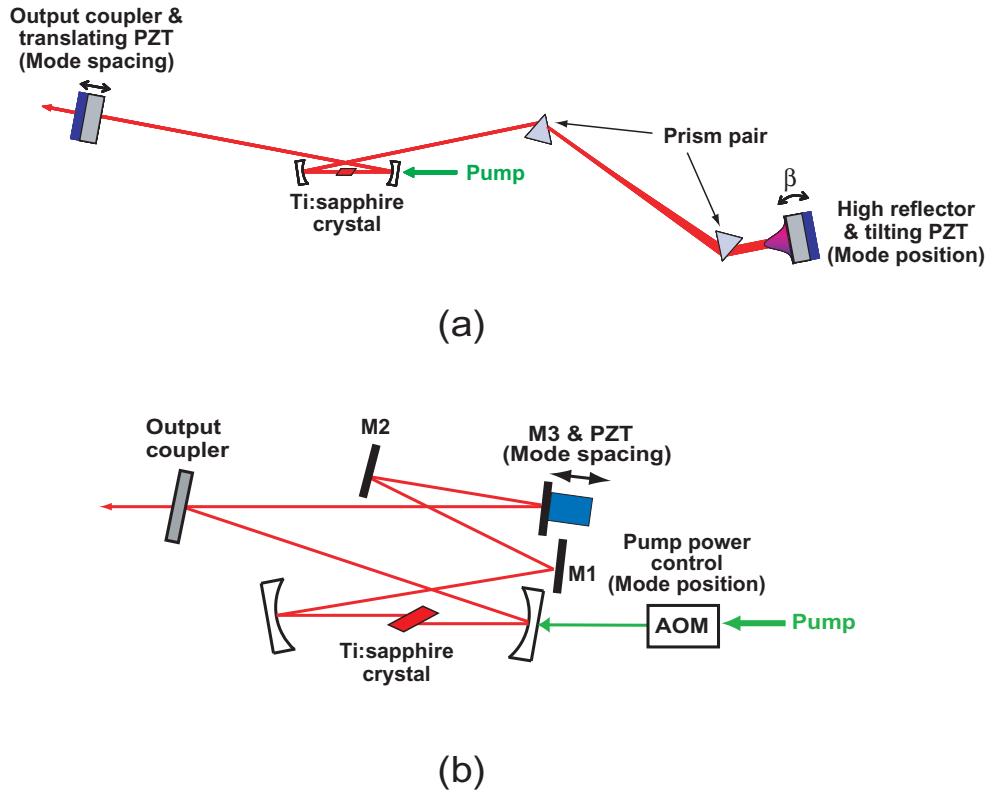

Figure 3.1: Schematic of two Kerr-lens mode-locked Ti:sapphire lasers with (a) standing-wave configuration and (b) ring-cavity configuration. M1−M3 are chirped mirrors.

effect and can be written as [89]

$$n = n_0 + n_2 I, \tag{3.1}$$

where I is the optical intensity and $n_2 > 0$ for Ti:sapphire gain medium. When a light beam passes through the Kerr medium, it creates an index profile that resembles the beam's transverse intensity distribution. Because this index profile is equivalent to a convex lens (Kerr lens), the beam is focused toward the center and its intensity is amplified.

The nonlinear Kerr-lens mechanism initiates and enforces the passive mode-locking process. When one of the folding mirrors[1] is translated away from its optimized position for the CW-laser operation, the lasing mode in the cavity can no longer saturate the Ti:sapphire gain medium. However, the spatially focused pulses with enhanced peak intensity can still saturate the gain medium and pass through the small gain region. Noise spikes in the cavity provide the seed from which the Kerr-lens mode-locking (KLM) [90] starts. In addition, the KLM tends to temporally compress the pulse because only the central portion of the pulse has enough intensity to burn its way through the saturable absorber, whereas the pulse tails experience a net loss.

As circulating pulses are continuously compressed by the KLM process, the self-phase modulation (SPM) plays an important role in pulse shaping [89]. The Ti:sapphire crystal exhibits positive dispersion[2] within its gain bandwidth. To compensate for this positive dispersion, a prism pair or chirped mirrors are introduced into the cavity, resulting in a negative net dispersion. A nonzero dispersion leads to a rapid breakup of the pulse as it travels through a dispersive medium. However, this "cold" cavity picture is completely modified by the SPM process. An intensity-

[1] One of the curved mirrors away from the pump laser.

[2] A positive dispersion refers to $\frac{d^2k(\omega)}{d\omega^2} > 0$, which gives a negative GVD: $\frac{dv_g}{d\omega} = -v_g^2 \frac{d^2k(\omega)}{d\omega^2} < 0$. k is the propagation constant.

dependent refractive index means that when a pulse passes through the Kerr medium it sees a time-varying phase shift. For positive optical Kerr coefficients ($n_2 > 0$), the SPM lowers the frequency at the leading edge of the pulse, while the frequency at the trailing edge of the pulse is blue chirped[3] . Because the group velocity v_g increases with increasing frequency for a negative dispersion, the leading edge of the chirped pulse will begin to slow down and fall back to the pulse center. Similarly, the trailing edge of the pulse will catch up with the main pulse. Furthermore, the SPM acts together with the KLM in a mutual-enforced manner. As a result of this delicate balance between the SPM and the negative dispersion, different groups of spectral components are merged into the pulse spectrum and move at a single group velocity, producing an ultrashort and stable pulse with an enormous bandwidth.

3.2.2 Comb Spectrum

To appreciate the strictly uniform distribution of the comb spectrum, it is helpful to first have an understanding of the cavity-mode structure [85]. The cavity supports longitudial modes with discrete frequencies ω_m (in radians/second) such that the phase accumulated through a round trip inside the cavity is an integral multiple of 2π:

$$k(\omega_m) = \frac{2\pi}{L} m, \tag{3.2}$$

where k is the propagation constant and L is the round-trip length. The discrete frequencies ω_m are determined by equation 3.2 and the dispersion relation

$$k(\omega) = \frac{\omega}{c} \overline{n}(\omega), \tag{3.3}$$

[3] This phenomenon bears an analogy to the Doppler effect. A receiver experiences a increasing or decreasing frequency depending on whether the source is approaching to or receding from the receiver. Similarly, a time-varying refractive index stretches or compresses the optical path, leading to chirped frequencies.

where $\overline{n}$ is the averaged refractive index of the cavity and is defined through

$$\overline{n}L = \int_0^L n(z)dz. \tag{3.4}$$

In a cavity without dispersion, i.e., $\overline{n}$ does not depend on the frequency, the dispersion relation 3.3 is strictly linear, meaning that all the modes are separated by an equal distance $2\pi c/\overline{n}L$ from their neighboring components. However, for a CW laser with intracavity dispersion, these frequencies are pulled away from the uniform distribution of an empty cavity, as illustrated in figure 3.2. Furthermore, in CW operations, the

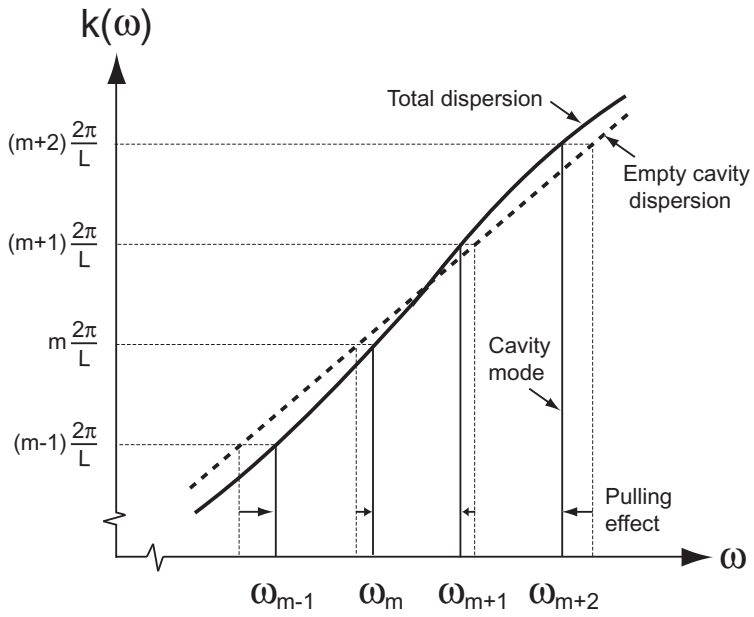

Figure 3.2: Frequency pulling effect in a dispersive laser cavity. The cavity modes are pulled away from an equal-spaced distribution by a small amount because of intracavity dispersions.

lasing modes are only restricted to a few longitudinal and transverse modes because of the mode competition. This severely limits the bandwidth of the laser output.

The spectrum of a mode-locked laser differs essentially from that of a CW laser. As discussed in section 3.2.1, the ultrashort pulses emerging from the KLM process experience zero *effective* GVD because of a balance between the negative

dispersion of the "cold" cavity and the nonlinear SPM process. Accordingly, the effective dispersion relation within the pulse bandwidth is strictly linear:

$$k(\omega) = k(\omega_c) + \frac{\partial k}{\partial \omega}(\omega - \omega_c), \tag{3.5}$$

where ω_c is the carrier frequency and $\frac{\partial k}{\partial \omega} = \frac{1}{v_g}$ holds in the mode-locked bandwidth (see figure 3.3). This linear dispersion relation again gives uniformly distributed

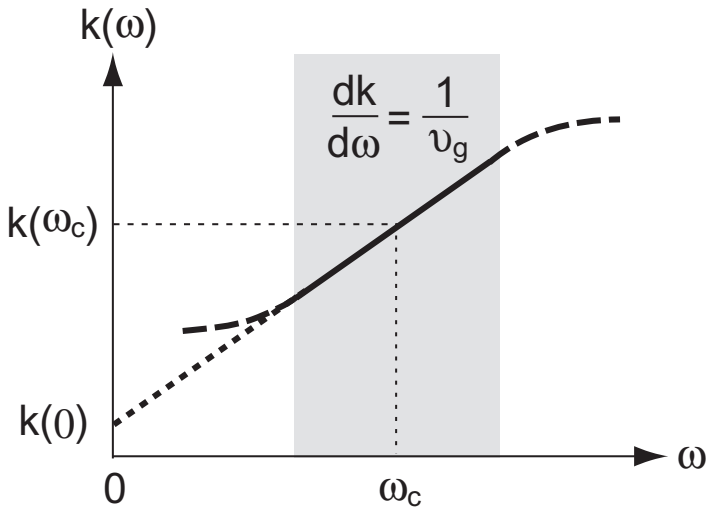

Figure 3.3: Effective dispersion relation of a mode-locked laser. The shaded region represents the mode-locked bandwidth.

modes with a global shift associated with $k(0)$, the propagation constant extrapolated to zero frequency. Combining the above dispersion relation with equation 3.2, the frequencies of these modes can be written as

$$\omega_m = \frac{2\pi v_g}{L} m + \omega_c \left[1 - \frac{v_g}{v_p(\omega_c)}\right], \tag{3.6}$$

where $v_p(\omega_c)$ is the phase velocity at which the wavefront of the carrier advances. These frequencies can be rewritten in the units of hertz as

$$\nu_m = m f_{rep} + f_{ceo}, \tag{3.7}$$

where $f_{rep} = \frac{v_g}{L}$ is the repetition frequency and $f_{ceo} = \frac{\omega_c}{2\pi}(1 - \frac{v_g}{v_p})$ is the carrier-envelope offset frequency.

That the frequency comb is globally shifted by an amount of f_{ceo} relative to the empty cavity modes can also be understood in the time domain. The pulse envelopes propagate with group velocity while the wavefront of the carrier advances with phase velocity. The difference in these two velocities results in a pulse-to-pulse phase slippage $\Delta\phi_{ce}$ between the envelope and the carrier, as illustrated in figure 3.4. The phase slippage $\Delta\phi_{ce}$ accumulated through a round trip is

$$\Delta\phi_{ce} = k(\omega_c)[\overline{n}_g - \overline{n}_p(\omega_c)]L, \tag{3.8}$$

where $\overline{n}_g$ and $\overline{n}_p$ are averaged group and phase refractive indices of the cavity, respectively. In the frequency domain, this phase shift is corresponding to a frequency shift $\frac{\Delta\phi_{ce}}{2\pi} f_{rep}$, which gives the same result for f_{ceo}.

Applying femtosecond mode-locked lasers to optical frequency measurements relies on the uniformity of the comb components across the whole mode-locked bandwidth. A number of experiments have been devoted to the verification of this uniformity. In one of these experiments [14], a frequency comb spanning about 20.12 THz ($\approx 267,200$ modes) was tested. The test was based on the fact that if an odd total number of modes is chosen and if these modes are uniformly distributed, then there is a mode located exactly at the center of the spectrum. In this experiment, the optical frequency that bisects the lowest and highest modes of the selected comb spectrum was independently obtained using a frequency-interval divider [91, 76]. By comparing this optical frequency with the expected center mode in the comb spectrum under test, the uniform distribution of the modes was verified within the experimental uncertainty of 3.0×10^{-17}.

3.2.3 Frequency Stabilization of the Femtosecond Comb

To use mode-locked lasers for optical frequency metrology, their comb frequencies need to be stabilized and referenced to some existing frequency standard. With-

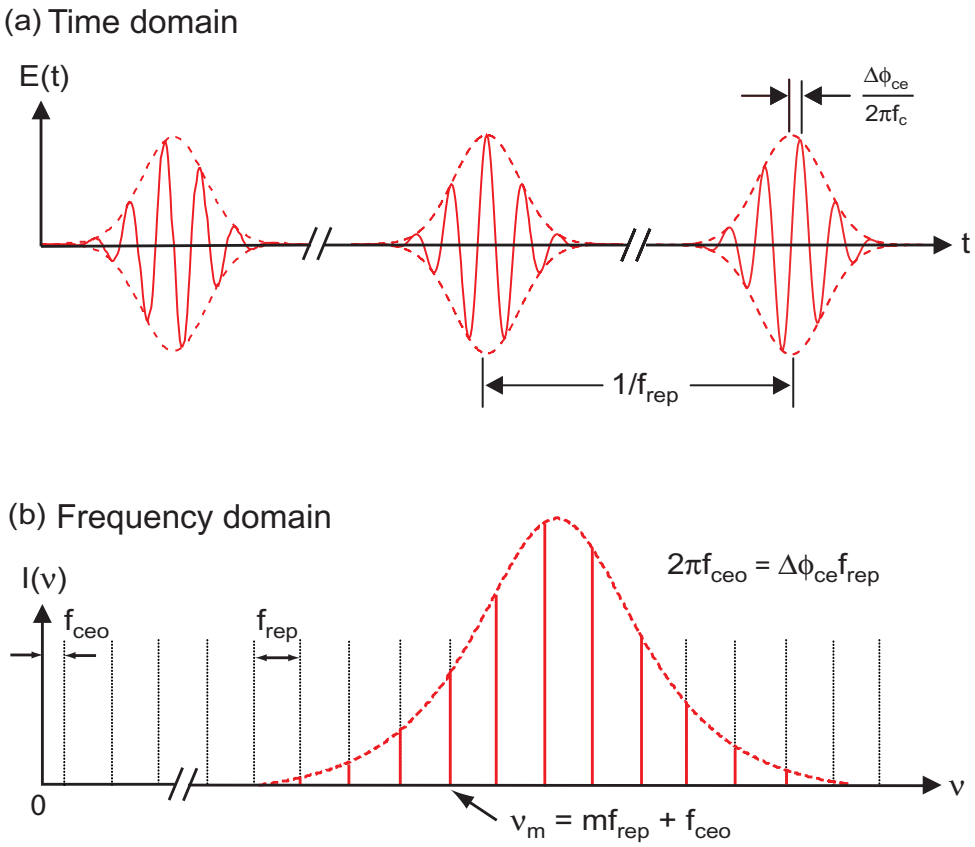

Figure 3.4: A pulse train from a mode-locked laser and its frequency-domain representation. The pulse envelopes propagate at group velocity while the wavefront of the carrier advances with phase velocity. The difference in these two velocities causes a pulse-to-pulse phase shift $\Delta\phi_{ce}$ between the carrier and the envelop that shifts the entire comb by an amount of $f_{ceo} = \Delta\phi_{ce} f_{rep}/2\pi$.

out active stabilization, f_{rep} and f_{ceo} are perturbed by various noise sources such as cavity length changes and pulse intensity fluctuations. The techniques developed for CW laser stabilization can be applied to this task. However, two degrees of freedom, namely f_{rep} and f_{ceo}, will need to be controlled independently.

The mode spacing f_{rep} can be controlled and servo-locked by adjusting the cavity length L, which in practice is performed by translating a piezoelectric transducer mounted on one of the cavity mirrors. This method is used for both prism-based and prismless mode-locked lasers such as those illustrated in figure 3.1. For these two systems, controlling of the carrier-envelope offset frequency f_{ceo} is implemented differently. With prism-based lasers, f_{ceo} can be adjusted by rotating the back mirror located after the prism pair [92, 13, 80], as indicated in figure 3.1 (a). The rotation produces an extra amount of cavity dispersion because the comb components are spatially spread across the back mirror. The change of linear dispersion results in a shift of f_{ceo}, while other high-order dispersions incurred during the rotation will be balanced by the nonlinear SPM in the mode-locking process. In prismless lasers, where the spatially-separated modes are not available, an acousto-optic modulator (AOM) is inserted into the pump beam path to control the pump power [93, 94], which affects υ_g and υ_p in a different way. Figure 3.5 gives a simplified interpretation for the comb frequency control.

There are cross-couplings between the two control channels for f_{rep} and f_{ceo} [95, 96]. Cavity-length changes used to control f_{rep} also modify the cavity-filling factor (the length of the dispersive medium divided by the overall cavity length) and hence affect f_{ceo}, though this effect is small compared with the direct response [95]. Control of f_{ceo} affects f_{rep} too. Rotating the back mirror in prism-based systems has a very small cross-coupling to f_{rep} compared to the direct channel, while responses of f_{ceo} and f_{rep} to pump power in prismless systems can have comparable magnitudes and opposite signs [95, 97].

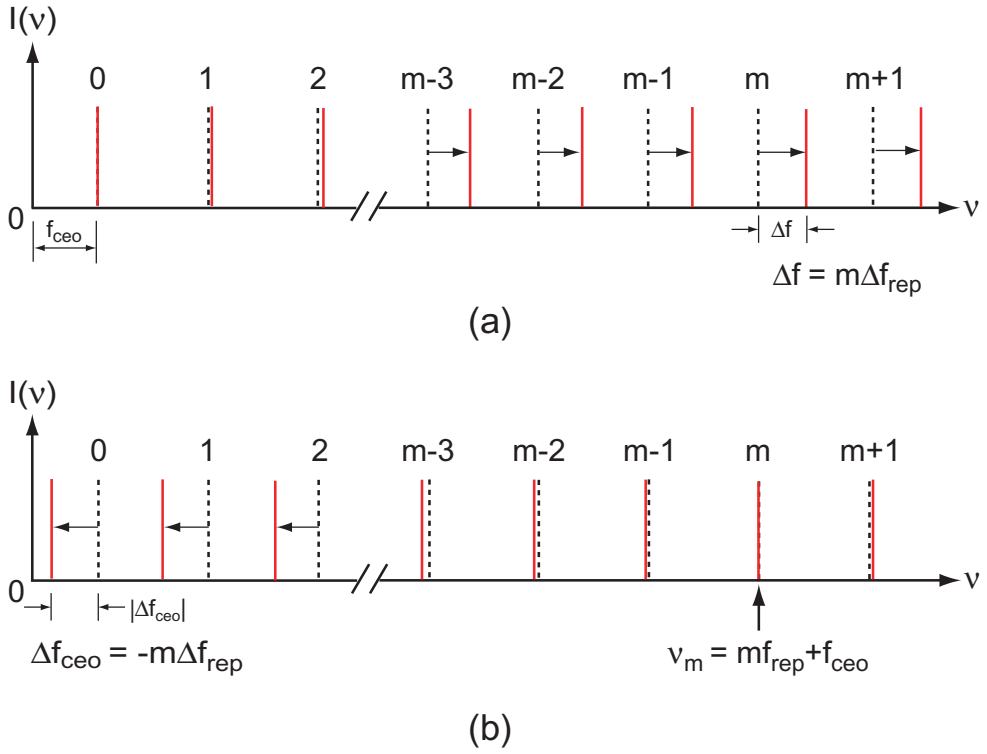

Figure 3.5: A simplified picture for the frequency control of mode-locked Ti:sapphire lasers. (a) A small change in cavity length modifies the mode spacing f_{rep}, giving rise to a large frequency shift at optical frequencies because of their large mode orders ($m \sim 10^5 - 10^6$). Note that the changes of mode frequencies near the zero frequency are greatly exaggerated. (b) With the anchor position moved to a mode in optical region, a small change in f_{rep} has a large effect on f_{ceo}. In practice, this is achieved by rotating the end mirror in prism-based femtosecond lasers. In prismless lasers, the effect of the pump-power change can be viewed as a linear combination of (a) and (b).

To summarize the above discussion, figure 3.6 shows simplified block diagrams [98] for the comb frequency stabilization, where G_{11} and G_{22} are plant transfer functions for f_{rep} and f_{ceo}, respectively. G_{12} and G_{21} represent the cross-couplings between the two channels, and D_1 and D_2 are transfer functions of two loop filters. This simplified model of the comb frequency stabilization provides some general guidance for servo-locking both f_{rep} and f_{ceo}. For example, in prism-based systems, a qualitative analysis of cross-couplings resulting from cavity-length and mirror-angle adjustments shows that $\frac{G_{21}}{G_{11}} > 0$ and $\frac{G_{12}}{G_{22}} < 0$. Thus the transfer function characterizing the relative strength of the cross-coupling, defined as $S = \frac{G_{12}G_{21}}{G_{11}G_{22}}$, is negative, implying a potential oscillatory instability when both feedback loops are closed [98, 99]. In this case, decoupling of the two channels can be introduced in the loop filters to improve the locking performance.

3.2.4 Self-Referencing Carrier-Envelope Offset Frequency

The detection of f_{rep} is straightforward. A fast photodetector is used to measure the heterodyne beats among adjacent comb components. The S/N is enhanced in a sense that a large number of modes contribute to the beat notes at f_{rep} and its harmonics. On the other hand, the carrier-envelope offset frequency f_{ceo} cannot be detected in this manner because it is a common variable for all the comb components. Several methods have been developed to detect this value such as the cross-correlation measurement of the pulse-to-pulse phase slippage $\Delta\phi_{ce}$ [93], a heterodyne beat with a stabilized CW optical frequency, and self-referencing techniques [78, 100]. A ν-to-2ν detection scheme, which falls into the category of self-referencing techniques, is particularly suitable for the absolute frequency measurement because it allows f_{ceo} to be directly phase-locked to an RF reference.

Figure 3.7 illustrates the basic idea of the ν-to-2ν detection scheme. A comb component ν_m at the "red" end is frequency doubled by sum-frequency generation

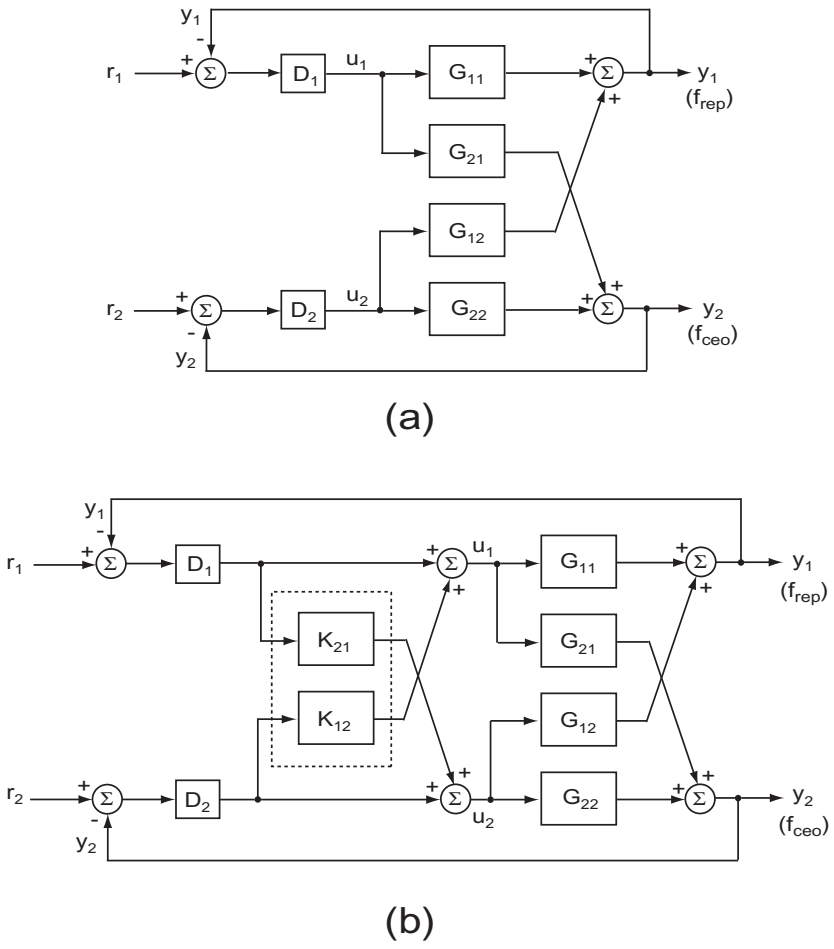

Figure 3.6: Simplified block diagrams for feedback control of comb frequencies. G_{11} and G_{22} are plant transfer functions for f_{rep} and f_{ceo}, respectively. G_{12}, and G_{21} represent the cross-couplings between two channels. D_1 and D_2 are transfer functions of two loop filters. In (b), decouplers K_{12} and K_{21} are introduced to reduce the cross-couplings through G_{21} and G_{12}.

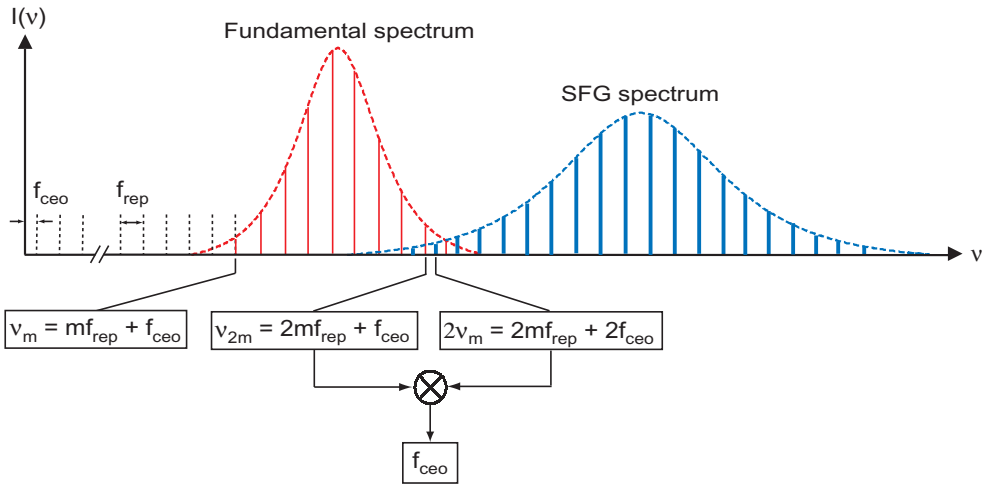

Figure 3.7: Self-referencing determination of the comb offset frequency f_{ceo}. The fundamental comb spectrum spanning an octave is further expanded using sum-frequency generation (SFG). In the overlapping region of the fundamental and SFG spectra, a heterodyne beat between ν_{2m} and frequency-doubled ν_m gives f_{ceo}. The extracted f_{ceo} can be referenced to an RF frequency standard.

(SFG) in a nonlinear crystal and is heterodyne beat against the component ν_{2m} at the "blue" end. The beat frequency gives the carrier-envelope offset frequency f_{ceo}:

$$2\nu_m - \nu_{2m} = 2(mf_{rep} + f_{ceo}) - (2mf_{rep} + f_{ceo}) = f_{ceo} \tag{3.9}$$

This scheme requires that the comb spectrum spans an octave[4] such that between the fundamental and SFG spectra there is an overlap in which the heterodyne beat can be performed. An octave-spanning frequency comb is usually obtained by externally broadening the spectrum from a mode-locked laser, using a segment of specially designed microstructure fibre [101, 102, 103]. Alternatively, an octave-spanning comb can be directly generated inside the cavity of a femtosecond laser with exquisite intracavity dispersion management [104, 105, 106].

3.3 Optical Frequency Measurement

3.3.1 Iodine Spectrometer

Figure 3.8 shows the experimental scheme for precision scanning and control of the laser frequency based on a highly stable optical cavity augmented by a sub-Doppler I_2 resonance recovered from the spectrometer. The femtosecond comb system used for frequency measurement is also shown. The experimental details of the iodine spectrometer have already been discussed in the previous chapter. Some modifications are made to suit the optical frequency measurement of a particular I_2 hyperfine component.

The single-mode Ti:sapphire laser employed in the I_2 spectrometer can be tuned from 953 to 1080 nm. It provides about 300 mW of useful output power at 1030 nm. A small portion of the fundamental power is used for laser frequency prestabilization to an evacuated, vibration-isolated, and thermally stabilized optical cavity. The operational laser linewidth is limited by the vibration noise and drift associated with the

[4] The interval between any two frequencies having a ratio of 2 to 1.

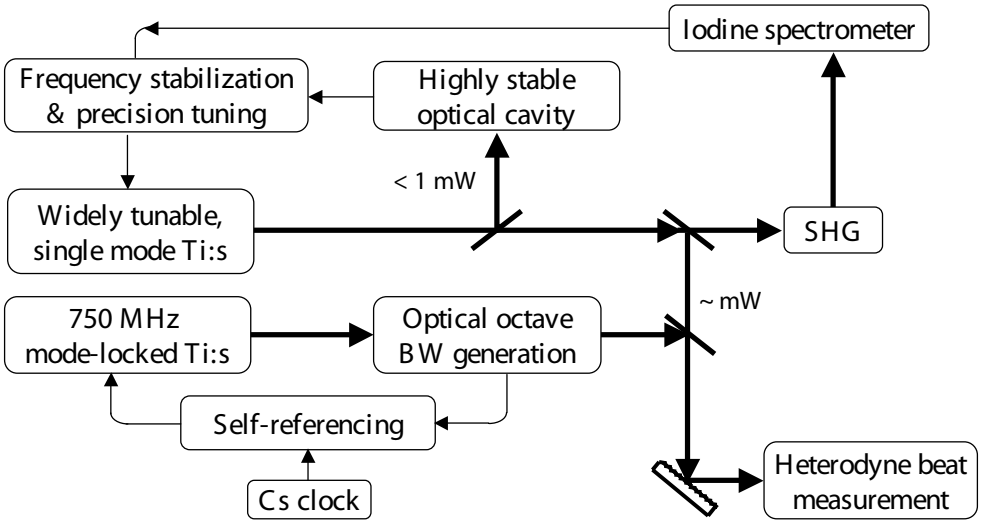

Figure 3.8: A precision I_2 spectrometer based on a widely tunable Ti:sapphire laser. The femtosecond comb system used for frequency measurement is also shown.

cavity. Most of the Ti:sapphire laser power is used for second harmonic generation (SHG) to probe I_2 transitions. The I_2 spectrometer is configured for frequency modulation (FM) spectroscopy, with additional chopping of the pump beam to further reduce the influence of the Doppler background. The size of both pump and probe beams is 3 mm in diameter. We typically maintain < 100 μW for the probe beam while the pump-beam power can be varied from 1 to 6 mW to study power-related frequency shift and broadening of I_2 transitions. The high-purity I_2 cell was prepared by the Bureau International des Poids et Mesures (BIPM) and it has an 8-cm useful length with Brewster windows at both ends. For studies of pressure-related effects, the I_2 vapor pressure is controlled by varying the temperature of the cell cold finger. For frequency measurement of the a_3, P(13) 43-0 transition, we use a cold finger temperature of -5 °C (vapor pressure = 2.38 Pa), in compliance with the CIPM recommendation.

In addition to locking the single-mode Ti:sapphire laser to the external cavity, the long-term stabilization of the laser is obtained by referencing its frequency to an I_2 transition. The double-passed AOM, shown as AOM 2 in figure 2.1, fulfils this task. Drift and low-frequency noise on the laser stemming from the external cavity can be suppressed by feeding the error signal derived from the I_2 resonance into a voltage control oscillator (VCO), which in turn determines the optical frequency shift of the double-passed AOM. The laser light, now carries the information of I_2 resonance, is then directed to a femtosecond laser comb for frequency measurement. Since there is more power available in the fundamental laser light near 1030 nm, it is used for frequency measurement.

3.3.2 Self-Referenced Femtosecond Laser Frequency Comb

Figure 3.9 shows the details of the experimental setup for the frequency comb system. In our experiment, the Kerr-lens mode-locked femtosecond laser used for

the frequency comb generation has a repetition rate of 750 MHz and produces an optical spectrum spanning $\sim$ 30 nm, centered at 800 nm [84]. An octave bandwidth of the comb is generated by coupling 100 mW of laser light through a 20 cm long microstructure fiber. The input to the ν-to-2ν interferometer is divided into infrared (IR) and visible wavelengths by a dichroic beam splitter. After the IR light is frequency doubled by a BBO (β-BaB_2O_4) crystal, the beams in the two arms of the interferometer are recombined and detected with a photodiode. A prism is inserted into one of the beam path to match the lengths of the two arms to achieve temporal overlap of the pulses.

Both the repetition frequency f_{rep} and the carrier-envelope offset frequency f_{ceo} are stabilized with reference to the Cs standard, thus establishing an optical frequency grid of 750 MHz spacing, extending from 500 to 1100 nm. In practice, an intracavity piezo-activated mirror is used to control f_{rep} while the pump power for the femtosecond laser is used to control f_{ceo}. The frequency of the m^{th} comb component is then given by $f_m = mf_{rep} + f_{ceo}$. The absolute frequency of the I_2-stabilized CW laser can thus be determined by counting its heterodyne beat frequency against a corresponding comb line. The comb order, m, is determined from a medium-resolution (500 MHz) wavemeter.

3.3.3 Absolute Frequency of the Iodine-Based Length Standard at 514.67 nm.

A remarkable feature of the femtosecond comb system is its reliability. It is now possible to acquire hours of measurement data without interruption. This will be important for the future development of an optical clock [107, 54]. Furthermore, the S/N of the beat signal between the CW laser and the comb exceeds 45 dB within a 100-kHz bandwidth, permitting a direct frequency count without further signal processing. Figure 3.10 (a) shows the line shape of the a_3, P(13) 43-0 transition

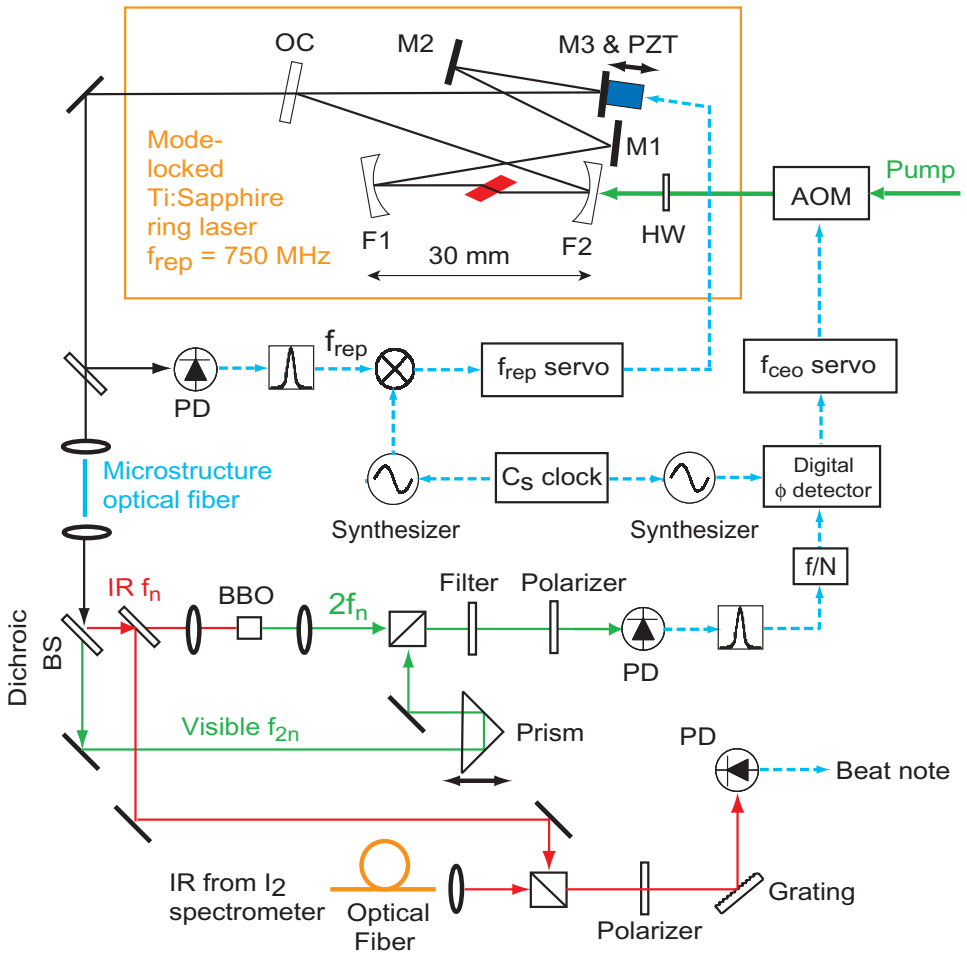

Figure 3.9: Experimental setup for a self-referenced frequency comb. The system employs a mirror-dispersion-controlled Ti:sapphire laser with a ring-cavity configuration and a repetition frequency of 750 MHz. Both f_{rep} and f_{ceo} are locked to the Cs clock. The absolute frequency of the I_2-stabilized CW Ti:sapphire laser (not shown) at IR is determined by counting its heterodyne beat frequency against a nearby comb component with predetermined mode order. Note that several half wave plates used to rotate polarizations are not shown. F1, F2, chirped folding mirrors with f = 15 mm; M1–M3, flat chirped mirrors; OC, output coupler; PZT, piezoelectric transducer; AOM, acousto-optic modulator; HW, half wave plate; PD, photo detector; BS, beam splitter; BBO, β-BaB_2O_4 crystal.

recovered using FM saturation spectroscopy with a modulation frequency of 6 MHz and a 5-ms time constant. Figure 3.10 (b) shows a record of the frequency count of the length-standard transition, i.e., a_3, P(13) 43-0, $^{127}I_2$. The corresponding Allan deviation determined from the measurement is presented in Fig. 3.10 (c). It is clear that the measurement noise is dominated by the instability of the Cs clock as well, just as that for the 532-nm system.

To check the reliability of the 750-MHz femtosecond comb, we use a frequency-doubled Nd:YAG laser stabilized on a hyperfine component of $^{127}I_2$ transition [a_{10}, R(56) 32-0] at 532 nm as a calibration tool [108, 41]. The absolute frequency of the 532-nm system has been measured for over two years with a standard deviation of less than 120 Hz at 1064 nm [54]. Previous measurements were carried out using a well-characterized 100-MHz femtosecond laser system referenced to a Cs clock. Figure 3.11 shows the augmented record of the absolute frequency measurements performed at a_{10}, R(56) 32-0, accumulated during a two-year period. The last four data points represent measurements of the same I_2 transition using the current 750-MHz comb system. The agreement between the two systems is within 20 Hz. At the present stage, the frequency noise of the 532-nm system is limited by the instability of the Cs clock (5×10^{-12} at 1 s). A H-maser-referenced optical comb system is also used in the system.

Figure 3.12 shows a two-week record of the frequency-measurement performed at a_3, P(13) 43-0. Our measurement gives an average value of 71.8 ± 0.3 kHz higher than the CIPM-recommended value of 582 490 603 307 $\pm$ 150 kHz [40]. To include other unforeseeable effects on the transition frequency, we quote a 5-σ value of $\pm$ 1.5 kHz for the uncertainty of the measurement. To be more specific, further evaluations should include studies of beam size and wavefront curvature, signal-recovery techniques other than FM spectroscopy, and a large collection of various I_2 cells. However, we emphasize that even for the present work, we have used three different

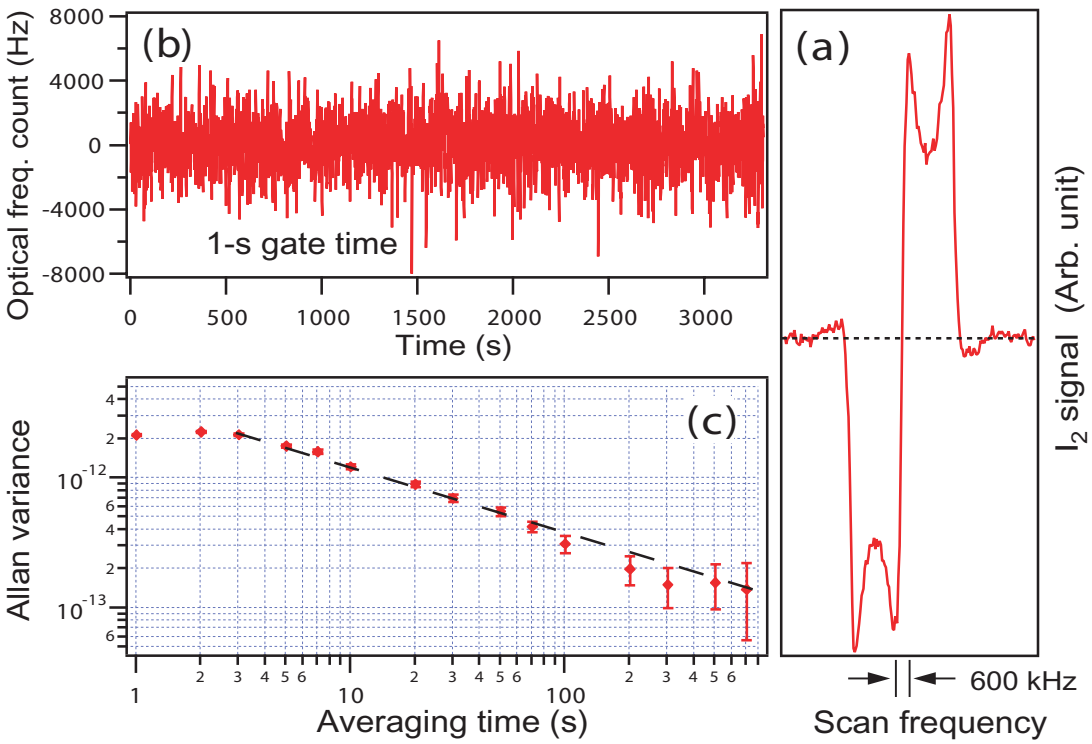

Figure 3.10: Frequency measurement at the a_3 component of the P(13) 43-0 transition. (a) Line shape recovered from FM spectroscopy. Cell cold-finger temperature near -5°C, 5-ms averaging time. (b) Direct frequency measurement of a_3 at P(13) 43-0 by the Cs-referenced fs comb. Gate time 1 s. Standard deviation is limited by the Cs clock. (c) Allan variance is determined from the time record in (b).

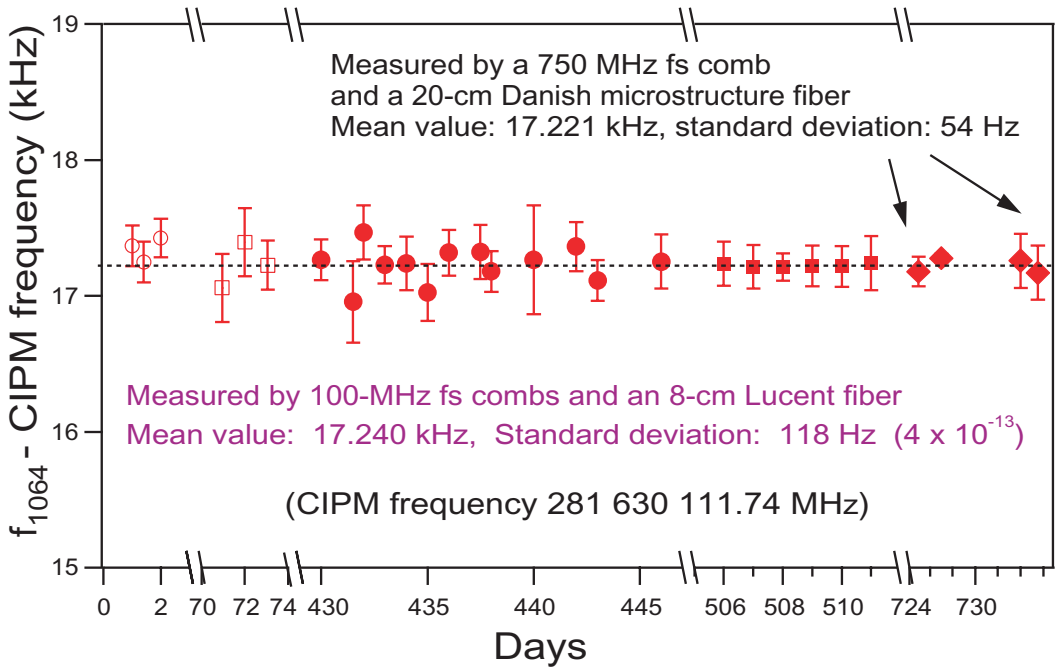

Figure 3.11: Long-term frequency measurement of the Nd:YAG/I_2-532 nm system. Agreement is excellent with previous measurements based on 100-MHz systems with different microstructure fibers.

I_2 cells. Two of the cells were made in the same run while a third one was made more than eight years ago, also at BIPM. We observe no statistically significant difference among these three cells, as shown in Fig. 3.12. While we congratulate our BIPM colleagues for making cells on a consistent basis, it is clear that the capability of absolute frequency measurement referenced to the Cs standard gives us a new approach to characterize reference cells and track their long-term variations.

3.3.4 Characterizing the Iodine Spectrometer

The capability of absolute frequency measurement greatly facilitates the characterization of systematic effects of the spectrometer. While traditionally one employs a heterodyne beat between two similar systems to characterize optical standards, we can now evaluate the performance of a single system and calibrate it using Cs frequency standard. We have carefully studied frequency shifts depending upon the following experimental parameters: optical power, modulation frequency and amplitude, vapor pressure, and optical alignment. To minimize subjective influences in the frequency measurement, we typically have a few experimenters align the spectrometer independently, with the only common objective being maximization of the signal size. Residual amplitude modulation (RAM) in FM saturation spectroscopy is a common source of systematic errors. The RAM on the frequency-modulated probe beam is minimized by careful adjustment of the polarization optics throughout the I_2 spectrometer. When RAM is minimized, we can choose different values of the modulation frequency (4, 6, 8, and 10 MHz, for example) with various modulation amplitudes and still obtain consistent and reproducible results for frequency measurement. Within this optimized operation regime, optical-power-related frequency shifts are small, usually less than the measurement standard deviation, in the normal operation range of 1 mW to 4 mW for a 3-mm diameter pump beam. By a controlled variation of the cold-finger temperature of the iodine cell, we change the sample den-

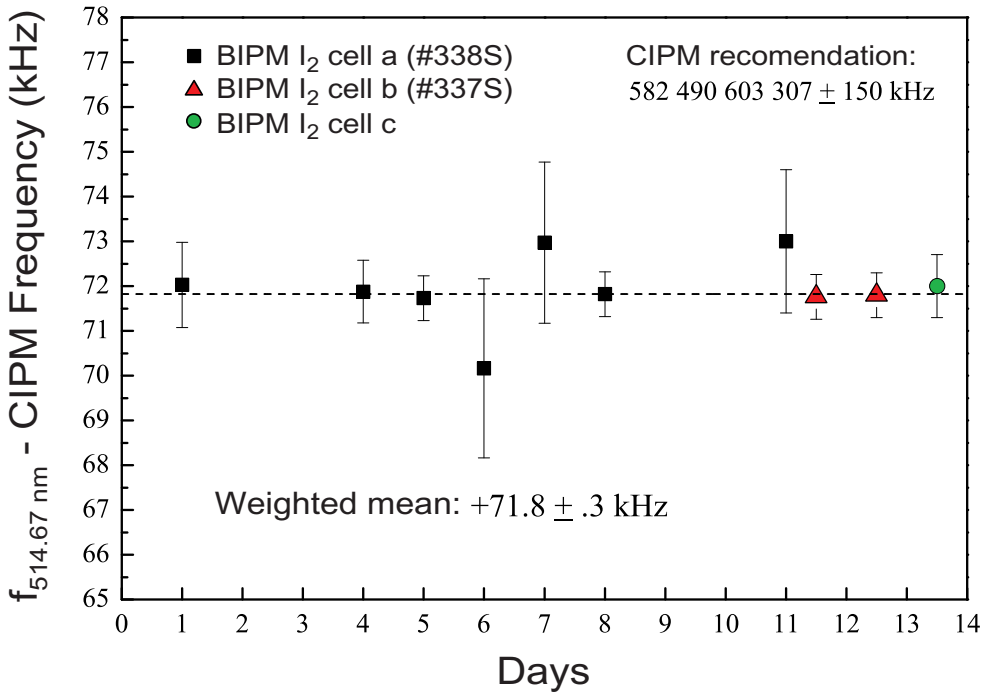

Figure 3.12: Long-term frequency measurement at the a_3 component of the P(13) 43-0 transition. Three different I_2 cells are used in the measurement, as indicated by squares, triangles, and circles. The BIPM-designated numbers for cells a and b are shown in parenthesis.

sity in the cell. The related pressure-dependent frequency shift is measured for this length standard transition, with a linear shift of -2.5 ± 0.5 kHz/Pa, as shown in Fig. 3.13.

3.4 Summary

A femtosecond laser based optical comb spanning an octave bandwidth is employed conveniently to check systematic errors and measure absolute frequencies of selected optical standards. The transition frequency of the length standard at 514.67 nm, i.e. the a_3 hyperfine component at transition P(13) 43-0, $^{127}I_2$, has been determined to be 71.8 kHz $\pm$1.5 kHz above the recommended value of 582 490 603 307 kHz. The measurement was performed with a pump power of $1 - 4$ mW, a beam size of 3 mm in diameter, and a cold-finger temperature of -5°C for the iodine cell (as specified in reference [40]). The average value of the frequency measurements is obtained over a 15-day measurement period. This result is well within the 1-σ uncertainty (150 kHz) of the recommended value. The coefficient of the pressure shift is found to be $-2.5(5)$ kHz/Pa.

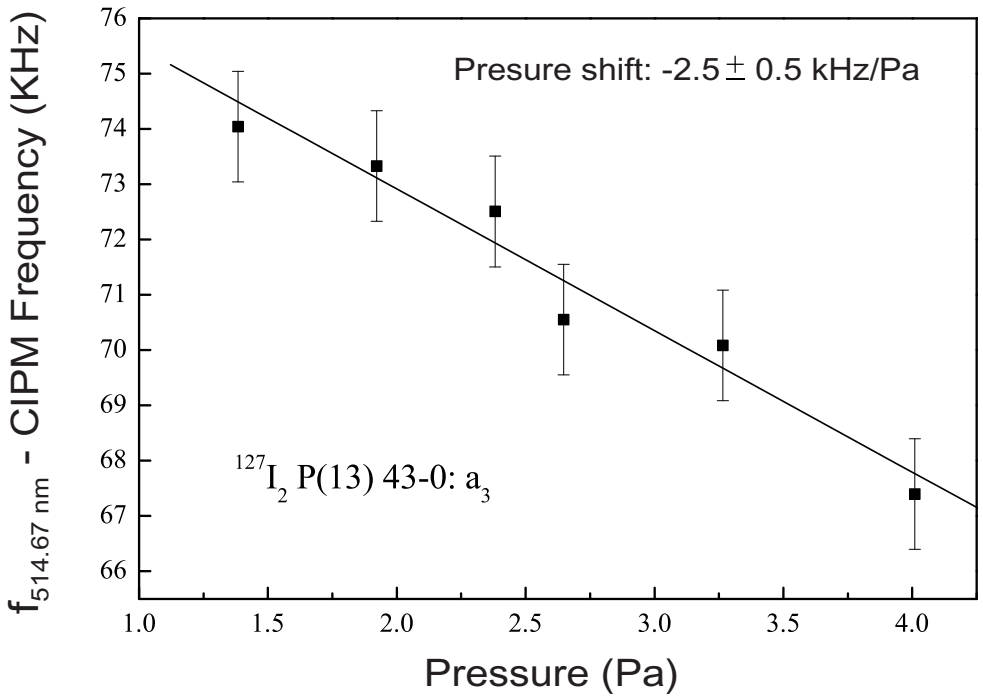

Figure 3.13: Pressure shift of the a_3 component at P(13) 43-0.

Chapter 4

HYPERFINE INTERACTIONS AND PERTURBATION EFFECTS IN THE $B0_u^+(^3\Pi_u)$ STATE OF $^{127}I_2$

4.1 Introduction

High-precision measurement of hyperfine spectrum in molecular iodine over an extended range of rovibrational levels is valuable both for studying the molecular structure and selecting references for laser frequency stabilization. The hyperfine structure in atoms and molecules originates from the electromagnetic interaction between the nuclear and surrounding charge distributions. This seemingly weak effect has a subtle but noticeable influence on molecular structure. For instance, the hyperfine coupling between the B state and the repulsive $B''1_u(^1\Pi_u)$ state is responsible for the predissociation of the molecules [66, 67], an effect that results in a variation of the lifetime of the hyperfine levels belonging to a single rovibrational level. Another example of this effect is the hyperfine-induced u-g mixing of the $B0_u^+(^3\Pi_u)$ and the $1_g(^1\Pi_g)$ states that dramatically modifies the hyperfine structure at vibrational levels $\upsilon' = 76 - 78$ in the $B0_u^+(^3\Pi_u)$ state [44, 45]. Considering the broad scope within which the hyperfine effect operates, it is of great interest to examine the evolution of this effect with the progression of the vibrational levels toward the dissociation limit or, equivalently, with the stretch of the molecular bond from its equilibrium length to large internuclear separations, where a separated-atom model represents a good approximation to the molecular electronic wave function. Hyperfine structures in the

$X0_g^+(^1\Sigma_g^+)$ and the $B0_u^+(^3\Pi_u)$ states have received extensive investigations through the prominent $B \longleftarrow X$ transition manifold in the visible and near-IR regions. By use of sub-Doppler detection schemes such as saturation spectroscopy and supersonic molecular beams, hyperfine spectra of $B \longleftarrow X$ transitions were measured for a large number of rovibrational levels with a precision that reached the kilohertz level for each hyperfine component. Broyer *et al.* developed an effective Hamiltonian to describe the hyperfine interaction that can couple different electronic states [16]. Derived from this Hamiltonian are effective hyperfine parameters that characterize hyperfine coupling strength. Among these parameters, electric quadrupole (eqQ), spin-rotation (C), tensorial spin-spin (d), and scalar spin-spin (δ) represent the four dominant parameters that have been widely used to analyze experimental spectrum.

For the B state in $^{127}I_2$, perturbations from other electronic states can contribute significantly to various terms in the hyperfine Hamiltonian. Located above the B state on the molecular energy scale are a total of nine weakly bounded electronic states (0_g^+, 0_g^-, 0_u^-, two 1_g, two 1_u, 2_g, and 2_u) [109, 59, 110], which share the same $^2P_{\frac{3}{2}} + {}^2P_{\frac{1}{2}}$ dissociation limit with the B state. Furthermore, rovibrational levels in the B state are not far removed in energy from this cluster of states. As a result, these electronic states perturb the B state to various degrees through hyperfine coupling. Indeed, this qualitative estimate of the perturbation strength is confirmed by the observed global trend of a monotonic increase of the magnitude of the effective hyperfine parameters C_B, d_B, and δ_B along with the ascending vibrational level, a trend especially remarkable for those levels approaching the dissociation limit [111, 50, 46, 112]. More quantitatively, for levels with vibrational quantum numbers $v' < 43$ the four-term effective Hamiltonian describes satisfactorily the hyperfine spectrum with small residual errors ranging from a few tens to several kilohertz or even less [42], indicating that in this region second-order perturbation is sufficient to account for the contributions from states other than the B state.

Moreover, hyperfine interaction in the region $71 < \upsilon' < 82$ has been systematically investigated by Pique *et al* [44, 45, 43]. In addition to the second-order effect, strong hyperfine perturbation from the $1_g(^1\Pi_g)$ state was found at levels $\upsilon' = 76$, 77, 78 owing to small energy differences and large Franck-Condon overlaps between the rovibrational levels in the B and the $1_g(^1\Pi_g)$ states. In particular, to deal with the strong perturbations at $\upsilon' = 77$ and $\upsilon' = 78$ requires that basis functions of the $1_g(^1\Pi_g)$ state be included in the construction of the Hamiltonian matrix: A direct diagonalization of this new matrix gives the correct hyperfine spectrum. The resultant strong u-g mixing was directly confirmed by the extra hyperfine lines recorded at the 78-0 band head.

Despite the fact that ample data were collected in the regions summarized above, the intermediate levels that spread from $\upsilon' = 44$ to $\upsilon' = 70$ will require more information. This is an important region for study of the molecular structure of $^{127}I_2$ because vibrational wave functions of these levels sample a relatively large range of internuclear separations. Direct hyperfine-spectrum measurements in this region have been made only for a limited number of transitions to which access is gained primarily by isolated laser lines such as 514.5- and 501.7-nm argon-ion laser wavelengths [55, 48, 113].

Using a widely tunable and high-resolution spectrometer based on a frequency-doubled CW Ti:sapphire laser, we carried out systematic investigations of the hyperfine spectra of $B \longleftarrow X$ transitions in the wavelength range $500 - 517$ nm and determined the detailed rovibrational dependence of the four effective hyperfine parameters in the region $42 < \upsilon' < 70$. In addition to the usual monotonic trend that results from the second-order effect, we observed strong perturbations at $\upsilon' = 57 - 60$. The source of this perturbation was confirmed, and its properties were studied. We also established a systematic dependence of the hyperfine interactions on internuclear separation R.

This chapter describes a systematical investigation of $^{127}I_2$ hyperfine spectrum in the wavelength range $500 - 517$ nm. After a brief overview of the hyperfine spectrum in molecular iodine, the experimental setup and data collection are covered in section 4.3. Section 4.4 gives the four effective hyperfine parameters extracted from hyperfine spectra of nearly 80 rovibrational transitions. These results are then examined and discussed in the following sections. First, these date are combined with previous measurements to give a global picture of the vibrational dependence of the hyperfine parameters in the B sate. Second, this vibrational dependence is converted to the radial dependence. Third, the rotational dependence of the four hyperfine parameters are examined in detail. Finally, a strong perturbation observed at vibrational levels $v' = 57 - 60$ is discussed in section 4.8. Section 4.9 summarizes the chapter.

4.2 Effective Hyperfine Hamiltonian

4.2.1 Hyperfine Spectra of Molecular Iodine

Figure 4.1 shows the simplified energy level diagram of the molecular iodine. There are totally 23 valence states that converge to three atomic states ($^2P_J + {}^2P_J$, J=$\frac{3}{2}, \frac{1}{2}$) at large internuclear separations. Shown in this simplified energy level diagram are the potential energy curves (PECs) of four electronic states: the ground state X, the second excited sate B, the $1_g(^1\Pi_g)$ state converging with the B state to the second dissociation limit, and the $0_g^+(^1\Sigma_g^+)$ state converging to the third dissociation limit. Several rovibrational levels in the X and the B states are also shown in the diagram.

A rovibrational transition of $B \leftarrow X$ manifold occurs between two rovibrational levels (v'', J'') and (v', J') in the ground state X and the second excited state B, respectively. The selection rule for an electric dipole transition is $\Delta J = J' - J'' = \pm 1$

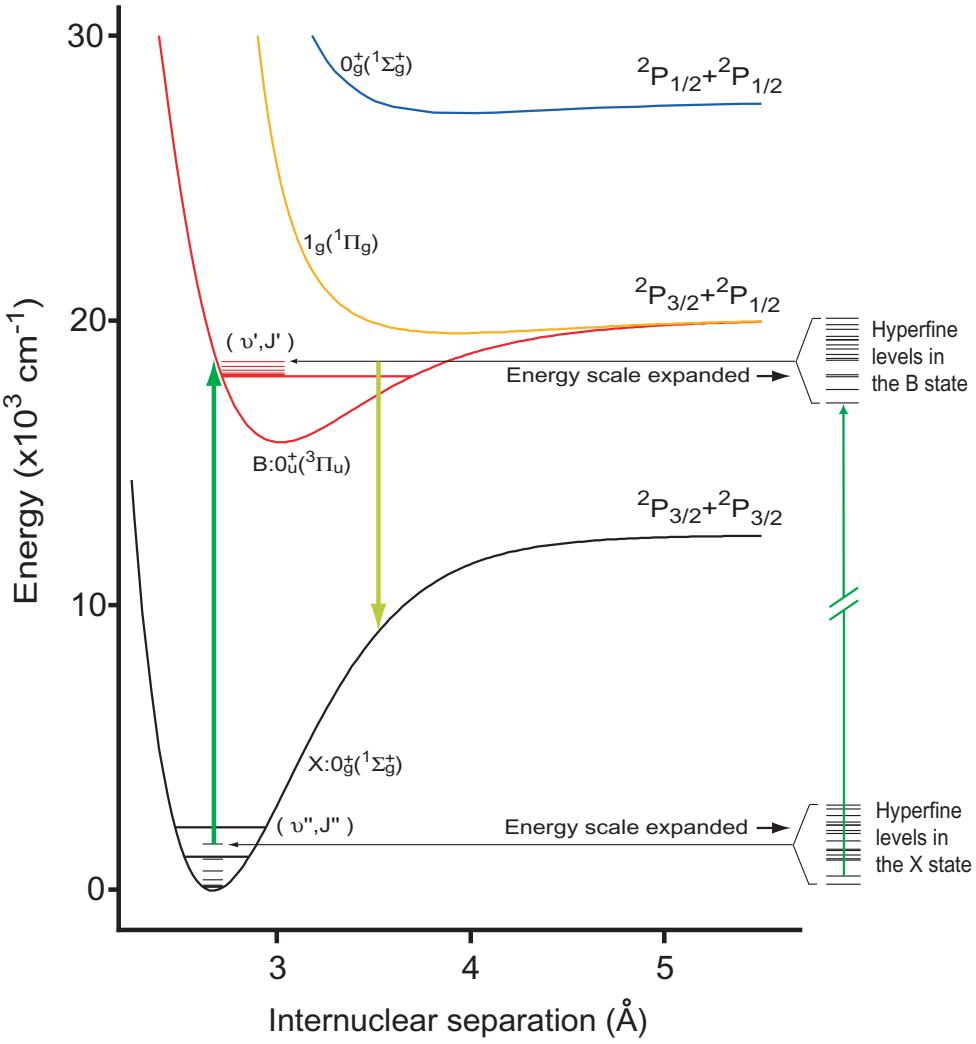

Figure 4.1: A simplified energy level diagram of molecular iodine. Several rovibrational levels in the X and the B states are shown. The thick vertical line on the left indicates a $B \leftarrow X$ rovibrational transition between two rovibrational levels (υ'', J'') and (υ', J') in the X and the B states, respectively. The selection rule involved is $\Delta J = J' - J'' = \pm 1$ ($\Delta J = 1$: P branch, $\Delta J = -1$: R branch). A rovibrational transition is labeled as P(J'') υ'-υ'' or R(J'') υ'-υ''. Each rovibrational level is further split into hyperfine sublevels. Thus one rovibrational transition contains many hyperfine components. Such a hyperfine component is indicated as a thin vertical line on the right.

($\Delta J = 1$: P branch, $\Delta J = -1$: R branch)[1] . Each rovibrational transition is labeled as P(J'') v'-v'' or R(J'') v'-v'' according to the value of ΔJ.

Because of the hyperfine interaction, each rovibrational level is further split into hyperfine sublevels. The iodine nucleus has a nuclear spin of $I_a = \frac{5}{2}$. Thus I, the total nuclear spin of a iodine molecule, can take on the possible values of 0, 1, 2, 3, 4, and 5. The coupling of the nuclear spin $\mathbf{I}$ and the molecular angular momentum $\mathbf{J}$ gives the total angular momentum $\mathbf{F} = \mathbf{J} + \mathbf{I}$. For each I and J, the quantum number F can take on the values of $|J + I|, |J + I - 1|, \cdots |J - I + 1|, |J - I|$. The hyperfine interaction between the nucleus and the surrounding charge distributions breaks the degeneracy on I and F, resulting in many hyperfine sublevels.

The total number of hyperfine sublevels at a rovibrational level is further limited by the nuclear statistics. An iodine molecule contains two identical femionic nuclei, which demands that the total nuclear wave function must be antisymmetric under the exchange of the two nuclei. This requirement imposes additional restrictions on the possible values of the nuclear spin. In particular, for the ground state X, rovibrational levels with even (odd) J'' can have hyperfine sublevels with even (odd) I''. Consequently, levels with even (odd) J'' are split into 15 (21) hyperfine sublevels. The restriction is reversed for the B state: even (odd) J' can have hyperfine sublevels with odd (even) I'. Figure 4.1 illustrates two sets of hyperfine sublevels for the X and the B states.

The selection rule for the electric dipole transition between two hyperfine sublevels in two different electronic states is $\Delta F = F' - F'' = \Delta J$. Thus each $B \leftarrow X$ rovibrational transition contains either 15 (even J'') or 21 (odd J'') hyperfine components. Such a hyperfine component is illustrated as a thin vertical line on the right of figure 4.1. Transitions with $\Delta F = 0$ or $\Delta F = -\Delta J$ do occur, but they are usually

[1] $B \leftarrow X$ transitions do not possess Q branch ($\Delta J = 0$) because there is no angular momentum parallel to the internuclear axis for the B and the X states.

much weaker than the main lines ($\Delta F = \Delta J$) and therefore are not considered here.

4.2.2 Matrix Elements of the Four Effective Hyperfine Hamiltonian

The hyperfine Hamiltonian in a homonuclear diatomic molecule with two nuclei, labeled a and b, can be formally written as

$$H_{hf} = H_{hf}(a) + H_{hf}(b) + H_{hf}(a,b), \tag{4.1}$$

where $H_{hf}(a)$ $[H_{hf}(b)]$ and $H_{hf}(a,b)$ represent the nucleus-electron and nucleus-nucleus interactions, respectively. The fact that $H_{hf}(a)$ and $H_{hf}(b)$ can couple different electronic states was studied through the introduction of an effective hyperfine Hamiltonian [16]. This effective Hamiltonian acts only on one electronic state but has its matrix elements modified by second-order perturbation to take into account hyperfine couplings with external electronic states. The advantage of this treatment is that, despite their different origins, various tensorial terms can be incorporated into a small set of effective hyperfine parameters according to their overall geometrical dependences evaluated with irreducible tensorial algebra, thereby simplifying the experimental analysis of hyperfine structure. The effective Hamiltonian can be summarized as

$$H_{hf,eff} = H_{eqQ} + H_{SR} + H_{TSS} + H_{SSS} + H_e + H_f + H_h + H_{hH}, \tag{4.2}$$

where the four leading terms on the right-hand side represent major contributions from nuclear electric quadrupole, spin-rotation, tensorial spin-spin, and scalar spin-spin interactions, respectively. The last four terms arise primarily from second-order contributions not included in the four major terms and have been examined experimentally only for a few transitions without confirming evidence of their existence [55]. The matrix elements of all the terms in equation 4.2 have be derived and can be found in the literature [114, 16]. For the four major terms, their matrix elements

are

$$\langle FIJ|\, H_{eqQ}\, |FI'J'\rangle = (-1)^{F+J+2I_a}\frac{1}{2}[(2I+1)(2I''+1)]^{1/2}eQq(J,J')\times \left[\begin{pmatrix} I_a & I_a & 2 \\ I_a & -I_a & 0 \end{pmatrix}\begin{pmatrix} J' & J & 2 \\ J & -J & 0 \end{pmatrix}\right]^{-1}\times \begin{Bmatrix} I_a & I_a & I \\ 2 & I' & I_a \end{Bmatrix}\begin{Bmatrix} F & J & I \\ 2 & I' & J' \end{Bmatrix},$$

$$q(J,J+2) = 3(J+1)^{1/2}q/[(2J+3)(2J+5)]^{1/2},$$

$$q(J,J) = -Jq/(2J+3), \tag{4.3}$$

$$\langle FIJ|\, H_{SR}\, |FI'J'\rangle = \delta_{JJ'}\delta_{II'}\frac{1}{2}C\left[F\left(F+1\right)-I\left(I+1\right)-J\left(J+1\right)\right], \tag{4.4}$$

$$\langle FIJ|\, H_{TSS}\, |FI'J'\rangle = \delta_{JJ'}\left(-1\right)^{F+I'+1}d(2J+1)[I_a\left(I_a+1\right)\left(2I_a+1\right)]\times \sqrt{30\left(2I+1\right)\left(2I'+1\right)}\begin{pmatrix} J & 2 & J \\ 0 & 0 & 0 \end{pmatrix}\times \begin{Bmatrix} F & J & I \\ 2 & I' & J' \end{Bmatrix}\begin{Bmatrix} I_a & I_a & 1 \\ I_a & I_a & 1 \\ I & I' & 2 \end{Bmatrix}, \tag{4.5}$$

$$\langle FIJ|\, H_{SSS}\, |FI'J'\rangle = \delta_{JJ'}\delta_{II'}\frac{1}{2}\delta\left[I\left(I+1\right)-2I_a\left(I_a+1\right)\right], \tag{4.6}$$

where I, J, and F are the quantum numbers of the total nuclear spin, total angular momentum, and total angular momentum including nuclear spin, respectively, large parentheses are 3-j symbols, large curly braces are 6-j and 9-j symbols, and eqQ, C, d, and δ, which characterize the hyperfine-coupling strength, are electric quadrupole, spin-rotation, tensorial spin-spin, and scalar spin-spin parameters, respectively. Each matrix element in equations 4.3 - 4.6 is expressed as a product of a hyperfine parameter and a geometrical function G depending only on the quantum numbers I, J,

and F. This is true also for the last four terms in equation 4.2. Thus the the matrix element of the hyperfine Hamiltonian in a particular electronic state Ω (either the X or the B state) can be expressed as

$$\langle \Omega, I'J'F \left| H_{hf,eff} \right| \Omega, IJF \rangle = eqQ \cdot G_{eqQ} + C \cdot G_{SR} + d \cdot G_{TSS} + \delta \cdot G_{SSS} + e \cdot G_e + f \cdot G_f + h \cdot G_h + hH \cdot G_{hH}, \quad (4.7)$$

The hyperfine parameters, i.e., eqQ, C, d, etc., can be determined by fitting this effective Hamiltonian to the hyperfine spectrum of a rovibrational transition. A detailed investigation of this effective Hamiltonian and the second-order calculation of its hyperfine parameters will be given in chapter 5.

4.3 Experimental Setup and Data Collection

4.3.1 Experimental Setup

A schematic of the experimental setup is depicted in figure 4.2. The system consists of a widely tunable frequency-doubled Ti:sapphire laser, a cell-based $^{127}I_2$ spectrometer for saturation spectroscopy with the frequency modulation (FM) technique, and a self-referenced optical frequency comb [115] that makes the absolute frequency measurement. The experimental details of the Ti:sapphire laser and the I_2 spectrometer can be found in chapter 2.

The details of the cell-based $^{127}I_2$ saturation spectroscopy have been described in chapter 2. Some aspects of the system are summarized briefly as follows. The $^{127}I_2$ cell was prepared at the Bureau International des Poids et Mesures, and it has an 8-cm useful length and Brewster windows at both ends. The $^{127}I_2$ vapor pressure is maintained at 3.3 Pa (22.3 °C) by temperature control of the cold finger of the cell. Whereas for a majority of the transitions investigated the collimated pump and probe beams are of $\sim$ 3-mm diameter and typical pump powers are $2 - 4$ mW, for some weak transitions with $v' > 60$ the beams are focused and pump powers are

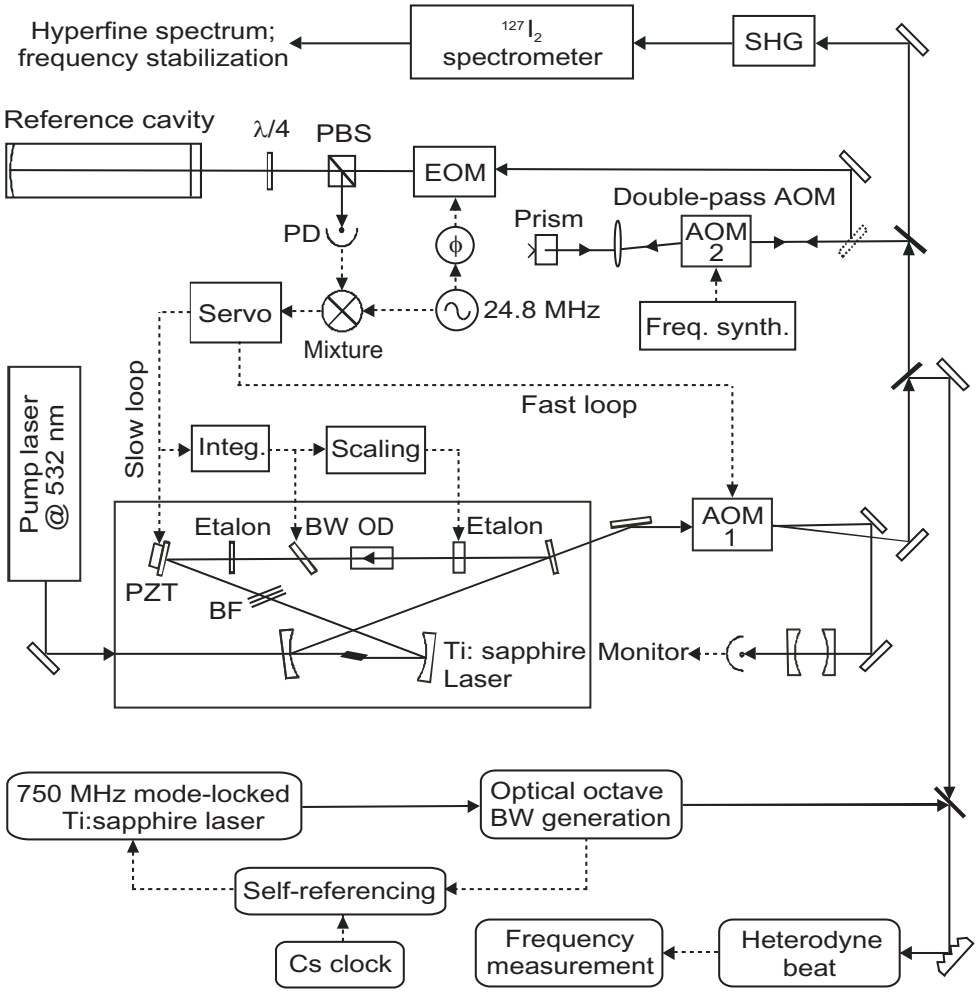

Figure 4.2: Schematic diagram of saturation spectroscopy in the wavelength range $500 - 517$ nm. A frequency-doubled Ti:sapphire laser is stabilized by a reference cavity and scanned by a RF synthesizer. Hyperfine spectra are extracted by the FM sideband technique. Introducing a self-referenced optical frequency comb into the system significantly simplifies the absolute frequency calibration. AOMs, acousto-optic modulators; BF, birefringent filter; BW, Brewster window plate; EOM, electro-optic modulator; OD, optical diode; PBS, polarization beam splitter; PD, photodiode; SHG, second-harmonic generator; $\lambda/4$, quarter-wave plate; ϕ, phase delay.

increased to $7 - 10$ mW to compensate for the large saturation intensity. The probe beam has 1-MHz frequency modulation sidebands and the pump beam is amplitude modulated by an in-line AOM.

Crucial to this high-resolution spectroscopy is precise and continuous scanning of the laser frequency over 1 GHz (a typical span of the hyperfine spectrum for one transition) without mode hop. The laser frequency, which is locked to the reference cavity, is scanned by a frequency synthesizer that drives a double-pass AOM (AOM 2 in figure 4.2) inserted between the laser and the reference cavity. The feedback signal applied to the PZT is integrated and then supplied to an intracavity Brewster plate, providing a large tuning range that is limited mostly by the RF bandwidth of the double-pass AOM. During the course of a frequency scan, the angle of the thick etalon is controlled in a feed-forward manner to synchronize the transmission peak of the thick etalon with the laser mode. We obtain continuous tuning in the green over a 1-GHz range, which we can enlarge greatly by locking the laser to different modes of the reference cavity. Figures 4.3 - 4.5 show several hyperfine spectra scanned by the Ti:sapphire laser.

Hyperfine splittings are measured in a pairwise manner. For each rovibrational transition measured, we typically select an isolated hyperfine component, roughly in the middle of the hyperfine spectrum whenever possible, as a reference line to form a pair with another component. The laser, locked to the reference cavity, is scanned across this pair of hyperfine components. The direction of the frequency scan is then reversed to take the laser frequency back to the initial position. For each scan direction, the corresponding resonance structure is recorded and a line-shape analysis of the saturation resonance determines the frequency difference between the two components. The bidirectional average of the frequency difference is then adopted to circumvent the slow and quasi-linear cavity drift (< 20 Hz/s) that dominates in a short period. This procedure is followed for all hyperfine components that are isolated

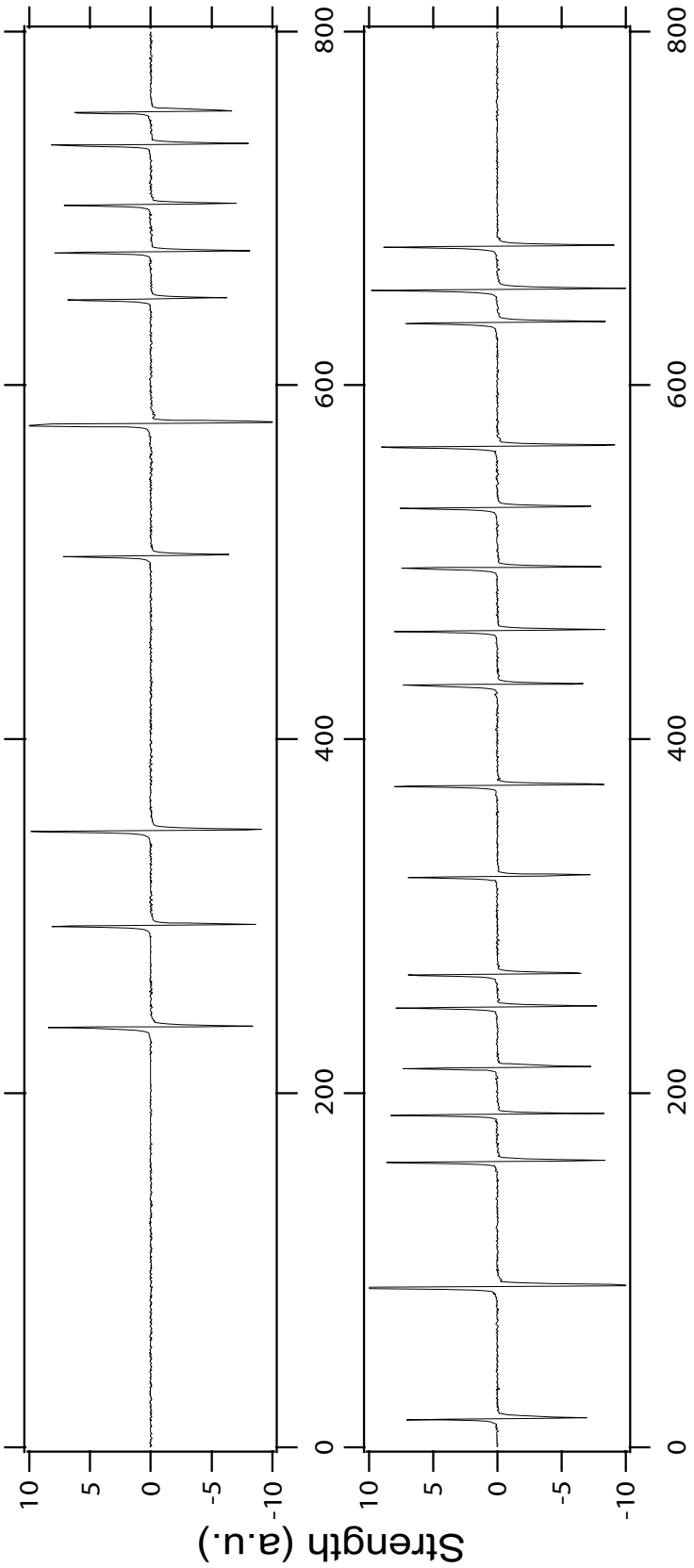

Figure 4.3: Hyperfine spectrum recorded at R(41) 42-0

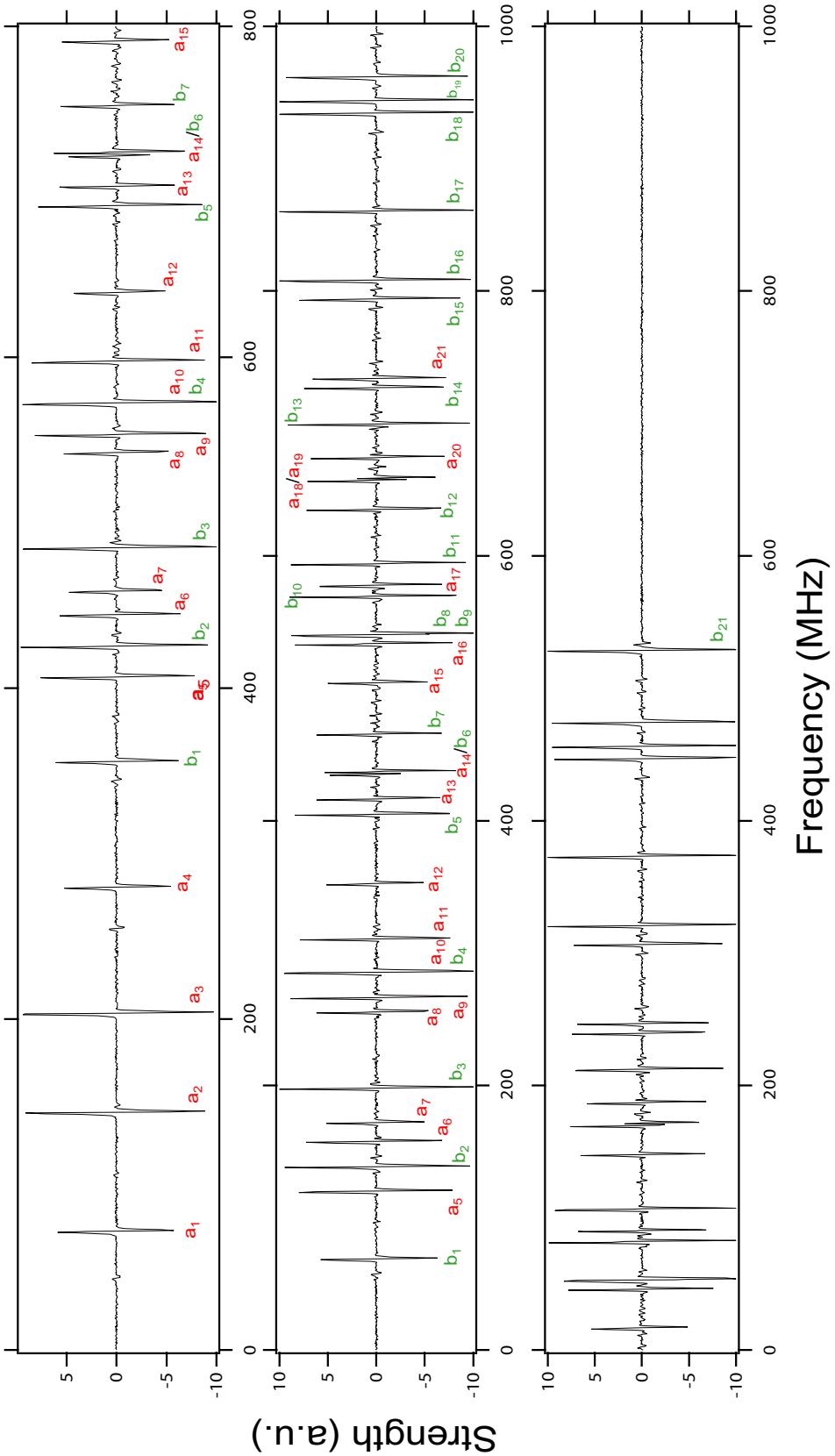

Figure 4.4: Hyperfine spectrum recorded at P(13) 43-0 and R(15) 43-0. Hyperfine components a_1 - a_{21} belong to P(13) 43-0, b_1-b_{21} belong to R(15) 43-0.

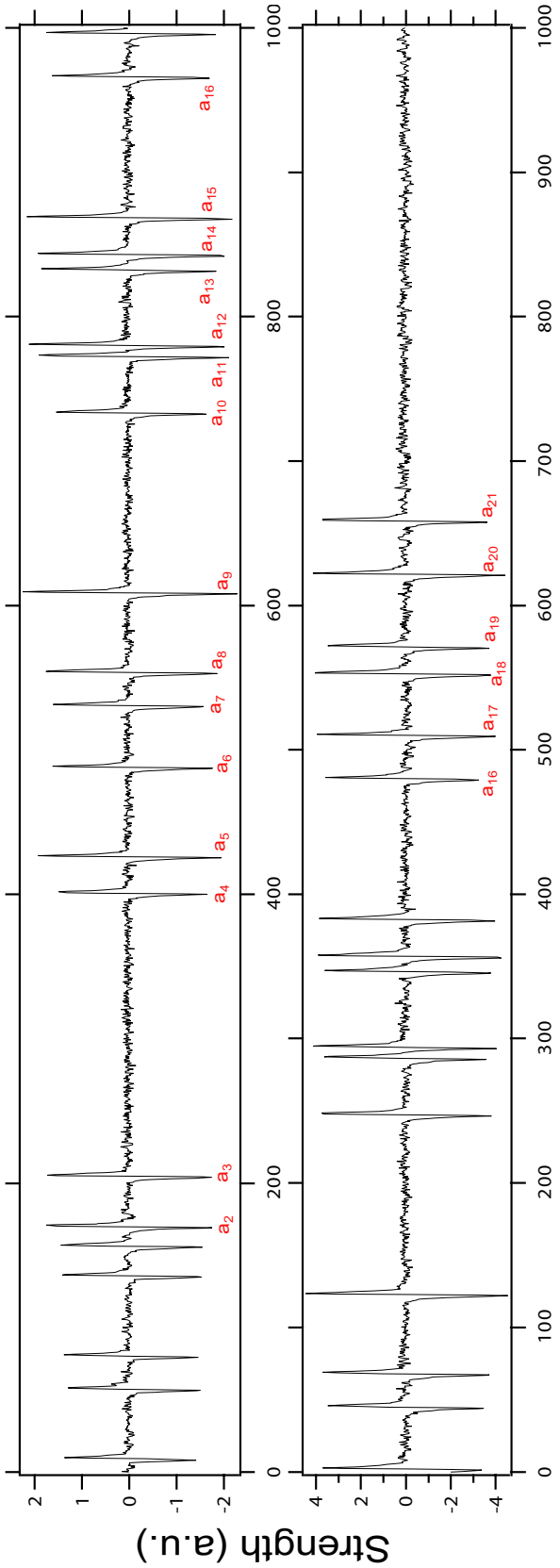

Figure 4.5: Hyperfine spectrum recorded at P(35) 70-0.

and hence can be well resolved by the FM sideband technique with a modulation frequency of 1 MHz.

The performance of the system can be evaluated by comparisons made at transitions where the hyperfine splittings obtained from high-precision beat experiments are available. For example, the frequency scan of the a_1 and a_3 components at transition P(13) 43-0 gives a frequency difference of 131.764(8) MHz between these two components, consistent with the published value of 131.7701(2) MHz [55]. Absolute frequency measurement of any desired $^{127}I_2$ transition is facilitated by a self-referenced optical frequency comb based on a mode-locked femtosecond laser, which has been described in chapter 3. Various system parameters, such as frequency and pressure shift, optical alignment, and residual amplitude modulation [116], are characterized or optimized with the help of the optical frequency comb. Whereas some of the hyperfine components have their absolute frequencies measured by the comb, most of the hyperfine-splitting measurements are carried out by the cavity-based laser scan with its intrinsic frequency-calibrated scale coming from the frequency synthesizer that drives the AOM tuning element.

4.3.2 Extracting the Effective Hyperfine Parameters from the Hyperfine Spectrum

Based on Bordé's FORTRAN code, a computer program that performs the nonlinear least-squares fit is developed to extract the effective hyperfine parameters from the hyperfine spectrum. We select a rotational basis set that spans $\Delta J = 0, \pm 2, \pm 4$ to construct the Hamiltonian matrix with vibrational and rotational constants E_v, B_v, D_v, H_v, L_v, and M_v taken from the I_2 atlas [68]. Although two neighboring vibrational levels with different J values can have a nonvanishing Franck-Condon overlap, their large energy separation ensures that the hyperfine coupling to different vibrational levels inside the B state is negligible. A practical issue inherent in the

measurement of main lines (transitions with $\Delta F = \Delta J$) is that the fit does not permit simultaneous determination of the hyperfine parameters both for the B and the X states. Without additional information, only the difference between the hyperfine parameters in the upper and the ground levels can be reliably obtained. To separate the B-state parameters from those of the X state we selectively excite the transitions with low vibrational level $v'' = 0$ [transitions P(49) 59-1 and R(45) 60-1 are two exceptions] and relate the J dependence of the ground-level parameters eqQ_X and C_X to that predetermined by interpolation formulas [42, 117]. The other two major parameters for the ground state, i.e., the tensorial and scalar spin-spin parameters d_X and δ_X , are fixed in the fit to the values of 1.524 and 3.705 kHz [42], respectively, which are good approximations for low-lying vibrational levels in the ground state X [42].

The nonlinear least-squares fit has been explained in great detail elsewhere [118, 119] and hence will not be discussed here. However, it is worth mentioning a special case of the fit. It was observed that at transition P(121) 35-0, the a_8 and a_{12} components could not be fitted by the program used at the time [120, 121], though these two components are isolated and their transition frequencies were measured with about the same S/N as that of other components.

This problem arises from the matching of the upper and lower hyperfine levels after the diagonalization of the associated Hamiltonians in the fitting procedure. Keeping track of I' and I'' before and after the diagonalization of the Hamiltonians for the B and the X states works for most levels in that it can generate the correct frequency of a hyperfine component by identifying the upper and lower levels involved. However, it occasionally gives erroneous pairing of the two levels and consequently one sees interchanged frequencies for two hyperfine components. Here we show explicitly the matching of the relevant hyperfine levels for the a_8 and a_{12} components of transition P(121) 35-0. After switching on the hyperfine Hamiltonian,

the total nuclear wave functions for the two relevant hyperfine levels in the B state evolve as

$$|I' = 3\rangle \longrightarrow |\varepsilon'(1)\rangle = 0.714\,|I' = 3\rangle + 0.701\,|I' = 5\rangle\,,$$
$$|I' = 5\rangle \longrightarrow |\varepsilon'(2)\rangle = -0.701\,|I' = 3\rangle + 0.714\,|I' = 5\rangle\,, \tag{4.8}$$

and likewise for the two levels in the X state:

$$|I'' = 3\rangle \longrightarrow |\varepsilon''(1)\rangle = 0.709\,|I'' = 3\rangle - 0.706\,|I'' = 5\rangle\,,$$
$$|I'' = 5\rangle \longrightarrow |\varepsilon''(2)\rangle = 0.706\,|I'' = 3\rangle + 0.709\,|I'' = 5\rangle\,. \tag{4.9}$$

Note that an overall phase factor is dropped for these wave functions. Because the dipole transition operator acts only on electronic degrees of freedom, the matching criterion is $|\langle\varepsilon'\,|\varepsilon''\rangle| = 1$, which indicates that $|\varepsilon'(1)\rangle$ $[|\varepsilon'(2)\rangle]$ is matched to $|\varepsilon''(2)\rangle$ $[|\varepsilon''(1)\rangle]$. Thus if the fitting procedure only tracks the total nuclear spins, then it will attempt to use the pairing $|\varepsilon''(1)\rangle \rightarrow |\varepsilon'(1)\rangle$ $[|\varepsilon''(2)\rangle \rightarrow |\varepsilon'(2)\rangle]$ to calculate the hyperfine splittings of the $a_8(a_{12})$ component with respect to a reference position. The matching criterion $|\langle\varepsilon'\,|\varepsilon''\rangle| = 1$ can be readily incorporated into the fitting procedure by using the eigenvectors obtained from the diagonalization of the Hamiltonians for the upper and lower electronic states.

4.4 B-State Effective Hyperfine Parameters in the Region $42 \leqslant v' \leqslant 70$

In the wavelength range $500 - 517$ nm we measured hyperfine spectra of 79 $B \longleftarrow X$ rovibrational transitions that cover a large set of rotational and vibrational quantum numbers in the B state. These transitions were chosen to include upper vibrational levels starting at $v' = 42, 43$ and thence progressing in increments of 2 to $v' = 63$: For each of these vibrational levels, we measured four to seven rotational levels that spread roughly from $J' = 10$ to $J' = 100$. Above $v' = 63$, three vibrational levels, $v' = 65$, 69, 70, were accessed, and the rotational levels measured for each

vibrational level are restricted to the range $J' = 30-60$ because of the weak transition moment associated with this region. In addition to the above data set, six rotational levels at $v' = 60$ and two rotational levels at $v' = 50$, 58 were also measured. Most of the hyperfine spectra recorded have been fitted by the four-term effective Hamiltonian described in section 4.2.2, and the extracted hyperfine parameters, together with the corresponding standard deviations, are listed in table 4.1. The hyperfine splittings for all the transitions measured are listed in appendix B. The list of table at the beginning of this thesis can be used to locate the spectrum for a specific transition.

Table 4.1: B-state effective hyperfine parameters derived from the measurement of $^{127}I_2$ rovibrational transitions in the wavelength range $500 - 517$ nm[a,b,c]

Transition	eqQ_B (MHz)	C_B (MHz)	d_B (MHz)	δ_B (MHz)	S. D. (KHz)
P(10) 42-0	-557.119(20)[d]	0.176138(96)	-0.08916(86)	-0.00520(85)	7.6
P(19) 42-0	-556.988(66)	0.17666(17)	-0.0921(43)	-0.0016(39)	33
R(30) 42-0	-557.184(44)	0.177751(85)	-0.0946(22)	0.0099(33)	22
R(41) 42-0	-557.553(30)	0.179178(24)	-0.0929(20)	-0.0003(16)	17
R(49) 42-0	-557.612(50)	0.180487(46)	-0.0915(25)	0.0051(23)	30
P(13) 43-0	-558.613(18)	0.190361(78)	-0.09899(62)	-0.00083(56)	10
P(25) 43-0	-558.823(15)	0.191161(39)	-0.1009(12)	0.0025(11)	9.4
R(27) 43-0	-558.667(23)	0.191593(38)	-0.0988(16)	0.0015(12)	11
P(38) 43-0	-558.565(12)	0.192839(21)	-0.10109(69)	-0.00001(81)	5.9
R(40) 43-0	-558.604(17)	0.193497(14)	-0.10303(86)	0.00034(86)	6.4
R(63) 43-0	-559.456(16)	0.198545(12)	-0.10629(90)	0.00234(85)	11
R(21) 45-0	-560.838(13)	0.223669(23)	-0.12073(80)	0.00623(57)	7.6
R(52) 45-0	-561.356(22)	0.229843(18)	-0.1239(10)	0.0095(15)	10
P(69) 45-0	-561.804(11)	0.2349204(71)	-0.12617(80)	0.00739(59)	6.8
P(91) 45-0	-562.546(13)	0.2452897(55)	-0.1324(10)	0.00975(82)	7.9
R(31) 47-0	-562.816(27)	0.264762(35)	-0.1390(16)	0.0172(12)	12
R(51) 47-0	-563.294(12)	0.270529(10)	-0.14741(84)	0.01588(64)	7
R(92) 47-0	-564.742(23)	0.293399(10)	-0.1598(10)	0.0200(13)	9.4
R(111) 47-0	-565.651(56)	0.310759(29)	-0.1626(44)	0.0254(35)	37
P(19) 49-0	-564.6327(72)	0.309250(21)	-0.16923(43)	0.02631(31)	4.6
P(41) 49-0	-564.886(26)	0.314896(28)	-0.1706(18)	0.0262(13)	16
P(62) 49-0	-565.295(39)	0.324667(25)	-0.1794(17)	0.0326(22)	16
R(93) 49-0	-566.485(19)	0.3509271(87)	-0.1940(13)	0.0403(10)	11
P(108) 49-0	-567.273(24)	0.3662298(84)	-0.1996(10)	0.0427(13)	9.7
R(55) 50-0	-566.0544(80)	0.3504090(55)	-0.19199(56)	0.03910(46)	4.7
R(20) 51-0	-566.275(21)	0.366031(35)	-0.20074(96)	0.0469(11)	7.1
P(30) 51-0	-566.415(29)	0.368223(40)	-0.2005(13)	0.0401(19)	13
P(50) 51-0	-566.763(14)	0.377297(11)	-0.20747(63)	0.05024(66)	5.6
P(73) 51-0	-567.132(23)	0.394644(14)	-0.2134(16)	0.0552(12)	12
P(90) 51-0	-567.872(28)	0.413339(14)	-0.2258(13)	0.0628(19)	13
R(32) 53-0	-567.752(27)	0.437830(32)	-0.2383(12)	0.0785(16)	11
R(51) 53-0	-568.171(11)	0.450037(11)	-0.24241(82)	0.08388(55)	6.6
P(70) 53-0	-568.623(34)	0.466803(19)	-0.2535(15)	0.0937(19)	14
P(89) 53-0	-569.274(40)	0.493524(21)	-0.2664(27)	0.1073(19)	21
R(21) 55-0	-568.807(18)	0.513082(32)	-0.2718(12)	0.12206(91)	10
P(61) 55-0	-569.444(22)	0.544230(21)	-0.2854(16)	0.1444(13)	15
P(83) 55-0	-570.208(27)	0.579914(17)	-0.3006(16)	0.1701(13)	15
P(102) 55-0	-571.145(42)	0.626595(27)	-0.3212(21)	0.2092(28)	22

(Table Continued)

Table 4.1: Continued

Transition	eqQ_B (MHz)	C_B (MHz)	d_B (MHz)	δ_B (MHz)	S. D. (KHz)
P(19) 57-0	-569.534(27)	0.605935(82)	-0.3091(19)	0.1993(11)	15
P(33) 57-0	-569.335(44)	0.614577(46)	-0.3103(26)	0.2058(20)	23
R(65) 57-0	-571.765(86)	0.660831(90)	-0.4260(68)	0.3647(59)	60
R(74) 57-0	-570.210(94)	0.678716(54)	-0.3092(44)	0.2500(65)	44
P(80) 57-0	-570.38(12)	0.688579(74)	-0.298(14)	0.240(21)	37
R(83) 57-0	-570.632(90)	0.702332(76)	-0.311(12)	0.280(11)	46
R(95) 57-0	-570.701(83)	0.741636(48)	-0.3270(59)	0.3323(50)	51
P(17) 59-0	-568.58(15)	0.72125(42)	-0.290(13)	0.141(11)	73
P(27) 59-0	-573.49(28)	0.71536(54)	-0.569(14)	0.382(14)	131
R(28) 59-0	-573.32(48)	0.72088(55)	-0.476(24)	0.316(18)	93
P(49) 59-1	-571.695(39)	0.750322(35)	-0.4326(26)	0.3335(20)	22
R(81) 59-0	-572.12(11)	0.840592(60)	-0.4355(78)	0.4337(59)	65
P(87) 59-0	-572.555(90)	0.856503(46)	-0.4360(65)	0.4444(55)	55
P(21) 60-0	-569.937(20)	0.783323(37)	-0.3773(13)	0.34612(86)	11
R(34) 60-0	-569.964(45)	0.799015(53)	-0.3820(20)	0.3619(30)	21
R(45) 60-1	-570.446(92)	0.816760(82)	-0.3800(62)	0.3793(37)	43
R(99) 60-0	-573.28(23)	1.03267(11)	-0.499(17)	0.688(14)	121
P(17) 61-0	-569.550(24)	0.850067(59)	-0.3944(14)	0.4414(10)	13
R(36) 61-0	-569.603(42)	0.875111(89)	-0.4056(19)	0.4638(27)	16
P(53) 61-0	-570.037(79)	0.906087(75)	-0.4162(42)	0.5154(42)	44
P(83) 61-0	-570.14(14)	1.02283(10)	-0.422(10)	0.6224(83)	87
P(23) 63-0	-568.464(78)	1.01785(15)	-0.4219(56)	0.6974(44)	46
R(31) 63-0	-568.62(11)	1.03395(15)	-0.4281(76)	0.7225(58)	70
P(43) 63-0	-568.854(83)	1.05691(12)	-0.4436(43)	0.7560(36)	40
P(52) 63-0	-569.08(11)	1.084930(90)	-0.4532(49)	0.7987(73)	51
P(19) 65-0	-566.342(63)	1.21056(14)	-0.4648(37)	1.0373(32)	43
P(33) 65-0	-566.504(73)	1.24010(14)	-0.4893(33)	1.0966(34)	46
R(43) 65-0	-567.21(11)	1.28195(20)	-0.4901(68)	1.1712(49)	57
P(33) 69-0	-558.63(12)	1.85049(22)	-0.6800(72)	2.3114(69)	44
P(39) 69-0	-560.05(23)	1.89425(41)	-0.696(12)	2.422(10)	119
R(44) 69-0	-561.17(27)	1.96255(38)	-0.732(12)	2.5258(96)	76
R(49) 69-0	-559.39(26)	2.02075(33)	-0.854(14)	2.559(14)	116
P(53) 69-0	-562.09(50)	2.04973(57)	-0.793(28)	2.691(22)	252
P(35) 70-0	-557.32(24)	2.08735(37)	-0.809(12)	2.8335(88)	111
R(37) 70-0	-557.47(35)	2.12619(51)	-0.867(22)	2.886(14)	173
R(45) 70-0	-558.80(44)	2.22994(62)	-0.937(24)	3.045(17)	196

[a] A four-term effective Hamiltonian is used in the fit. Transitions P(69) 58-0, R(18) 59-0, P(84) 60-0, P(77) 60-0, and P(63) 70-0 are not included in this table because their upper-level hyperfine spectra are altered considerably by the hyperfine perturbation from a $1_g(^1\Pi_g)$ state.

[b] eqQ_X and C_X are determined by equations (14) and (10), respectively, in reference [42] and are held fixed in the fit.

[c] d_X and δ_X are fixed in the fit to 1.524 and 3.705 kHz [42], respectively.

[d] Quoted uncertainties (1σ) are estimated from the standard deviations of the fits.

First, for the transition P(13) 43-0 the four effective parameters obtained by our measurement are in good agreement with previous results within the measurement uncertainties. The standard deviation of the fit is typically $10-20$ kHz for levels below $v' = 55$ and is caused primarily by various experimental sources such as background interference fringes superimposed upon the saturation resonance, residual cavity drift, variations of the optical power and alignment arising from the frequency scan, and residual amplitude modulation in the saturation spectroscopy.

At rovibrational levels above $v' = 55$, transitions R(65) and R(74) of the 57-0 band and P(17), P(27), and R(28) of the 59-0 band distinguish themselves from adjacent transitions by large standard deviations that cannot be explained by the experimental sources mentioned above. Furthermore, fits for transitions P(69) 58-0, R(18)59-0, P(77) 60-0, and P(63) 70-0 produce very large standard deviations ($0.3 - 1$ MHz), and the hyperfine spectrum of the P(84) 60-0 transition cannot be fitted at all by the effective hyperfine Hamiltonian[2] . The spectra of these transitions are provided in appendix B. We attribute this abnormality to the influence of the same $1_g(^1\Pi_g)$ state that strongly perturbs the $v' = 76$, 77, 78 vibrational levels close to the dissociation limit. Because of the strong perturbation, hyperfine spectra at these transitions cannot be fully described by the effective Hamiltonian based on second-order perturbation theory. The source of this perturbation is confirmed and its specific properties in the intermediate region that we investigate are discussed further in section 4.8. We have also attempted to introduce the last four terms in equation 4.7. At levels of $v' = 57 - 65$, these four additional terms do not improve the standard deviations of the fits. Besides, effective hyperfine parameters e, f, g, and hH derived from the new fits all have large uncertainties that are comparable to the fitted values, and contradict the smooth trend of the second-order contribution

[2] With a_2 and a_{10} components excluded, the spectrum can be fitted to the four-term effective hyperfine Hamiltonian with large residual error (1.1 MHz). See appendix B.58 for details.

by altering their signs across adjacent rotational levels. Although vibrational levels with $\upsilon' = 65$ would be better candidates for testing these additional terms because of the increasing perturbation, the present large uncertainties associated with these weak transitions preclude any accurate assessment. Also, as pointed out in reference [16], the total number of hyperfine parameters that can be fitted reliably is restricted by the use of a maximum of 15 or 21 main lines in the hyperfine spectrum.

4.5 Vibrational Dependence of Hyperfine Parameters in the B State

Combining the data from the study reported here and from the literature [45, 42, 55, 117, 40, 120, 122, 123, 124, 125, 126, 127, 128, 129] has facilitated investigations of the hyperfine spectra that now cover a majority of the vibrational levels ($3 < \upsilon' < 82$) in the B state. Therefore it is now possible to explore the global trend of these hyperfine parameters in the B state and uncover systematic variations of the corresponding hyperfine interactions. With the rotational dependence being suppressed, the hyperfine parameters as functions of pure vibrational energy $E(\upsilon')$ are illustrated in figure 4.6. As shown in the figure, the values of these hyperfine parameters increase rapidly when the molecule approaches the dissociation limit, which is a result of the perturbations from the cluster of electronic states that share the same dissociation limit with the B state. While the variation of C_B is essentially smooth over the whole range of vibrational energies, eqQ_B, d_B, and δ_B all have local irregularities at several regions. First, in the region $3 < \upsilon' < 17$ [16 000 cm^{-1} $< E(\upsilon') <$ 17 700 cm^{-1}], both d_B and δ_B have visible fluctuations because of the magnetic dipole coupling between the B and the $B''1_u(^1\Pi_u)$ states that arises from a potential crossover near level $\upsilon' = 5$ [67]. Meanwhile, the absence of such fluctuation in C_B at these levels is due to the fact that the accompanying gyroscopic coupling, which is involved only in C_B, is a weak effect compared with the magnetic-dipole coupling [66, 67, 42, 61]. Second, irregularities in hyperfine parameters are found

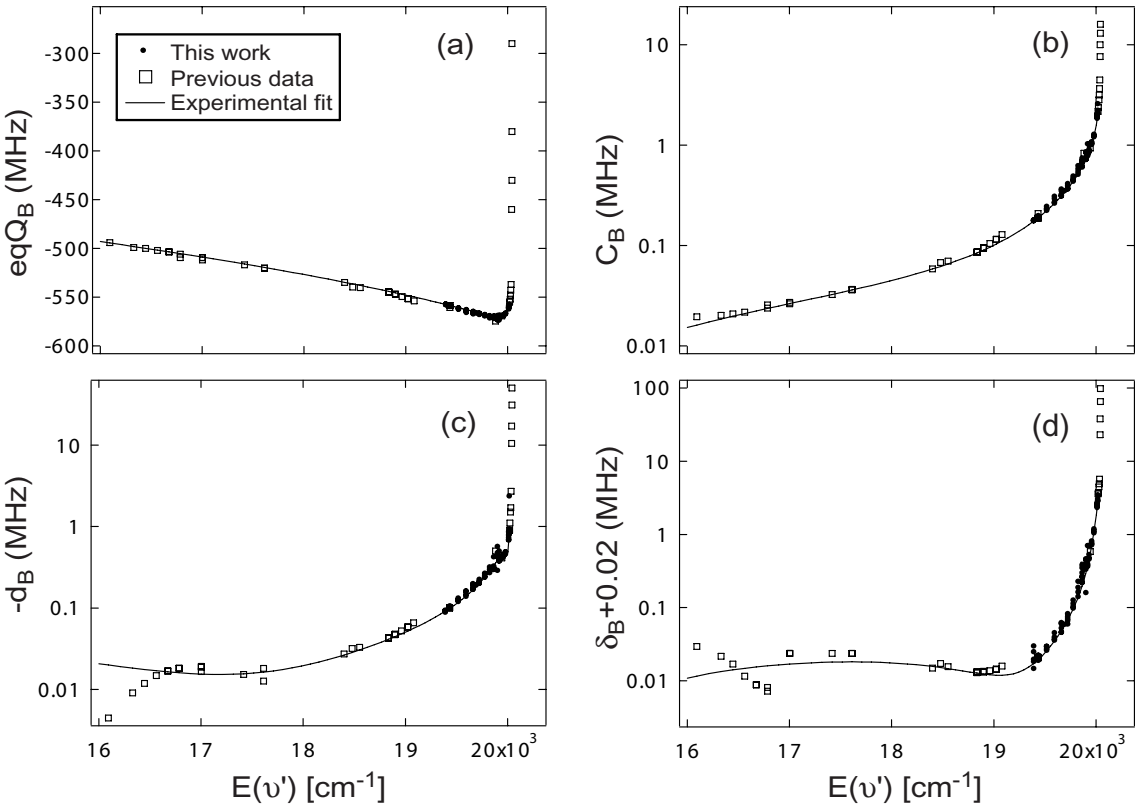

Figure 4.6: Vibrational dependence of the B-state hyperfine parameters eqQ_B, C_B, d_B, and δ_B. Note that a semilog plot is used for C_B, d_B, and δ_B. The steep trend near the dissociation energy is due to the perturbations from the electronic states converging with the B state to the second dissociation limit: $^2\mathrm{P}_{3/2}$+ $^2\mathrm{P}_{1/2}$.

for levels near $v' = 57 - 60$ [19 863 cm^{-1} $< E(v') <$ 19 915 cm^{-1}] at which eqQ_B, d_B, and δ_B deviate from the smooth trend for a small range of rotational levels in a certain vibrational level. As will be discussed in section 4.8, this resonance feature results from the hyperfine coupling between the B and the $1_g(^1\Pi_g)$ states through the rotational coincidence. Finally, the same $1_g(^1\Pi_g)$ state strongly perturbs levels from $v' = 76$ to $v' = 78$ [$E(v') \approx$ 20 034 cm^{-1}] with the favorable Franck-Condon overlaps and the small energy separations [45, 43]. In last two perturbing regions, C_B also keeps its smooth trend because the gyroscopic Hamiltonian cannot couple the B state with the $1_g(^1\Pi_g)$ state [16].

The v dependence of eqQ_B reverses its trend after $v' = 60$ [$E(v') \approx$ 19 915 cm^{-1}]; hence its values for higher v' levels overlap those of lower v' levels, a consequence of the two effects that dominate at different regions: a first-order term—the interaction between nuclear quadrupole moment Q and electric field gradient q—increases with decreasing vibrational energy but approaches a constant value at large energies at which the second-order term from perturbing electronic states moves in gradually and causes a steep trend near the dissociation energy.

4.6 Radial Dependence of Hyperfine Interactions

In this section we examine the variation of the hyper-fine interaction with internuclear separation R. Because hyperfine parameters already involve averaging over the molecular rotation, the electronic motion in the molecular frame, and the nuclear vibration, it is desirable to remove the last vibrational average in these hyperfine parameters such that a straightforward relation between the hyperfine interaction and the internuclear separation can be obtained.

We remove the vibrational average in the hyperfine parameters by inverting the expression

$$O(v', J') = \langle v'_{J'} \left| O(R) \right| v'_{J'} \rangle \,, \tag{4.10}$$

where $O(\upsilon', J')$ denotes one of the four hyperfine parameters for a particular level (υ', J') in the B state and $|\upsilon'_{J'}\rangle$ is the corresponding vibrational wave function (properly normalized). The inversion is performed by expanding the function $O(R)$ as a polynomial with its coefficients determined from an experimental fit [130, 131]. Le Roy's program LEVEL [132] is used in the process to calculate the vibrational wave functions from the B-state potential energy curve [133]. Figure 4.7 plots $eqQ_B(R)$, $C_B(R)$, $d_B(R)$, and $\delta_B(R)$, along with the corresponding residual errors of the interpolation. Consistent with the smooth variation in C_B , interpolation function $C_B(R)$ has small residual errors (within ± 0.02, relative) for the entire range $\upsilon' = 3 - 70$, as shown in the inset of figure 4.7(b). Conversely, the large residual errors in the interpolation of eqQ_B, d_B, and δ_B for $\upsilon' > 56$ reflect the abnormal variations observed near $\upsilon' = 57$, 59 [see the insets in figure 4.7], restricting a reliable interpolation only to levels of $\upsilon' < 56$.

The hyperfine parameters extracted from the spectra are directly associated with specific quantum numbers (υ', J') but not internuclear separation R. Alternatively, these hyperfine parameters can be plotted against R-centroid $\langle \upsilon'_{J'} |R| \upsilon'_{J'} \rangle$, which is the expectation value of the internuclear separations sampled by the nuclear vibration and evaluated by use of the B-state potential [133]. Figure 4.8 shows such plots for eqQ_B, C_B, d_B, and δ_B, where solid curves are calculated from $\langle \upsilon'_{J'} |O(R)| \upsilon'_{J'} \rangle$ and symbols are experimental data. Again, the visible scatter of data points in eqQ_B, d_B, and δ_B near 5 Å is due to the strong perturbation from the $1_g(^1\Pi_g)$ state.

In the region $R < 5$ Å valuable information can readily be extracted from eqQ_B to assist the investigation of the electronic structure of $^{127}I_2$. Unlike the other three hyperfine parameters whose major parts originate from perturbations at nearly all possible values of R, a significant part of eqQ_B is due to the interaction between the nuclear quadrupole moment Q and the electric field gradient $q(R)$ generated by the surrounding charge distribution of a largely B-state character [16, 47]. This

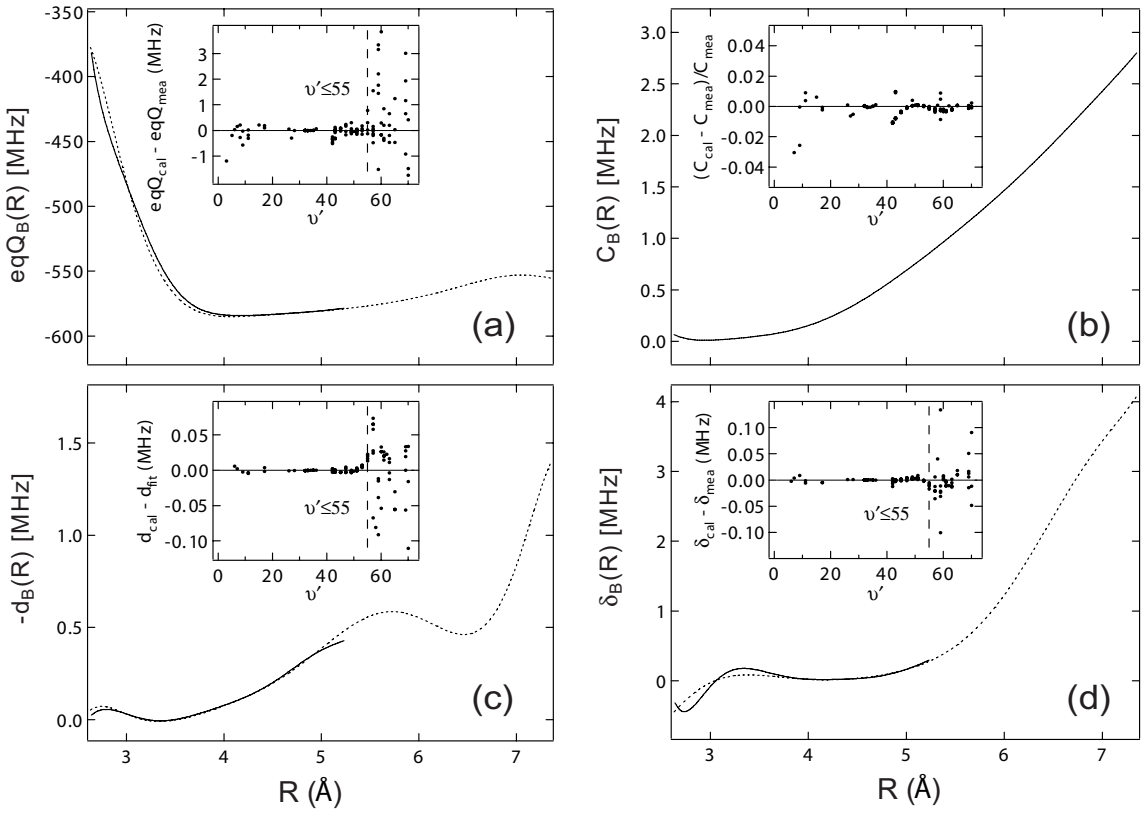

Figure 4.7: R dependence of the hyperfine operators $eqQ_B(R)$, $C_B(R)$, $d_B(R)$, and $\delta_B(R)$. These hyperfine operators are obtained by inverting the expression $O_{v'J'} = \langle v'_{J'}| O(R) |v'_{J'}\rangle$, where O represents one of the hyperfine parameters. Insets are residual errors of the interpolation. (a), (c), (d) Solid and dashed curves are fits up to $v' = 55$ and $v' = 70$, respectively. The fit in (b) is up to $v' = 70$. The large residual errors for eqQ_B, d_B, and δ_B in the region $55 < v' \leqslant 70$ are due to the strong perturbation from the $1_g(^1\Pi_g)$ state.

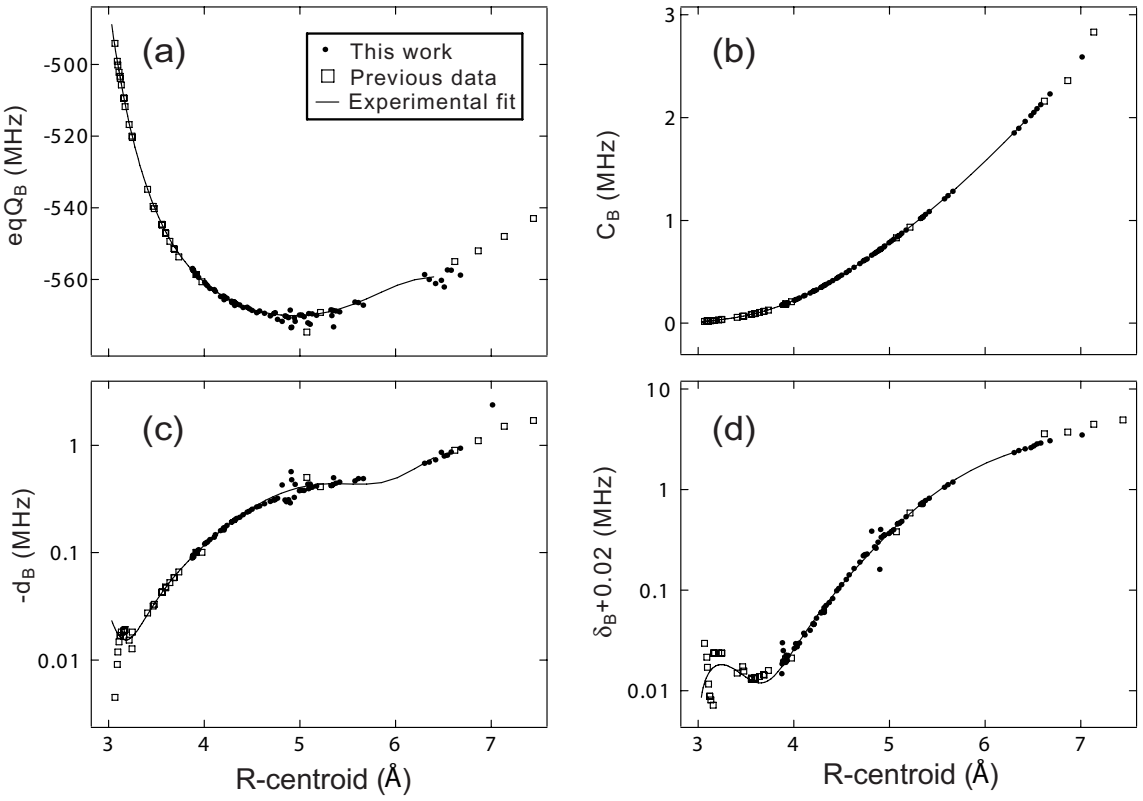

Figure 4.8: eqQ_B, C_B, d_B, and δ_B versus R centroid $\langle v'_{J'} | R | v'_{J'} \rangle$. Solid curves are calculated from the interpolation functions for these hyperfine parameters. The data presented here cover a relatively large range of internuclear separation and join the previous results at both small and large R-centroids. The visible scatter of the data points in eqQ_B , C_B, and δ_B near 5 Å is due to the strong perturbation from the $1_g(^1\Pi_g)$ state.

fact is more evident if we focus on the region $R < 5$ Å where perturbations from other electronic states are negligible by comparison. Moreover, when they move from a separated-atom model to small internuclear separation, the two atomic wave functions are increasingly distorted, their overlapping also increases, and hence eqQ_B deviates gradually from the value calculated from a separated-atom basis set or linear combinations of atomic orbitals. Therefore, when $R < 5$ Å the vibration-removed interpolation function $eqQ_B(R)$, coupled with a prior information on $q(R)$, can be used to determine iodine's nuclear quadrupole moment or to serve as a benchmark for molecular *ab initio* calculations of the electronic structure at various values of R. For this purpose the coefficients of the interpolation function for $eqQ_B(R)$ over the range $R = 3 - 5$ Å is given in table 4.2.

Table 4.2: Vibration-removed interpolation function $eqQ_B(R)^a$

i	a_i
0	2487.80(17)[b]
1	2236(11)
2	112(26)
3	163(28)
4	2210(18)
5	87.8(6.5)
6	212.73(94)
Standard deviation (MHz)	0.21

[a] $eqQ_B(R) = \sum_{i=0}^{6} a^i (R - R_e)^i$, 3 Å $< R <$ 5 Å, and R_e= 3.02708Å. The fit includes 69 levels with $v' < 57$, which are taken from this study and from published data summarized in [42, 117].
[b] Quoted uncertainties (1σ) are estimated from the standard deviations of the fit.

4.7 Rovibrational Dependence of Hyperfine Parameters as a Result of the Second-Order Effect

Four hyperfine parameters, eqQ_B, C_B, d_B, and δ_B, all exhibit systematic rovibrational dependence in the measured vibrational levels from $v' = 42$ to $v' = 70$.

Figures 4.9–4.11 display variations of these parameters. In the figures each solid line is a fit of experimental data that belong to a single vibrational level υ' (υ' is indicated as a number attached to each line in the figures). In general, these parameters have monotonic dependence on both rotational and vibrational quantum numbers, except for the levels in the vicinity of $\upsilon' = 57 - 59$, where strong perturbation from the $1_g(^1\Pi_g)$ state produces irregularities that superpose upon the smooth second-order background. Except for the variation of eqQ_B at vibrational levels lower than $\upsilon' = 60$, the smooth and monotonic trend of these effective hyperfine parameters is well characterized by second-order perturbation theory. For instance, spin-rotation parameter C_B can be expressed as [45, 16, 46, 134]

$$C_B(\upsilon, J) = C_D(\upsilon, J) - \sum_{\Omega'} \left[\sum_{\upsilon'} \frac{\langle V^0 \rangle \langle V^1 \rangle}{E_{0_u^+ \upsilon J} - E_{\Omega' \upsilon' J}} + \int \frac{\langle V^0 \rangle \langle V^1 \rangle}{E_{0_u^+ \upsilon J} - E_{\Omega' J}} \rho(E_{\Omega' J}) dE_{\Omega' J} \right]. \tag{4.11}$$

The first-order contribution C_D is less than 0.15 kHz [16], which is negligible compared with the second-order contribution. The summation on υ' and the integral in brackets in equation 4.11 together account for the second-order contribution from both discrete levels (υ', J) and energy continuum E_J. In the numerators $\langle V^0 \rangle$ and $\langle V^1 \rangle$ denote gyroscopic and magnetic dipole couplings, respectively, which can be approximated as a product of a Franck-Condon integral and an electronic matrix element with the assumption that the latter has a weak R dependence [16]. The other three effective parameters can be expressed in the same manner with different types of hyperfine coupling [45, 16].

As the B-state rovibrational levels (υ, J) progress toward the dissociation limit, their overall Franck-Condon overlaps with the perturbing levels continue to increase while the corresponding energy denominators decrease, thereby creating monotonic trends in hyperfine parameters, with large slopes near the dissociation limit. More specifically, in a given vibrational level υ, as the rotational quantum number J in-

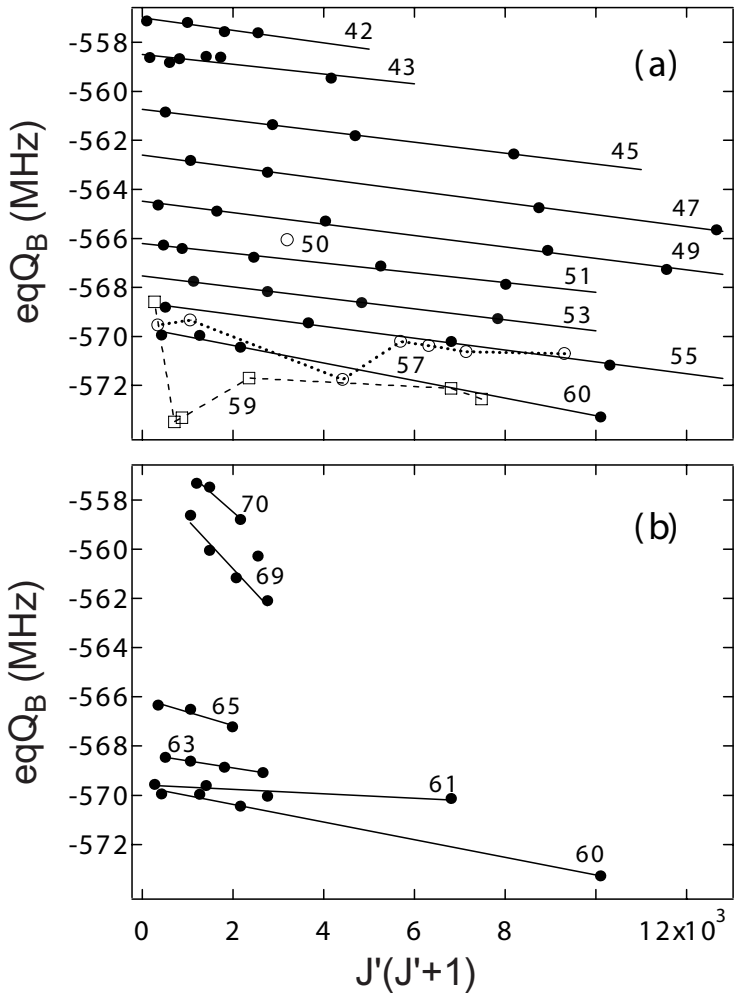

Figure 4.9: Rovibrational dependence of eqQ_B. Each solid line is the linear fit in $J'(J'+1)$ of experimental data that belong to one vibrational level, υ' (υ' is indicated as a number attached to each line). Experimental data (open squares and circles) show abnormal variations near $\upsilon' = 57$, 59. The vibrational dependence of eqQ_B reverses its trend after $\upsilon' = 60$ and overlaps that of lower υ' levels. Also, in the region $\upsilon' = 57 - 60$ several rovibrational levels experience strong perturbation from the $1_g(^1\Pi_g)$ state; thus eqQ_B for these levels are not shown in the figure.

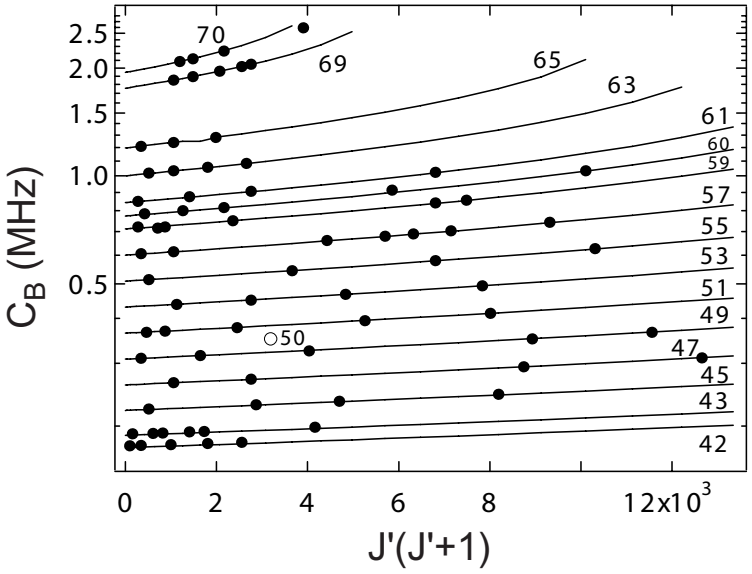

Figure 4.10: Semilog plot of rovibrational dependence of C_B. Each solid line, calculated from interpolation function $C_B(R)$ [see figure 4.7 (b)], is the J dependence for one vibrational level v' (v' is indicated as a number attached to each line). Unlike eqQ_B, d_B, and δ_B, C_B does not have abnormal variations near $v' = 57$, 59 because the gyroscopic Hamiltonian, which is involved only in C_B, cannot couple the B and the $1_g(^1\Pi_g)$ states.

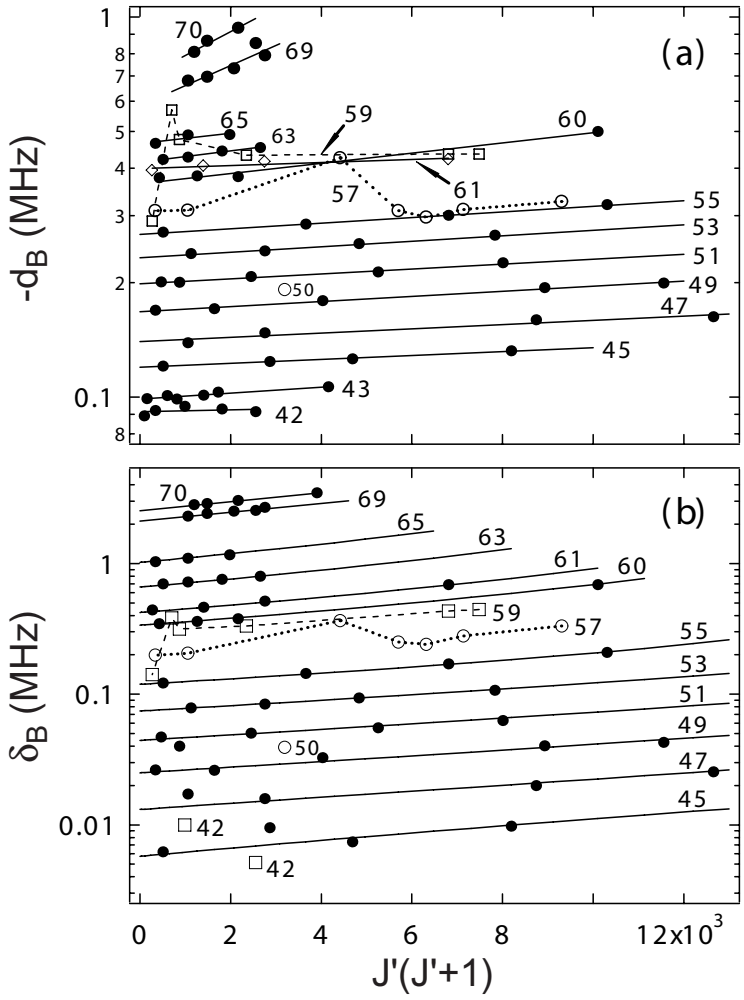

Figure 4.11: Semilog plot of rovibrational dependence of d_B and δ_B. Note that the vertical scale has been inverted for d_B. Each solid line is the linear fit in $J'(J'+1)$ of experimental data that belong to one vibrational level, v' (v' is indicated as a number attached to each line). Experimental data (open squares and circles) show abnormal variations near $v' = 57$, 59. In the region $v' = 57 - 60$ several rovibrational levels experience strong perturbation from the $1_g(^1\Pi_g)$ state; thus hyperfine parameters for these levels are not shown in the figure.

creases the total number of discrete vibrational levels inside each perturbing electronic state drops, whereas the contribution from energy continuum increases. The combined contribution from discrete levels and continuous spectrum gives a smooth variation of the hyperfine parameters even for large J values.

The systematic data from this study and from the literature offer a means for a complementary approach to analyzing the electronic structure of the states converging to the second dissociation limit, $^2P_{\frac{3}{2}} + {}^2P_{\frac{1}{2}}$. Previous calculations [45, 46, 134] of hyperfine parameters can be extended to low vibrational levels as well as to the rotational dependence at each vibrational level, using the available information on the electronic wave functions and the related potential energy curves (PEC) determined either by experiment [133, 135] or by theoretical calculation [110]. Several interesting issues can be addressed with the help of these calculations, such as (1) to what extent the separated-atom wave functions can be extrapolated to short internuclear separations, (2) an estimation of the admixtures of the basis wave functions in the separated-atom model, and (3) how sensitively the hyperfine parameters depend on the choice of PECs. This line of investigation is beyond the scope of current chapter and will be detailed in chapter 5.

4.8 Strong Perturbation from the $1_g(^1\Pi_g)$ State

Apart from second-order effect, we observed strong perturbation in the intermediate region that spans $v' = 42 - 70$. Hyperfine parameters eqQ_B, d_B, and δ_B all exhibit abnormal J dependence for levels $v' = 57$, 59, which are clearly present in figures 4.9 and 4.11. Moreover, as pointed out in section 4.4, hyperfine spectra of several transitions have exceptionally large residual errors in the fit or cannot be fitted by the effective hyperfine Hamiltonian in the region $v' = 57 - 60$.

The nature of this perturbation is analogous to that of the rotational and vibrational perturbations studied in a variety of molecules [136]. Among the cluster

of electronic states converging with the B state, the $1_g(^1\Pi_g)$ state has a potential whose outer limb is closest to that of the B state. It is possible that an approximate energy coincidence and a moderate Franck-Condon overlap between the B and the $1_g(^1\Pi_g)$ rovibrational levels arise simultaneously as two sets of rovibrational levels progress respectively inside the B and the $1_g(^1\Pi_g)$ states. This perturbation depends sensitively on the energy differences among the levels involved and hence cannot be treated by the effective Hamiltonian based on second-order perturbation theory.

The strong u-g mixing that we recorded at transition P(84) 60-0 permits a more quantitative analysis. The hyperfine spectrum of this transition is shown in figure 4.12, where vertical bars labeled $a_1 - a_{15}$ above the spectrum are simulated by the four-term effective Hamiltonian with the hyperfine parameters obtained by interpolation of the parameters of neighboring rovibrational levels. This simulation produces the spectrum in the absence of strong perturbation. As shown in figure 4.12, the a_{10} component does not show up at the position predicted by the simulation; instead, at least four new components, namely, $b_1 - b_4$, emerge nearby: Apparently the upper level of a_{10} is strongly perturbed by hyperfine levels of a perturbing electronic state and the mixed levels appear as b_1 and b_3 , with the crossover b_2 appearing in the middle.

The upper level of a_{10} ($F = 87$, $J = 83$, and $I = 4$) is isolated from other hyperfine levels inside the B state because it is coupled to only two hyperfine levels with large energy separations (~ 111 GHz). However, calculation that uses the B and $1_g(^1\Pi_g)$ empirical PECs [133, 135] shows that the perturbing levels could be the two hyper-fine levels (resulting from linear combinations of $I' = 3, 5$) at rovibrational level ($\upsilon' = 15$, $J' = 84$) inside the $1_g(^1\Pi_g)$ state. Nevertheless, judging from the relatively large strength of the b_1 and b_3 components, an effective two-level model, characterized by a energy difference ΔE and an coupling matrix element H_{12}, is adequate for estimating the hyperfine-coupling strength between the B and the $1_g(^1\Pi_g)$ states.

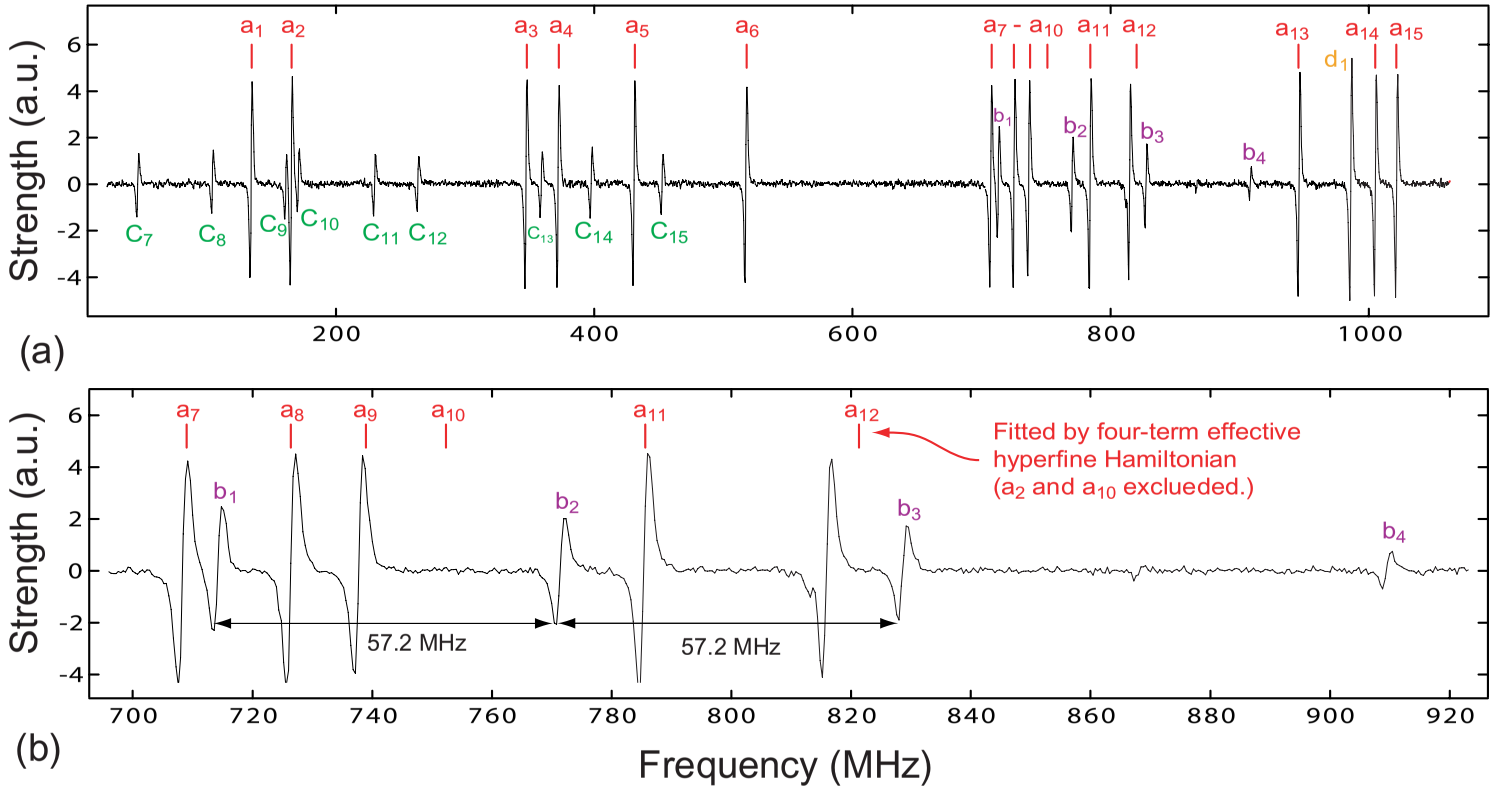

Figure 4.12: Strong u-g perturbation observed at transition P(84) 60–0. (a) The whole spectrum; the part of interest ($700-920$ MHz) is expanded and replotted in (b), where b_1– b_4 arise from u-g mixing between the B and the $1_g(^1\Pi_g)$ states and b_2 is the crossover of b_1 and b_3. In (a) c_7– c_{15} are identified as lines of a neighboring transition R(30) 64-1, and d_1, left of a_{14}, belongs to another transition, P(81) 59-0. The vertical bars labeled a_1– a_{15} indicate the hyperfine spectrum that the P(84) 60-0 transition would assume if there were no such strong perturbation from the $1_g(^1\Pi_g)$ state. Note that the $1_g(^1\Pi_g)$ state is also designated as 1_g or $c1_g$ in the literature.

Accordingly, the two mixed states can be written as

$$|1\rangle = \alpha\,|B, \upsilon JIF\rangle + \beta\,|1_g, \upsilon' J' \varepsilon' F\rangle \tag{4.12}$$

$$|2\rangle = -\beta\,|B, \upsilon JIF\rangle + \alpha\,|1_g, \upsilon' J' \varepsilon' F\rangle \tag{4.13}$$

where ε' labels the nuclear spin wave function of the perturbing level. Simple calculation that uses the frequency differences among b_1, b_3, and simulated a_{10} gives the energy difference $\Delta E = 39$ MHz, the hyperfine coupling $H_{12} = 54$ MHz, and mixing parameters $\alpha = 0.82$ and $\beta = 0.57$. With the PECs of the B and the $1_g(^1\Pi_g)$ states the Franck-Condon overlap $|\langle \upsilon' | \upsilon \rangle|$ is calculated to be 0.1 and then the electronic matrix element for the hyperfine coupling is estimated as $|\langle B0_u^+ | H_{hf} | 1_g(^1\Pi_g)\rangle| = 540$ MHz.

Electronic states other than the $1_g(^1\Pi_g)$ state are unlikely to produce such strong perturbation because the associated Franck-Condon overlaps for levels at which the energy coincidence could happen are at least two orders of magnitude smaller. Even if the perturbation from such a state can shift a particular hyperfine level on the kilohertz level, it cannot produce a noticeable influence on the whole hyperfine structure at a certain rovibrational level in this intermediate region because the strict energy equality can be satisfied only for a small number of hyperfine levels.

In this intermediate region, owing to the relatively large differences in the vibrational and rotational constants and the moderate Franck-Condon overlap between the $1_g(^1\Pi_g)$ and the B states, these resonances each spans only a small range of rotational levels, a property that is clearly identified in figures 4.9 and 4.11.

These abnormal variations directly confirm the previously observed u-g mixing in the optical-optical double-resonance (OODR) experiments [137, 138, 139, 135]. In these OODR experiments it was found that high-lying ion-pair states with u symmetry can be accessed by a two-photon excitation starting from the ground state $X0_g^+$. This seems to contradict the symmetry requirement of a two-photon transition,

which requires that the initial and the final states must have the same $u(g)$ symmetry. However, if the two-photon transition takes a two-step pathway, namely, $\left|X0_g^+\right\rangle \rightarrow \alpha\left|B0_u^+\right\rangle + \beta\left|1_g(^1\Pi_g)\right\rangle \rightarrow \left|\Omega_u\right\rangle$, then the symmetry requirement is satisfied in each of the two steps. In one of these OODR experiments [135], a strong hyperfine u-g mixing was inferred from the rovibrational spectrum that exhibits a resonance feature at vibrational level $v' = 59$ and around rotational levels centered on $J' = 22$. Clearly, this resonance feature is consistent with the abnormal variations of eqQ_B, d_B, and δ_B in figures 4.9 and 4.11.

4.9 Summary and Conclusions

In this chapter hyperfine interactions in the $B0_u^+(^3\Pi_u)$ state of $^{127}I_2$ have been systematically studied. By saturation spectroscopy of hyperfine spectra of the $B \longleftarrow X$ transitions in the wavelength range $500-517$ nm, four effective hyperfine parameters, eqQ_B, C_B, d_B, and δ_B, have been determined for a large number of rovibrational levels spanning the intermediate region ($42 < v' < 70$), yielding rich information about the rovibrational dependence of the hyperfine parameters. In addition to the second-order effect that is responsible for the smooth trend of these hyperfine parameters, abnormal variations in eqQ_B, d_B, and δ_B at vibrational levels $v' = 57-60$ have been observed, and it was found that some hyperfine spectra in this region cannot be fully described by the effective hyperfine Hamiltonian. By examining the cluster of electronic states converging with the B state and the strong u-g mixing recorded at transition P(84) 60-0, we have concluded that these anomalies are caused by the hyperfine perturbation from the $1_g(^1\Pi_g)$ electronic state through the rotational coincidence, which confirms the previous observation of u-g mixing at level $v' = 59$ in the optical-optical double-resonance excitation of the ion-pair states with u symmetry. Various perturbation effects in the B state so far identified have been summarized briefly. We also examined the radial dependence of the hyperfine interactions by

removing the vibrational average in the hyperfine parameters.

The systematic determination of hyperfine parameters in the intermediate region provides useful information for applications of optical frequency stabilization that explore the transitions with wavelengths below 517 nm. Also, extensions of the calculation of the hyperfine parameters to low-lying vibrational levels as well as to their rotational dependence permits a detailed analysis of the molecular electronic structure from the perspective of hyperfine interactions. Such a follow-up investigation is given in chapter 5.

Chapter 5

CHARACTERIZING MOLECULAR-IODINE ELECTRONIC STRUCTURE THROUGH HYPERFINE INTERACTIONS

5.1 Introduction

Comprehensive and high-precision measurements on hyperfine spectra of molecular iodine provide a unique opportunity for a detailed examination of the molecule's electronic structure. Molecular iodine is a rare case in that its hyperfine spectra in the $B \leftarrow X$ system have been recorded not only with high precision at the kilohertz level, but also for a large set of rovibrational levels, extending from $v' = 2$ to just below the dissociation limit ($v' = 82$) in the excited $B0_u^+(^3\Pi_u)$ electronic state [55, 42, 45, 117, 140, 141]. These vibrational levels cover a broad range of internuclear separation, with R-centroids (R_c, the mean of internuclear separations weighted by the B-state vibrational wave function) ranging from about 3 Å to 12 Å. Because hyperfine interactions can exert large influences on electronic structure, experimentally determined hyperfine parameters over a large range of R_c allow a sensitive test of the relevant electronic wave functions and potential energy curves (PECs).

Hyperfine parameters from precision measurements have been used to test several relevant electronic states, i.e., X, B, and E in molecular iodine [45, 46, 47, 134, 142, 48, 112] and in other diatomic molecules [131]. In the case of the $B0_u^+(^3\Pi_u)$ state in molecular iodine, second-order contributions to the four hyperfine parameters, the electric quadrupole parameter eqQ_B, spin-rotation parameter C_B, tensorial spin-spin

parameter d_B, and scalar spin-spin parameter δ_B, have been calculated for several vibrational levels ($v' \sim 40 - 82$) in the B state [45, 46, 47, 48, 43]. In these analyses, the molecular wave functions involved were constructed from a separated-atom basis set because the molecule spends much of its time at large internuclear separations for high-lying vibrational levels close to the dissociation limit. The good agreement with the experimental data achieved in these calculations justifies the separated-atom model as a simple and effective tool in characterizing the electronic structure at large internuclear separations. Nonetheless, there is room to improve this approach. First, the same calculation can be carried out with improved resolution for vibrational levels lower than $v' \sim 40$ as well as for the detailed rotational dependence in each vibrational level. This approach has become particularly relevant given the latest spectroscopic data with an extensive coverage of rovibrational dependence of the hyperfine interactions as described in the previous chapter and in references [140, 141]. In addition, detailed information on the short- and intermediate-range ($R < 7$ Å) PEC of the perturbing electronic state, obtained either empirically or theoretically, was largely unavailable when these calculations were performed, and therefore the properties of the molecular wave functions of the corresponding electronic state could not be independently inferred from these analyses. In contrast, with adequate constraints on the PECs, a correct account of the hyperfine parameters enables either the determination of the admixture of the basis wave functions in the separated-atom model or the verification of more-sophisticated molecular wave functions.

In this chapter we extend calculations of hyperfine parameters to low vibrational levels and to rotational dependence at each vibrational level, using electronic wave functions derived from the separated-atom basis set and the related empirical/theoretical PECs. In doing so, we are able to quantitatively address several issues such as (1) to what extent the separated-atom wave functions can be extrapolated to small internuclear separations, (2) the estimation of the admixture of the basis

wave functions in the separated-atom model, and (3) how sensitively the hyperfine parameters depend on the choice of PECs. For the spin-rotation parameter C_B, the results of both vibrational and rotational dependence are in good agreement with the experimental data for $\upsilon' \geqslant 42$ and the admixture of the two 1_u states is independently determined. Moreover, calculations of the other three parameters, eqQ_B, d_B, and δ_B, place a stringent constraint on the long-range PECs of the relevant electronic states. Here we consider the smooth second-order contributions. Thus the calculation does not cover the abnormal variations of the hyperfine parameters around $\upsilon' = 57 - 60$ and $\upsilon' = 76 - 78$ because of the strong hyperfine coupling, which has already been analyzed in chapter 4 and in references [45, 140].

This chapter is outlined as follows. Section 5.2 gives a close examination of the effective hyperfine Hamiltonian developed by Broyer *et al.*, which is the basis of our calculations of the effective hyperfine parameters. This section also lists the formulae of second-order contributions to the four hyperfine parameters. Section 5.3 prepares the PECs and the electronic wave functions that are used to calculate the rovibrational levels and coupling matrix elements. Section 5.5 presents the results for the four effective hyperfine parameters at various internuclear separations. The calculation is performed and discussed in three steps to demonstrate a maximum separation of the contributions from different perturbing electronic states. In this section we also make comparisons between the results and the experimental data and the information of the electronic structure is deduced from these comparisons. The conclusions are given in section 5.7.

5.2 Effective Hyperfine Hamiltonian in Molecular Iodine

In chapter 4 an effective hyperfine Hamiltonian is introduced to describe the hyperfine spectra in molecular iodine. In this section we begin with an introduction of the origins of various terms in this effective hyperfine Hamiltonian, which provides

the theoretical background for the calculations of the effective hyperfine parameters performed in this chapter.

The hyperfine interaction, which is not included in the Born-Oppenheimer molecular Hamiltonian, may couple the B state to several electronic states sharing the same $^2\mathrm{P}_{\frac{3}{2}} + {}^2\mathrm{P}_{\frac{1}{2}}$ dissociation limit [111, 16]. Consequently, the hyperfine spectra of the $X \leftarrow B$ transitions are altered to various degrees depending on the coupling strength and the energy differences between the B and the perturbing states.

A direct approach to address these perturbing electronic states is to deal with a hyperfine-Hamiltonian matrix that spans not only the B electronic state but also all the perturbing states involved. In principle, a diagonalization of this Hamiltonian matrix gives the hyperfine spectra of all the electronic states spanned by the matrix. However, this approach is not feasible in the spectroscopic analysis. First, to construct such a Hamiltonian matrix, one needs detailed information on the perturbing electronic states, such as their rovibrational constants, which are largely not available in spectroscopic date. Second, this Hamiltonian matrix contains a large number of hyperfine parameters. Similar to the B state, each perturbing state has its own hyperfine parameters. In addition, extra parameters have to be used to characterize the couplings between the B and the perturbing states. Such a large number of parameters cannot be determined from the spectroscopic fit that uses at most 15 or 21 hyperfine lines for each rovibrational transitions.

An *effective* Hamiltonian based on second-order perturbation theory was developed by Broyer *et al.* [16] to treat hyperfine couplings with the external electronic states. Reference [143] explains the notion of an effective Hamiltonian in a much more broad context. This effective-Hamiltonian matrix spans only one electronic state (B state in this case) but has its matrix elements modified by second-order perturbation theory to take into account indirect hyperfine couplings with external electronic states. The benefit of this treatment is that despite their different origins, various per-

turbation terms from different perturbing electronic states can be incorporated into a small set of parameters according to their overall geometrical dependences evaluated with irreducible tensorial algebra, thereby simplifying the experimental analysis of hyperfine structure. This effective Hamiltonian, which includes four major terms, can be summarized as

$$H_{hf,eff} = H_{eqQ} + H_{SR} + H_{TSS} + H_{SSS}, \tag{5.1}$$

where the four terms on the right-hand side stand respectively for nuclear electric quadrupole, spin-rotation, tensorial spin-spin, and scalar spin-spin interactions. The matrix elements of this effective Hamiltonian can be written as

$$\langle \Omega, I'J'F \left| H_{hf,eff} \right| \Omega, IJF \rangle = eqQ \cdot G_{eqQ} + C \cdot G_{SR} + d \cdot G_{TSS} + \delta \cdot G_{SSS}, \tag{5.2}$$

where eqQ, C, d, and δ are *effective* hyperfine parameters and G's are geometrical functions depending only on the quantum numbers I, J, and F, whose explicit forms are given by equations 4.3 - 4.6. Except for levels where strong coupling is present, perturbed hyperfine spectra can generally be described by this effective hyperfine Hamiltonian with high precision using the four effective hyperfine parameters, which are extracted from fitting the spectroscopic data to the effective Hamiltonian.

Second-order calculations of these parameters relate their experimental values to the relevant PECs and the admixture of the basis wave functions, imposing stringent constraints on the associated electronic structure. References [44] and [16] first give the matrix elements of the hyperfine Hamiltonian that can couple different electronic states. The evaluation of these matrix elements is detailed in appendix A. Based on these matrix elements, the effective hyperfine parameters, which encompass the contributions from the perturbing states, are then derived in reference [16] with tensorial algebra and second-order perturbation theory. For clarity of the notation and discussion, we will provide an overview of this derivation before we list the explicit expressions for the effective hyperfine parameters.

5.2.1 Matrix Elements of the Hyperfine Hamiltonian

The hyperfine Hamiltonian of the iodine molecule can be formally written as

$$H_{hf} = H_{hf}(a) + H_{hf}(b) + H_{hf}(a,b), \tag{5.3}$$

where a and b label the two iodine nuclei, respectively, and $H_{hf}(a)$ $[H_{hf}(b)]$ and $H_{hf}(a,b)$ represent the nucleus-electron and nucleus-nucleus hyperfine interactions, respectively. The last term in the above Hamiltonian is left out in the following discussion because it only contains nuclear coordinates and thus cannot couple different electronic states. With the last term dropped, this Hamiltonian can be expressed in tensorial form:

$$H_{hf} = \sum_{\beta=a,b} \sum_{k} \sum_{q=-k}^{k} (-1)^q \, Q_q^k \left(\mathbf{I}_\beta\right) V_{-q}^k \left(e_\beta\right), \tag{5.4}$$

where the rank-k spherical tensor operators $Q^k(\mathbf{I}_\beta)$ and $V^k(e_\beta)$ act on the nuclear spin $\mathbf{I}_\beta$ and the electronic degrees of freedom, respectively.

Considering the strong spin-orbit interaction in this heavy molecule, a Hund's case c coupling scheme at large internuclear separations is appropriate for the molecular basis set, which we denote as

$$|\psi\rangle = |\Omega \upsilon J I F M_F\rangle, \tag{5.5}$$

where Ω is the projection of the total angular momentum $\mathbf{J}$ on to the molecular axis connecting the two nuclei, υ the vibrational quantum number, $\mathbf{I}$ the total nuclear spin, $\mathbf{F} = \mathbf{I} + \mathbf{J}$, and M_F the projection of $\mathbf{F}$ onto a quantization axis. Note that in the energy continuum, the discrete level index υ is replaced by a continuous energy spectrum E, while J is always a good quantum number.

Appendix A provides a detailed evaluation of the matrix elements of the hyperfine Hamiltonian in a Hund's case c coupling scheme. Here we briefly summarize the result. Averaging explicitly over the molecular rotation in the laboratory frame

gives the matrix elements of the hyperfine Hamiltonian in terms of 3-j (bracket) and 6-j (curly bracket) symbols and electronic matrix elements:

$$\begin{aligned}\langle\psi'|\, H^k_{hf}(a)\,|\psi\rangle = \delta_{FF'}\delta_{M_F M'_F}\,(-1)^{F+k+2I_a+\Delta I+\Delta J}\times \\ \sqrt{(2J'+1)\,(2J+1)\,(2I'+1)\,(2I+1)}\times \\ \begin{pmatrix} J' & k & J \\ -\Omega' & \Delta\Omega & \Omega \end{pmatrix} \begin{Bmatrix} J' & k & J \\ I & F & I' \end{Bmatrix} \begin{Bmatrix} k & I_a & I_a \\ I_a & I' & I \end{Bmatrix}\times \\ f_k\,(a,\Omega',\upsilon'_{J'},\Omega,\upsilon_J)\,, \end{aligned} \tag{5.6}$$

where $\Delta J = J' - J$, $\Delta I = I' - I$, $\Delta\Omega = \Omega' - \Omega$, and $f_k\,(a,\Omega',\upsilon'_{J'},\Omega,\upsilon_J)$ encapsulates the averaging over the electronic motion in the molecular frame and the molecular vibration in the laboratory frame, which is written as

$$f_k\,(a,\Omega',\upsilon'_{J'},\Omega,\upsilon_J) = (-1)^{\Omega'}\,\frac{C_k}{\begin{pmatrix} k & I_a & I_a \\ 0 & I_a & -I_a \end{pmatrix}}\times\langle\Omega'\upsilon'_{J'}|\, V^k_{\Delta\Omega}\,(a)\,|\Omega\upsilon_J\rangle\,. \tag{5.7}$$

Here $C_1 = \mu_n g I_a$ is the nuclear magnetic dipole moment with μ_n being the nuclear magneton and g the Landé factor for the iodine nucleus and $C_2 = \frac{1}{2}eQ_{I_a}$ is the nuclear electric quadrupole moment with e being the proton charge and Q_{I_a} defined as

$$Q_{I_a} = e\,\langle I_a, M_{I_a} = I_a|\sum_p \left(3z_p^2 - r_p^2\right)|I_a, M_{I_a} = I_a\rangle\,, \tag{5.8}$$

where z_p and r_p refer to the coordinates of the protons p in the iodine nucleus.

For $\Omega \neq 0$, the projection of the angular momentum $\mathbf{J}$ onto the molecular axis can take either the positive or negative direction, a degeneracy that is lifted by the hyperfine interaction or other couplings with external states. In this case the molecular wave function is represented by [44]

$$|\psi_\varepsilon\rangle = \left(\frac{1}{\sqrt{2}}\right)^{|\varepsilon|}\left[|\Omega,\upsilon JIFM_F\rangle + \varepsilon\,|-\Omega,\upsilon JIFM_F\rangle\right], \tag{5.9}$$

where ε can take on the values of 0 ($\Omega = 0$) and ± 1 ($\Omega > 0$). The net effect of this Ω-doubling on the matrix elements of the hyperfine Hamiltonian is to replace the $f_k\left(a, \Omega', v'_{J'}, \Omega, v_J\right)$ defined in equation 5.7 by

$$\left(\frac{1}{\sqrt{2}}\right)^{|\varepsilon|+|\varepsilon'|} \{\left[1 + \varepsilon\varepsilon' \left(-1\right)^{\Delta J}\right] f_k\left(a, \Omega', v'_{J'}, \Omega, v_J\right) + C\left(\Omega^+\right) \left[\varepsilon + \varepsilon' \left(-1\right)^{\Delta J}\right] f_k\left(a, \Omega', v'_{J'}, -\Omega, v_J\right)\}, \tag{5.10}$$

where $C\left(\Omega^+\right) = \dfrac{\begin{pmatrix} J' & k & J \\ -\Omega' & \Omega^+ & -\Omega \end{pmatrix}}{\begin{pmatrix} J' & k & J \\ -\Omega' & \Delta\Omega & \Omega \end{pmatrix}}$ and $\Omega^+ = \Omega' + \Omega$. Expression 5.10 is equivalent to equation (6) in reference [44] when $\varepsilon \neq 0$. For the case of the B state, expression 5.10 is reduced to

$$\left(\frac{1}{\sqrt{2}}\right)^{|\varepsilon'|} \left[1 + \varepsilon' \left(-1\right)^{\Delta J}\right] f_k\left(a, \Omega', v'_{J'}, 0_u^+, v_J\right). \tag{5.11}$$

The matrix elements of the hyperfine Hamiltonian for the second nucleus b is related to that of the first nucleus a because of symmetry considerations [44, 16]:

$$\begin{aligned} \left\langle \psi'_{u,I'} \right| H^k_{hf}(b) \left|\psi_{u,I}\right\rangle &= (-1)^{\Delta I} \left\langle \psi'_{u,I'} \right| H^k_{hf}(a) \left|\psi_{u,I}\right\rangle, \\ \left\langle \psi'_{u,I'} \right| H^k_{hf}(b) \left|\psi_{g,I}\right\rangle &= (-1)^{\Delta I+1} \left\langle \psi'_{u,I'} \right| H^k_{hf}(a) \left|\psi_{g,I}\right\rangle, \end{aligned} \tag{5.12}$$

where the $u(g)$ symmetry refers to the odd (even) electronic wave functions under reflection with respect to the center of the molecule.

Apart from the hyperfine Hamiltonian, the off-diagonal part of the rotational Hamiltonian, V^0, can also couple the B state to other electronic states:

$$V^0 = -\frac{\hbar^2}{2\mu R^2} \left[J_+ \left(L_- + S_-\right) + J_- \left(L_+ + S_+\right)\right], \tag{5.13}$$

where μ is the reduced mass of two nuclei and R is the internuclear separation. V^0 can only couple electronic states with $\Delta\Omega = \pm 1$ and $\Delta J = 0$ because of [144]

$$\left\langle J, \Omega \pm 1\right| J_\mp \left|J, \Omega\right\rangle = \sqrt{(J \mp \Omega)(J \pm \Omega + 1)}. \tag{5.14}$$

In addition, V^0 cannot couple u and g states. As a result of these restrictions, V^0 can only couple the B state to 1_u states. Using equation 5.14 and notice that the wave function of the $1_u(\varepsilon' = \pm 1)$ state is $|1_{u,\varepsilon'=\pm 1}\rangle = \frac{1}{\sqrt{2}}[|1_u\,(\Omega' = 1)\rangle \pm |1_u\,(\Omega' = -1)\rangle]$, the matrix element of V^0 between the B state and a 1_u state with Ω-doubling $\varepsilon' = 1$ is evaluated as

$$\langle 1_{u,\varepsilon'=1}|\, V^0\, \left|0_u^+\right\rangle = -\sqrt{2J(J+1)}\sqrt{2} f_0\left(1_u, 0_u^+\right), \tag{5.15}$$

where

$$f_0 = \langle 1_u\,(\Omega' = 1)\,, \upsilon'_{J'}|\, \frac{\hbar^2}{2\sqrt{2}\mu R^2}\,(L_+ + S_+)\left|0_u^+ \upsilon_J\right\rangle. \tag{5.16}$$

The extra factor of $\sqrt{2}$ in equation 5.15 arises from the Ω-doubling of the 1_u state.

5.2.2 Second-Order Contributions to the Effective Hyperfine Parameters

With the matrix elements of hyperfine Hamiltonian given in the section 5.2.1, the hyperfine parameters are calculated by second-order perturbation theory to include the contributions of all rovibrational levels allowed by the selection rules in each of the six perturbing states [C:1_u, 1_u, $1_g(^1\Pi_g)$, $1_g(^3\Sigma_g^-)$, $0_g^-(^3\Pi_g)$, and $(3)0_u^-$]. In the derivation of these parameters (see Appendix I in reference [16]), a weak J' dependence of $f_k\,(a, \Omega', \upsilon'_{J'}, \Omega, \upsilon_J)$ across neighboring rotational levels is assumed when the summation on J' is performed. However, to account for the Ω-doubling, $f_k\,(a, \Omega', \upsilon'_{J'}, \Omega, \upsilon_J)$ defined in equation 5.7 has to be replaced by expression 5.10. In fact, this modification does not interfere with the just-mentioned assumption because the coupling selection rules for $\Delta J = J' - J$ are different for $\varepsilon' = +1$ and -1; hence the combined effect adds no extra J' dependence to the modified $f_k\,(a, \Omega', \upsilon'_{J'}, \Omega, \upsilon_J)$. After summations on I' and J' and reorganizing various terms according to their angular momentum dependence, the explicit expressions for the four effective para-

meters are obtained and are listed below [16].

$$C_B = C_D - \frac{4}{\sqrt{I_a\left(I_a+1\right)\left(2I_a+1\right)}}\times$$
$$\sum_{1_u}\left[\sum_{\upsilon'}\frac{f_0\left(1_u,0_u^+\right)f_1\left(a,0_u^+,1_u\right)}{\left(E_{0_u^+\upsilon J}-E_{1_u\upsilon' J}\right)}+\frac{2}{\pi}\sqrt{\frac{\mu}{2\hbar^2}}\int_{E_0}^{\infty}dE_{1_uJ}\frac{f_0\left(1_u,0_u^+\right)f_1\left(a,0_u^+,1_u\right)}{\sqrt{E_u}\left(E_{0_u^+\upsilon J}-E_{1_uJ}\right)}\right], \tag{5.17}$$

$$\delta_B = -\frac{2}{3I_a\left(I_a+1\right)\left(2I_a+1\right)}\times$$
$$\sum_{\Omega'}\chi_i\left(1+|\varepsilon'|\right)\left[\sum_{\upsilon'}\frac{\left|f_1\left(a,\Omega',0_u^+\right)\right|^2}{\left(E_{0_u^+\upsilon J}-E_{\Omega'\upsilon' J}\right)}+\frac{2}{\pi}\sqrt{\frac{\mu}{2\hbar^2}}\int_{E_0}^{\infty}dE_{\Omega' J}\frac{\left|f_1\left(a,\Omega',0_u^+\right)\right|^2}{\sqrt{E_u}\left(E_{0_u^+\upsilon J}-E_{\Omega' J}\right)}\right], \tag{5.18}$$

$$d_B = -\frac{1}{3I_a\left(I_a+1\right)\left(2I_a+1\right)}\sum_{\Omega'}\chi_i\left(3\Omega'^2-2\right)\left(1+|\varepsilon'|\right)\left[\sum_{\upsilon'}\frac{\left|f_1\left(a,\Omega',0_u^+\right)\right|^2}{\left(E_{0_u^+\upsilon J}-E_{\Omega'\upsilon' J}\right)}+\right.$$
$$\left.\frac{2}{\pi}\sqrt{\frac{\mu}{2\hbar^2}}\int_{E_0}^{\infty}dE_{\Omega' J}\frac{\left|f_1\left(a,\Omega',0_u^+\right)\right|^2}{\sqrt{E_u}\left(E_{0_u^+\upsilon J}-E_{\Omega' J}\right)}\right], \tag{5.19}$$

$$eqQ_B = eqQ_0 - 4\sqrt{2}\sum_{1_u}\left[\sum_{\upsilon'}\frac{4f_0\left(1_u,0_u^+\right)f_2\left(a,0_u^+,1_u\right)}{\left(E_{0_u^+\upsilon J}-E_{1_u\upsilon' J}\right)}+\right.$$
$$\left.\frac{2}{\pi}\sqrt{\frac{\mu}{2\hbar^2}}\int_{E_0}^{\infty}dE_{1_uJ}\frac{4f_0\left(1_u,0_u^+\right)f_2\left(a,0_u^+,1_u\right)}{\sqrt{E_u}\left(E_{0_u^+\upsilon J}-E_{1_uJ}\right)}\right]+$$
$$10\sum_{k',k=1,2}\sum_{\Omega'}\left(-1\right)^{2I_a+\Omega'}\left(1+|\varepsilon'|\right)\left[\sum_{\upsilon'}\frac{2f_k^*\left(a,\Omega',0_u^+\right)f_{k'}\left(a,\Omega',0_u^+\right)}{\left(E_{0_u^+\upsilon J}-E_{\Omega'\upsilon' J}\right)}+\right.$$
$$\left.\frac{2}{\pi}\sqrt{\frac{\mu}{2\hbar^2}}\int_{E_0}^{\infty}dE_{\Omega' J}\frac{2f_k^*\left(a,\Omega',0_u^+\right)f_{k'}\left(a,\Omega',0_u^+\right)}{\sqrt{E_u}\left(E_{0_u^+\upsilon J}-E_{\Omega' J}\right)}\right]\times$$
$$\left(\begin{array}{ccc} k & k' & 2 \\ \Delta\Omega & -\Delta\Omega & 0 \end{array}\right)\left\{\begin{array}{ccc} I_a & 2 & I_a \\ k & I_a & k' \end{array}\right\}\left\{\begin{array}{ccc} 2 & I_a & I_a \\ 0 & I_a & -I_a \end{array}\right\}. \tag{5.20}$$

C_D and eqQ_0 are the first-order contributions to the corresponding parameters in equations 5.17 and 5.20, respectively. In equations 5.18 – 5.20, $\Omega' \geqslant 0$ and ε' can take on values of 0 ($\Omega' = 0$) and ± 1 ($\Omega' > 0$). For each perturbing electronic

state Ω', $\chi_i = 1(-1)$ if Ω' has $g(u)$ symmetry and its contribution to the hyperfine parameters comes from both discrete levels (υ', J) and the energy continuum E_J, whose density of state is $\frac{2}{\pi}\sqrt{\frac{\mu}{2\hbar^2 E_u}}$, where E_u is the radial kinetic energy. E_0, the lower limit of the integrals for the energy continuum, is the energy just above the last discrete rovibrational level that an attractive potential can support. In the equations for δ_B, d_B, and eqQ_B, the extra factor $(1 + |\varepsilon'|)$ arises from the Ω-doubling of the perturbing state Ω'.

5.3 Preparation of Potential Energy Curves and Electronic Wave Functions

We move on now to several computational issues concerning the preparation of the PECs, the electronic wave functions constructed from the separated-atom basis set, and the electronic matrix elements. The information is used in the calculation of the various electronic matrix elements in equations 5.17 - 5.20.

5.3.1 Potential Energy Curves

We use the available empirical and theoretical I_2 PECs to construct the rovibrational structure and the associated wave functions inside each electronic state. The B-state empirical PEC is adopted from the analysis performed by Gerstenkorn *et al.* [133]. This empirical PEC was constructed from Fourier spectroscopic data by using an "inverted perturbation approach" (IPA) method. For the six states that perturb the B state, we adopt the empirically improved relativistic PECs obtained by de Jong *et al.* [110], and these PECs are used in the short and intermediate internuclear separations ($R \leq 6.5$ Å). Figure 5.1 plots these PECs over the range 2.5 Å $< R <$ 6.5 Å, along with the B-state empirical PEC and the other three PECs belonging to the same dissociation limit. For the large internuclear separations ($R > 7$ Å), the PECs take the inverse-power form, $V(R) = \frac{C_5}{R^5} + \frac{C_6}{R^6} + E_{diss}$, which includes quadrupolar

electrostatic and dispersion energy terms, with the corresponding coefficients C_5 and C_6 determined by Saute *et al.* [109]. Figure 5.2 shows these long-rang PECs for all ten electronic states that share the same dissociation limit, $^2\mathrm{P}_{\frac{3}{2}}+^2\mathrm{P}_{\frac{1}{2}}$. To make a smooth transition between the two segments of the PEC, each short-range PEC is shifted vertically to match the corresponding long-rang PEC at around $R = 7$ Å. The matched short- and long-range PECs are illustrated in figure 5.3.

5.3.2 Electronic Wave Functions in the Separated-Atom Model

At large internuclear separations ($R >\sim 7$ Å) the iodine molecule is treated as two separated atoms with their charge distributions barely distorted. In this separated-atom model the molecular basis functions can be constructed from symmetrized products of two atomic wave functions:

$$|\Omega\rangle = \sum_l C_l \, |j_l m_l\rangle_a \, |j'_l m'_l\rangle_b \tag{5.21}$$

where a and b denote two iodine atoms. A subset of these basis functions relevant to the B and six perturbing states [C:1_u, 1_u, $1_g(^1\Pi_g)$, $1_g(^3\Sigma_g^-)$, $0_g^-(^3\Pi_g)$, and $(3)0_u^-$] is listed below [109].

$$\begin{aligned}
\left|0_u^+\right\rangle &= \tfrac{1}{2}[\left|\tfrac{3}{2},\tfrac{1}{2}\right\rangle\left|\tfrac{1}{2},-\tfrac{1}{2}\right\rangle + \left|\tfrac{1}{2},-\tfrac{1}{2}\right\rangle\left|\tfrac{3}{2},\tfrac{1}{2}\right\rangle + \left|\tfrac{3}{2},-\tfrac{1}{2}\right\rangle\left|\tfrac{1}{2},\tfrac{1}{2}\right\rangle + \left|\tfrac{1}{2},\tfrac{1}{2}\right\rangle\left|\tfrac{3}{2},-\tfrac{1}{2}\right\rangle],\\
|1'_u\rangle &= \tfrac{1}{\sqrt{2}}[\left|\tfrac{3}{2},\tfrac{1}{2}\right\rangle\left|\tfrac{1}{2},\tfrac{1}{2}\right\rangle + \left|\tfrac{1}{2},\tfrac{1}{2}\right\rangle\left|\tfrac{3}{2},\tfrac{1}{2}\right\rangle],\\
|1''_u\rangle &= \tfrac{1}{\sqrt{2}}[\left|\tfrac{3}{2},\tfrac{3}{2}\right\rangle\left|\tfrac{1}{2},-\tfrac{1}{2}\right\rangle + \left|\tfrac{1}{2},-\tfrac{1}{2}\right\rangle\left|\tfrac{3}{2},\tfrac{3}{2}\right\rangle],\\
\left|1'_g\right\rangle &= \tfrac{1}{\sqrt{2}}[\left|\tfrac{3}{2},\tfrac{1}{2}\right\rangle\left|\tfrac{1}{2},\tfrac{1}{2}\right\rangle - \left|\tfrac{1}{2},\tfrac{1}{2}\right\rangle\left|\tfrac{3}{2},\tfrac{1}{2}\right\rangle],\\
\left|1''_g\right\rangle &= \tfrac{1}{\sqrt{2}}[\left|\tfrac{3}{2},\tfrac{3}{2}\right\rangle\left|\tfrac{1}{2},-\tfrac{1}{2}\right\rangle - \left|\tfrac{1}{2},-\tfrac{1}{2}\right\rangle\left|\tfrac{3}{2},\tfrac{3}{2}\right\rangle],\\
\left|0_g^-\right\rangle &= \tfrac{1}{2}[\left|\tfrac{3}{2},\tfrac{1}{2}\right\rangle\left|\tfrac{1}{2},-\tfrac{1}{2}\right\rangle - \left|\tfrac{1}{2},-\tfrac{1}{2}\right\rangle\left|\tfrac{3}{2},\tfrac{1}{2}\right\rangle - \left|\tfrac{3}{2},-\tfrac{1}{2}\right\rangle\left|\tfrac{1}{2},\tfrac{1}{2}\right\rangle + \left|\tfrac{1}{2},\tfrac{1}{2}\right\rangle\left|\tfrac{3}{2},-\tfrac{1}{2}\right\rangle],\\
\left|0_u^-\right\rangle &= \tfrac{1}{2}[\left|\tfrac{3}{2},\tfrac{1}{2}\right\rangle\left|\tfrac{1}{2},-\tfrac{1}{2}\right\rangle + \left|\tfrac{1}{2},-\tfrac{1}{2}\right\rangle\left|\tfrac{3}{2},\tfrac{1}{2}\right\rangle - \left|\tfrac{3}{2},-\tfrac{1}{2}\right\rangle\left|\tfrac{1}{2},\tfrac{1}{2}\right\rangle - \left|\tfrac{1}{2},\tfrac{1}{2}\right\rangle\left|\tfrac{3}{2},-\tfrac{1}{2}\right\rangle].
\end{aligned} \tag{5.22}$$

Each electronic wave function is a linear combination of the basis functions given in equation 5.22. For example, the wave functions of two 1_u states, $1_u(^3\Sigma_u^+)$ and

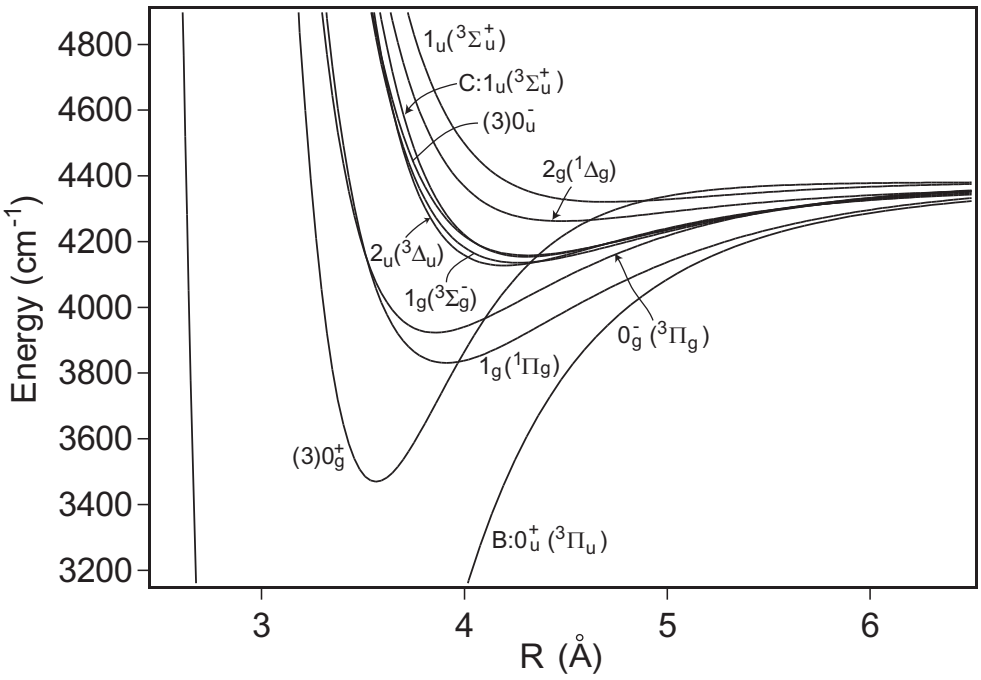

Figure 5.1: Potential energy curves (PECs) for ten electronic states converging to the $^2P_{\frac{3}{2}} + {}^2P_{\frac{1}{2}}$ dissociation limit over the range 2.5 Å $< R <$ 6.5 Å. These PECs are adopted from the relativistic calculations by de Jong *et al* [110] except for the B state, for which an empirical PEC [133] is used.

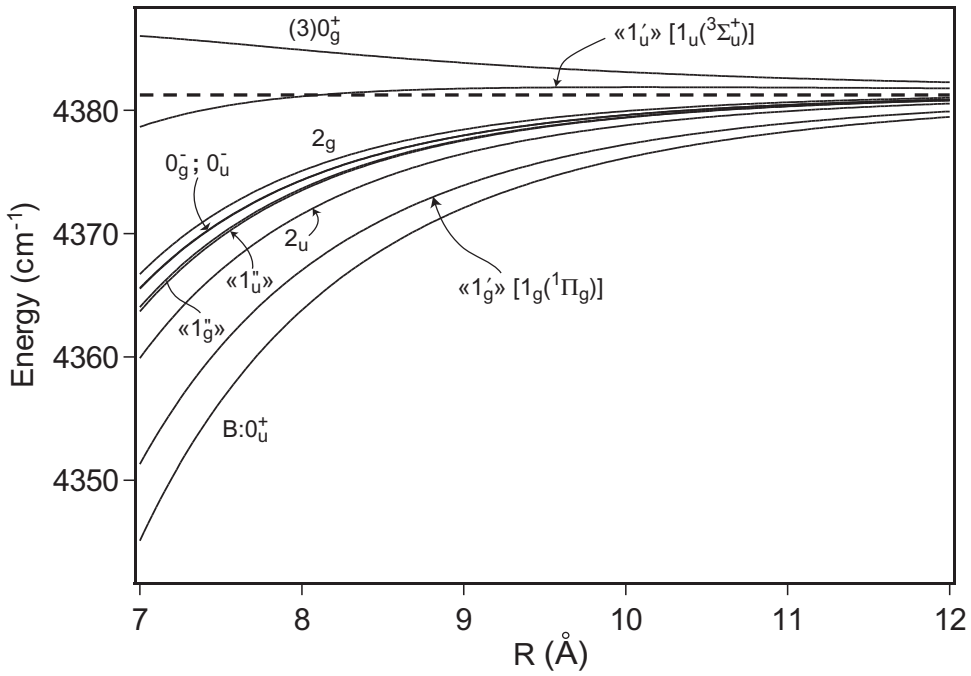

Figure 5.2: Long-range PECs for the ten electronic states. These PECs are adopted from reference [109]. The dashed line indicates the $^2\mathrm{P}_{\frac{3}{2}} + {}^2\mathrm{P}_{\frac{1}{2}}$ dissociation limit. Note that the $\ll 1''_u \gg$ and the $\ll 1''_g \gg$ states refer to the $C{:}1u(^3\Sigma_u^+)$ and the $1g(^3\Sigma_g^-)$ states, respectively.

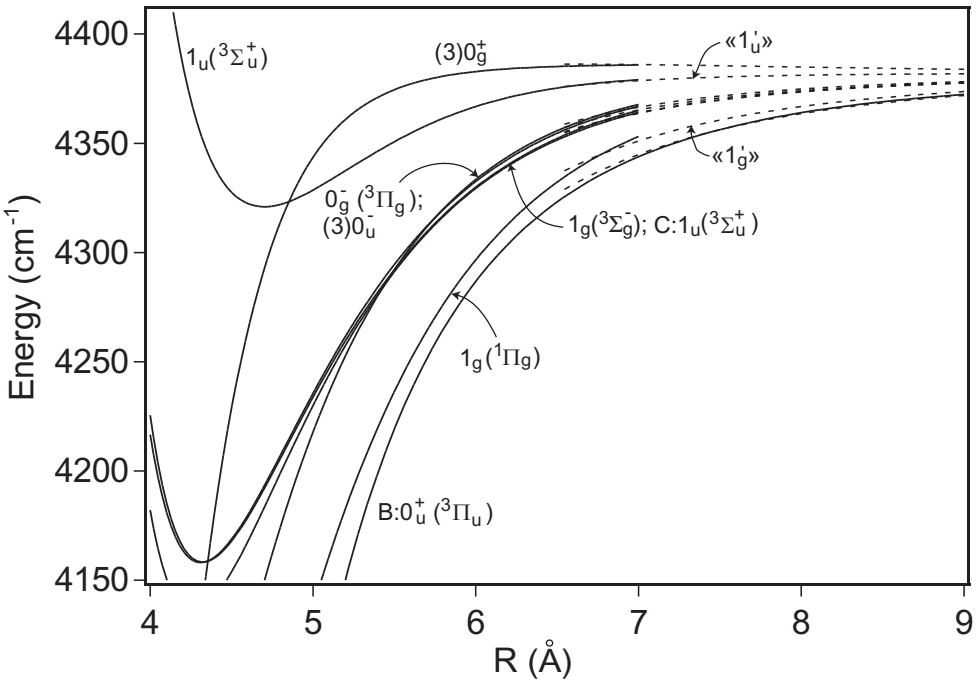

Figure 5.3: Combining the short- and long-range potentials. The solid lines are the short-range ($R < 7$ Å) PECs from the *ab initio* calculation [110], and the dashed lines are the *ab initio* long-range PECs from reference [109]. To make a smooth connection between two segments of the PEC, each short-range ($R < 7$ Å) PEC has been shifted vertically to match the corresponding long-range one. The unchanged B-state empirical PEC [133] and its *ab initio* long-range PEC are also included.

C:$1_u(^3\Sigma_u^+)$, also designated as $\ll 1'_u \gg$ and $\ll 1''_u \gg$ respectively, are linear combinations of two basis functions:

$$|\ll 1'_u \gg\rangle = \alpha\,|1'_u\rangle - \sqrt{1-\alpha^2}\,|1''_u\rangle$$
$$|\ll 1''_u \gg\rangle = \alpha\,|1''_u\rangle + \sqrt{1-\alpha^2}\,|1'_u\rangle \tag{5.23}$$

with α being the admixture of the two basis functions. Likewise, the wave functions of two 1_g states, $1_g(^1\Pi_g)$ and $1_g(^3\Sigma_g^-)$, are also linear combinations of two basis functions:

$$\left|\ll 1'_g \gg\right\rangle = \beta\left|1'_g\right\rangle + \sqrt{1-\beta^2}\left|1''_g\right\rangle$$
$$\left|\ll 1''_g \gg\right\rangle = \beta\left|1''_g\right\rangle - \sqrt{1-\beta^2}\left|1'_g\right\rangle, \tag{5.24}$$

where $\ll 1'_g \gg$ and $\ll 1''_g \gg$ refer to the $1_g(^1\Pi_g)$ and the $1_g(^3\Sigma_g^-)$ states, respectively. The R dependence of the mixing parameters α and β will be examined in section 5.5. Each of the wave functions of the other three electronic states, $B0_u^+(^3\Pi_u)$, $0_g^-(^3\Pi_g)$, and $(3)0_u^-$, consists of only one basis function.

5.3.3 Hyperfine Matrix Elements in the Separated-Atom Model

With molecular wave functions derived from the basis functions in the separated-atomic model, the hyperfine matrix elements, $\langle V^0\rangle$, $\langle V^1\rangle$, and $\langle V^2\rangle$, can be readily determined from the experimental values of atomic hyperfine constants [46, 44]. In this section two 1_u basis wave functions are used to demonstrate the evaluation of various hyperfine matrix elements. A complete list of values of those matrix elements between the B and six perturbing electronic states are given in reference [44].

5.3.3.1 Gyroscopic Matrix Elements $\langle V^0\rangle$

The matrix element of V^0 between the B state and a 1_u state with Ω-doubling $\varepsilon' = 1$ is given by equations 5.15 and 5.16. In Born-Oppenheimer approximation, f_0

in equation 5.16 be rewritten as,

$$f_0\left(1_u, 0_u^+\right) = \frac{\hbar^2}{2\sqrt{2}\mu}\left\langle v'_{J'}\right| \frac{1}{R^2}\left[\left\langle 1_u\left(\Omega'=1\right)\right|\left(L_+ + S_+\right)\left|0_u^+\right\rangle\right]\left|v'_{J'}\right\rangle, \tag{5.25}$$

where $1_u\left(\Omega'=1\right)$ can be either the $\ll 1'_u \gg [1_u(^3\Sigma_u^+)]$ or $\ll 1''_u \gg [C{:}1_u(^3\Sigma_u^+)]$ state. The electronic matrix element $\left\langle 1_u\left(\Omega'=1\right)\right|\left(L_+ + S_+\right)\left|0_u^+\right\rangle$ in equation 5.25 is in general R dependent and can be evaluated by rewriting the operator $L_+ + S_+$ as

$$L_+ + S_+ = j_+ = j_+(a) + j_+(b), \tag{5.26}$$

where j is the total angular momentum of the electrons in the molecular frame and it is decomposed to $j(a)$ and $j(b)$, which are the electronic angular momenta of the two separated iodine atoms a and b, respectively. Then it is straightforward to write down the matrix elements $\langle V^0\rangle$ for the two 1_u basis wave functions in the separated-atom model:

$$\begin{aligned}
\left\langle 1'_u\right| V^0\left|0_u^+\right\rangle &= -3\sqrt{2J(J+1)}\frac{\hbar^2}{2\sqrt{2}\mu}\left\langle v'_{J'}\right|\frac{1}{R^2}\left|v_J\right\rangle, \\
\left\langle 1''_u\right| V^0\left|0_u^+\right\rangle &= -\sqrt{3}\sqrt{2J(J+1)}\frac{\hbar^2}{2\sqrt{2}\mu}\left\langle v'_{J'}\right|\frac{1}{R^2}\left|v_J\right\rangle.
\end{aligned} \tag{5.27}$$

According to equation 5.23, the matrix elements $\langle V^0\rangle$ for the $\ll 1'_u \gg$ and $\ll 1''_u \gg$ states are simply the linear combinations of the two matrix elements in equation 5.27:

$$\left\langle \ll 1'_u \gg\right| V^0\left|0_u^+\right\rangle = -\sqrt{2J(J+1)}\frac{\hbar^2}{2\sqrt{2}\mu}\left(3\left\langle v'_{J'}\right|\frac{\alpha}{R^2}\left|v_J\right\rangle - \sqrt{3}\left\langle v'_{J'}\right|\frac{1}{R^2}\sqrt{1-\alpha^2}\left|v_J\right\rangle\right), \tag{5.28}$$

$$\left\langle \ll 1''_u \gg\right| V^0\left|0_u^+\right\rangle = -\sqrt{2J(J+1)}\frac{\hbar^2}{2\sqrt{2}\mu}\left(3\left\langle v'_{J'}\right|\frac{1}{R^2}\sqrt{1-\alpha^2}\left|v_J\right\rangle + \sqrt{3}\left\langle v'_{J'}\right|\frac{\alpha}{R^2}\left|v_J\right\rangle\right). \tag{5.29}$$

5.3.3.2 Hyperfine Magnetic Dipolar $\langle V^1\rangle$ and Electric Quadrupolar Matrix Elements $\langle V^2\rangle$

The hyperfine magnetic dipolar matrix element $\left\langle \Omega' v'_{J'}\right| V^1_{\Delta\Omega}\left(a\right)\left|\Omega v_J\right\rangle$ contained in $f_1\left(a, \Omega', v'_{J'}, \Omega, v_J\right)$ can be approximated as a product of the Franck-Condon over-

lap and an electronic matrix element, namely,

$$\langle \Omega' \upsilon'_{J'} | \, V^1_{\Delta\Omega}(a) \, | \Omega \upsilon_J \rangle \approx \langle \upsilon'_{J'} | \, \upsilon_J \rangle \, \langle \Omega' | \, V^1_{\Delta\Omega}(a) \, | \Omega \rangle \,, \tag{5.30}$$

assuming that the latter has a weak R dependence over the range sampled by the vibrational wave function. Here we use the $1'_u$ basis state and the B state to show how the electronic matrix element $\langle 1'_u | \, V^1_1(a) \, | 0^+_u \rangle$ is related to the experimentally determined atomic hyperfine constants. In the separated-atom model, $\langle 1'_u | \, V^1_1(a) \, | 0^+_u \rangle$ is evaluated as

$$\langle 1'_u | \, V^1_1(a) \, \left| 0^+_u \right\rangle = \tfrac{1}{2\sqrt{2}} [\left\langle \tfrac{3}{2}, \tfrac{1}{2} \right| V^1_1(a) \left| \tfrac{3}{2}, -\tfrac{1}{2} \right\rangle + \left\langle \tfrac{1}{2}, \tfrac{1}{2} \right| V^1_1(a) \left| \tfrac{1}{2}, -\tfrac{1}{2} \right\rangle], \tag{5.31}$$

while the atomic magnetic hyperfine constant A_j is defined as [145]

$$A_j = \langle j, m = j | \left[-\frac{\mu_n g V^1_1(a)}{j} \right] | j, m = j \rangle \,. \tag{5.32}$$

To relate $\langle V^1 \rangle$ to the atomic hyperfine constant A_j, we apply the Winger-Eckart theorem to both equations 5.31 and 5.32. Equation 5.31 is then expressed in terms of reduced matrix elements:

$$\langle 1'_u | \, V^1_1(a) \, \left| 0^+_u \right\rangle = \tfrac{1}{2} [\tfrac{1}{\sqrt{15}} \left\langle \tfrac{3}{2} \right\| V^1(a) \left\| \tfrac{3}{2} \right\rangle + \tfrac{1}{\sqrt{6}} \left\langle \tfrac{1}{2} \right\| V^1(a) \left\| \tfrac{1}{2} \right\rangle], \tag{5.33}$$

and A_j is also related to the same set of reduced matrix elements:

$$A_j = j \begin{pmatrix} j & 1 & j \\ -j & 0 & j \end{pmatrix} \langle j \| \left[-\mu_n g V^1(a) \right] \| j \rangle \,,$$

$$\begin{aligned} A_{\frac{3}{2}} &= \tfrac{1}{\sqrt{15}} \left\langle \tfrac{3}{2} \right\| \left[-\mu_n g V^1(a) \right] \left\| \tfrac{3}{2} \right\rangle , \\ A_{\frac{1}{2}} &= \sqrt{\tfrac{2}{3}} \left\langle \tfrac{1}{2} \right\| \left[-\mu_n g V^1(a) \right] \left\| \tfrac{1}{2} \right\rangle . \end{aligned} \tag{5.34}$$

By comparing equations 5.33 and 5.34 the matrix element $\langle 1'_u | \, V^1_1(a) \, | 0^+_u \rangle$ is determined by,

$$\langle 1'_u | \left[-\mu_n g V^1_1(a) \right] \left| 0^+_u \right\rangle = -\frac{1}{4} (2 A_{\frac{3}{2}} + A_{\frac{1}{2}}), \tag{5.35}$$

where $A_{\frac{3}{2}} = 827.127$ MHz and $A_{\frac{1}{2}} = 6587.34$ MHz [146]. Similarly, the matrix element $\langle 1''_u | V_1^1(a) | 0_u^+ \rangle$ is found to be

$$\langle 1''_u | \left[-\mu_n g V_1^1(a) \right] | 0_u^+ \rangle = -\frac{\sqrt{3}}{4} A_{\frac{3}{2}}. \tag{5.36}$$

The matrix elements $\langle V^1 \rangle$ for other basis wave functions can be evaluated in the same way. With the same method, the electric quadrupolar matrix elements $\langle V^2 \rangle$ can be related to the atomic electric quadrupolar parameter $|e| q_{\frac{3}{2}} Q_{I_a} = 1146.356$ MHz [147].

5.4 Computing the Effective Hyperfine Parameters

FORTRAN codes LEVEL [132] and BCONT [148] developed by Le Roy *et al.* are used to calculate the Franck-Condon integrals $\langle \upsilon'_{J'} | \upsilon_J \rangle$ and $\langle \upsilon'_{J'} | \frac{1}{R^2} | \upsilon_J \rangle$ for the discrete levels and energy continua, respectively. The rovibrational energies obtained from LEVEL are also used to compute the energy denominators in equations 5.17 - 5.20. As an example, a portion of the B-state rovibrational structure is sketched in figure 5.4, and the vibrational levels inside a perturbing state $C{:}1_u$ are shown in figure 5.5. A special case arises when a potential can support rotational levels above its asymptotic energy because of a potential barrier located at the PEC outer limb. Wave functions of such levels can tunnel through the potential barrier. As a result, their energy spectra can be broadened significantly and can no longer be treated as discrete or quasi-discrete levels. We isolate these levels from the rest of the discrete levels and treat them instead as part of the energy continuum.

5.5 Numerical Analysis of Effective Hyperfine Parameters and Related Electronic Structure

In this section we present results for the calculated effective hyperfine parameters, eqQ_B, C_B, d_B, and δ_B, together with a detailed analysis of the electronic structure of the associated states. The calculation covers nearly all the vibrational

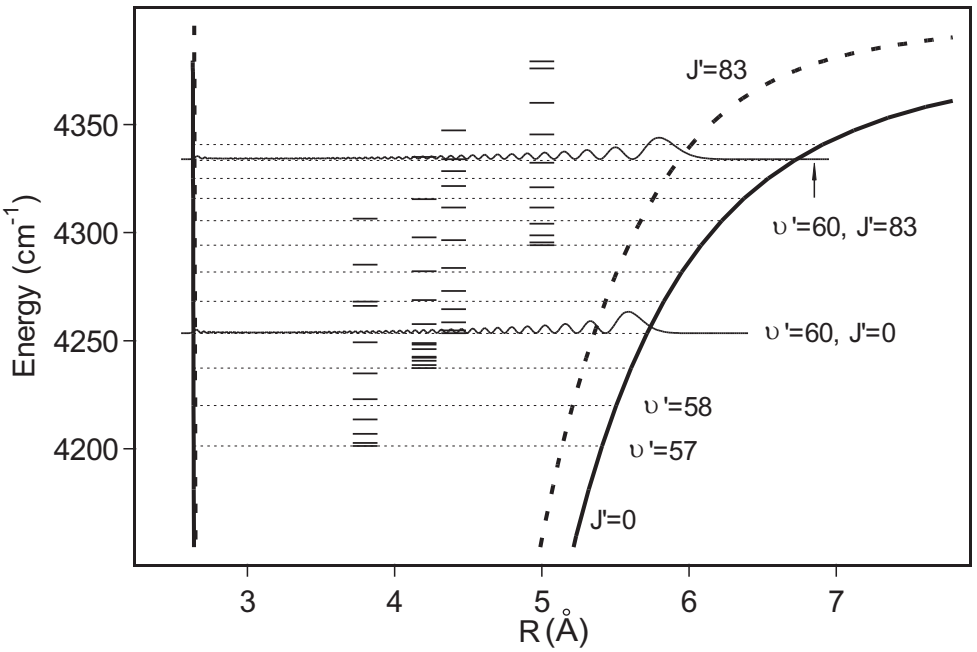

Figure 5.4: The B-state rovibrational structure. The thick solid curves are the empirical B-state rotationless potential [133]. Vibrational levels $v' = 57 - 68$ are indicated as dotted lines. The rotational levels belonging to several vibrational levels are also drawn as short bars. The line of long dashes is the effective potential (a sum of the rotationless and centrifugal potentials) associated with a rotational level ($v' = 60$, $J' = 83$). The probability distributions of the molecular vibration for levels ($v' = 60$, $J' = 0$) and ($v' = 60$, $J' = 83$) are plotted as thin solid curves for comparison of the internuclear separations sampled by the two levels.

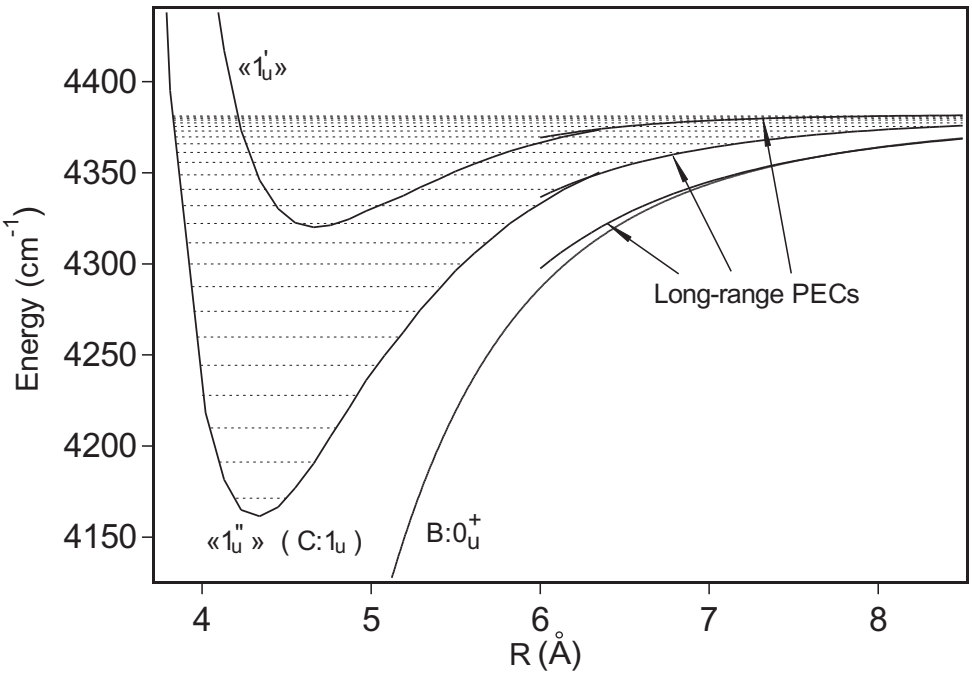

Figure 5.5: Two 1_u PECs used in the calculation of C_B. Also plotted is the B state empirical potential [133], which is used for all internuclear separations. $C{:}1_u$ and 1_u PECs ($R < 7$ Å) are constructed from theoretical [110] ($R < 7$ Å) and long-range PECs [109] ($R \geqslant 7$ Å). Those from *ab initio* calculation are shifted vertically to match the corresponding long-range one. The dotted lines indicate the vibrational levels of $C{:}1_u$ state. In the literature, the 1_u and $C{:}1_u$ states are also denoted as $\ll 1'_u \gg$ and $\ll 1''_u \gg$, respectively.

levels ($3 \leqslant v' \leqslant 82$) in the B state with R_c extending from ~ 3.5 Å to ~ 12.5 Å.

These results are discussed in three steps to demonstrate the maximum separation of the contributions from different perturbing electronic states. First, a detailed analysis of C_B is required for the determination of the admixture of the two 1_u states. Then, through the calculation of δ_B, contributions from the other two states (0_u^- and 0_g^-) are separated from the rest (two 1_g states), and the corresponding long-range PECs are tested. Finally, we present results for eqQ_B and d_B, which are in part based upon the information derived in previous two steps. Additionally, to demonstrate the numerical analysis on a finer energy scale, we give the calculated rotational dependence of the hyperfine parameter C_B for several vibrational levels. New information of electronic structure is inferred at each step of this numerical analysis by comparing the result of the calculation with the high-precision spectroscopic data. In these comparisons we incorporated, to the best of our knowledge, all available experimental data reported in previous publications [55, 42, 45, 117, 40, 120, 122, 123, 124, 125, 126, 127, 128, 129, 140, 141].

5.5.1 Spin-Rotation Parameter C_B and the Admixture of Two 1_u States

The states that contribute to C_B are restricted to the 1_u states by the coupling selection rule associated with the off-diagonal rotational Hamiltonian V^0. Thus the calculation of C_B automatically isolates the second-order contributions of the two 1_u states from those of the other four perturbing states. Furthermore, this allows a determination of the mixing parameter α between the two 1_u states that in turn can serve as a consistency check of the *ab initio* calculation of the PECs based on the separated-atom model. The details of the PECs and molecular wave functions used in equation 5.17 have already been described in section 5.3. Here we stress that in the calculation the same value for mixing parameter α can be used at a wide range

of internuclear separations, especially in the intermediate and long range, and this value is adjusted until a global agreement with experimental data is achieved.

Figure 5.6 summarizes the comparison between the calculation and the experiment. The R-centroid used for the horizontal axis is the averaged internuclear separations weighted by the B-state vibrational wave function (not by the wave function of the perturbing electronic state). In the figure, open squares, circles, and diamonds are calculations performed with the mixing parameter $\alpha = 0.9$, 0.9, and 1, respectively. The experimental data are also plotted as solid circles. First, the result shows a sensitive dependence on the mixing parameter α at large internuclear separations $R >\sim 7$ Å, as shown in figure 5.6 (a). In contrast, we verify that the uncertainty in the two 1_u PECs has merely a small influence on the calculation for large R. For instance, we intentionally decrease the potential depths of the two 1_u states by 50 cm^{-1} and 30 cm^{-1}, respectively, and repeat the calculation. While this modification results in a noticeable reduction of C_B between 4.0 Å and 5.5 Å as indicated by triangles in figure 5.6 (b), it induces less than a 2% change of C_B at $R_c >\sim 7$ Å. Additional diagnostic tests on the different parts of the two 1_u PECs produce similar outcomes. Consequently, the mixing parameter α is essentially constant and takes the value of 0.99 for internuclear separation $R > 7$ Å. Moreover, a calculation using the same α at even shorter R_c is in good agreement with the experiment until R_c reaches 4 Å, as shown in panels (b) and (c) in figure 5.6. On the other hand, a close examination of C_B at $R_c < 4$ Å in figure 5.6 (c) shows that the calculated results gradually deviate from the experiment, quantitatively illustrating a transition from the separated-atom model to the overlapped and distorted charge distribution that calls for a description employing more sophisticated molecular wave functions.

Figure 5.7 plots the calculated rotational dependence for two vibrational levels, $v' = 70$ and $v' = 47$, with the mixing parameter $\alpha = 0.99$. Given a large energy difference between the two levels and a fixed mixing parameter, the agreement with

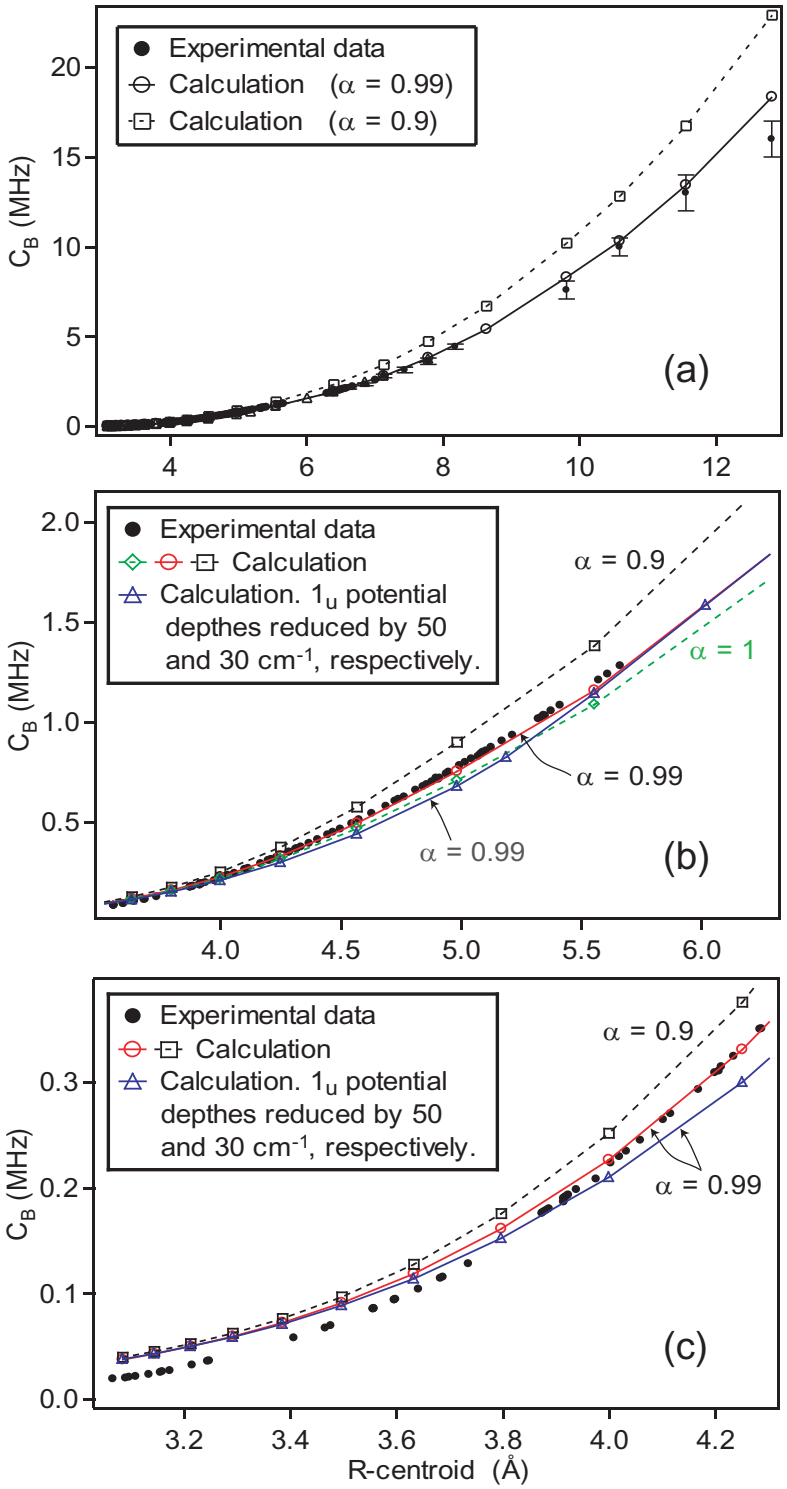

Figure 5.6: Second-order calculations of the spin-rotation parameter C_B. (a) With a mixing parameter $\alpha = 0.99$ for two 1_u states, the calculations agree well with the experimental data, while changing α to 0.9 results in a large global deviation from the experimental data. (b) A deliberate modification of the two 1_u PECs produces a noticeable discrepancy at $R_c = 4.2 - 5.5$ Å. (c) At $R_c < \sim 4$ Å, the calculation begins to depart from the experimental data.

the experimental data is reasonably good on both vibrational levels. Similar to the global trend exhibited in the figure 5.6, The rotational dependence of C_B is due to smooth variations of the Franck-Condon overlap and the energy denominator in equation 5.17, which is also responsible for the perturbation-induced rovibrational dependence in the other three hyperfine parameters.

When dealing with high-lying levels of the B state, we estimate the possible contributions beyond the second-order perturbation. The strength of the perturbation is characterized by the parameter $\lambda = \left|\frac{\eta}{\Delta E}\right|$, where η is the coupling between the two discrete levels inside the B and the 1_u states, and ΔE is their energy difference. Numerical estimation shows that λ is well below 1 for these high-lying levels. Moreover, when there is a possibility of energy coincidence, the coupling η between the two levels involved is verified to be below a few megahertz. Given this coupling strength, ΔE has to be less than a few tens of megahertz for a strong perturbation to occur, which is unlikely because of the large mismatch in the rovibrational constants of the B and the 1_u states. Thus second-order perturbation theory is sufficient for the calculation of C_B and the analysis of the related 1_u states. However, for the other three hyperfine parameters precautions should be taken because the B state can be strongly coupled to a discrete level in a particular electronic state. This strong coupling will be discussed in section 5.5.3.

5.5.2 Separation of Contributions from $0_g^-(^3\Pi_g)$ and $(3)0_u^-$ States

While only two 1_u states contribute to C_B, the other three parameters, δ_B, d_B, and eqQ_B, contain perturbations from all six perturbing states. In section 5.5.1 we determined the mixing parameter α associated with the two 1_u states, and the sensitivity of the C_B to the related PECs was investigated. With the help of this information, we decompose the hyperfine parameter δ_B to contributions from several groups of perturbing states, or even from individual perturbing states when it is

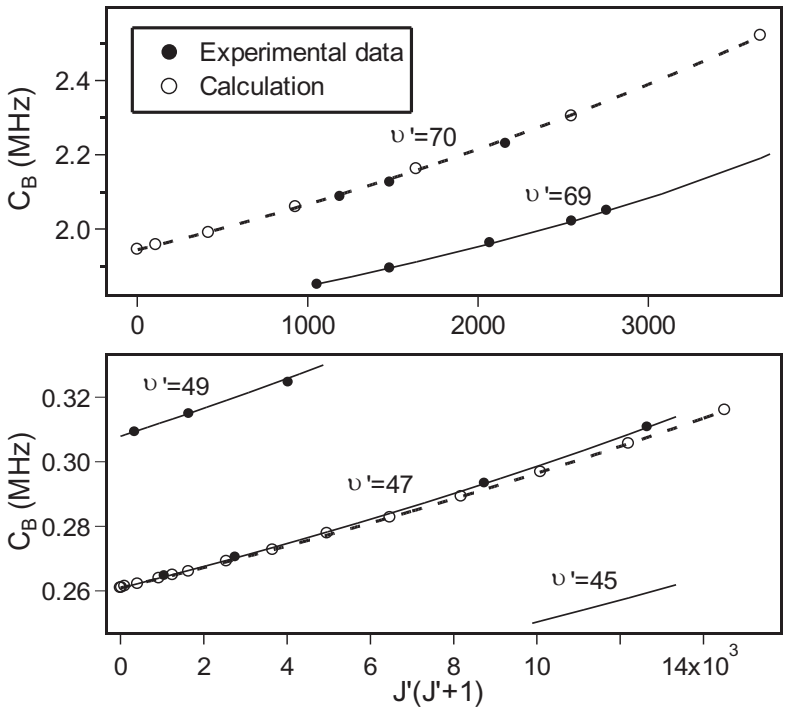

Figure 5.7: Rotational dependence of C_B around two vibrational levels $\upsilon' = 47$ and 70. Solid circles and lines are experimental data and fit, respectively. Empty circles are calculation by second-order perturbation theory. The dotted lines are fits to the computed points.

possible. This decomposition allows a sensitive characterization of the 0_g^- and the 0_u^- states and their long-range potentials.

We divide the six states into four groups: two 1_u states, the 0_g^- state, the 0_u^- state, and two 1_g states. Each of the three hyperfine parameters, namely eqQ_B, d_B, and δ_B, can be decomposed into terms that correspond to the contributions from these four groups of electronic states. For instance, the scalar spin-spin parameter δ_B can be written as

$$\delta_B = \delta\left(1_u\right) + \delta\left(1_g\right) + \delta\left(0_g^-\right) + \delta\left(0_u^-\right). \tag{5.37}$$

From equations 5.18 and 5.19, it follows that d_B is closely related to δ_B by

$$d_B = \frac{1}{2}\delta\left(1_u\right) + \frac{1}{2}\delta\left(1_g\right) - \delta\left(0_g^-\right) - \delta\left(0_u^-\right). \tag{5.38}$$

Using equations 5.37 and 5.38, we can isolate the contributions of the 0_g^- and the 0_u^- states from those of the other four states by

$$\left[\delta\left(0_g^-\right) + \delta\left(0_u^-\right)\right] = \frac{1}{3}\left(\delta_B - 2d_B\right), \tag{5.39}$$

where the right-hand side can be determined experimentally by using the values of δ_B and d_B extracted from the spectroscopic fit. The left-hand side of equation 5.39 is calculated and plotted (open squares on dashed curve) in figure 5.8 (a). For comparison we also plot the experimental values (solid circles) according to the right-hand side of equation 5.39. Recall that in the calculation there is no adjustable parameter for the electronic wave functions of the 0_g^- and the 0_u^- states. As can be seen in figure 5.8 (a), there is a noticeable discrepancy between the experiment and the calculation, which increases with the increasing R_c.

To resolve the source of this discrepancy, the contributions from 0_g^- and 0_u^- need to be further distinguished from each other. We notice that the last term in equation 5.20 for eqQ_B dominates when k and k' equal 1. Thus one can keep only these terms

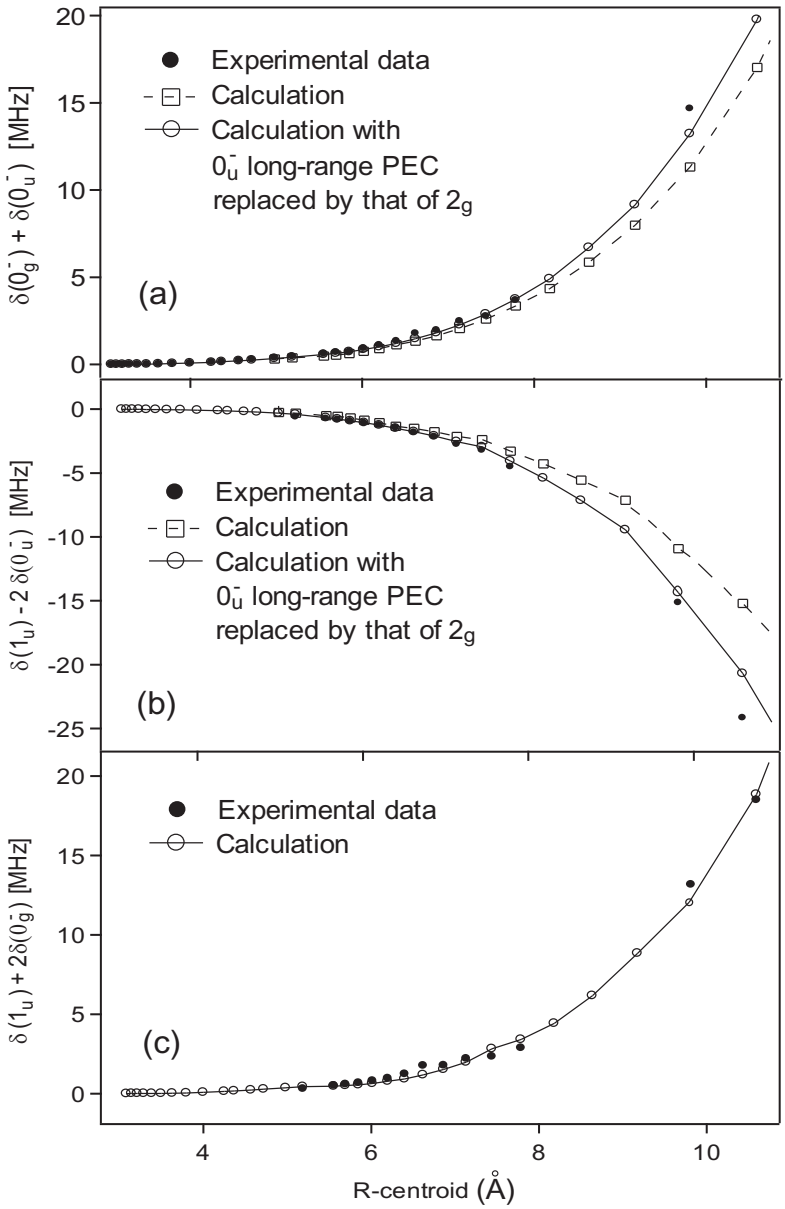

Figure 5.8: Separation of the contributions from the 0_u^- and 0_g^- states. The overall contribution of the 0_u^- and 0_g^- states to δ_B is plotted in (a), while the two separated contributions are plotted in (b) and (c), respectively. Solid circles are values deduced from the experimental data on δ_B, d_B, and eqQ_B [see equation 5.39, 5.41, and text for detail]. Open squares on dashed line represent the calculation; open circles on solid line are the calculation with the 0_u^- state long-range PEC replaced by that of 2_g state (see figure 5.2 for the two long-rang PECs). In this calculation, there is no adjustable parameter for the electronic wave functions.

and compare them with equation 5.18. This leads to the following relation between eqQ_B and δ_B:

$$\frac{1}{20}\left[eqQ_B - eqQ_0\right] \approx -\frac{1}{2}\delta\left(1_u\right) + \frac{1}{2}\delta\left(1_g\right) - \delta\left(0_g^-\right) + \delta\left(0_u^-\right), \tag{5.40}$$

where eqQ_0 is the first-order contribution, which is calculated in the separated-atom basis set at large internuclear separations. From equations 5.37, 5.38, and 5.40, the contributions from 0_u^- and 0_g^- are isolated from each other by

$$\begin{aligned}\left[\delta\left(1_u\right) - 2\delta\left(0_u^-\right)\right] &= d_B - \frac{1}{20}\left(eqQ_B - eqQ_0\right), \\ \left[\delta\left(1_u\right) + 2\delta\left(0_g^-\right)\right] &= \frac{2}{3}\delta_B - \frac{1}{3}d_B - \frac{1}{20}\left(eqQ_B - eqQ_0\right),\end{aligned} \tag{5.41}$$

where the right-hand side again can be determined experimentally by using the values of δ_B, d_B, and eqQ_B extracted from the spectroscopic fit. In the section 5.5.1, we have determined the mixing parameter α of two 1_u states. This information is incorporated into the calculation of the left-hand side of equation 5.41 that also involves the contribution from two 1_u states. In figure 5.8, panels (b) and (c) show our results for the 0_g^- (open squares on dashed curve) and 0_u^- (open circles on solid curve) states, respectively, along with the experimental data (solid circles) plotted in both panels according to the right-hand side of equation 5.41. While the calculation for 0_g^- agrees with experimental data, a discrepancy exists for the 0_u^- state that is consistent with the discrepancy observed in figure 5.8 (a). Evidently, the calculation of 0_u^- is the source of this discrepancy.

We perform additional diagnostic calculations of $\delta(0_u^-)$. We verify that moderate modifications to the short- and intermediate-range potential of the 0_u^- state cannot be responsible for the large discrepancy at $R_c >\sim 8$ Å, as shown in figure 5.8 (b). Conversely, $\delta(0_u^-)$ is sensitive to the C_5 and C_6 parameters of the 0_u^- long-range potential. In fact, at large R_c, the magnitude of $\delta(0_u^-)$ has a steep increase that is dominated by the perturbations from the last few discrete levels in the 0_u^- state whose

energies depend sensitively on the shape of long-range potential. We therefore adjust the C_5 and C_6 parameters of the 0_u^- long-range potential to compensate for the error in the calculation of $\delta(0_u^-)$. The modified long-rang potential is very close to the 2_g long-range potential as shown in figure 5.2. In light of this observation, we repeat the calculation of $\delta(0_u^-)$ with the 0_u^- long-range potential replaced by that of the 2_g state. These new results (open circles on solid curve) are also presented in figures 5.8 (a) and (b). The discrepancy is greatly reduced in comparison with the dashed curves using the original 0_u^- long-range potential. We also estimate the coupling-strength λ introduced in section 5.5.1 for each discrete level in the 0_u^- state to confirm the validity of the above analysis using second-order perturbation theory.

5.5.3 Strong Perturbation from the $1_g(^1\Pi_g)$ State and its Contribution to the Effective Hyperfine Parameters δ_B, d_B, and eqQ_B

In section 5.5.2 we divided six perturbing states into four groups, and the contributions of three groups to the effective hyperfine parameters were analyzed in detail. Once the contributions from the last two 1_g states are determined, the three hyperfine parameters δ_B, d_B, and eqQ_B can be calculated by summing up contributions from the four groups of perturbing states.

Among the two 1_g states, the outer branch of the $1_g(^1\Pi_g)$ PEC is close to that of the B state (see figures 5.1 and 5.2), resulting in a strong hyperfine coupling to high-lying levels ($70 \leqslant v'_B \leqslant 82$) of the B state through favorable Franck-Condon overlaps [45]. Furthermore, this perturbation is enhanced because for each high-lying level in the B state, there is a nearby discrete level in the $1_g(^1\Pi_g)$ state whose energy separation with the perturbed level is typically only a few gigahertz. In calculating the contribution of the 1_g states, we monitor the coupling strength between the B and the $1_g(^1\Pi_g)$ states for these high-lying levels. For $v'_B \leqslant 78$, the parameter λ of the coupling strength is verified to be < 0.1, whereas at the last four levels $v'_B = 79 - 82$,

λ can be as large as 0.4. Therefore, the second-order calculation of the contribution from the $1_g(^1\Pi_g)$ state is primarily restricted to levels below $v'_B = 78$.

Despite the inadequacy of the second-order calculation at levels $v'_B > 78$, the strong perturbation allows a high-resolution examination of the $1_g(^1\Pi_g)$ long-rang potential. We find that only a minor adjustment on the $1_g(^1\Pi_g)$ long-range PEC (see figure 5.2) is needed for the calculation of δ_B to achieve good agreement with the experimental data, as shown in figure 5.9. In the calculation, the value of the mixing parameter β for the two 1_g states is taken from reference [45] and kept fixed.

Considering the linear independence of equations 5.37, 5.38, and 5.40, the calculations of d_B and eqQ_B provide a cross-check for the modified $1_g(^1\Pi_g)$ long-range PEC and the mixing parameters α and β. Based on this observation, we proceed to perform the calculations of d_B and eqQ_B using the modified $1_g(^1\Pi_g)$ long-range PEC and the mixing parameters α and β. The hyperfine parameter d_B is calculated using equation 5.38. In the case of eqQ_B, our calculation includes both major contributions in equation 5.40 and other minor terms in equation 5.20. The results for d_B, and eqQ_B agree reasonably well with experimental data, as shown respectively in figures 5.10 and 5.11. Compared with d_B, our calculation of eqQ_B has a relatively large discrepancy because the residual error of $\delta(1_g)$ is amplified by a factor of 20 in the case of eqQ_B according to equations 5.38 and 5.40. Once the mixing parameter β of the two 1_g states is independently determined, the calculations of d_B and eqQ_B can be further improved by a global fit of the $1_g(^1\Pi_g)$ long-range PEC to all three hyperfine parameters δ_B, d_B, and eqQ_B.

5.6 First-Order Electric Quadrupole Interaction

Unlike C_B, δ_B, and d_B, which result solely from perturbations given by external electronic states over the whole range of internuclear separation, eqQ_B has both first-order and second-order components that are important in different regions. Our

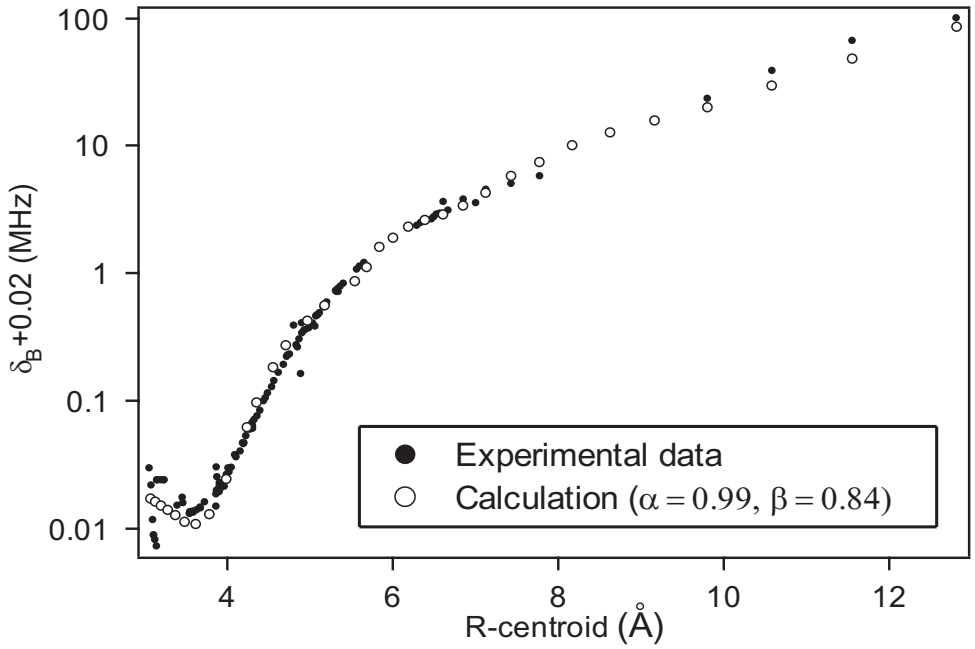

Figure 5.9: Semilog plot of the second-order calculation of the scalar spin-spin parameter δ_B. Solid circles are experimental data and open circles represent calculations. In the calculation the mixing parameters for the two 1_u and the two 1_g states are fixed to $\alpha = 0.99$ and $\beta = 0.84$, respectively. Because the contribution from the $1_g(^1\Pi_g)$ state is extremely sensitive to the corresponding long-range potential, the $1_g(^1\Pi_g)$ long-range potential is fine-tuned to obtain good agreement with the experimental data.

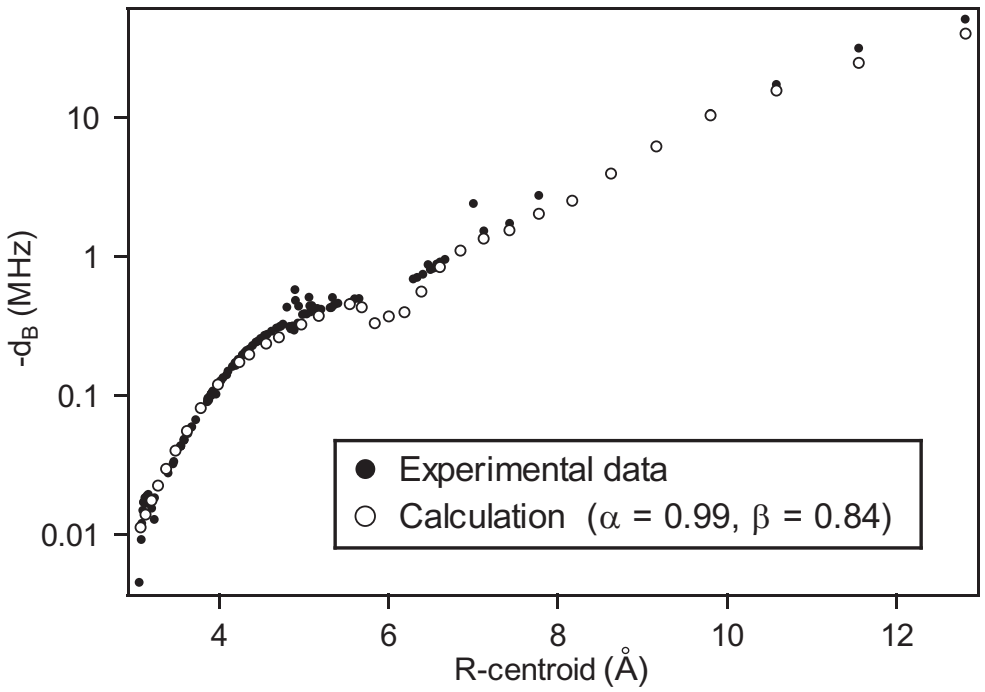

Figure 5.10: Semilog plot of the second-order calculation of the tensor spin-spin parameter d_B. Solid circles are experimental data and open circles represent calculations. The calculation combines the contributions from all six states (see equation 5.38) that are determined in the calculations of δ_B. The calculation provides a cross-check of the 1_g long-rang PEC and the mixing parameters α and β.

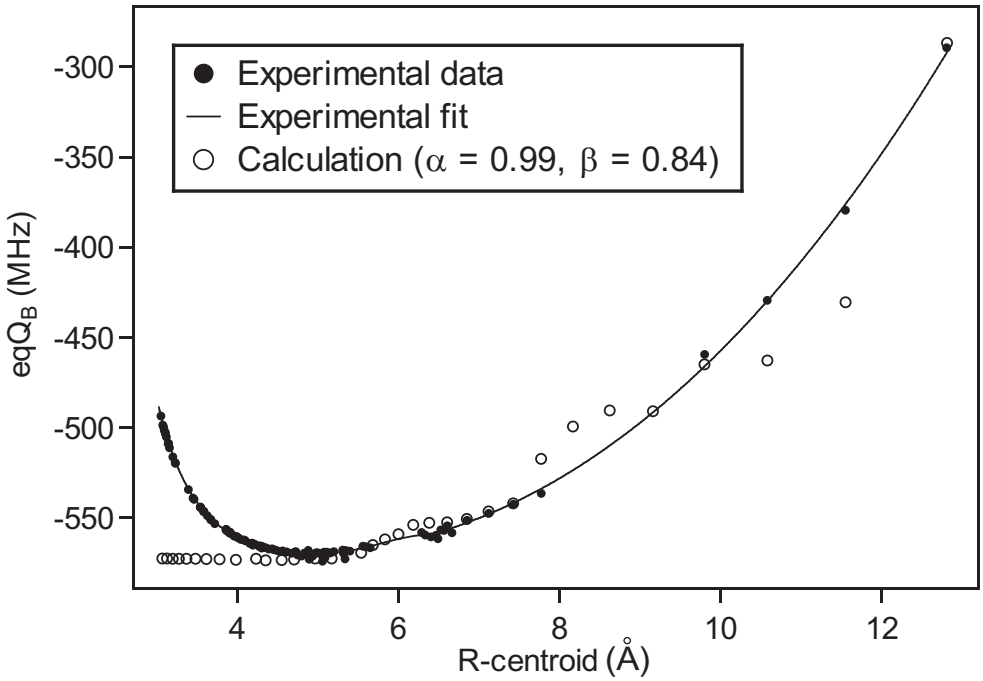

Figure 5.11: Second-order calculation of the electric quadrupole parameter eqQ_B. Solid circles are experimental data and open circles represent calculations. The calculation combines the contributions from the same six states used for figures 5.9 and 5.10. The calculation provides a cross-check of the 1_g long-rang PEC and the mixing parameters α and β. The relatively large discrepancy is due to the fact that the residual error of $\delta(1_g)$ (the contribution of the 1_g states to δ_B) has been amplified by a factor of 20 in the case of eqQ_B (see equations 5.38 and 5.40).

numerical analysis makes it possible to locate more accurately the regions at which each component dominates. As shown in figure 5.11, at short internuclear separations ($R_c < 5$ Å), the perturbation from the external states is negligible. The perturbation sets in at $R_c \sim 5$ Å and increases along with the internuclear separation. Finally, it is worth noting that at $R_c < 5$ Å the first-order component of eqQ_B departs from the constant value predicated by both SAB (separated-atom basis) and LCAO (linear combination of atomic orbitals) models with the decreasing internuclear separation because of a combined effect of (1) the nuclear quadrupole-quadrupole interaction and (2) the distortion and overlapping of the electric charge distributions of two iodine atoms.

5.7 Summary and Conclusions

We have performed second-order calculations of four hyperfine parameters C_B, δ_B, d_B, and eqQ_B, using the available molecular PECs and electronic wave functions derived from the separated-atom basis set. We have shown that by dividing the six perturbing electronic states into four groups, their contributions to the hyperfine parameters can be separated and directly compared with the corresponding experimental data. For the spin-rotation parameter C_B, the results for both vibrational and rotational dependence agree well with the experimental data for a wide range of internuclear separations ($R_c > \sim 4$ Å), and the mixing parameter of the two 1_u states is independently determined as $\alpha = 0.99$. However, calculations depart from experimental data at short internuclear separations ($R_c < \sim 4$ Å), indicating the breakdown of the separated-atom model. Moreover, calculations of the other three hyperfine parameters verify the mixing parameter of two 1_g states and place a stringent constraint on the long-range PECs of the relevant electronic states.

The numerical analysis of effective hyperfine parameters based on the separated-atom model is in remarkably good agreement with the experimental data over a broad

range of internuclear separations. This implies that the electronic structure of a large number of B-state rovibrational levels, not limited to those high-lying ones ($v' > 70$), preserves a long-range character.

The analysis presented in this chapter can also be applied to the gyroscopic and hyperfine predissociation of molecular iodine in the B state [66, 67, 61]. In this decay channel, molecules in the B sate are predissociated through the repulsive $B''1_u(^1\Pi_u)$ state that converges with the ground state X to the first dissociation limit, $^2\mathrm{P}_{\frac{3}{2}}+^2\mathrm{P}_{\frac{3}{2}}$. In particular, this new analysis may help to elucidate the source of the large discrepancy found in the calculation of the predissociation matrix element C_v [149], which is related to the gyroscopic predissociation.

Bibliography

[1] E. Peik, B. Lipphardt, H. Schnatz, T. Schneider, and Chr. Tamm, "Limit on the present temporal variation of the fine structure constant", Phys. Rev. Lett., vol. 93, pp. 170801, 2004.

[2] H. Marion, F. Pereira Dos Santos, M. Abgrall, S. Zhang, Y. Sortais, S. Bize, I. Maksimovic, D. Calonico, J. Grünert, C. Mandache, P. Lemonde, G. Santarelli, Ph. Laurent, and A. Clairon, "Search for variations of fundamental constants using atomic fountain clocks", Phys. Rev. Lett., vol. 90, pp. 150801, 2003.

[3] S. Bize, S. A. Diddams, U. Tanaka, C. E. Tanner, W. H. Oskay, R. E. Drullinger, T. E. Paker, T. P. Heavner, S. R. Jefferts, L. Hollberg, W. M. Itano, and J. C. Bergquist, "Testing the stability of fundamental constants with the $^{199}\mathrm{H}_g^+$ single-ion opttical clock", Phys. Rev. Lett., vol. 90, pp. 150802, 2003.

[4] B. C. Regan, E. D. Commins, C. J. Schmidt, and D. DeMille, "New limit on the electron electric dipole moment", Phys. Rev. Lett., vol. 88, pp. 071805, 2002.

[5] J. J. Hudson, B. E. Sauer, M. R. Tarbutt, and E. A. Hinds, "Measurement of the electron electric dipole moment using YbF molecules", Phys. Rev. Lett., vol. 89, pp. 023003, 2002.

[6] D. Wilkening, N. Ramsey, and D. Larson, "Search for P and T violations in the hyperfine structure of thallium fluoride", Phys. Rev. A, vol. 29, pp. 425, 1984.

[7] D. Cho, K. Sangster, and E. E. Hinds, "Tenfold improvement of limits on T violation in thallium fluoride", Phys. Rev. Lett., vol. 63, pp. 2559, 1989.

[8] T. W Hänsch and A. L. Schawlow, "Cooling of gases by laser radiation", Opt. Commun., vol. 13, pp. 68, 1975.

[9] E. L. Raab, M. Prentiss, A. Cable, S. Chu, and D. E. Pritchard, "Trapping of neutral sodium atoms with radiation pressure", Phys. Rev. Lett., vol. 59, pp. 2631, 1987.

[10] Dalibard J. and C. Cohen-Tannoudji, "Laser cooling below the Doppler limit by polarization gradients: simple theoretical models", J. Opt. Soc. Am. B, vol. 6, pp. 2023, 1989.

[11] P. D. Lett, W. D. Phillips, S. L. Rolston, C. E. Tanner, R. N. Watts, and C. I. Westbrook, "Optical molasses", J. Opt. Soc. Am. B, vol. 6, pp. 2084, 1989.

[12] D. S. Weiss, E. Riis, Y. Shevy, P. J. Ungar, and S. Chu, "Optical molasses and multilevel atoms: experiment", J. Opt. Soc. Am. B, vol. 6, pp. 2072, 1989.

[13] T. Udem, J. Reichert, R. Holzwarth, and T. W. Hänsch, "Absolute optical frequency measurement of the cesium D_1 line with a mode-locked laser", Phys. Rev. Lett., vol. 82, no. 18, pp. 3568, 1999.

[14] T. Udem, J. Reichert, R. Holzwarth, and T. W. Hänsch, "Accurate measurement of large optical frequency differences with a mode-locked laser", Opt. Lett., vol. 24, no. 13, pp. 881, 1999.

[15] H. R. Telle, G. Steinmeyer, A. E. Dunlop, J. Stenger, D. H. Sutter, and U. Keller, "Carrier-envelope offset phase control: A novel concept for absolute optical frequency measurement and ultrashort pulse generation", Appl. Phys. B, vol. 69, no. 4, pp. 327, 1999.

[16] M. Broyer, J. Vigué, and J. C. Lehmann, "Effective hyperfine hamiltonian in homonuclear diatomic molecules. Application to the B state of molecular iodine", J. Phys. (Paris), vol. 39, pp. 591, 1978.

[17] J. C. Bergquist, "Doppler-free spectroscopy", in Atom, molecular, and optical physics: electromagnetic radiation, F. B. Dunning and R. G. Hulet, Eds., vol. 29B. Academic Press, San Diego, 1996.

[18] W. Demtröder, Laser spectroscopy Basic concepts and instrumentation, Springer, Berlin, 1998.

[19] L. D. Landau and E. M. Lifshitz, Statistical physics, vol. 5 of Course of theoretical physics, Butterworth-Heinemann, Oxford, 1980.

[20] T. Ido, T. H. Loftus, M. M. Boyd, A. D. Ludlow, K. W. Holman, and J. Ye, "Precision spectroscopy and density-dependent frequency shifts in ultracold Sr", arXiv:physics/0410110 v1, 2004.

[21] R.H. Dicke, "The effect of collisions upon the doppler width of spectral lines", Phys. Rev., vol. 89, pp. 472, 1953.

[22] R. W. P. Drever, J. L. Hall, F. V. Kowalski, J. Hough, G. M. Ford, A. J. Munley, and H. Ward, "Laser phase and frequency stabilization using an optical-resonator", Appl. Phys. B, vol. 31, no. 2, pp. 97, 1983.

[23] B. C. Young, F. C. Cruz, W. M. Itano, and J. C. Bergquist, "Visible lasers with subhertz linewidths", Phys. Rev. Lett., vol. 82, no. 19, pp. 3799, 1999.

[24] C. Salomon, D. Hils, and J. L. Hall, "Laser stabilization at the millihertz level", J. Opt. Soc. Am. B, vol. 5, no. 8, pp. 1576, 1988.

[25] D. Hils and J. L. Hall, "Frequency standards and metrology", in Frequency standards and metrology, A. De Marchi, Ed. Springer-Verlag Berlin, Heidelberg, 1989.

[26] M. Zhu and J. L. Hall, "Stabilization of optical-phase frequency of a laser system - application to a commercial dye-laser with an external stabilizer", J. Opt. Soc. Am. B, vol. 10, no. 5, pp. 802, 1993.

[27] W. R. bennet, Jr., "Hole-burining effects in a He-Ne-optical maser", Phys. Rev., vol. 126, pp. 580, 1962.

[28] A. Szöke and A. Javan, "Isotope shift and saturation behavior of the 1.15-μ transition of Ne", Phys. Rev. Lett., vol. 10, pp. 521, 1963.

[29] R. A. MacFarlane, W. R. Bennett, Jr., and W. E. Lamb, Jr., "Single mode tuning dip in the power output of an He-Ne maser", Appl. Phys. Lett., vol. 2, pp. 189, 1963.

[30] W. E. Lamb, Jr., "Theory of an optical maser", Phys. Rev., vol. 134, pp. A1429, 1964.

[31] C. Bordé, "Saturated absorption spectroscopy of various molecules using lasers with carbonic gas and nitrogen protoxide", Cr. Acad. Sci. B Phys., vol. 271, no. 6, pp. 371, 1970.

[32] T. W. Hänsch, M. D. Levenson, and A. L. Schawlow, "Complete hyperfine structure of a molecular iodine line", Phys. Rev. Lett., vol. 26, no. 16, pp. 946, 1971.

[33] T. W. Hänsch, "High resolution laser spectroscopy", in Advances in laser spectroscopy, F. T. Arecchi, F. Strumia, and H. Walther, Eds., vol. 95. Plenum Press, New York, 1981.

[34] G. C. Bjorklund, "Frequency-modulation spectroscopy - new method for measuring weak absorptions and dispersions", Opt. Lett., vol. 5, no. 1, pp. 15, 1980.

[35] J. L. Hall, L. Hollberg, T. Baer, and H. G. Robinson, "Optical heterodyne saturation spectroscopy", Appl. Phys. Lett., vol. 39, no. 9, pp. 680, 1981.

[36] J. L. Hall, H. G. Robinson, T. Baer, and L. Hollberg, "The lineshapes of sub-Doppler resonances observable with FM side-band (optical heterodyne) laser techniques", in Advances in laser spectroscopy, F. T. Arecchi, F. Strumia, and H. Walther, Eds., vol. 95. Plenum Press, New York, 1981.

[37] J. Ye, L. S. Ma, and J. L. Hall, "Sub-Doppler optical frequency reference at 1.064 μm by means of ultrasensitive cavity-enhanced frequency modulation spectroscopy of a C_2HD overtone transition", Opt. Lett., vol. 21, no. 13, pp. 1000, 1996.

[38] J. Ye, L. S. Ma, and J. L. Hall, "Ultrastable optical frequency reference at 1.064 μm using a C_2HD molecular overtone transition", IEEE Trans. Instrum. Meas., vol. 46, no. 2, pp. 178, 1997.

[39] J. Ye, L. S. Ma, and J. L. Hall, "Ultrasensitive detections in atomic and molecular physics: demonstration in molecular overtone spectroscopy", J. Opt. Soc. Am. B, vol. 15, no. 1, pp. 6, 1998.

[40] T. J. Quinn, "Practical realization of the definition of the metre (1997)", Metrologia, vol. 36, pp. 211, 1999.

[41] J. Ye, L. Robertsson, S. Picard, L.-S. Ma, and J. L. Hall, "Absolute frequency atlas of molecular I_2 lines at 532 nm", IEEE Trans. Instrum. Meas., vol. 48, pp. 544, 1999.

[42] B. Bodermann, H. Knöckel, and E. Tiemann, "Widely usable interpolation formulae for hyperfine splittings in the $^{127}I_2$ spectrum", Eur. Phys. J. D, vol. 19, pp. 31, 2002.

[43] J. P. Pique, F. Hartmann, R. Bacis, S. Churassy, and J. B. Koffend, "Hyperfine-induced ungerade-gerade symmetry breaking in a homonuclear diatomic molecule near a dissociation limit: $^{127}I_2$ at the $^2P_{3/2}$ - $^2P_{1/2}$ limit", Phys. Rev. Lett., vol. 52, pp. 267, 1984.

[44] J. P. Pique, F. Hartmann, S. Churassy, and R. Bacis, "Hyperfine interactions in homonuclear diatomic molecules and u-g perturbations. I. theory", J. Phys. (Paris), vol. 47, pp. 1909, 1986.

[45] J. P. Pique, F. Hartmann, S. Churassy, and R. Bacis, "Hyperfine interactions in homonuclear diatomic molecules and u-g perturbations. II. experiments on I_2", J. Phys. (Paris), vol. 47, pp. 1917, 1986.

[46] J. Vigué, M. Broyer, and J. C. Lehmann, "Ab initio calculation of hyperfine and magnetic parameters in the I_2 B state", Phys. Rev. Lett., vol. 42, pp. 883, 1979.

[47] R. Bacis, M. Broyer, S. Churassy, J. Vergès, and J. Vigué, "eQq measurements in the X, 1_g, 0_g^+ and B state of I_2: A test of the electronic molecular eigenfunctions", J. Chem. Phys., vol. 73, pp. 2641, 1980.

[48] J. P. Pique, F. Hartmann, R. Bacis, and S. Churassy, "Hyperfine structure of higher rovibrational levels in the iodine B state studied by Ar^+ laser induced fluorescence", Opt. Commun., vol. 36, pp. 354, 1981.

[49] S. Ezekiel and R. Weiss, "Laser-induced fluorescence in a molecular beam of iodine", Phys. Rev. Lett., vol. 20, pp. 91, 1968.

[50] M. D. Levenson and A. L. Schawlow, "Hyperfine interactions in molecular iodine", Phys. Rev. A, vol. 6, pp. 10, 1972.

[51] G. R. Hanes and C. E. Dahlstrom, "Iodine hyperfine structure observed in saturated absorption at 633 nm", Appl. Phys. Lett., vol. 14, pp. 362, 1969.

[52] A. Arie, S. Schiller, E. K. Gustafson, and R. L. Byer, "Absolute frequency stabilization of diode-laser-pumped NdYAG lasers to hyperfine transitions in molecular iodine", Opt. Lett., vol. 17, no. 17, pp. 1204, 1992.

[53] M. L. Eickhoff and J. L. Hall, "Optical frequency standard at 532 nm", IEEE Trans. Instrum. Meas., vol. 44, no. 2, pp. 155, 1995.

[54] J. Ye, L. S. Ma, and J. L. Hall, "Molecular iodine clock", Phys. Rev. Lett., vol. 8727, no. 27, art. no.-270801, 2001.

[55] Ch. J. Bordé, G. Camy, B. Decomps, and J.-P. Descoubes, "High precision saturation spectroscopy of $^{127}I_2$ with argon lasers at 5 145 Å and 5 017 Å: - main resonances", J. Phys. (Paris), vol. 42, pp. 1393, 1981.

[56] A. N. Goncharov, M. N. Skvortsov, and V. P. Chebotayev, "Study of relaxation of molecular-iodine by the method of saturated absorption-spectroscopy", Appl. Phys. B, vol. 51, no. 2, pp. 108, 1990.

[57] R. E. Tench and S. Ezekiel, "Precision measurements of hyperfine predissociation in I_2 vapor using a two-photon resonant scattering technique", Chem. Phys. Lett., vol. 96, pp. 253, 1983.

[58] K. Shimoda, "Line broadening and narrowing effects", in High-resolution spectroscopy, K. Shimoda, Ed. Springer, Berlin, Heidelberg, 1976.

[59] C. Teichteil and M. Pelissier, "Relativistic calculations of excited states of molecular iodine", Chem. Phys., vol. 180, pp. 1, 1994.

[60] W. Y. Cheng and J. T. Shy, "Wavelength standard at 543 nm and the corresponding $^{127}I_2$ hyperfine transitions", J. Opt. Soc. Am. B, vol. 18, no. 3, pp. 363, 2001.

[61] J. Vigué, M. Broyer, and J. C. Lehmann, "Natural hyperfine and magentic predissociation of the I_2 B state III. - experiments on magnetic predissociation", J. Phys. (Paris), vol. 42, pp. 961, 1981.

[62] M. Lamrini, R. Bacis, D. Cerny, S. Churassy, P. Crozet, and A. J. Ross, "The electronic transition dipole moment of the $B0_u^+ \rightarrow X0_g^+$ transition in iodine", J. Chem. Phys., vol. 100, no. 12, pp. 8780, 1994.

[63] J. Tellinghuisen, "The electronic transition moment function for the $B0_u^+(^3\Pi) \leftrightarrow X^1\Sigma_g^+$ transition in I_2", J. Chem. Phys., vol. 106, no. 4, pp. 1305, 1997.

[64] P. Dubé and M. Trinczek, "Hyperfine-structure splittings and absorption strengths of molecular-iodine transitions near the trapping frequencies of francium", J. Opt. Soc. Am. B, vol. 21, no. 6, pp. 1113, 2004.

[65] J. P. Pique, R. Bacis, F. Hartmann, N. Sadeghi, and S. Churassy, "Hyperfine predissociation in the B state of iodine investigated through lifetime measurements of individual hyperfine sublevels", J. Phys. (Paris), vol. 44, pp. 347, 1983.

[66] J. Vigué, M. Broyer, and J. C. Lehmann, "Natural hyperfine and magnetic predissociation of the I_2 B state I. - Theory", J. Phys. (Paris), vol. 42, pp. 937, 1981.

[67] J. Vigué, M. Broyer, and J. C. Lehmann, "Natural hyperfine and magnetic predissociation of the I_2 B state II. - Experiments on natural and hyperfine predissociation", J. Phys. (Paris), vol. 42, pp. 949, 1981.

[68] S. Gerstenkorn and P. Luc, Atlas du Spectre d'Absorption de la Molécule d'Iode 14 800 cm^{-1} - 20 000 cm^{-1}, Editions du CNRS, Paris, 1985.

[69] J. I. Steinfeld, Molecules and radiation, MIT Press, New York, 1986.

[70] K. M. Evenson, J. S. Wells, F. R. Petersen, B. L. Danielson, and G. W. Day, "Accurate frequencies of molecular transitions used in laser stabilization 3.39-μm transition in CH_4 and 9.33- and 10.18-μm transitions in CO_2", Appl. Phys. Lett., vol. 22, no. 4, pp. 192, 1973.

[71] H. Schnatz, B. Lipphardt, J. Helmcke, F. Riehle, and G. Zinner, "First phase-coherent frequency measurement of visible radiation", Phys. Rev. lett., vol. 76, no. 1, pp. 18, 1996.

[72] B. G. Whitford, "Phase-locked frequency chains to 130 THz at NRC", in Frequency standards and metrology, A. De Marchi, Ed. Springer-Verlag Berlin, Heidelberg, 1989.

[73] J. E. Bernard, A. A. Madej, L. Marmet, B. G. Whitford, K. J. Siemsen, and S. Cundy, "Cs-based frequency measurement of a single, trapped ion transition in the visible region of the spectrum", Phys. Rev. Lett., vol. 82, no. 16, pp. 3228, 1999.

[74] T. Udem, A. Huber, B. Gross, J. Reichert, M. Prevedelli, M. Weitz, and T. W. Hänsch, "Phase-coherent measurement of the hydrogen 1S-2S transition frequency with an optical frequency interval divider chain", Phys. Rev. Lett., vol. 79, no. 14, pp. 2646, 1997.

[75] T. Udem, A. Huber, M. Weitz, D. Leibfried, W. Konig, M. Prevedelli, A. Dimitriev, H. Geiger, and T. W. Hänsch, "Phase-coherent measurement of the hydrogen 1S-2S frequency with an optical frequency interval divider chain", IEEE Trans. Instrum. Meas., vol. 46, no. 2, pp. 166, 1997.

[76] H. R. Telle, D. Meschede, and T. W. Hänsch, "Realization of a new concept for visible frequency division: phase locking of harmonic and sum frequencies", Opt. Lett., vol. 15, no. 10, pp. 532, 1990.

[77] D. A. Jennings, K. M. Evenson, and D. J. E. Knight, "Optical frequency measurements", Proceedings of the IEEE, vol. 74, no. 1, pp. 168, 1986.

[78] S. A. Diddams, D. J. Jones, J. Ye, S. T. Cundiff, J. L. Hall, J. K. Ranka, R. S. Windeler, R. Holzwarth, T. Udem, and T. W. Hänsch, "Direct link between microwave and optical frequencies with a 300 THz femtosecond laser comb", Phys. Rev. Lett., vol. 84, no. 22, pp. 5102, 2000.

[79] D. J. Jones, S. A. Diddams, J. K. Ranka, A. Stentz, R. S. Windeler, J. L. Hall, and S. T. Cundiff, "Carrier-envelope phase control of femtosecond mode-locked lasers and direct optical frequency synthesis", Science, vol. 288, no. 5466, pp. 635, 2000.

[80] J. Reichert, M. Niering, R. Holzwarth, M. Weitz, T. Udem, and T. W. Hänsch, "Phase coherent vacuum-ultraviolet to radio frequency comparison with a mode-locked laser", Phys. Rev. Lett., vol. 84, no. 15, pp. 3232, 2000.

[81] J. Ye, T. H. Yoon, J. L. Hall, A. A. Madej, J. E. Bernard, K. J. Siemsen, and L. Marmet, "Accuracy comparison of absolute optical frequency measurement between harmonic-generation synthesis and a frequency-division femtosecond comb", Phys. Rev. Lett., vol. 85, no. 18, pp. 3797, 2000.

[82] J. Reichert, R. Holzwarth, T. Udem, and T. W. Hänsch, "Measuring the frequency of light with mode-locked lasers", Opt. Commun., vol. 172, no. 1-6, pp. 59, 1999.

[83] J. Ye and S. T. Cundiff, Eds., Femtosecond optical frequency comb: principle, operation, and applications, Kluwer Academic Publishers / Springer, Norwell, 2004.

[84] A. Bartels, T. Dekorsy, and H. Kurz, "Femtosecond Ti:sapphire ring laser with a 2-GHz repetition rate and its application in time-resolved spectroscopy", Opt. Lett., vol. 24, no. 14, pp. 996, 1999.

[85] S. T. Cundiff, "Phase stabilization of ultrashort optical pulses", J. Phys. D, vol. 35, no. 8, pp. R43, 2002.

[86] M. T. Asaki, C. P. Huang, D. Garvey, J. P. Zhou, H. C. Kapteyn, and M. M. Murnane, "Generation of 11-fs pulses from a self-mode-locked Ti-sapphire laser", Opt. Lett., vol. 18, no. 12, pp. 977, 1993.

[87] R. L. Fork, O. E. Martinez, and J. P. Gordon, "Negative dispersion using pairs of prisms", Opt. Lett., vol. 9, no. 5, pp. 150, 1984.

[88] R. Szipöcs, K. Ferencz, C. Spielmann, and F. Krausz, "Chirped multilayer coatings for broad-band dispersion control in femtosecond lasers", Optics Letters, vol. 19, no. 3, pp. 201, 1994.

[89] A. E. Siegman, Lasers, University Science Books, Mill Valley, 1986.

[90] D. E. Spence, P. N. Kean, and W. Sibbett, "60-fsec pulse generation from a self-mode-locked Ti-sapphire laser", Opt. Lett., vol. 16, no. 1, pp. 42, 1991.

[91] T. W. Hänsch, "High resolution spectroscopy of hydrogen", in The hydrogen atom, G. F. Bussani, M. Inguscio, and T. W. Hänsch, Eds. Springer, Berlin, Heidelberg, 1989.

[92] K. F. Kwong, D. Yankelevich, K. C. Chu, J. P. Heritage, and A. Dienes, "400-Hz mechanical scanning optical delay-line", Opt. Lett., vol. 18, no. 7, pp. 558, 1993.

[93] L. Xu, C. Spielmann, A. Poppe, T. Brabec, F. Krausz, and T. W. Hänsch, "Route to phase control of ultrashort light pulses", Opt. Lett., vol. 21, no. 24, pp. 2008, 1996.

[94] A. Poppe, R. Holzwarth, A. Apolonski, G. Tempea, C. Spielmann, T. W. Hänsch, and F. Krausz, "Few-cycle optical waveform synthesis", Appl. Phys. B, vol. 72, no. 8, pp. 977, 2001.

[95] K. W. Holman, R. J. Jones, A. Marian, S. T. Cundiff, and J. Ye, "Detailed studies and control of intensity-related dynamics of femtosecond frequency combs from mode-locked Ti:sapphire lasers", IEEE J. Sel. Top. Quant., vol. 9, no. 4, pp. 1018, 2003.

[96] K. W. Holman, R. J. Jones, A. Marian, S. T. Cundiff, and J. Ye, "Intensity-related dynamics of femtosecond frequency combs", Opt. Lett., vol. 28, no. 10, pp. 851, 2003.

[97] K. W. Holman, D. J. Jones, J. Ye, and E. P. Ippen, "Orthogonal control of the frequency comb dynamics of a mode-locked laser diode", Optics Letters, vol. 28, no. 23, pp. 2405, 2003.

[98] A. H. Glattfelder and W. Schaufelberger, Control systems with input and output constraints, Springer, London, 2003.

[99] G. F. Franklin, J. D. Powell, and A. Emami-Naeini, Feedback control of dynamic systems, Addison-Wesley, Reading, 1994.

[100] R. Holzwarth, T. Udem, T. W. Hänsch, J. C. Knight, W. J. Wadsworth, and P. S. J. Russell, "Optical frequency synthesizer for precision spectroscopy", Phys. Rev. Lett., vol. 85, no. 11, pp. 2264, 2000.

[101] B. J. Eggleton, P. S. Westbrook, C. A. White, C. Kerbage, R. S. Windeler, and G. L. Burdge, "Cladding-mode-resonances in air-silica microstructure optical fibers", J. Lightwave Technol., vol. 18, no. 8, pp. 1084, 2000.

[102] J. K. Ranka, R. S. Windeler, and A. J. Stentz, "Visible continuum generation in air-silica microstructure optical fibers with anomalous dispersion at 800 nm", Opt. Lett., vol. 25, no. 1, pp. 25, 2000.

[103] J. K. Ranka, R. S. Windeler, and A. J. Stentz, "Optical properties of high-delta air-silica microstructure optical fibers", Opt. Lett., vol. 25, no. 11, pp. 796, 2000.

[104] R. Ell, U. Morgner, F. X. Kartner, J. G. Fujimoto, E. P. Ippen, V. Scheuer, G. Angelow, T. Tschudi, M. J. Lederer, A. Boiko, and B. Luther-Davies, "Generation of 5-fs pulses and octave-spanning spectra directly from a Ti:sapphire laser", Opt. Lett., vol. 26, no. 6, pp. 373, 2001.

[105] T. M. Fortier, D. J. Jones, and S. T. Cundiff, "Phase stabilization of an octave-spanning Ti:sapphire laser", Opt. Lett., vol. 28, no. 22, pp. 2198, 2003.

[106] L. Matos, D. Kleppner, O. Kuzucu, T. R. Schibli, J. Kim, E. P. Ippen, and F. X. Kaertner, "Direct frequency comb generation from an octave-spanning, prismless Ti:sapphire laser", Opt. Lett., vol. 29, no. 14, pp. 1683, 2004.

[107] S. A. Diddams, T. Udem, J. C. Bergquist, E. A. Curtis, R. E. Drullinger, L. Hollberg, W. M. Itano, W. D. Lee, C. W. Oates, K. R. Vogel, and D. J. Wineland, "An optical clock based on a single trapped $^{199}Hg^{+}$ ion", Science, vol. 293, no. 5531, pp. 825, 2001.

[108] J. L. Hall, L. S. Ma, M. Taubman, B. Tiemann, F. L. Hong, O. Pfister, and J. Ye, "Stabilization and frequency measurement of the I_2-stabilized Nd:YAG laser", IEEE Trans. Instrum. Meas., vol. 48, no. 2, pp. 583, 1999.

[109] M. Saute and M. Aubert-Frécon, "Calculated long-range potential-energy curves for the 23 molecular states of I_2", J. Chem. Phys., vol. 77, pp. 5639, 1982.

[110] W. A. de Jong, L. Visscher, and W. C. Nieuwpoort, "Relativistic and correlated calculations on the ground, excited, and ionized states of iodine", J. Chem. Phys., vol. 107, pp. 9046, 1997.

[111] N. F. Ramsey and E. M. Purcell, "Interactions between nuclear spins in molecules", Phys. Rev., vol. 85, pp. 143L, 1952.

[112] A. Morinaga, "Hyperfine structure and hyperfine coupling constant of molecular iodine", Jpn. J. Appl. Phys., vol. 23, pp. 774, 1984.

[113] H. J. Foth and F Spieweck, "Hyperfine structure of the R(98), 58-1 line of $^{127}I_2$ at 514.5 nm", Chem. Phys. Lett., vol. 65, pp. 347, 1979.

[114] G. R. Hanes, J. Lapierre, P. R. Bunker, and K. C. Shotton, "Nuclear hyperfine structure in the electronic spectrum of $^{127}I_2$ by saturated absorption spectroscopy, and comparison with theory", J. Mol. Spectrosc., vol. 39, pp. 506, 1971.

[115] R. J. Jones, W. Y. Cheng, K. W. Holman, L. Chen, J. L. Hall, and J. Ye, "Absolute-frequency measurement of the iodine-based length standard at 514.67 nm", Appl. Phys. B, vol. 74, pp. 597, 2002.

[116] C. Ishibashi, J. Ye, and J. L. Hall, "Issues and applications in ultra-sensitive molecular spectroscopy", in Methods for Ultrasensitive Detection II, C. W. Wilkerson, Jr., ed., Proc. SPIE, vol. 4634, pp. 58, 2002.

[117] F.-L. Hong, J. Ye, L.-S. Ma, S. Picard, Ch. J. Bordé, and J. L. Hall, "Rotation dependence of electric quadrupole hyperfine interaction in the ground state of molecular iodine by high-resolution laser spectroscopy", J. Opt. Soc. Am. B, vol. 18, pp. 379, 2001.

[118] S. Picard-Fredin, "On the hyperfine structure of iodine: 1. how to calculate hyperfine transition energies", Tech. Rep. BIPM-90/5.

[119] S. Picard-Fredin and A. Razet, "On the hyperfine structure of iodine: 2. to calculate hyperfine constants on the basis of experimental data", Tech. Rep. BIPM-91/2.

[120] F. L. Hong and J. Ishikawa, "Hyperfine structures of the R(122) 35-0 and P(84) 33-0 transitions of $^{127}I_2$ near 532 nm", Opt. Commun., vol. 183, pp. 101, 2000.

[121] Y. R. Lin, S. Picard, T. L. Huang, and J. T. Shy, "New hyperfine structures of iodine molecule near 532 nm".

[122] C. S. Edwards, G. P. Barwood, P. Gill, F. RodriguezLlorente, and W. R. C. Rowley, "Frequency-stabilised diode lasers in the visible region using doppler-free iodine spectra", Opt. Commun., vol. 132, no. 1-2, pp. 94, 1996.

[123] C. S. Edwards, G. P. Barwood, P. Gill, and W. R. C. Rowley, "A 633 nm iodine-stabilized diode-laser frequency standard", Metrologia, vol. 36, no. 1, pp. 41, 1999.

[124] A. Razet, J. Gagniere, and P. Juncar, "Hyperfine-structure analysis of the 33P (6-3) line of $^{127}I_2$ at 633 nm using a continuous-wave tunable dye-laser", Metrologia, vol. 30, no. 2, pp. 61, 1993.

[125] H. R. Simonsen, "Iodine-stabilized extended cavity diode laser at lambda=633 nm", IEEE Trans. Instrum. Meas., vol. 46, no. 2, pp. 141, 1997.

[126] A. Morinaga, K. Sugiyama, and N. Ito, "Hyperfine-structure of low-lying vibrational levels in the B-electronic state of molecular-iodine", J. Opt. Soc. Am. B, vol. 6, no. 9, pp. 1656, 1989.

[127] P. Gill and J. A. Clancy, "A microprocessor-controlled iodine-stabilized ion laser", J. Phys. E, vol. 21, no. 2, pp. 213, 1988.

[128] F. Bertinetto, P. Cordiale, S. Fontana, and G. B. Picotto, "Helium-neon lasers stabilized to iodine at 605-nm", IEEE Trans. Instrum. Meas., vol. 36, no. 2, pp. 609, 1987.

[129] W. Y. Cheng, J. T. Shy, and T. Lin, "A compact iodine-stabilized HeNe laser and crossover resonances at 543 nm", Opt. Commun., vol. 156, no. 1-3, pp. 170, 1998.

[130] V. Špirko and J. Blabla, "Nuclear-quadrupole coupling functions of the $^1\Sigma_g^+$ and $^3\Pi_{0u}^+$ states of molecular-iodine", J. Mol. Spectrosc., vol. 129, no. 1, pp. 59, 1988.

[131] W. S. Barney, C. M. Western, and K. C. Janda, "Measurement of the electronic wave function: Separated atom wave function analysis of the R-dependent hyperfine constants of the iodine monochloride A state", J. Chem. Phys., vol. 113, no. 17, pp. 7211, 2000.

[132] R. J. Le Roy, "LEVEL 7.5: A computer program for solving the radial Schrödinger equation for bound and quasibound levels", University of Waterloo Chemical Physics Research Report CP-655 (2002). The source code and manual for this program may be obtained from the "Computer Programs" link on the www site http://leroy.uwaterloo.ca.

[133] S. Gerstenkorn, P. Luc, and C. Amiot, "Analysis of the long range potential of iodine in the B $^3\Pi_{0u}^+$ state", J. Phys. (Paris), vol. 46, pp. 355, 1985.

[134] J. P. Pique, R. Bacis, M. Broyer, S. Churassy, and J. B. Koffend, "Calculation of the magnetic hyperfine interaction in the E and X state of iodine with the separated-atom theory", J. Chem. Phys., vol. 80, pp. 1390, 1984.

[135] P. J. Jewsbury, T. Ridley, K. P. Lawley, and R. J. Donovan, "Parity mixing in the valence states of I_2 probed by optical-optical double-resonance excitation of ion-pair states - characterization of a new ion-pair state, $H1_u(^3P_1)$, and a valence state, $c1_g$", J. Mol. Spectrosc., vol. 157, pp. 33, 1993.

[136] G. Herzberg, Molecular spectra and molecular structure, vol. I, Krieger, Malabar, 1989.

[137] M. D. Danyluk and G. W. King, "2 photon sequential absorption spectroscopy of iodine molecule", Chem. Phys., vol. 22, no. 1, pp. 59, 1977.

[138] T. Ishiwata, H. Ohtoshi, M. Sakaki, and I. Tanaka, "Spectroscopic study on the iodine molecule by a sequential 3-photon excitation", J. Chem. Phys., vol. 80, no. 4, pp. 1411, 1984.

[139] T. Ishiwata, A. Tokunaga, T. Shinzawa, and I. Tanaka, "An analysis of the F'(0_u^+) ion-pair state of I_2 by optical optical double-resonance", J. Mol. Spectrosc., vol. 117, no. 1, pp. 89, 1986.

[140] L. Chen, W. Y. Cheng, and J. Ye, "Hyperfine interactions and perturbation effects in the B0_u^+($^3\Pi_u$) state of $^{127}I_2$", J. Opt. Soc. Am. B, vol. 21, no. 4, pp. 820, 2004.

[141] L. S. Chen and J. Ye, "Extensive, high-resolution measurement of hyperfine interactions: precise investigations of molecular potentials and wave functions", Chem. Phys. Lett., vol. 381, no. 5-6, pp. 777, 2003.

[142] F. Martin, S. Churassy, R. Bacis, R. W. Field, and J. Vergès, "Long range behavior of the gerade states near the $^2p_{3/2}$+ $^2p_{3/2}$ iodine dissociation limit by laser-induced-fluorescence fourier-transform spectroscopy", J. Chem. Phys., vol. 79, no. 8, pp. 3725, 1983.

[143] C. Cohen-Tannoudji, J. Dupont-Roc, and G. Grynberg, Atom-photon interactions Basic process and applications, John Wiley Sones, New York, 1992.

[144] Jon T. Hougen, The calculation of rotational energy levels and rotational line intensities in diatomic moledcules, NBS Monograph 115. Nat. Bur. Stand., U.S. Department of Commerce, 1970.

[145] H. G. Kuhn, Atomic spectra, Academic Press, New York, 1969.

[146] R. Engleman, R. A. Keller, Jr., and B. A. Palmer, "Hyperfine structure and isotope shift of the 1.3-μm transition of ^{129}I", Appl. opt., vol. 19, pp. 2767, 1980.

[147] V. Jaccarino, J. G. King, R. A. Satten, and H. H. Stroke, "Hperfine structure of ^{127}I. Nuclear magentic octupole moment", Phys. Rev., vol. 94, pp. 1798L, 1954.

[148] R. J. Le Roy and G.T. Kraemer, "BCONT 2.0. computer program for calculating absorption coefficients, emission intensities or (golden rule) predissociation rates", University of Waterloo Chemical Physics Research Report CP-650 (2001). The source code and manual for this program may be obtained from the www site http://leroy.uwaterloo.ca.

[149] E. A. Pazyuk, A. V. Stolyarov, V. I. Pupyshev, N. F. Stepanov, S. Ya. Umanskii, and A. A. Buchachenko, "The I_2(B) predissociation by solving an inverse atoms-in-molecule problem", Molec. Phys., vol. 99, pp. 91, 2001.

[150] A. R. Edmonds, Angular Momentum in Quantum Mechanics, Princeton University Press, Princeton, New Jersey, 2nd edition, 1960.

[151] J. Y. Zeng, Quantum mechanics, vol. II, Science Press, Beijing, 1993.

Appendix A

Matrix Elements of the Hyperfine Hamiltonian

A.1 Tensorial Form of the Hyperfine Hamiltonian

The hyperfine Hamiltonian of iodine molecule can be formally written as

$$H_{hf} = H_{hf}(a) + H_{hf}(b) + H_{hf}(a,b), \tag{A.1}$$

where a and b label the two iodine nuclei, respectively, and $H_{hf}(a)$ $[H_{hf}(b)]$ and $H_{hf}(a,b)$ represent the nucleus-electron and nucleus-nucleus hyperfine interactions, respectively. The last term acts only on nuclear coordinates and thus cannot couple different electronic states. This last term is left out in the following discussion because only terms that can couple different electronic states are relevant to the second-order calculation of effective hyperfine parameters [16]. With the last term dropped, various multipole interactions in this Hamiltonian can be expressed in tensorial form [16, 44]:

$$\begin{aligned} H_{hf} &= \sum_{\beta=a,b} \sum_{k} \mathbf{Q}^k \left(\mathbf{I}_\beta\right) \cdot \mathbf{V}^k \left(e_\beta^L\right) \\ &= \sum_{\beta=a,b} \sum_{k} \sum_{q=-k}^{k} (-1)^q \, Q_q^k \left(\mathbf{I}_\beta\right) V_{-q}^k \left(e_\beta^L\right), \end{aligned} \tag{A.2}$$

where the rank-k spherical tensor operators $Q^k(\mathbf{I}_\beta)$ and $V^k(e_\beta^L)$ act on the nuclear spin $\mathbf{I}_\beta$ and the electronic degrees of freedom, respectively. By labeling e_β, the coordinates of the electrons, with a superscript L, we emphasize that the tensor operator $\mathbf{V}^k \left(e_\beta^L\right)$ acts on the coordinates of electrons expressed in the *laboratory* frame. Later in section A.3 we will explain the significance of making this seemingly redundant clarification.

In evaluating the matrix elements of H_{hf}, we choose a Hund's case c coupling scheme that is suitable for the dominance of a strong spin-orbit coupling in the iodine molecule at intermediate and large internuclear separations. At short internuclear separations such as $R <\sim 3$ Å for the electronic state B, a Hund's case a coupling scheme is more appropriate. As long as these short internuclear separations are barely sampled by the vibrational wave functions, the Hund's case c coupling scheme can still be used in the evaluation.

The basis wave function in the Hund's case c coupling scheme is denoted as

$$|\psi\rangle = |\Omega \upsilon J I F M_F\rangle \,, \tag{A.3}$$

where Ω is the projection of the total angular momentum $\mathbf{J}$ (nuclear spin excluded) onto the molecular axis connecting the two nuclei, υ the vibrational quantum number, I the total nuclear spin, $\mathbf{F} = \mathbf{I} + \mathbf{J}$, and M_F the projection of $\mathbf{F}$ onto a quantization axis.

Each rank-k component of H_{hf} is a scalar product of two commuting tensor operators:

$$H^k_{hf}(a) = \mathbf{Q}^k(\mathbf{I}_a) \cdot \mathbf{V}^k\left(e^L_a\right). \tag{A.4}$$

A direct application of (7.1.6) in reference [150] gives the matrix element of this component in terms of the reduced matrix elements of $\mathbf{Q}^k$ and $\mathbf{V}^k$ in the uncoupled scheme[1] :

$$\begin{aligned}
&\langle \Omega' \upsilon' J' I'; F' M'_F | \, H^k_{hf}(a) \, | \Omega \upsilon J I; F M_F \rangle \\
&= \langle \Omega' \upsilon' J' I'; F' M'_F | \left[\mathbf{Q}^k(\mathbf{I}_a) \cdot \mathbf{V}^k\left(e^L_a\right) \right] | \Omega \upsilon J I; F M_F \rangle \qquad \text{(A.5)} \\
&= \delta_{FF'} \delta_{M_F M'_F} (-1)^{J+I'+F} \left\{ \begin{array}{ccc} F & I' & J' \\ k & J & I \end{array} \right\} \langle I' \| \, Q^k(\mathbf{I}_a) \, \| I \rangle \, \langle \Omega' \upsilon' J' \| \, V^k\left(e^L_a\right) \| \Omega \upsilon J \rangle \,,
\end{aligned} \tag{A.6}$$

[1] Here the uncoupled scheme means that the nuclear spin $\mathbf{I}$ is decoupled from the angular momentum $\mathbf{J}$.

where $\langle I' \| Q^k(\mathbf{I}_a) \| I \rangle$ and $\langle \Omega' \upsilon' J' \| V^k\left(e_a^L\right) \| \Omega \upsilon J \rangle$ are reduced nuclear and electronic matrix elements, respectively. In the following two sections we will show the evaluations of these two reduced matrix elements.

A.2 Reduced Nuclear Matrix Element

The reduced nuclear matrix element $\langle I' \| Q^k(\mathbf{I}_a) \| I \rangle$ in equation A.6 are expressed in the coupled scheme $\mathbf{I} = \mathbf{I}_a + \mathbf{I}_b$. We rewrite this matrix element in the uncoupled scheme $\mathbf{I}_a$ so that it can be related to the nuclear multipole moments such as the magnetic dipole and electrical quadrupole moments, which in turn are linked to the experimentally determined atomic hyperfine constants. By using (7.1.7) in reference [150], $\langle I' \| Q^k(\mathbf{I}_a) \| I \rangle$ is rewritten in the uncoupled scheme:

$$\begin{aligned}\langle I' \| Q^k(\mathbf{I}_a) \| I \rangle &= \langle I_a I_a; I' \| Q^k(\mathbf{I}_a) \| I_a I_a; I \rangle \\ &= (-1)^{2I_a+I+k} \sqrt{(2I+1)(2I'+1)} \begin{Bmatrix} I_a & I' & I_a \\ I & I_a & k \end{Bmatrix} \langle I_a \| Q^k(\mathbf{I}_a) \| I_a \rangle .\end{aligned} \tag{A.7}$$

Note that in above equation we have put $I_a = I_b$. Using the Winger-Eckart theorem, the reduced matrix element $\langle I_a \| Q^k(\mathbf{I}_a) \| I_a \rangle$ for each nucleus can be related to the matrix element of $Q_0^k(\mathbf{I}_a)$ evaluated with a specific nuclear wave function $|I_a M_{I_a} = I_a\rangle$, i.e.,

$$\begin{aligned}\langle I_a \| Q^k(\mathbf{I}_a) \| I_a \rangle &= \frac{C_k}{\begin{pmatrix} I_a & k & I_a \\ -I_a & 0 & I_a \end{pmatrix}}, \\ C_k &= \langle I_a I_a | Q_0^k(\mathbf{I}_a) | I_a I_a \rangle ,\end{aligned} \tag{A.8}$$

where the atomic matrix element $C_k = \langle I_a I_a | Q_0^k(\mathbf{I}_a) | I_a I_a \rangle$ can be related to the corresponding atomic hyperfine constants. For $k = 1$, $C_1 = \mu_n g I_a$ is the nuclear

magnetic dipole moment with μ_n being the nuclear magneton and g the Landé factor for the iodine nucleus. For $k = 2$, $C_2 = \frac{1}{2}eQ_{I_a}$ is the nuclear electric quadrupole moment with e being the proton charge and Q_{I_a} defined as

$$Q_{I_a} = e \left\langle I_a, M_{I_a} = I_a \right| \sum_p \left(3z_p^2 - r_p^2\right) \left| I_a, M_{I_a} = I_a \right\rangle, \tag{A.9}$$

where z_p and r_p refer to the coordinates of the protons p in the iodine nucleus.

Plugging equation A.8 into equation A.7, the reduced matrix element $\langle I' \| Q^k(\mathbf{I}_a) \| I \rangle$ in equation A.6 is evaluated as

$$\langle I' \| Q^k(\mathbf{I}_a) \| I \rangle = (-1)^{2I_a+I+k} \sqrt{(2I+1)(2I'+1)} \times \frac{C_k}{\begin{pmatrix} I_a & k & I_a \\ -I_a & 0 & I_a \end{pmatrix}} \begin{Bmatrix} I_a & I' & I_a \\ I & I_a & k \end{Bmatrix}. \tag{A.10}$$

A.3 Reduced Electronic Matrix Element

We proceed to evaluate the reduced matrix element $\langle \Omega' \upsilon' J' \| V^k\left(e_a^L\right) \| \Omega \upsilon J \rangle$ in equation A.6. Similar to the procedure used in the evaluation of the reduced matrix element $\langle I_a \| Q^k(\mathbf{I}_a) \| I_a \rangle$, we first relate $\langle \Omega' \upsilon' J' \| V^k\left(e_a^L\right) \| \Omega \upsilon J \rangle$ to a specific matrix element $\langle \Omega' \upsilon' J' M_J' | V_{-q}^k\left(e_a^L\right) | \Omega \upsilon J M_J \rangle$ by applying the Winger-Eckart theorem:

$$\begin{aligned} &\langle \Omega' \upsilon' J' M_J' | V_{-q}^k\left(e_a^L\right) | \Omega \upsilon J M_J \rangle \\ &= (-1)^{J'-M_J'} \begin{pmatrix} J' & k & J \\ -M_J' & -q & M_J \end{pmatrix} \langle \Omega' \upsilon' J' \| V^k\left(e_a^L\right) \| \Omega \upsilon J \rangle \end{aligned} \tag{A.11}$$

The evaluation of matrix element $\langle \Omega' \upsilon' J' M_J' | V_{-q}^k\left(e_a^L\right) | \Omega \upsilon J M_J \rangle$ involves the averaging of $V_{-q}^k\left(e_a^L\right)$ over the electronic motion, the molecular rotation, and the molecular vibration. Note that the tensor operator $\mathbf{V}^k\left(e_a^L\right)$ acts on the coordinates of electrons expressed in the *laboratory* frame, which ensures that the hyperfine Hamiltonian can

directly describe the hyperfine spectrum observed in the laboratory frame. This explicit choice of the coordinate system poses no difficulty for the averaging over the molecular rotation and vibration. However, the averaging over the electronic motion demands a special treatment because the electronic wave function obtained in the Born-Oppenheimer approximation is expressed in the *molecular* frame (body fixed coordinate system). To work with the Born-Oppenheimer electronic wave function, one can first use the tensor operator $\mathbf{V}^k(e_a)$ expressed in the molecular frame, and then adopts an active rotation to transform this operator to the laboratory frame, i.e.,

$$V_{-q}^k\left(e_a^L\right) = \sum_{q'} D_{-qq'}^{(k)*}(\omega)\, V_{q'}^k(e_a)\,, \tag{A.12}$$

where $D_{-qq'}^{(k)*}(\omega)$ is the rotation operator (Wigner D function), ω represents the three Eular angles α, β, and γ, and e_a represents the electronic coordinates in the molecular frame. The operator $V_{q'}^k(e_a)$ and the electronic wave function $|\Omega\rangle$, both expressed in the molecular frame, are used to perform the averaging over the electronic motion in the molecular frame. The rotational wave function can also be written in terms of the Wigner D function [151]:

$$|J\Omega M_J\rangle = \sqrt{\frac{2J+1}{8\pi^2}} D_{M_J\Omega}^{(J)*}(\omega)\,. \tag{A.13}$$

Using equations A.12 and A.13, we can explicitly perform the averaging over the molecular rotation:

$$\begin{aligned}
&\langle \Omega' \upsilon' J' M_J'|\, V_{-q}^k\left(e_a^L\right) |\Omega \upsilon J M_J\rangle \\
&= \sum_{q'} (-1)^{q+q'} \frac{\sqrt{(2J+1)(2J'+1)}}{8\pi^2} \langle \Omega' \upsilon_{J'}'|\, V_{q'}^k(e_a)\, |\Omega \upsilon_J\rangle \times \\
&\int d\omega D_{M_J\Omega}^{(J)*}(\omega)\, D_{q-q'}^{(k)}(\omega)\, D_{M_J'\Omega'}^{(J')}(\omega)\,.
\end{aligned} \tag{A.14}$$

The integral of the product of three Wigner D functions has been evaluated in reference [151]:

$$\int d\omega D^{(J)*}_{M_J\Omega}(\omega)\, D^{(k)}_{q-q'}(\omega)\, D^{(J')}_{M'_J\Omega'}(\omega)$$
$$= \delta_{q,M_J-M'_J}\delta_{q',\Omega'-\Omega}(-1)^{\Omega+k+\Delta J+M_J}\, 8\pi^2 \begin{pmatrix} k & J' & J \\ q' & -\Omega' & \Omega \end{pmatrix} \begin{pmatrix} J' & k & J \\ -M'_J & -q & M_J \end{pmatrix}, \tag{A.15}$$

where $\Delta J = J' - J$, $\Delta\Omega = \Omega' - \Omega$, and $\Delta M_J = M_J - M'_J$. Inserting integral A.15 into equation A.14 gives

$$\begin{aligned} &\langle \Omega' \upsilon' J' M'_J | \, V^k_{-q}\left(e^L_a\right) | \Omega \upsilon J M_J \rangle \\ &= (-1)^{k+\Omega'+\Delta J+M'_J} \sqrt{(2J+1)(2J'+1)} \times \\ &\begin{pmatrix} k & J' & J \\ \Delta\Omega & -\Omega' & \Omega \end{pmatrix} \begin{pmatrix} J' & k & J \\ -M'_J & -q & M_J \end{pmatrix} \langle \Omega' \upsilon'_{J'} | \, V^k_{\Delta\Omega}(e_a) | \Omega \upsilon_J \rangle . \end{aligned} \tag{A.16}$$

The matrix element $\langle \Omega' \upsilon'_{J'} | \, V^k_{\Delta\Omega}(e_a) | \Omega \upsilon_J \rangle$ encapsulates the averaging over the vibration and the electronic motion. Combining equations A.11 and A.16, the reduced matrix element $\langle \Omega' \upsilon' J' \| \, V^k\left(e^L_a\right) \| \Omega \upsilon J \rangle$ in equation A.6 is evaluated as

$$\begin{aligned} &\langle \Omega' \upsilon' J' \| \, V^k\left(e^L_a\right) \| \Omega \upsilon J \rangle \\ &= (-1)^{k+\Omega'+J} \sqrt{(2J+1)(2J'+1)} \begin{pmatrix} k & J' & J \\ \Delta\Omega & -\Omega' & \Omega \end{pmatrix} \langle \Omega' \upsilon'_{J'} | \, V^k_{\Delta\Omega}(e_a) | \Omega \upsilon_J \rangle . \end{aligned} \tag{A.17}$$

A.4 Matrix Elements of the Hyperfine Hamiltonian

The final form of the matrix element $\langle \Omega' \upsilon' J' I'; FM_F | \, H^k_{hf}(a) \, | \Omega \upsilon J I; FM_F \rangle$ is obtained by substituting equations A.10 and A.17 into equation A.6, which gives

$$\begin{aligned}
&\langle \Omega' \upsilon' J' I'; FM_F | \, H^k_{hf}(a) \, | \Omega \upsilon J I; FM_F \rangle \\
&= (-1)^{F+k+2I_a+\Delta I+\Delta J+\Omega'} \sqrt{(2J'+1)(2J+1)(2I'+1)(2I+1)} \times \\
&\frac{C_k}{\begin{pmatrix} k & I_a & I_a \\ 0 & I_a & -I_a \end{pmatrix}} \begin{Bmatrix} k & I_a & I_a \\ I_a & I' & I \end{Bmatrix} \begin{pmatrix} J' & k & J \\ -\Omega' & \Delta\Omega & \Omega \end{pmatrix} \begin{Bmatrix} J' & k & J \\ I & F & I' \end{Bmatrix} \times \\
&\langle \Omega' \upsilon'_{J'} | \, V^k_{\Delta\Omega}(a) \, | \Omega \upsilon_J \rangle \,, \qquad \text{(A.18)}
\end{aligned}$$

where C_k is given in equation A.8. As reference [16], we define a function $f_k(a, \Omega', \upsilon'_{J'}, \Omega, \upsilon_J)$ that encapsulates the averaging over the electronic motion in the molecular frame and the molecular vibration in the laboratory frame:

$$f_k(a, \Omega', \upsilon'_{J'}, \Omega, \upsilon_J) = (-1)^{\Omega'} \frac{C_k}{\begin{pmatrix} k & I_a & I_a \\ 0 & I_a & -I_a \end{pmatrix}} \times \langle \Omega' \upsilon'_{J'} | \, V^k_{\Delta\Omega}(a) \, | \Omega \upsilon_J \rangle \,. \qquad \text{(A.19)}$$

Then the matrix element $\langle \Omega' \upsilon' J' I'; FM_F | \, H^k_{hf}(a) \, | \Omega \upsilon J I; FM_F \rangle$ can be expressed as

$$\begin{aligned}
&\langle \Omega' \upsilon' J' I'; FM_F | \, H^k_{hf}(a) \, | \Omega \upsilon J I; FM_F \rangle \\
&= (-1)^{F+k+2I_a+\Delta I+\Delta J} \sqrt{(2J'+1)(2J+1)(2I'+1)(2I+1)} \times \\
&\begin{pmatrix} J' & k & J \\ -\Omega' & \Delta\Omega & \Omega \end{pmatrix} \begin{Bmatrix} J' & k & J \\ I & F & I' \end{Bmatrix} \begin{Bmatrix} k & I_a & I_a \\ I_a & I' & I \end{Bmatrix} \times \\
&f_k(a, \Omega', \upsilon'_{J'}, \Omega, \upsilon_J) \,. \qquad \text{(A.20)}
\end{aligned}$$

This expression and equation A.19 can be directly compared with those given in reference [16] for a Hund's case a coupling scheme.

Appendix B

Hyperfine Spectra and Effective Hyperfine Parameters for 79 B-state levels ($\upsilon' = 42 - 70$, $\lambda = 500 - 517$ nm)

This appendix supplies spectroscopic data for all measured I_2 rovibrational transitions in the wavelength range $500 - 517$ nm. For each transition, the hyperfine splittings and experimental conditions are summarized in a table, together with the fitted B-state effective hyperfine parameters. The list of table at the beginning of this thesis can be used to locate a specific transition.

The hyperfine spectrum of each rovibrational transition is fitted to a four-term effective Hamiltonian [16]

$$H_{hf,eff} = H_{eqQ} + H_{SR} + H_{TSS} + H_{SSS}, \tag{B.1}$$

where the four leading terms on the right-hand side represent major contributions from nuclear electric quadrupole, spin-rotation, tensorial spin-spin, and scalar spin-spin interactions, respectively. The four B-state effective hyperfine parameters, eqQ_B, C_B, d_B, and δ_B are derived from the fit. In the fit, the four hyperfine parameters for the X ground state are determined by [42]

$$\begin{aligned} eqQ_X[\text{MHz}] = &-2452.2916 - 0.542(\upsilon'' + \frac{1}{2}) \\ &+ 0.4535 \times 10^{-1}(\upsilon'' + \frac{1}{2})^2 \\ &- 0.1927 \times 10^{-3}(\upsilon'' + \frac{1}{2})^2 J''(J''+1) \\ &+ 0.694 \times 10^{-5}(\upsilon'' + \frac{1}{2}) J''(J''+1) \end{aligned} \tag{B.2}$$

and

$$C_X[\mathrm{MHz}] = 1.9245 + 0.01356(\upsilon'' + \frac{1}{2}) - \frac{15098}{E(\upsilon'')[\mathrm{cm}^{-1}] - 12340}, \qquad \text{(B.3)}$$

respectively, and the values for d_B and δ_B are fixed to 1.524 and 3.705 kHz, respectively.

For transitions P(69) 58-0, P(84) 60-0, P(77) 60-0, and P(63) 70-0, their hyperfine levels in the B state are altered considerably by the strong perturbation from the $1_g(^1\Pi_g)$ state. Therefore hyperfine spectra at these transitions cannot be fitted to the above-mentioned effective Hamiltonian. In this case, the spectrograms for the relevant transitions are also given in addition to their hyperfine splittings.

B.1 P(10) 42-0

Table B.1: Hyperfine spectrum recorded at P(10) 42-0. Pump power: 2.4 mW, probe power: 0.22 mW, time constant of lock-in amplifier: 100 ms, cold-finger temperature: -2.28°C (vapor pressure: 3.3 Pa).

a	**F′**	Measurement (MHz)	Calculation (MHz)	Mea.-Cal. (MHz)
1	9	−484.613	−484.621	0.007
2	5	−244.156	−244.152	−0.004
3	10	−228.548	−228.536	−0.012
4	8	−178.269	−178.277	0.008
5	13	−168.798	−168.800	0.002
6	6	−135.256	−135.257	0.001
7	7	−87.017	−87.018	0.001
8	11	−61.017	−61.011	−0.006
9	12	0	−	−
10	9	71.654	71.664	−0.010
13	10	246.617	246.609	0.008
14	11	263.601	263.605	−0.005
15	9	359.347	359.343	0.004

Fitted hyperfine parameters for the excited state B

standard dev. (MHz)	0.0076
eqQ_B (MHz)	$-557.119(20)^{\ddagger}$
C_B (MHz)	0.176138(96)
d_B (MHz)	−0.08916(86)
δ_B (MHz)	−0.00520(85)

Hyperfine parameters for the ground state X used in th fit

eqQ_X (MHz)*	−2452.57
C_X (MHz)*	0.00315478
d_X (MHz)†	0.001524
δ_X (MHz)†	0.003705

* eqQ_X and C_X are determined by equations B.2 and B.3, respectively.

†d_X and δ_X are fixed in the fit to 1.524 and 3.705 kHz, respectively.

‡Quoted uncertainties (1σ) are estimated from the standard deviation of the fit.

B.2 P(19) 42-0

Table B.2: Hyperfine spectrum recorded at P(19) 42-0. Pump power: 2.7 mW, probe power: 0.2 mW, time constant of lock-in amplifier: 30 ms, cold-finger temperature: -2.28°C (vapor pressure: 3.3 Pa).

a	**F′**	Measurement (MHz)	Calculation (MHz)	Mea.-Cal. (MHz)
1	13	−621.512	−621.452	−0.059
2	18	−564.180	−564.166	−0.014
3	23	−513.899	−513.891	−0.008
4	14	−387.729	−387.773	0.044
5	19	−292.759	−292.792	0.033
6	17	−269.423	−269.458	0.034
7	15	−208.705	−208.718	0.013
8	22	−184.469	−184.475	0.007
9	16	−155.325	−155.347	0.022
10	20	−131.746	−131.754	0.008
11	21	−109.967	−109.986	0.019
12	15	−58.389	−58.419	0.030
13	18	0	–	–

Fitted hyperfine parameters for the excited state B

standard dev. (MHz)	0.033
eqQ_B (MHz)	−556.988(66)‡
C_B (MHz)	0.1766(17)
d_B (MHz)	−0.0921(43)
δ_B (MHz)	−0.0016(39)

Hyperfine parameters for the ground state X used in th fit

eqQ_X (MHz)*	−2452.62
C_X (MHz)*	0.00315478
d_X (MHz)†	0.001524
δ_X (MHz)†	0.003705

* eqQ_X and C_X are determined by equations B.2 and B.3, respectively.

†d_X and δ_X are fixed in the fit to 1.524 and 3.705 kHz, respectively.

‡Quoted uncertainties (1σ) are estimated from the standard deviation of the fit.

B.3 R(30) 42-0

Table B.3: Hyperfine spectrum recorded at R(30) 42-0. Time constant of lock-in amplifier: 30 ms, cold-finger temperature: -2.28°C (vapor pressure: 3.3 Pa).

a	**F′**	Measurement (MHz)	Calculation (MHz)	Mea.-Cal. (MHz)
1	31	−566.231	−566.197	−0.034
2	27	−316.504	−316.492	−0.012
3	32	−287.001	−287.018	0.016
4	30	−278.416	−278.443	0.027
5	35	−250.426	−250.443	0.017
6	28	−180.707	−180.707	0.001
7	29	−156.209	−156.219	0.010
8	33	−128.855	−128.861	0.006
9	34	−103.198	−103.175	−0.024
10	31	0	−	−
13	32	159.272	159.300	−0.029
14	33	167.739	167.736	0.003
15	31	284.698	284.706	−0.008

Fitted hyperfine parameters for the excited state B

standard dev. (MHz)	0.021
eqQ_B (MHz)	$-557.184(44)^{\ddagger}$
C_B (MHz)	0.177751(85)
d_B (MHz)	−0.0946(22)
δ_B (MHz)	0.0099(33)

Hyperfine parameters for the ground state X used in th fit

eqQ_X (MHz)*	−2452.73
C_X (MHz)*	0.00315478
d_X (MHz)†	0.001524
δ_X (MHz)†	0.003705

* eqQ_X and C_X are determined by equations B.2 and B.3, respectively.

†d_X and δ_X are fixed in the fit to 1.524 and 3.705 kHz, respectively.

‡Quoted uncertainties (1σ) are estimated from the standard deviation of the fit.

B.4 R(41) 42-0

Table B.4: Hyperfine spectrum recorded at R(41) 42-0. Pump power: 2.2 mW, probe power: 0.26 mW, time constant of lock-in amplifier: 30 ms, cold-finger temperature: -2.28°C (vapor pressure: 3.3 Pa).

a	**F′**	Measurement (MHz)	Calculation (MHz)	Mea.-Cal. (MHz)
1	37	−437.984	−438.007	0.023
2	42	−380.721	−380.734	0.013
3	47	−326.979	−326.971	−0.008
4	38	−171.674	−171.721	0.046
7	46	−26.633	−26.631	−0.002
8	39	0	−	−
9	40	26.674	26.670	0.005
10	44	60.643	60.653	−0.010
11	45	79.270	79.277	−0.007
12	39	134.667	134.661	0.005
13	42	186.006	186.001	0.004
14	45	242.928	242.921	0.006
15	40	273.458	273.447	0.011
16	41	309.117	309.089	0.028
17	43	342.946	342.937	0.009
18	44	377.681	377.671	0.010
19	41	447.497	447.496	0.001
20	42	466.190	466.202	−0.012
21	43	490.582	490.571	0.011

Fitted hyperfine parameters for the excited state B

standard dev. (MHz)	0.0173732
eqQ_B (MHz)	$-557.553(30)^{\ddagger}$
C_B (MHz)	0.179178(24)
d_B (MHz)	−0.0929(20)
δ_B (MHz)	−0.0003(16)

Hyperfine parameters for the ground state X used in th fit

eqQ_X (MHz)*	−2452.88
C_X (MHz)*	0.00315478
d_X (MHz)†	0.001524
δ_X (MHz)†	0.003705

* eqQ_X and C_X are determined by equations B.2 and B.3, respectively.

†d_X and δ_X are fixed in the fit to 1.524 and 3.705 kHz, respectively.

‡Quoted uncertainties (1σ) are estimated from the standard deviation of the fit.

B.5 R(49) 42-0

Table B.5: Hyperfine spectrum recorded at R(49) 42-0. Pump power: 2.6 mW, probe power: 0.26 mW, time constant of lock-in amplifier: 30 ms, cold-finger temperature: -2.28°C (vapor pressure: 3.3 Pa).

a	**F′**	Measurement (MHz)	Calculation (MHz)	Mea.-Cal. (MHz)
1	45	−576.746	−576.750	0.003
2	50	−515.333	−515.291	−0.042
3	55	−456.864	−456.856	−0.007
4	46	−304.832	−304.839	0.007
7	54	−161.791	−161.812	0.021
8	47	−134.469	−134.513	0.045
9	48	−110.056	−110.105	0.049
10	52	−70.926	−70.9601	0.034
11	53	−52.322	−52.3213	−0.001
12	47	0	−	−
13	50	51.750	51.7212	0.029
14	53	107.133	107.151	−0.018
15	48	142.691	142.721	−0.030
16	49	175.505	175.507	−0.001
17	51	209.070	209.088	−0.018
18	52	240.809	240.847	−0.038
20	50	332.847	332.837	0.011
21	51	355.802	355.772	0.029

Fitted hyperfine parameters for the excited state B

standard dev. (MHz)	0.030
eqQ_B (MHz)	$-557.612(50)^{\ddagger}$
C_B (MHz)	0.180487(46)
d_B (MHz)	−0.0915(25)
δ_B (MHz)	0.0051(23)

Hyperfine parameters for the ground state X used in th fit

eqQ_X (MHz)*	−2453.01
C_X (MHz)*	0.00315478
d_X (MHz)†	0.001524
δ_X (MHz)†	0.003705

* eqQ_X and C_X are determined by equations B.2 and B.3, respectively.

†d_X and δ_X are fixed in the fit to 1.524 and 3.705 kHz, respectively.

‡Quoted uncertainties (1σ) are estimated from the standard deviation of the fit.

B.6 P(13) 43-0

Table B.6: Hyperfine spectrum recorded at P(13) 43-0. Pump power: 2.2 mW, probe power: 0.23 mW, time constant of lock-in amplifier: 30 ms, cold-finger temperature: -2.28°C (vapor pressure: 3.3 Pa).

a	**F′**	Measurement (MHz)	Calculation (MHz)	Mea.-Cal. (MHz)
1	7	−567.371	−567.380	0.009
2	12	−495.511	−495.509	−0.003
3	17	−435.604	−435.603	−0.001
4	8	−359.570	−359.561	−0.008
5	13	−232.354	−232.373	0.019
6	11	−194.828	−194.829	0.001
7	9	−180.603	−180.605	0.002
8	10	−96.926	−96.907	−0.020
9	16	−85.893	−85.895	0.002
11	15	−41.650	−41.634	−0.016
12	9	0	−	−
13	12	64.104	64.108	−0.004
15	11	151.780	151.788	−0.008
16	15	181.156	181.145	0.011
17	13	225.322	225.331	−0.009
20	12	322.024	322.022	0.003
21	13	381.739	381.731	0.008

Fitted hyperfine parameters for the excited state B

standard dev. (MHz)	0.011
eqQ_B (MHz)	−558.613(18)‡
C_B (MHz)	0.190361(78)
d_B (MHz)	−0.09899(62)
δ_B (MHz)	−0.00083(56)

Hyperfine parameters for the ground state X used in th fit

eqQ_X (MHz)*	−2452.59
C_X (MHz)*	0.00315478
d_X (MHz)†	0.001524
δ_X (MHz)†	0.003705

* eqQ_X and C_X are determined by equations B.2 and B.3, respectively.
†d_X and δ_X are fixed in the fit to 1.524 and 3.705 kHz, respectively.
‡Quoted uncertainties (1σ) are estimated from the standard deviation of the fit.

B.7 P(25) 43-0

Table B.7: Hyperfine spectrum recorded at P(25) 43-0. Pump power: 2.6 - 3.1 mW, probe power: 0.2 mW, time constant of lock-in amplifier: 100 ms, cold-finger temperature: -2.28°C (vapor pressure: 3.3 Pa).

a	**F′**	Measurement (MHz)	Calculation (MHz)	Mea.-Cal. (MHz)
1	19	−736.133	−736.128	−0.005
2	24	−681.548	−681.563	0.015
3	29	−632.257	−632.259	0.002
4	20	−488.441	−488.449	0.008
5	25	−405.369	−405.361	−0.008
6	23	−391.711	−391.697	−0.014
9	22	−272.136	−272.126	−0.010
10	26	−246.431	−246.428	−0.003
11	27	−226.166	−226.163	−0.003
12	21	−171.678	−171.677	−0.001
13	24	−116.559	−116.559	0.000
16	23	0	–	–
17	25	40.811	40.804	0.007
20	24	158.852	158.863	−0.011

Fitted hyperfine parameters for the excited state B

standard dev. (MHz)	0.0094
eqQ_B (MHz)	$-558.823(15)^{\ddagger}$
C_B (MHz)	0.191161(39)
d_B (MHz)	−0.1009(12)
δ_B (MHz)	0.0025(11)

Hyperfine parameters for the ground state X used in th fit

eqQ_X (MHz)*	−2452.67
C_X (MHz)*	0.00315478
d_X (MHz)†	0.001524
δ_X (MHz)†	0.003705

* eqQ_X and C_X are determined by equations B.2 and B.3, respectively.

†d_X and δ_X are fixed in the fit to 1.524 and 3.705 kHz, respectively.

‡Quoted uncertainties (1σ) are estimated from the standard deviation of the fit.

B.8 R(27) 43-0

Table B.8: Hyperfine spectrum recorded at R(27) 43-0: 2.6 - 3.1 mW, probe power: 0.2 mW, time constant of lock-in amplifier: 100 ms, cold-finger temperature: -2.28°C (vapor pressure: 3.3 Pa).

a	**F′**	Measurement (MHz)	Calculation (MHz)	Mea.-Cal. (MHz)
1	23	0	–	–
3	33	108.536	108.534	0.002
4	24	250.629	250.638	−0.009
5	29	334.396	334.383	0.013
6	27	345.334	345.333	0.002
7	32	422.632	422.644	−0.013
8	25	427.231	427.249	−0.018
10	30	493.499	493.507	−0.008
13	28	622.000	622.021	−0.021
16	27	739.288	739.279	0.009
17	29	779.734	779.724	0.011
18	30	826.140	826.124	0.016
19	27	878.055	878.058	−0.003
20	28	898.204	898.203	0.002
21	29	930.144	930.145	−0.000

Fitted hyperfine parameters for the excited state B

standard dev. (MHz)	0.012
eqQ_B (MHz)	$-558.662(26)^{\ddagger}$
C_B (MHz)	0.191579(37)
d_B (MHz)	−0.0980(17)
δ_B (MHz)	0.0006(13)

Hyperfine parameters for the ground state X used in th fit

eqQ_X (MHz)**	−2452.69
C_X (MHz)**	0.00315478
d_X (MHz)†	0.001524
δ_X (MHz)†	0.003705

**eqQ_X and C_X are determined by equations B.2 and B.3, respectively.

†d_X and δ_X are fixed in the fit to 1.524 and 3.705 kHz, respectively.

‡Quoted uncertainties (1σ) are estimated from the standard deviation of the fit.

B.9 P(38) 43-0

Table B.9: Hyperfine spectrum recorded at P(38) 43-0. Pump power: 2 - 3 mW, probe power: 0.18 mW, time constant of lock-in amplifier: 100 ms, cold-finger temperature: -2.28°C (vapor pressure: 3.3 Pa).

a	**F′**	Measurement (MHz)	Calculation (MHz)	Mea.-Cal. (MHz)
1	37	0	–	–
2	33	245.633	245.635	−0.001
5	41	319.675	319.673	0.003
7	35	407.707	407.698	0.008
8	39	440.260	440.256	0.004
9	40	462.861	462.864	−0.003
10	37	566.241	566.243	−0.002
11	35	684.788	684.794	−0.006
12	36	691.039	691.040	−0.001
13	38	724.433	724.436	−0.003
14	39	733.674	733.679	−0.005
15	37	850.653	850.644	0.009

Fitted hyperfine parameters for the excited state B

standard dev. (MHz)	0.0059
eqQ_B (MHz)	$-558.565(12)^{\ddagger}$
C_B (MHz)	0.192839(21)
d_B (MHz)	−0.10109(69)
δ_B (MHz)	−0.00001(81)

Hyperfine parameters for the ground state X used in th fit

eqQ_X (MHz)*	−2452.83
C_X (MHz)*	0.00315478
d_X (MHz)†	0.001524
δ_X (MHz)†	0.003705

* eqQ_X and C_X are determined by equations B.2 and B.3, respectively.

†d_X and δ_X are fixed in the fit to 1.524 and 3.705 kHz, respectively.

‡Quoted uncertainties (1σ) are estimated from the standard deviation of the fit.

B.10 R(40) 43-0

Table B.10: Hyperfine spectrum recorded at R(40) 43-0. Pump power: 2 - 3 mW, probe power: 0.18 mW, time constant of lock-in amplifier: 100 ms, cold-finger temperature: -2.28°C (vapor pressure: 3.3 Pa).

a	**F′**	Measurement (MHz)	Calculation (MHz)	Mea.-Cal. (MHz)
1	41	−383.822	−383.823	0.001
5	45	−61.284	−61.286	0.002
6	38	0	–	–
7	39	22.442	22.440	0.002
8	43	58.002	58.004	−0.002
9	44	80.828	80.830	−0.002
10	41	182.464	182.468	−0.004
11	39	299.737	299.729	0.009
12	40	306.832	306.823	0.009
13	42	341.128	341.126	0.002
14	43	351.060	351.057	0.002
15	41	466.834	466.845	−0.011

Fitted hyperfine parameters for the excited state B

standard dev. (MHz)	0.0064
eqQ_B (MHz)	$-558.604(17)^{\ddagger}$
C_B (MHz)	0.193497(14)
d_B (MHz)	−0.10303(86)
δ_B (MHz)	0.00034(86)

Hyperfine parameters for the ground state X used in th fit

eqQ_X (MHz)*	−2452.86
C_X (MHz)*	0.00315478
d_X (MHz)†	0.001524
δ_X (MHz)†	0.003705

* eqQ_X and C_X are determined by equations B.2 and B.3, respectively.

†d_X and δ_X are fixed in the fit to 1.524 and 3.705 kHz, respectively.

‡Quoted uncertainties (1σ) are estimated from the standard deviation of the fit.

B.11 R(63) 43-0

Table B.11: Hyperfine spectrum recorded at R(63) 43-0. Pump power: 2 - 3 mW, probe power: 0.18 mW, time constant of lock-in amplifier: 100 ms, cold-finger temperature: -2.28°C (vapor pressure: 3.3 Pa).

a	**F′**	Measurement (MHz)	Calculation (MHz)	Mea.-Cal. (MHz)
1	59	−585.205	−585.200	−0.004
2	64	−508.804	−508.795	−0.009
3	69	−435.562	−435.565	0.002
4	60	−305.174	−305.192	0.018
5	63	−233.362	−233.369	0.007
6	65	−217.508	−217.522	0.014
7	68	−148.841	−148.831	−0.010
8	61	−134.901	−134.895	−0.006
9	62	−110.741	−110.719	−0.022
10	66	−57.767	−57.762	−0.005
11	67	−37.348	−37.354	0.006
12	61	0	−	−
13	64	57.826	57.823	0.003
14	67	117.403	117.402	0.001
15	62	148.618	148.614	0.004
16	63	180.107	180.090	0.016
17	65	217.406	217.400	0.006
18	66	247.556	247.550	0.006
19	63	319.064	319.063	0.001
20	64	339.379	339.388	−0.010
21	65	362.791	362.803	−0.012

Fitted hyperfine parameters for the excited state B

standard dev. (MHz)	0.011
eqQ_B (MHz)	$-559.456(16)^{\ddagger}$
C_B (MHz)	0.198545(12)
d_B (MHz)	−0.10629(90)
δ_B (MHz)	0.00234(85)

Hyperfine parameters for the ground state X used in th fit

eqQ_X (MHz)*	−2453.31
C_X (MHz)*	0.00315478
d_X (MHz)†	0.001524
δ_X (MHz)†	0.003705

* eqQ_X and C_X are determined by equations B.2 and B.3, respectively.

†d_X and δ_X are fixed in the fit to 1.524 and 3.705 kHz, respectively.

‡Quoted uncertainties (1σ) are estimated from the standard deviation of the fit.

B.12 R(21) 45-0

Table B.12: Hyperfine spectrum recorded at R(21) 45-0. Pump power: 1.4 - 1.7 mW, probe power: 0.14 mW, time constant of lock-in amplifier: 100 ms, cold-finger temperature: -2.28°C (vapor pressure: 3.3 Pa).

a	**F′**	Measurement (MHz)	Calculation (MHz)	Mea.-Cal. (MHz)
1	17	−238.548	−238.553	0.005
2	22	−175.128	−175.125	−0.003
3	27	−118.645	−118.640	−0.005
4	18	0	−	−
5	23	98.410	98.410	0.000
6	21	116.180	116.181	−0.001
7	19	179.723	179.711	0.012
8	26	205.151	205.145	0.005
9	20	230.346	230.339	0.007
10	24	259.859	259.857	0.002
11	25	282.533	282.529	0.004
12	19	326.388	326.379	0.008
13	22	388.084	388.091	−0.008
14	20	442.094	442.091	0.003
15	25	472.740	472.739	0.002
16	21	497.713	497.707	0.006
17	23	547.330	547.324	0.006
18	24	604.238	604.242	−0.005
19	21	638.454	638.472	−0.018

Fitted hyperfine parameters for the excited state B

standard dev. (MHz)	0.0076
eqQ_B (MHz)	−560.838(13)‡
C_B (MHz)	0.223669(23)
d_B (MHz)	−0.12073(80)
δ_B (MHz)	0.00623(57)

Hyperfine parameters for the ground state X used in th fit

eqQ_X (MHz)*	−2452.64
C_X (MHz)*	0.00315478
d_X (MHz)†	0.001524
δ_X (MHz)†	0.003705

* eqQ_X and C_X are determined by equations B.2 and B.3, respectively.

†d_X and δ_X are fixed in the fit to 1.524 and 3.705 kHz, respectively.

‡Quoted uncertainties (1σ) are estimated from the standard deviation of the fit.

B.13 R(52) 45-0

Table B.13: Hyperfine spectrum recorded at R(52) 45-0. Pump power: 2.2- 2.9 mW, probe power: 0.2 mW, time constant of lock-in amplifier: 100 ms, cold-finger temperature: -2.28°C (vapor pressure: 3.3 Pa).

a	**F′**	Measurement (MHz)	Calculation (MHz)	Mea.-Cal. (MHz)
1	53	−337.180	−337.164	−0.016
2	49	−109.749	−109.760	0.011
3	52	−60.715	−60.730	0.014
4	54	−47.772	−47.780	0.007
5	57	0	−	−
6	50	37.289	37.300	−0.011
7	51	60.792	60.796	−0.003
8	55	112.364	112.349	0.014
9	56	135.798	135.791	0.006
10	53	228.501	228.498	0.003
11	51	339.039	339.042	−0.003
12	52	350.586	350.593	−0.008
13	54	389.084	389.091	−0.007
14	55	402.748	402.751	−0.003
15	53	512.392	512.388	0.004

Fitted hyperfine parameters for the excited state B

standard dev. (MHz)	0.010
eqQ_B (MHz)	$-561.356(22)^{\ddagger}$
C_B (MHz)	0.229843(18)
d_B (MHz)	−0.1239(10)
δ_B (MHz)	0.0095(15)

Hyperfine parameters for the ground state X used in th fit

eqQ_X (MHz)*	−2453.07
C_X (MHz)*	0.00315478
d_X (MHz)†	0.001524
δ_X (MHz)†	0.003705

* eqQ_X and C_X are determined by equations B.2 and B.3, respectively.

†d_X and δ_X are fixed in the fit to 1.524 and 3.705 kHz, respectively.

‡Quoted uncertainties (1σ) are estimated from the standard deviation of the fit.

B.14 P(69) 45-0

Table B.14: Hyperfine spectrum recorded at R(69) 45-0. Pump power: 2.8 - 3.4 mW, probe power: 0.3 mW, time constant of lock-in amplifier: 30 ms, cold-finger temperature: -2.28°C (vapor pressure: 3.3 Pa).

a	**F′**	Measurement (MHz)	Calculation (MHz)	Mea.-Cal. (MHz)
1	63	−548.614	−548.613	−0.001
2	68	−456.865	−456.850	−0.015
3	73	−368.565	−368.553	−0.012
4	64	−264.184	−264.194	0.010
5	67	−185.571	−185.569	−0.001
6	69	−162.293	−162.286	−0.007
7	65	−92.046	−92.047	0.002
8	72	−86.986	−86.983	−0.002
9	66	−65.786	−65.789	0.004
10	70	0	−	−
11	71	22.999	22.998	0.002
12	65	43.000	43.002	−0.002
13	68	108.963	108.963	0.000
14	71	176.045	176.046	−0.001
15	66	195.318	195.317	0.000
16	67	228.449	228.457	−0.008
17	69	271.141	271.150	−0.009
18	70	302.706	302.706	0.000
19	67	367.416	367.425	−0.009
20	68	390.220	390.224	−0.004
21	69	415.931	415.934	−0.003

Fitted hyperfine parameters for the excited state B

standard dev. (MHz)	0.0068
eqQ_B (MHz)	$-561.804(11)^{\ddagger}$
C_B (MHz)	0.2349204(71)
d_B (MHz)	−0.12617(80)
δ_B (MHz)	0.00739(59)

Hyperfine parameters for the ground state X used in th fit

eqQ_X (MHz)*	−2453.47
C_X (MHz)*	0.00315478
d_X (MHz)†	0.001524
δ_X (MHz)†	0.003705

* eqQ_X and C_X are determined by equations B.2 and B.3, respectively.

†d_X and δ_X are fixed in the fit to 1.524 and 3.705 kHz, respectively.

‡Quoted uncertainties (1σ) are estimated from the standard deviation of the fit.

B.15 P(91) 45-0

Table B.15: Hyperfine spectrum recorded at P(91) 45-0. Pump power: 3.8 - 4.0 mW, probe power: 0.39 mW, time constant of lock-in amplifier: 100 ms, cold-finger temperature: -2.28°C (vapor pressure: 3.3 Pa).

a	**F′**	Measurement (MHz)	Calculation (MHz)	Mea.-Cal. (MHz)
1	85	−469.110	−469.108	−0.001
2	90	−349.744	−349.743	−0.001
3	95	−233.796	−233.789	−0.008
4	86	−175.156	−175.142	−0.014
5	89	−85.540	−85.532	−0.008
6	91	−48.142	−48.146	0.003
7	87	0	−	−
8	88	29.615	29.611	0.003
9	94	38.333	38.328	0.005
10	92	118.993	118.982	0.011
11	87	136.025	136.020	0.005
12	93	146.439	146.433	0.006
13	90	216.099	216.104	−0.005
16	89	331.122	331.137	−0.015
17	91	383.234	383.245	−0.012
18	92	416.858	416.858	0.000
19	89	470.571	470.573	−0.002
20	90	497.738	497.737	0.002
21	91	527.179	527.176	0.003

Fitted hyperfine parameters for the excited state B

standard dev. (MHz)	0.0079
eqQ_B (MHz)	$-562.546(13)^{\ddagger}$
C_B (MHz)	0.2452897(55)
d_B (MHz)	−0.1325(10)
δ_B (MHz)	0.00975(82)

Hyperfine parameters for the ground state X used in th fit

eqQ_X (MHz)*	−2454.14
C_X (MHz)*	0.00315478
d_X (MHz)†	0.001524
δ_X (MHz)†	0.003705

* eqQ_X and C_X are determined by equations B.2 and B.3, respectively.

†d_X and δ_X are fixed in the fit to 1.524 and 3.705 kHz, respectively.

‡Quoted uncertainties (1σ) are estimated from the standard deviation of the fit.

B.16 R(31) 47-0

Table B.16: Hyperfine spectrum recorded at R(31) 47-0. Pump power: 2.7- 3.0 mW, probe power: 0.33 mW, time constant of lock-in amplifier: 100 ms, cold-finger temperature: -2.28°C (vapor pressure: 3.3 Pa).

a	**F′**	Measurement (MHz)	Calculation (MHz)	Mea.-Cal. (MHz)
1	27	−470.966	−470.982	0.016
2*	32	−402.022	−402.119	0.097
3	37	−338.264	−338.254	−0.010
4	28	−212.885	−212.886	0.001
9	30	0	−	−
10	34	39.748	39.725	0.023
11	35	61.885	61.886	−0.001
12	29	100.491	100.494	−0.003
13	32	161.983	161.964	0.019
14*	35	233.666	233.547	0.119
16	31	278.810	278.805	0.005
18	34	365.406	365.405	0.001
19	31	416.858	416.855	0.003
20	32	438.774	438.774	−0.000
21	33	470.182	470.187	−0.005

Fitted hyperfine parameters for the excited state B

standard dev. (MHz)	0.012
eqQ_B (MHz)	$-562.816(27)^{\ddagger}$
C_B (MHz)	0.264762(35)
d_B (MHz)	−0.1390(16)
δ_B (MHz)	0.0172(12)

Hyperfine parameters for the ground state X used in th fit

eqQ_X (MHz)**	−2452.74
C_X (MHz)**	0.00315478
d_X (MHz)†	0.001524
δ_X (MHz)†	0.003705

* Not included in the fit.

**eqQ_X and C_X are determined by equations B.2 and B.3, respectively.

†d_X and δ_X are fixed in the fit to 1.524 and 3.705 kHz, respectively.

‡Quoted uncertainties (1σ) are estimated from the standard deviation of the fit.

B.17 R(51) 47-0

Table B.17: Hyperfine spectrum recorded at R(51) 47-0. Pump power: 2.0 - 2.25 mW, probe power: 0.17 mW, time constant of lock-in amplifier: 100 ms, cold-finger temperature: -2.28°C (vapor pressure: 3.3 Pa).

a	**F′**	Measurement (MHz)	Calculation (MHz)	Mea.-Cal. (MHz)
1	47	−480.121	−480.138	0.016
2	52	−393.354	−393.360	0.006
3	57	−310.700	−310.683	−0.017
4	48	−203.309	−203.309	0.001
5	51	−119.163	−119.161	−0.002
6	53	−102.583	−102.585	0.002
7	49	−28.885	−28.891	0.006
8	56	−22.577	−22.582	0.005
9	50	0	−	−
10	54	59.405	59.376	0.028
11	55	82.684	82.683	0.001
12	49	105.259	105.254	0.006
13	52	171.461	171.460	0.002
14	55	240.605	240.613	−0.008
15	50	252.819	252.824	−0.005
16	51	289.990	289.993	−0.003
17	53	333.136	333.129	0.006
18	54	368.690	368.683	0.006
19	51	428.227	428.222	0.005
20	52	451.387	451.387	0.000
21	53	478.967	478.966	0.001

Fitted hyperfine parameters for the excited state B

standard dev. (MHz)	0.010
eqQ_B (MHz)	−563.295(17)‡
C_B (MHz)	0.270541(14)
d_B (MHz)	−0.1473(12)
δ_B (MHz)	0.01565(88)

Hyperfine parameters for the ground state X used in th fit

eqQ_X (MHz)**	−2453.05
C_X (MHz)**	0.00315478
d_X (MHz)†	0.001524
δ_X (MHz)†	0.003705

**eqQ_X and C_X are determined by equations B.2 and B.3, respectively.

†d_X and δ_X are fixed in the fit to 1.524 and 3.705 kHz, respectively.

‡Quoted uncertainties (1σ) are estimated from the standard deviation of the fit.

B.18 R(92) 47-0

Table B.18: Hyperfine spectrum recorded at R(92) 47-0. Pump power: 1.7 - 2.3 mW, probe power: 0.2 mW, time constant of lock-in amplifier: 100 ms, cold-finger temperature: -2.28°C (vapor pressure: 3.3 Pa).

a	**F′**	Measurement (MHz)	Calculation (MHz)	Mea.-Cal. (MHz)
1	93	−478.463	−478.469	0.006
2	89	−308.818	−308.832	0.014
3	92	−219.986	−219.973	−0.012
4	94	−172.081	−172.081	0.000
5	90	−144.124	−144.114	−0.010
6	91	−110.288	−110.280	−0.008
7	97	−84.522	−84.515	−0.006
8	95	0	−	−
9	96	33.266	33.276	−0.010
10	93	86.463	86.472	−0.009
11	91	169.791	169.791	−0.000
12	92	196.460	196.455	0.005
13	94	258.805	258.793	0.012
14	95	286.950	286.949	0.001
15	93	369.907	369.912	−0.005

Fitted hyperfine parameters for the excited state B

standard dev. (MHz)	0.0094
eqQ_B (MHz)	$-564.742(23)^{\ddagger}$
C_B (MHz)	0.293399(10)
d_B (MHz)	−0.1598(10)
δ_B (MHz)	0.0200(13)

Hyperfine parameters for the ground state X used in th fit

eqQ_X (MHz)*	−2454.17
C_X (MHz)*	0.00315478
d_X (MHz)†	0.001524
δ_X (MHz)†	0.003705

* eqQ_X and C_X are determined by equations B.2 and B.3, respectively.

†d_X and δ_X are fixed in the fit to 1.524 and 3.705 kHz, respectively.

‡Quoted uncertainties (1σ) are estimated from the standard deviation of the fit.

B.19 R(111) 47-0

Table B.19: Hyperfine spectrum recorded at R(111) 47-0. Pump power: 2.4 mW, probe power: 0.18 mW, time constant of lock-in amplifier: 100 ms, cold-finger temperature: -2.28°C (vapor pressure: 3.3 Pa).

a	**F′**	Measurement (MHz)	Calculation (MHz)	Mea.-Cal. (MHz)
1	107	−432.018	−432.018	0.001
2	112	−250.387	−250.437	0.050
3	108	−123.928	−123.925	−0.004
4	117	−72.598	−72.562	−0.036
5	111	0	−	−
8	110	102.973	102.942	0.031
9	116	184.443	184.433	0.010
10	109	198.522	198.51	0.012
11	114	242.838	242.808	0.030
12	115	282.012	282.005	0.007
13	112	314.466	314.439	0.026
14	110	371.409	371.366	0.042
15	111	417.403	417.362	0.041
16	115	429.972	429.934	0.038
17	113	493.450	493.416	0.034
18	114	537.349	537.338	0.011
19	111	556.820	556.848	−0.028
20	112	595.553	595.592	−0.039
21	113	636.524	636.600	−0.075

Fitted hyperfine parameters for the excited state B

standard dev. (MHz)	0.037
eqQ_B (MHz)	$-565.651(56)^{\ddagger}$
C_B (MHz)	0.310759(29)
d_B (MHz)	−0.1626(44)
δ_B (MHz)	0.0254(35)

Hyperfine parameters for the ground state X used in th fit

eqQ_X (MHz)*	−2454.9
C_X (MHz)*	0.00315478
d_X (MHz)†	0.001524
δ_X (MHz)†	0.003705

* eqQ_X and C_X are determined by equations B.2 and B.3, respectively.

†d_X and δ_X are fixed in the fit to 1.524 and 3.705 kHz, respectively.

‡Quoted uncertainties (1σ) are estimated from the standard deviation of the fit.

B.20 P(19) 49-0

Table B.20: Hyperfine spectrum recorded at P(19) 49-0. Pump power: 4.6 - 5 mW, probe power: 0.3 mW, time constant of lock-in amplifier: 100 ms, cold-finger temperature: -2.28°C (vapor pressure: 3.3 Pa).

a	**F′**	Measurement (MHz)	Calculation (MHz)	Mea.-Cal. (MHz)
1	13	−631.145	−631.150	0.005
2	18	−561.147	−561.148	0.000
3	23	−499.371	−499.369	−0.002
4	14	−396.296	−396.291	−0.005
5	19	−288.728	−288.728	0.000
6	17	−270.560	−270.557	−0.002
7	15	−215.591	−215.587	−0.004
8	22	−174.032	−174.033	0.001
9	16	−159.690	−159.688	−0.002
10	20	−126.110	−126.108	−0.002
11	21	−102.016	−102.014	−0.002
12	15	−65.517	−65.521	0.004
13	18	0	–	–
14	16	46.623	46.619	0.004
15	21	91.701	91.698	0.003
16	17	105.592	105.592	0.000
17	19	160.216	160.209	0.006
18	20	220.933	220.927	0.007
19	17	247.383	247.386	−0.003
20	18	268.959	268.960	−0.002
21	19	312.608	312.619	−0.011

Fitted hyperfine parameters for the excited state B

standard dev. (MHz)	0.0046
eqQ_B (MHz)	$-564.6327(72)^{\ddagger}$
C_B (MHz)	0.309250(21)
d_B (MHz)	−0.16923(43)
δ_B (MHz)	0.02631(31)

Hyperfine parameters for the ground state X used in th fit

eqQ_X (MHz)*	−2452.62
C_X (MHz)*	0.00315478
d_X (MHz)†	0.001524
δ_X (MHz)†	0.003705

* eqQ_X and C_X are determined by equations B.2 and B.3, respectively.

†d_X and δ_X are fixed in the fit to 1.524 and 3.705 kHz, respectively.

‡Quoted uncertainties (1σ) are estimated from the standard deviation of the fit.

B.21 P(41) 49-0

Table B.21: Hyperfine spectrum recorded at P(41) 49-0. Pump power: 3.4 - 3.8 mW, probe power: 0.38 mW, time constant of lock-in amplifier: 100 ms, cold-finger temperature: -2.28°C (vapor pressure: 3.3 Pa).

a	**F′**	Measurement (MHz)	Calculation (MHz)	Mea.-Cal. (MHz)
1	35	−532.653	−532.664	0.012
2	40	−449.385	−449.390	0.005
3	45	−370.892	−370.875	−0.017
4	36	−262.237	−262.224	−0.012
5	39	−172.967	−172.936	−0.031
6	41	−161.763	−161.746	−0.017
7	37	−86.186	−86.191	0.005
8	44	−77.488	−77.494	0.006
9	38	−54.555	−54.560	0.006
10	42	0	−	−
11	43	23.542	23.538	0.004
12	37	48.011	47.999	0.012
13	40	114.420	114.420	0.000
14	43	185.772	185.793	−0.021
15	38	191.181	191.181	−0.001
16	39	231.748	231.770	−0.022
17	41	275.656	275.685	−0.029
18	42	314.638	314.638	0.000
19	39	369.603	369.603	0.000
20	40	392.932	392.922	0.010
21	41	422.354	422.341	0.012

Fitted hyperfine parameters for the excited state B

standard dev. (MHz)	0.016
eqQ_B (MHz)	−564.886(26)‡
C_B (MHz)	0.314896(28)
d_B (MHz)	−0.1706(18)
δ_B (MHz)	0.0262(13)

Hyperfine parameters for the ground state X used in th fit

eqQ_X (MHz)*	−2452.88
C_X (MHz)*	0.00315478
d_X (MHz)†	0.001524
δ_X (MHz)†	0.003705

* eqQ_X and C_X are determined by equations B.2 and B.3, respectively.

†d_X and δ_X are fixed in the fit to 1.524 and 3.705 kHz, respectively.

‡Quoted uncertainties (1σ) are estimated from the standard deviation of the fit.

B.22 P(62) 49-0

Table B.22: Hyperfine spectrum recorded at P(62) 49-0. Pump power: 3.0 - 3.5 mW, probe power: 0.26 mW, time constant of lock-in amplifier: 100 ms, cold-finger temperature: -2.28°C (vapor pressure: 3.3 Pa).

a	**F′**	Measurement (MHz)	Calculation (MHz)	Mea.-Cal. (MHz)
1	61	−463.477	−463.461	−0.016
2	57	−266.405	−266.427	0.022
3	60	−196.429	−196.440	0.011
4	62	−166.266	−166.261	−0.005
5	58	−111.003	−110.994	−0.008
6	65	−97.743	−97.716	−0.027
7	59	−81.646	−81.628	−0.018
8	63	0	−	−
9	64	28.966	28.977	−0.011
10	61	100.699	100.723	−0.024
11	59	196.833	196.837	−0.004
12	60	215.995	216.000	−0.005
13	62	267.353	267.359	−0.006
14	63	288.514	288.510	0.003
15	61	383.956	383.955	0.001

Fitted hyperfine parameters for the excited state B

standard dev. (MHz)	0.016
eqQ_B (MHz)	$-565.295(39)^{\ddagger}$
C_B (MHz)	0.324667(25)
d_B (MHz)	−0.1794(17)
δ_B (MHz)	0.0326(22)

Hyperfine parameters for the ground state X used in th fit

eqQ_X (MHz)*	−2453.29
C_X (MHz)*	0.00315478
d_X (MHz)†	0.001524
δ_X (MHz)†	0.003705

* eqQ_X and C_X are determined by equations B.2 and B.3, respectively.

†d_X and δ_X are fixed in the fit to 1.524 and 3.705 kHz, respectively.

‡Quoted uncertainties (1σ) are estimated from the standard deviation of the fit.

B.23 R(93) 49-0

Table B.23: Hyperfine spectrum recorded at R(93) 49-0. Pump power: 2.1 - 2.5 mW, probe power: 0.2 mW, time constant of lock-in amplifier: 100 ms, cold-finger temperature: -2.28°C (vapor pressure: 3.3 Pa).

a	**F′**	Measurement (MHz)	Calculation (MHz)	Mea.-Cal. (MHz)
1	89	−530.500	−530.505	0.005
2	94	−356.084	−356.107	0.023
3	90	−226.206	−226.222	0.015
4	99	−185.887	−185.887	0.001
5	93	−103.786	−103.785	−0.001
8	92	0	−	−
9	98	74.256	74.268	−0.012
10	91	95.189	95.186	0.004
11	96	133.201	133.197	0.005
12	97	171.449	171.457	−0.008
13	94	208.029	208.039	−0.010
14	92	265.469	265.468	0.000
15	93	311.768	311.751	0.017
16	97	320.691	320.687	0.005
17	95	385.677	385.660	0.017
18	96	429.766	429.764	0.002
19	93	450.802	450.795	0.007
20	94	488.630	488.634	−0.004
21	95	529.072	529.067	0.005

Fitted hyperfine parameters for the excited state B

standard dev. (MHz)	0.011
eqQ_B (MHz)	−566.485(19)‡
C_B (MHz)	0.3509271(87)
d_B (MHz)	−0.1940(13)
δ_B (MHz)	0.0403(10)

Hyperfine parameters for the ground state X used in th fit

eqQ_X (MHz)*	−2454.21
C_X (MHz)*	0.00315478
d_X (MHz)†	0.001524
δ_X (MHz)†	0.003705

* eqQ_X and C_X are determined by equations B.2 and B.3, respectively.

†d_X and δ_X are fixed in the fit to 1.524 and 3.705 kHz, respectively.

‡Quoted uncertainties (1σ) are estimated from the standard deviation of the fit.

B.24 P(108) 49-0

Table B.24: Hyperfine spectrum recorded at P(108) 49-0. Pump power: 2.5 - 2.7 mW, probe power: 0.25 mW, time constant of lock-in amplifier: 100 ms, cold-finger temperature: -2.28°C (vapor pressure: 3.3 Pa).

a	**F′**	Measurement (MHz)	Calculation (MHz)	Mea.-Cal. (MHz)
1	107	−343.852	−343.860	0.008
2	103	−221.718	−221.729	0.011
3	106	−98.224	−98.214	−0.010
4	104	−44.790	−44.803	0.013
5	108	−25.553	−25.558	0.005
6	105	0	–	–
7	111	96.563	96.578	−0.016
8	109	157.592	157.579	0.013
9	110	201.694	201.685	0.008
10	107	220.194	220.188	0.006
11	105	280.207	280.201	0.006
12	106	318.668	318.666	0.002
13	108	403.545	403.544	0.001
14	109	443.583	443.582	0.001
15	107	503.277	503.280	−0.003

Fitted hyperfine parameters for the excited state B

standard dev. (MHz)	0.0097
eqQ_B (MHz)	$-567.273(24)^{\ddagger}$
C_B (MHz)	0.3662298(84)
d_B (MHz)	−0.1996(10)
δ_B (MHz)	0.0427(13)

Hyperfine parameters for the ground state X used in th fit

eqQ_X (MHz)*	−2454.78
C_X (MHz)*	0.00315478
d_X (MHz)†	0.001524
δ_X (MHz)†	0.003705

* eqQ_X and C_X are determined by equations B.2 and B.3, respectively.

†d_X and δ_X are fixed in the fit to 1.524 and 3.705 kHz, respectively.

‡Quoted uncertainties (1σ) are estimated from the standard deviation of the fit.

B.25 R(55) 50-0

Table B.25: Hyperfine spectrum recorded at R(55) 50-0. Pump power: 3.2 - 3.7 mW, probe power: 0.3 mW, time constant of lock-in amplifier: 100 ms, cold-finger temperature: -2.28°C (vapor pressure: 3.3 Pa).

a	**F′**	Measurement (MHz)	Calculation (MHz)	Mea.-Cal. (MHz)
1	51	−461.997	−462.007	0.009
2	56	−348.169	−348.170	0.001
3	61	−238.876	−238.870	−0.006
4	52	−178.699	−178.697	−0.001
5	55	−80.590	−80.588	−0.002
6	57	−51.977	−51.978	0.001
7	53	0	−	−
8	54	33.276	33.283	−0.007
10	58	114.773	114.766	0.006
11	53	134.040	134.039	0.000
12	59	143.050	143.045	0.005
13	56	215.510	215.513	−0.003
14	54	287.561	287.564	−0.003
15	59	299.143	299.149	−0.006
16	55	328.873	328.876	−0.002
17	57	382.073	382.071	0.002
18	58	421.377	421.371	0.006
19	55	466.964	466.963	0.001
20	56	494.948	494.947	0.001
21	57	527.203	527.200	0.003

Fitted hyperfine parameters for the excited state B

standard dev. (MHz)	0.0047
eqQ_B (MHz)	$-566.0544(80)^{\ddagger}$
C_B (MHz)	0.3504090(55)
d_B (MHz)	−0.19199(56)
δ_B (MHz)	0.03910(46)

Hyperfine parameters for the ground state X used in th fit

eqQ_X (MHz)*	−2453.13
C_X (MHz)*	0.00315478
d_X (MHz)†	0.001524
δ_X (MHz)†	0.003705

* eqQ_X and C_X are determined by equations B.2 and B.3, respectively.

†d_X and δ_X are fixed in the fit to 1.524 and 3.705 kHz, respectively.

‡Quoted uncertainties (1σ) are estimated from the standard deviation of the fit.

B.26 R(20) 51-0

Table B.26: Hyperfine spectrum recorded at R(20) 51-0. Pump power: 2.8 - 3.2 mW, probe power: 0.27 mW, time constant of lock-in amplifier: 100 ms, cold-finger temperature: -2.28°C (vapor pressure: 3.3 Pa).

a	**F′**	Measurement (MHz)	Calculation (MHz)	Mea.-Cal. (MHz)
1	21	−476.456	−476.449	−0.007
2	17	−244.318	−244.320	0.001
3	22	−201.904	−201.912	0.008
4	20	−188.646	−188.650	0.004
5	25	−149.119	−149.110	−0.009
6	18	−113.232	−113.234	0.002
7	19	−77.998	−77.994	−0.004
8	23	−38.140	−38.145	0.004
9	24	0	−	−
10	21	84.216	84.220	−0.004
13	22	250.370	250.381	−0.011
14	23	263.803	263.798	0.005

Fitted hyperfine parameters for the excited state B

standard dev. (MHz)	0.0071
eqQ_B (MHz)	$-566.275(21)^{\ddagger}$
C_B (MHz)	0.366031(35)
d_B (MHz)	−0.20074(96)
δ_B (MHz)	0.0469(11)

Hyperfine parameters for the ground state X used in th fit

eqQ_X (MHz)*	−2452.63
C_X (MHz)*	0.00315478
d_X (MHz)†	0.001524
δ_X (MHz)†	0.003705

* eqQ_X and C_X are determined by equations B.2 and B.3, respectively.

†d_X and δ_X are fixed in the fit to 1.524 and 3.705 kHz, respectively.

‡Quoted uncertainties (1σ) are estimated from the standard deviation of the fit.

B.27 P(30) 51-0

Table B.27: Hyperfine spectrum recorded at P(30) 51-0. Pump power: 3 mW, probe power: 0.2 mW, time constant of lock-in amplifier: 100 ms, cold-finger temperature: -2.28°C (vapor pressure: 3.3 Pa).

a	**F′**	Measurement (MHz)	Calculation (MHz)	Mea.-Cal. (MHz)
1	29	−334.316	−334.323	0.007
2	25	−107.632	−107.643	0.011
5	33	0	−	−
6	26	32.685	32.687	−0.002
7	27	62.130	62.144	−0.014
8	31	110.609	110.620	−0.012
9	32	140.840	140.830	0.010
10	29	228.095	228.097	−0.002
11	27	336.702	336.717	−0.016
12	28	345.822	345.821	0.002
13	30	391.399	391.390	0.009
14	31	405.258	405.269	−0.011
15	29	511.372	511.351	0.021

Fitted hyperfine parameters for the excited state B

standard dev. (MHz)	0.013
eqQ_B (MHz)	−566.415(29)‡
C_B (MHz)	0.368223(40)
d_B (MHz)	−0.2005(13)
δ_B (MHz)	0.0401(19)

Hyperfine parameters for the ground state X used in th fit

eqQ_X (MHz)*	−2452.73
C_X (MHz)*	0.00315478
d_X (MHz)†	0.001524
δ_X (MHz)†	0.003705

* eqQ_X and C_X are determined by equations B.2 and B.3, respectively.

†d_X and δ_X are fixed in the fit to 1.524 and 3.705 kHz, respectively.

‡Quoted uncertainties (1σ) are estimated from the standard deviation of the fit.

B.28 P(50) 51-0

Table B.28: Hyperfine spectrum recorded at P(50) 51-0. Pump power: 3 mW, probe power: 0.2 mW, time constant of lock-in amplifier: 100 ms, cold-finger temperature: -2.28°C (vapor pressure: 3.3 Pa).

a	**F′**	Measurement (MHz)	Calculation (MHz)	Mea.-Cal. (MHz)
1	49	−490.442	−490.445	0.003
2	45	−290.131	−290.135	0.004
3	48	−221.508	−221.507	0.000
4	50	−196.015	−196.013	−0.001
5	46	−137.487	−137.488	0.001
6	53	−128.980	−128.968	−0.012
7	47	−107.257	−107.253	−0.003
8	51	−29.993	−29.994	0.000
9	52	0	−	−
10	49	72.790	72.798	−0.008
11	47	169.996	169.997	−0.001
12	48	187.690	187.698	−0.007
13	50	239.328	239.326	0.002
14	51	259.589	259.590	−0.001
15	49	355.790	355.783	0.007

Fitted hyperfine parameters for the excited state B

standard dev. (MHz)	0.0056
eqQ_B (MHz)	−566.763(14)‡
C_B (MHz)	0.377297(11)
d_B (MHz)	−0.20747(63)
δ_B (MHz)	0.05024(66)

Hyperfine parameters for the ground state X used in th fit

eqQ_X (MHz)*	−2453.03
C_X (MHz)*	0.00315478
d_X (MHz)†	0.001524
δ_X (MHz)†	0.003705

* eqQ_X and C_X are determined by equations B.2 and B.3, respectively.

†d_X and δ_X are fixed in the fit to 1.524 and 3.705 kHz, respectively.

‡Quoted uncertainties (1σ) are estimated from the standard deviation of the fit.

B.29 P(73) 51-0

Table B.29: Hyperfine spectrum recorded at P(73) 51-0. Pump power: 3.8 - 4.2 mW, probe power: 0.36 mW, time constant of lock-in amplifier: 100 ms, cold-finger temperature: -2.28°C (vapor pressure: 3.3 Pa).

a	**F′**	Measurement (MHz)	Calculation (MHz)	Mea.-Cal. (MHz)
1	67	−480.189	−480.197	0.008
2	72	−326.030	−326.029	−0.001
5	71	−68.699	−68.708	0.009
6	73	−19.894	−19.894	0.000
7	69	0	−	−
8	70	38.243	38.248	−0.005
9	76	90.816	90.823	−0.007
10	69	134.791	134.777	0.014
11	74	153.996	153.983	0.013
12	75	189.061	189.064	−0.003
13	72	237.443	237.452	−0.009
14	70	299.126	299.150	−0.024
17	73	411.323	411.334	−0.011
18	74	454.085	454.077	0.007
19	71	482.720	482.713	0.007
20	72	517.349	517.329	0.020
21	73	555.230	555.232	−0.003

Fitted hyperfine parameters for the excited state B

standard dev. (MHz)	0.012
eqQ_B (MHz)	−567.132(23)‡
C_B (MHz)	0.394644(14)
d_B (MHz)	−0.2134(16)
δ_B (MHz)	0.0552(12)

Hyperfine parameters for the ground state X used in th fit

eqQ_X (MHz)*	−2453.57
C_X (MHz)*	0.00315478
d_X (MHz)†	0.001524
δ_X (MHz)†	0.003705

* eqQ_X and C_X are determined by equations B.2 and B.3, respectively.
†d_X and δ_X are fixed in the fit to 1.524 and 3.705 kHz, respectively.
‡Quoted uncertainties (1σ) are estimated from the standard deviation of the fit.

B.30 P(90) 51-0

Table B.30: Hyperfine spectrum recorded at P(90) 51-0. Pump power: 1.7 - 2.1 mW, probe power: 0.15 mW, time constant of lock-in amplifier: 100 ms, cold-finger temperature: -2.28°C (vapor pressure: 3.3 Pa).

a	**F′**	Measurement (MHz)	Calculation (MHz)	Mea.-Cal. (MHz)
1	89	−431.434	−431.429	−0.005
2	85	−300.951	−300.955	0.004
3	88	−183.264	−183.246	−0.017
4	86	−127.129	−127.143	0.014
5	90	−116.265	−116.285	0.020
6	87	−83.606	−83.604	−0.002
7	93	0	–	–
8	91	65.019	65.004	0.015
9	92	107.884	107.870	0.014
10	89	131.971	131.977	−0.006
11	87	195.850	195.856	−0.006
12	88	231.921	231.935	−0.014
13	90	313.511	313.522	−0.011
14	91	351.392	351.388	0.004
15	89	414.856	414.845	0.012

Fitted hyperfine parameters for the excited state B

standard dev. (MHz)	0.013
eqQ_B (MHz)	$-567.872(28)^{\ddagger}$
C_B (MHz)	0.413339(14)
d_B (MHz)	−0.2258(13)
δ_B (MHz)	0.0628(19)

Hyperfine parameters for the ground state X used in th fit

eqQ_X (MHz)*	−2454.1
C_X (MHz)*	0.00315478
d_X (MHz)†	0.001524
δ_X (MHz)†	0.003705

* eqQ_X and C_X are determined by equations B.2 and B.3, respectively.

†d_X and δ_X are fixed in the fit to 1.524 and 3.705 kHz, respectively.

‡Quoted uncertainties (1σ) are estimated from the standard deviation of the fit.

B.31 R(32) 53-0

Table B.31: Hyperfine spectrum recorded at R(32) 53-0. Pump power: 2.7 - 3.1 mW, probe power: 0.25 mW, time constant of lock-in amplifier: 100 ms, cold-finger temperature: -2.28°C (vapor pressure: 3.3 Pa).

a	**F′**	Measurement (MHz)	Calculation (MHz)	Mea.-Cal. (MHz)
1	33	−452.076	−452.075	−0.001
2	29	−240.316	−240.335	0.019
3	32	−176.361	−176.355	−0.005
4	34	−165.370	−165.369	−0.001
5	37	−103.313	−103.296	−0.017
6	30	−95.918	−95.904	−0.014
7	31	−63.436	−63.423	−0.013
8	35	0	–	–
9	36	33.098	33.096	0.002
10	33	109.781	109.795	−0.014
11	31	211.158	211.153	0.006
12	32	224.113	224.112	0.001
13	34	276.222	276.216	0.006
14	35	293.751	293.756	−0.006
15	33	392.736	392.738	−0.002

Fitted hyperfine parameters for the excited state B

standard dev. (MHz)	0.011
eqQ_B (MHz)	$-567.752(27)^{\ddagger}$
C_B (MHz)	0.437830(32)
d_B (MHz)	−0.2383(12)
δ_B (MHz)	0.0785(16)

Hyperfine parameters for the ground state X used in th fit

eqQ_X (MHz)*	−2452.75
C_X (MHz)*	0.00315478
d_X (MHz)†	0.001524
δ_X (MHz)†	0.003705

* eqQ_X and C_X are determined by equations B.2 and B.3, respectively.

†d_X and δ_X are fixed in the fit to 1.524 and 3.705 kHz, respectively.

‡Quoted uncertainties (1σ) are estimated from the standard deviation of the fit.

B.32 R(51) 53-0

Table B.32: Hyperfine spectrum recorded at R(51) 53-0. Pump power: 3 - 3.5 mW, probe power: 0.3 mW, time constant of lock-in amplifier: 100 ms, cold-finger temperature: -2.28°C (vapor pressure: 3.3 Pa).

a	**F′**	Measurement (MHz)	Calculation (MHz)	Mea.-Cal. (MHz)
1	47	−696.728	−696.732	0.004
2	52	−562.532	−562.534	0.002
3	57	−433.120	−433.108	−0.012
4	48	−411.628	−411.632	0.004
5	51	−298.949	−298.956	0.007
6	53	−263.445	−263.452	0.007
7	49	−228.228	−228.223	−0.006
8	50	−189.830	−189.824	−0.006
9	56	−155.643	−155.645	0.002
12	55	−59.987	−60.000	0.013
13	52	0	−	−
14	50	61.708	61.710	−0.002
15	55	97.171	97.169	0.002
16	51	108.513	108.512	0.001
17	53	170.551	170.546	0.005
18	54	215.124	215.118	0.007
19	51	246.245	246.237	0.008
20	52	278.494	278.497	−0.003
21	53	315.689	315.690	−0.001

Fitted hyperfine parameters for the excited state B

standard dev. (MHz)	0.0066
eqQ_B (MHz)	−568.171(11)‡
C_B (MHz)	0.450037(11)
d_B (MHz)	−0.24241(82)
δ_B (MHz)	0.08388(55)

Hyperfine parameters for the ground state X used in th fit

eqQ_X (MHz)*	−2453.05
C_X (MHz)*	0.00315478
d_X (MHz)†	0.001524
δ_X (MHz)†	0.003705

* eqQ_X and C_X are determined by equations B.2 and B.3, respectively.

†d_X and δ_X are fixed in the fit to 1.524 and 3.705 kHz, respectively.

‡Quoted uncertainties (1σ) are estimated from the standard deviation of the fit.

B.33 P(70) 53-0

Table B.33: Hyperfine spectrum recorded at P(70) 53-0. Pump power: 3.7 - 4.2 mW, probe power: 0.2 mW, time constant of lock-in amplifier: 100 ms, cold-finger temperature: -2.28°C (vapor pressure: 3.3 Pa).

a	**F′**	Measurement (MHz)	Calculation (MHz)	Mea.-Cal. (MHz)
1	69	−487.144	−487.135	−0.009
2	65	−340.022	−340.037	0.016
3	68	−233.902	−233.886	−0.016
4	70	−177.705	−177.705	0.000
5	66	−171.985	−171.984	0.000
6	67	−131.193	−131.178	−0.015
7	73	−72.960	−72.937	−0.024
8	71	0	−	−
9	72	40.253	40.267	−0.013
10	69	75.550	75.562	−0.012
11	67	147.197	147.190	0.007
12	68	178.672	178.681	−0.009
13	70	253.581	253.593	−0.012
14	71	287.196	287.206	−0.010
15	69	358.195	358.190	0.005

Fitted hyperfine parameters for the excited state B

standard dev. (MHz)	0.014
eqQ_B (MHz)	$-568.623(34)^{\ddagger}$
C_B (MHz)	0.466803(19)
d_B (MHz)	−0.2535(15)
δ_B (MHz)	0.0937(19)

Hyperfine parameters for the ground state X used in th fit

eqQ_X (MHz)*	−2453.49
C_X (MHz)*	0.00315478
d_X (MHz)†	0.001524
δ_X (MHz)†	0.003705

* eqQ_X and C_X are determined by equations B.2 and B.3, respectively.

†d_X and δ_X are fixed in the fit to 1.524 and 3.705 kHz, respectively.

‡Quoted uncertainties (1σ) are estimated from the standard deviation of the fit.

B.34 P(89) 53-0

Table B.34: Hyperfine spectrum recorded at P(89) 53-0. Pump power: 3.9 - 4.1 mW, probe power: 0.2 mW, time constant of lock-in amplifier: 100 ms, cold-finger temperature: -2.28°C (vapor pressure: 3.3 Pa).

a	**F′**	Measurement (MHz)	Calculation (MHz)	Mea.-Cal. (MHz)
2	88	−472.286	−472.280	−0.006
3	84	−386.075	−386.088	0.013
4	93	−249.234	−249.212	−0.022
5	87	−231.148	−231.124	−0.024
6	85	−189.769	−189.783	0.014
7	89	−150.824	−150.845	0.022
8	86	−138.414	−138.407	−0.006
9	85	−54.504	−54.516	0.012
10	92	0	−	−
11	90	37.024	36.996	0.027
14	86	125.571	125.600	−0.028
15	87	182.974	183.008	−0.034
16	91	235.089	235.110	−0.021
17	89	278.320	278.310	0.011
18	87	321.650	321.639	0.011
19	90	333.204	333.197	0.007
20	88	370.022	370.018	0.004

Fitted hyperfine parameters for the excited state B

standard dev. (MHz)	0.021
eqQ_B (MHz)	−569.287(39)‡
C_B (MHz)	0.493519(20)
d_B (MHz)	−0.2670(27)
δ_B (MHz)	0.1078(18)

Hyperfine parameters for the ground state X used in th fit

eqQ_X (MHz)*	−2454.07
C_X (MHz)*	0.00315478
d_X (MHz)†	0.001524
δ_X (MHz)†	0.003705

* eqQ_X and C_X are determined by equations B.2 and B.3, respectively.

†d_X and δ_X are fixed in the fit to 1.524 and 3.705 kHz, respectively.

‡Quoted uncertainties (1σ) are estimated from the standard deviation of the fit.

B.35 R(21) 55-0

Table B.35: Hyperfine spectrum recorded at R(21) 55-0. Pump power: 4.5 - 5.0 mW, probe power: 0.37 mW, time constant of lock-in amplifier: 100 ms, cold-finger temperature: -2.28°C (vapor pressure: 3.3 Pa).

a	**F′**	Measurement (MHz)	Calculation (MHz)	Mea.-Cal. (MHz)
1	17	−428.467	−428.480	0.013
2	22	−332.184	−332.185	0.001
3	27	−243.711	−243.703	−0.008
4	18	−185.247	−185.227	−0.020
7	19	0	−	−
8	20	57.271	57.278	−0.007
9	26	71.524	71.519	0.005
10	24	113.118	113.112	0.006
13	22	227.333	227.342	−0.009
14	20	267.258	267.274	−0.016
17	23	392.239	392.238	0.002
18	24	454.918	454.910	0.008
19	21	469.676	469.673	0.004
20	22	496.595	496.595	−0.001
21	23	543.361	543.361	0.001

Fitted hyperfine parameters for the excited state B

standard dev. (MHz)	0.010
eqQ_B (MHz)	−568.807(18)‡
C_B (MHz)	0.513082(32)
d_B (MHz)	−0.2718(12)
δ_B (MHz)	0.12206(91)

Hyperfine parameters for the ground state X used in th fit

eqQ_X (MHz)*	−2452.64
C_X (MHz)*	0.00315478
d_X (MHz)†	0.001524
δ_X (MHz)†	0.003705

* eqQ_X and C_X are determined by equations B.2 and B.3, respectively.

†d_X and δ_X are fixed in the fit to 1.524 and 3.705 kHz, respectively.

‡Quoted uncertainties (1σ) are estimated from the standard deviation of the fit.

B.36 P(61) 55-0

Table B.36: Hyperfine spectrum recorded at P(61) 55-0. Pump power: 2.8 - 3.1 mW, probe power: 0.2 mW, time constant of lock-in amplifier: 100 ms, cold-finger temperature: -2.28°C (vapor pressure: 3.3 Pa).

a	**F′**	Measurement (MHz)	Calculation (MHz)	Mea.-Cal. (MHz)
1	55	−430.752	−430.769	0.017
2	60	−253.022	−253.047	0.025
3	56	−133.332	−133.342	0.010
4	65	−79.462	−79.447	−0.015
5	59	0	−	−
8	58	101.179	101.190	−0.010
9	64	185.056	185.068	−0.012
10	57	190.447	190.458	−0.011
11	62	234.852	234.829	0.022
12	63	275.478	275.458	0.020
13	60	309.023	309.018	0.004
14	58	357.424	357.435	−0.011
15	59	409.802	409.811	−0.008
16	63	429.101	429.112	−0.011
17	61	487.740	487.736	0.004
18	62	537.737	537.724	0.012
19	59	547.717	547.714	0.004
20	60	587.742	587.740	0.002
21	61	631.900	631.889	0.012

Fitted hyperfine parameters for the excited state B

standard dev. (MHz)	0.015
eqQ_B (MHz)	−569.444(22)‡
C_B (MHz)	0.544230(21)
d_B (MHz)	−0.2854(16)
δ_B (MHz)	0.1444(13)

Hyperfine parameters for the ground state X used in th fit

eqQ_X (MHz)*	−2453.27
C_X (MHz)*	0.00315478
d_X (MHz)†	0.001524
δ_X (MHz)†	0.003705

* eqQ_X and C_X are determined by equations B.2 and B.3, respectively.

†d_X and δ_X are fixed in the fit to 1.524 and 3.705 kHz, respectively.

‡Quoted uncertainties (1σ) are estimated from the standard deviation of the fit.

B.37 P(83) 55-0

Table B.37: Hyperfine spectrum recorded at P(83) 55-0. Pump power: 2.9 - 3.3 mW, probe power: 0.2 mW, time constant of lock-in amplifier: 100 ms, cold-finger temperature: -2.28°C (vapor pressure: 3.3 Pa).

a	**F′**	Measurement (MHz)	Calculation (MHz)	Mea.-Cal. (MHz)
1	77	−652.372	−652.398	0.027
2	82	−403.835	−403.828	−0.007
3	78	−335.857	−335.868	0.010
6	79	−134.909	−134.899	−0.010
9	79	0	–	–
10	86	86.447	86.473	−0.026
11	84	113.515	113.494	0.021
12	82	158.238	158.244	−0.006
13	85	167.113	167.104	0.009
14	80	183.712	183.722	−0.010
15	81	246.188	246.193	−0.005
16	85	316.773	316.781	−0.007
17	83	350.503	350.485	0.018
18	81	384.586	384.573	0.013
19	84	410.482	410.473	0.009
20	82	437.482	437.472	0.009
21	83	493.596	493.591	0.005

Fitted hyperfine parameters for the excited state B

standard dev. (MHz)	0.015
eqQ_B (MHz)	$-570.208(27)^{\ddagger}$
C_B (MHz)	0.579914(17)
d_B (MHz)	−0.3006(16)
δ_B (MHz)	0.1701(13)

Hyperfine parameters for the ground state X used in th fit

eqQ_X (MHz)*	−2453.87
C_X (MHz)*	0.00315478
d_X (MHz)†	0.001524
δ_X (MHz)†	0.003705

* eqQ_X and C_X are determined by equations B.2 and B.3, respectively.

†d_X and δ_X are fixed in the fit to 1.524 and 3.705 kHz, respectively.

‡Quoted uncertainties (1σ) are estimated from the standard deviation of the fit.

B.38 P(102) 55-0

Table B.38: Hyperfine spectrum recorded at P(102) 55-0. Pump power: 3.8 - 4.3 mW, probe power: 0.34 mW, time constant of lock-in amplifier: 100 ms, cold-finger temperature: -2.28°C (vapor pressure: 3.3 Pa).

a	**F′**	Measurement (MHz)	Calculation (MHz)	Mea.-Cal. (MHz)
1	101	−635.470	−635.471	0.000
2	97	−611.087	−611.111	0.023
5	99	−341.713	−341.666	−0.047
6	102	−294.079	−294.082	0.003
7	105	−98.506	−98.483	−0.023
8	103	−86.937	−86.969	0.031
9	101	−73.527	−73.529	0.002
10	99	−62.505	−62.499	−0.007
11	104	−18.193	−18.201	0.009
12	100	0	–	–
13	102	133.752	133.762	−0.011
14	103	198.269	198.265	0.004
15	101	208.666	208.664	0.002

Fitted hyperfine parameters for the excited state B

standard dev. (MHz)	0.022
eqQ_B (MHz)	−571.145(42)‡
C_B (MHz)	0.626595(27)
d_B (MHz)	−0.3212(21)
δ_B (MHz)	0.2092(28)

Hyperfine parameters for the ground state X used in th fit

eqQ_X (MHz)*	−2454.54
C_X (MHz)*	0.00315478
d_X (MHz)†	0.001524
δ_X (MHz)†	0.003705

* eqQ_X and C_X are determined by equations B.2 and B.3, respectively.

†d_X and δ_X are fixed in the fit to 1.524 and 3.705 kHz, respectively.

‡Quoted uncertainties (1σ) are estimated from the standard deviation of the fit.

B.39 P(19) 57-0

Table B.39: Hyperfine spectrum recorded at P(19) 57-0. Pump power: 2.2 - 2.2 mW, probe power: 0.14 mW, time constant of lock-in amplifier: 100 ms, cold-finger temperature: -2.28°C (vapor pressure: 3.3 Pa).

a	**F′**	Measurement (MHz)	Calculation (MHz)	Mea.-Cal. (MHz)
2	18	−558.632	−558.622	−0.010
3	23	−469.088	−469.074	−0.014
4	14	−416.678	−416.691	0.013
7	15	−231.451	−231.428	−0.024
8	16	−170.097	−170.108	0.011
9	22	−150.824	−150.842	0.018
10	20	−114.286	−114.301	0.015
13	18	0	–	–
14	16	35.121	35.114	0.007
15	17	99.434	99.431	0.002
16	21	108.059	108.055	0.004
17	19	165.132	165.148	−0.017
18	20	230.981	230.997	−0.016
19	17	240.902	240.911	−0.009
20	18	267.519	267.529	−0.009
21	19	316.778	316.764	0.014

Fitted hyperfine parameters for the excited state B

standard dev. (MHz)	0.015
eqQ_B (MHz)	−569.534(27)‡
C_B (MHz)	0.605935(82)
d_B (MHz)	−0.3091(19)
δ_B (MHz)	0.1993(11)

Hyperfine parameters for the ground state X used in th fit

eqQ_X (MHz)*	−2452.62
C_X (MHz)*	0.00315478
d_X (MHz)†	0.001524
δ_X (MHz)†	0.003705

* eqQ_X and C_X are determined by equations B.2 and B.3, respectively.

†d_X and δ_X are fixed in the fit to 1.524 and 3.705 kHz, respectively.

‡Quoted uncertainties (1σ) are estimated from the standard deviation of the fit.

B.40 P(33) 57-0

Table B.40: Hyperfine spectrum recorded at P(33) 57-0. Pump power: 4.4 - 4.9 mW, probe power: 0.31 mW, time constant of lock-in amplifier: 100 ms, cold-finger temperature: -2.28°C (vapor pressure: 3.3 Pa).

a	**F′**	Measurement (MHz)	Calculation (MHz)	Mea.-Cal. (MHz)
1	27	−456.274	−456.286	0.012
2	32	−332.844	−332.852	0.008
3	37	−213.728	−213.711	−0.018
4	28	−186.110	−186.066	−0.045
5	31	−63.368	−63.336	−0.032
6	33	−40.798	−40.802	0.004
7	29	0	−	−
8	30	44.532	44.555	−0.024
9	36	76.308	76.307	0.001
10	34	129.422	129.405	0.017
11	29	135.102	135.104	−0.002
12	35	162.236	162.217	0.018
13	32	228.139	228.152	−0.013
14	30	280.455	280.494	−0.038
18	34	449.815	449.811	0.005
19	31	471.647	471.659	−0.011
20	32	503.762	503.748	0.014

Fitted hyperfine parameters for the excited state B

standard dev. (MHz)	0.023
eqQ_B (MHz)	$-569.335(44)^{\ddagger}$
C_B (MHz)	0.614577(46)
d_B (MHz)	−0.3103(26)
δ_B (MHz)	0.2058(20)

Hyperfine parameters for the ground state X used in th fit

eqQ_X (MHz)*	−2452.76
C_X (MHz)*	0.00315478
d_X (MHz)†	0.001524
δ_X (MHz)†	0.003705

* eqQ_X and C_X are determined by equations B.2 and B.3, respectively.

†d_X and δ_X are fixed in the fit to 1.524 and 3.705 kHz, respectively.

‡Quoted uncertainties (1σ) are estimated from the standard deviation of the fit.

B.41 R(65) 57-0

Table B.41: Hyperfine spectrum recorded at R(65) 57-0. Pump power: 2.5 - 3 mW, probe power: 0.2 mW, time constant of lock-in amplifier: 100 ms, cold-finger temperature: -2.28°C (vapor pressure: 3.3 Pa).

a	**F′**	Measurement (MHz)	Calculation (MHz)	Mea.-Cal. (MHz)
2	66	0	–	–
3	62	77.885	77.867	0.018
4	71	229.054	229.027	0.027
5	65	241.469	241.416	0.053
6	63	277.207	277.210	−0.003
7	67	319.838	319.979	−0.141
8	64	331.932	331.898	0.034
9	63	410.792	410.864	−0.072
10	70	481.387	481.387	0.000
11	68	509.301	509.408	−0.108
14	64	589.635	589.674	−0.039
15	65	651.382	651.382	0.000
16	69	713.708	713.694	0.013
17	67	750.519	750.487	0.032
18	65	789.097	789.063	0.034
19	68	811.485	811.483	0.002
20	66	840.531	840.530	0.001
21	67	894.544	894.478	0.066

Fitted hyperfine parameters for the excited state B

standard dev. (MHz)	0.060
eqQ_B (MHz)	$-571.756(86)^{\ddagger}$
C_B (MHz)	0.660831(90)
d_B (MHz)	−0.4260(68)
δ_B (MHz)	0.3647(59)

Hyperfine parameters for the ground state X used in th fit

eqQ_X (MHz)*	−2453.36
C_X (MHz)*	0.00315478
d_X (MHz)†	0.001524
δ_X (MHz)†	0.003705

* eqQ_X and C_X are determined by equations B.2 and B.3, respectively.

†d_X and δ_X are fixed in the fit to 1.524 and 3.705 kHz, respectively.

‡Quoted uncertainties (1σ) are estimated from the standard deviation of the fit.

B.42 R(74) 57-0

Table B.42: Hyperfine spectrum recorded at R(74) 57-0. Pump power: 5.2 - 5.4 mW, probe power: 0.16 mW, time constant of lock-in amplifier: 100 ms, cold-finger temperature: -2.28°C (vapor pressure: 3.3 Pa).

a	**F′**	Measurement (MHz)	Calculation (MHz)	Mea.-Cal. (MHz)
1	75	−489.552	−489.561	0.009
2	71	−416.884	−416.943	0.059
3	74	−255.753	−255.691	−0.062
4	72	−230.555	−230.529	−0.026
5	73	−171.628	−171.568	−0.059
6	76	−161.499	−161.528	0.029
7	79	0	–	–
8	77	34.745	34.673	0.071
9	75	72.286	72.272	0.014
10	78	93.620	93.567	0.054
11	73	106.680	106.661	0.019
12	74	156.671	156.681	−0.010
13	76	268.664	268.677	−0.013
14	77	321.271	321.283	−0.012
15	75	354.572	354.571	0.001

Fitted hyperfine parameters for the excited state B

standard dev. (MHz)	0.044
eqQ_B (MHz)	−570.210(94)‡
C_B (MHz)	0.678716(54)
d_B (MHz)	−0.3092(44)
δ_B (MHz)	0.2500(65)

Hyperfine parameters for the ground state X used in th fit

eqQ_X (MHz)*	−2453.6
C_X (MHz)*	0.00315478
d_X (MHz)†	0.001524
δ_X (MHz)†	0.003705

* eqQ_X and C_X are determined by equations B.2 and B.3, respectively.

†d_X and δ_X are fixed in the fit to 1.524 and 3.705 kHz, respectively.

‡Quoted uncertainties (1σ) are estimated from the standard deviation of the fit.

B.43 P(80) 57-0

Table B.43: Hyperfine spectrum recorded at P(80) 57-0. Pump power: 5.7 - 6.0 mW, probe power: 0.19 mW, time constant of lock-in amplifier: 100 ms, cold-finger temperature: -2.28°C (vapor pressure: 3.3 Pa).

a	**F′**	Measurement (MHz)	Calculation (MHz)	Mea.-Cal. (MHz)
1	79	−561.844	−561.843	−0.001
2	75	−502.683	−502.701	0.019
3	78	−331.833	−331.780	−0.053
4	76	−312.486	−312.499	0.013
5	77	−250.721	−250.691	−0.030
6	80	−229.954	−230.014	0.060
7	83	−58.660	−58.642	−0.018
9	79	0	–	–
12	78	81.331	81.338	−0.007
13	80	199.481	199.476	0.005

Fitted hyperfine parameters for the excited state B

standard dev. (MHz)	0.037
eqQ_B (MHz)	−570.38(12)‡
C_B (MHz)	0.688579(74)
d_B (MHz)	−0.298(14)
δ_B (MHz)	0.240(21)

Hyperfine parameters for the ground state X used in th fit

eqQ_X (MHz)*	−2453.78
C_X (MHz)*	0.00315478
d_X (MHz)†	0.001524
δ_X (MHz)†	0.003705

* eqQ_X and C_X are determined by equations B.2 and B.3, respectively.

†d_X and δ_X are fixed in the fit to 1.524 and 3.705 kHz, respectively.

‡Quoted uncertainties (1σ) are estimated from the standard deviation of the fit.

B.44 R(83) 57-0

Table B.44: Hyperfine spectrum recorded at R(83) 57-0. Pump power: 4.2 - 4.8 mW, probe power: 0.2 mW, time constant of lock-in amplifier: 100 ms, cold-finger temperature: -2.28°C (vapor pressure: 3.3 Pa).

a	**F′**	Measurement (MHz)	Calculation (MHz)	Mea.-Cal. (MHz)
1	79	−641.420	−641.455	0.035
2	84	−336.607	−336.542	−0.066
3	80	−314.070	−314.079	0.009
4	83	−111.242	−111.164	−0.078
5	81	−101.945	−101.913	−0.031
8	85	0	−	−
9	81	32.891	32.905	−0.014
14	87	269.197	269.220	−0.023
15	83	301.691	301.713	−0.022
16	87	418.846	418.908	−0.062
17	85	429.085	429.072	0.013
18	83	440.033	440.021	0.011
21	85	572.169	572.135	0.035

Fitted hyperfine parameters for the excited state B

standard dev. (MHz)	0.046
eqQ_B (MHz)	−570.632(90)‡
C_B (MHz)	0.702332(76)
d_B (MHz)	−0.311(12)
δ_B (MHz)	0.280(11)

Hyperfine parameters for the ground state X used in th fit

eqQ_X (MHz)*	−2453.87
C_X (MHz)*	0.00315478
d_X (MHz)†	0.001524
δ_X (MHz)†	0.003705

* eqQ_X and C_X are determined by equations B.2 and B.3, respectively.

†d_X and δ_X are fixed in the fit to 1.524 and 3.705 kHz, respectively.

‡Quoted uncertainties (1σ) are estimated from the standard deviation of the fit.

B.45 R(95) 57-0

Table B.45: Hyperfine spectrum recorded at R(95) 57-0. Pump power: 4.6 - 5 mW, probe power: 0.18 mW, time constant of lock-in amplifier: 100 ms, cold-finger temperature: -2.28°C (vapor pressure: 3.3 Pa).

a	**F′**	Measurement (MHz)	Calculation (MHz)	Mea.-Cal. (MHz)
2	92	−387.112	−387.192	0.080
3	96	−364.004	−364.019	0.016
4	93	−164.377	−164.353	−0.024
5	95	−151.276	−151.193	−0.083
6	94	−86.081	−86.013	−0.068
7	93	−29.022	−29.054	0.032
8	97	−14.711	−14.779	0.068
9	101	0	–	–
10	94	178.608	178.632	−0.024
13	100	219.665	219.643	0.022
14	95	262.914	262.921	−0.007
15	99	277.825	277.728	0.097
16	95	401.440	401.469	−0.029
17	97	413.479	413.461	0.017
18	99	426.148	426.143	0.005
19	96	477.337	477.354	−0.017
20	98	495.774	495.771	0.003
21	97	556.222	556.223	−0.001

Fitted hyperfine parameters for the excited state B

standard dev. (MHz)	0.051
eqQ_B (MHz)	$-570.699(83)^{\ddagger}$
C_B (MHz)	0.741638(48)
d_B (MHz)	−0.3274(59)
δ_B (MHz)	0.3327(50)

Hyperfine parameters for the ground state X used in th fit

eqQ_X (MHz)*	−2454.28
C_X (MHz)*	0.00315478
d_X (MHz)†	0.001524
δ_X (MHz)†	0.003705

* eqQ_X and C_X are determined by equations B.2 and B.3, respectively.

†d_X and δ_X are fixed in the fit to 1.524 and 3.705 kHz, respectively.

‡Quoted uncertainties (1σ) are estimated from the standard deviation of the fit.

B.46 P(69) 58-0

Table B.46: Hyperfine spectrum recorded at P(69) 58-0. Pump power: 2.5 - 3 mW, probe power: 0.2 mW, time constant of lock-in amplifier: 100 ms, cold-finger temperature: -2.28°C (vapor pressure: 3.3 Pa).

a	**F′**	Measurement (MHz)	Calculation (MHz)	Mea.-Cal. (MHz)
1	63	0	–	–
3	64	314.464	314.574	−0.110
4	67	483.552	483.839	−0.287
9	65	653.996	653.967	0.029
10	72	760.887	761.106	−0.219
11	70	774.748	774.018	0.730
12	68	814.304	814.409	−0.105
15	67	902.211	902.524	−0.313
16	71	988.523	988.776	−0.253
17	69	1012.634	1012.631	0.003
18	67	1043.160	1043.097	0.063
19	70	1079.411	1079.318	0.093
20	68	1098.391	1098.213	0.178
21	69	1158.781	1158.773	0.009

Fitted hyperfine parameters for the excited state B

standard dev. (MHz)	0.30
eqQ_B (MHz)	−553.38(69)‡
C_B (MHz)	0.72696(53)
d_B (MHz)	0.589(49)
δ_B (MHz)	0.726(32)

Hyperfine parameters for the ground state X used in th fit

eqQ_X (MHz)*	−2453.47
C_X (MHz)*	0.00315478
d_X (MHz)†	0.001524
δ_X (MHz)†	0.003705

* eqQ_X and C_X are determined by equations B.2 and B.3, respectively.

†d_X and δ_X are fixed in the fit to 1.524 and 3.705 kHz, respectively.

‡Quoted uncertainties (1σ) are estimated from the standard deviation of the fit.

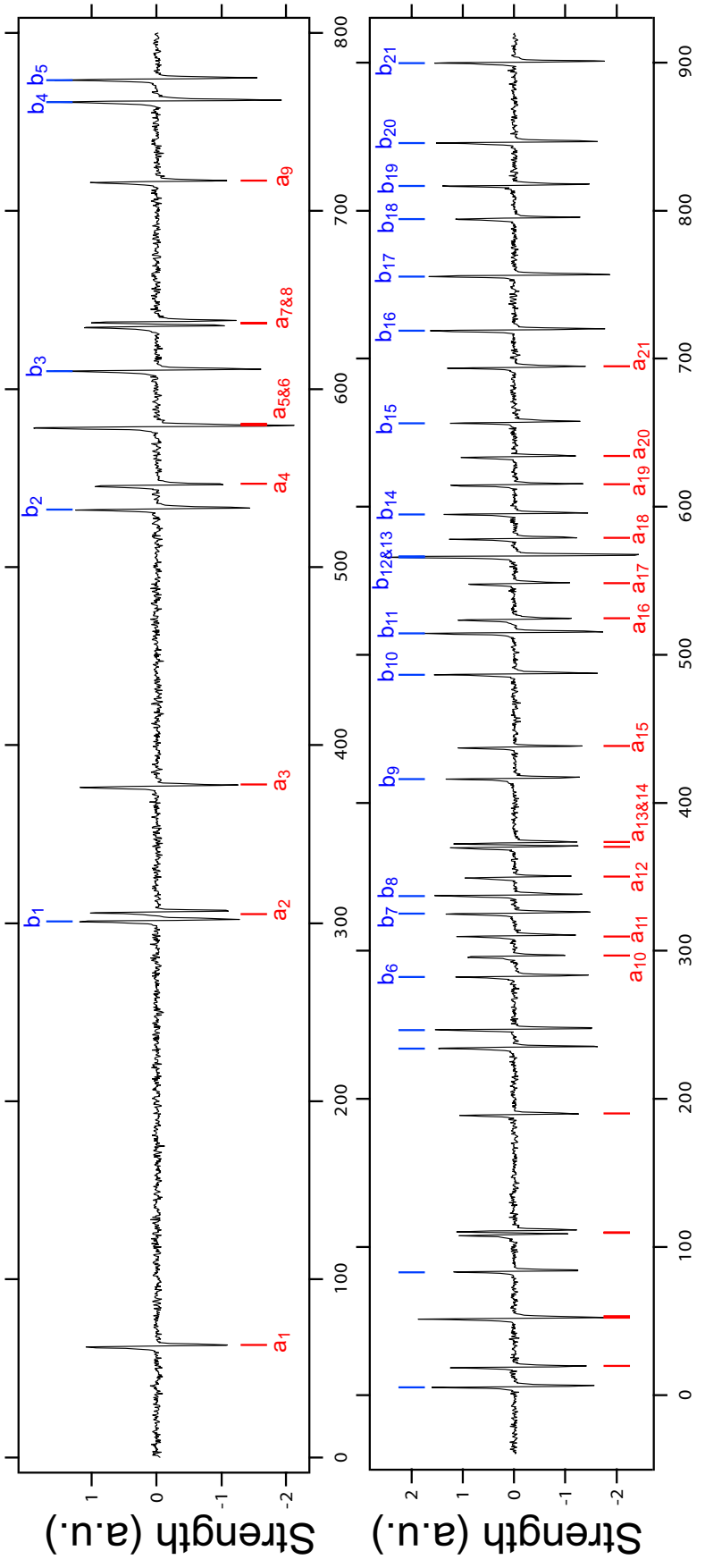

Figure B.1: Hyperfine spectrum recorded at P(69) 58-0 and R(65) 57-0. Hyperfine components a_1 - a_{21} belong to P(69) 58-0, b_1-b_{21} belong to R(65) 57-0. Vertical bars are fitting results using a four-term effective hyperfine Hamiltonian.

B.47 P(17) 59-0

Table B.47: Hyperfine spectrum recorded at P(17) 59-0. Pump power: 6.3 - 6.7 mW, probe power: 0.36 mW, time constant of lock-in amplifier: 100 ms, cold-finger temperature: -2.28°C (vapor pressure: 3.3 Pa).

a	**F′**	Measurement (MHz)	Calculation (MHz)	Mea.-Cal. (MHz)
1	11	0	–	–
2	16	105.642	105.664	−0.021
3	21	201.806	201.902	−0.096
4	12	232.772	232.805	−0.034
5*	17	381.348	381.216	0.132
6*	15	389.629	389.873	−0.244
7*	13	419.638	419.507	0.131
8*	14	489.586	489.846	−0.260
9	20	524.174	524.130	0.044
10	18	551.001	550.865	0.136
13	16	662.991	663.053	−0.062
14	14	686.773	686.808	−0.035
15	15	756.124	756.199	−0.076
16	19	781.578	781.537	0.041
21	17	982.114	982.092	0.021

Fitted hyperfine parameters for the excited state B

standard dev. (MHz)	0.080
eqQ_B (MHz)	$-568.61(21)^{\ddagger}$
C_B (MHz)	0.72138(46)
d_B (MHz)	−0.287(19)
δ_B (MHz)	0.139(16)

Hyperfine parameters for the ground state X used in th fit

eqQ_X (MHz)**	−2452.61
C_X (MHz)**	0.00315478
d_X (MHz)†	0.001524
δ_X (MHz)†	0.003705

* Not included in the fit.

** eqQ_X and C_X are determined by equations B.2 and B.3, respectively.

†d_X and δ_X are fixed in the fit to 1.524 and 3.705 kHz, respectively.

‡Quoted uncertainties (1σ) are estimated from the standard deviation of the fit.

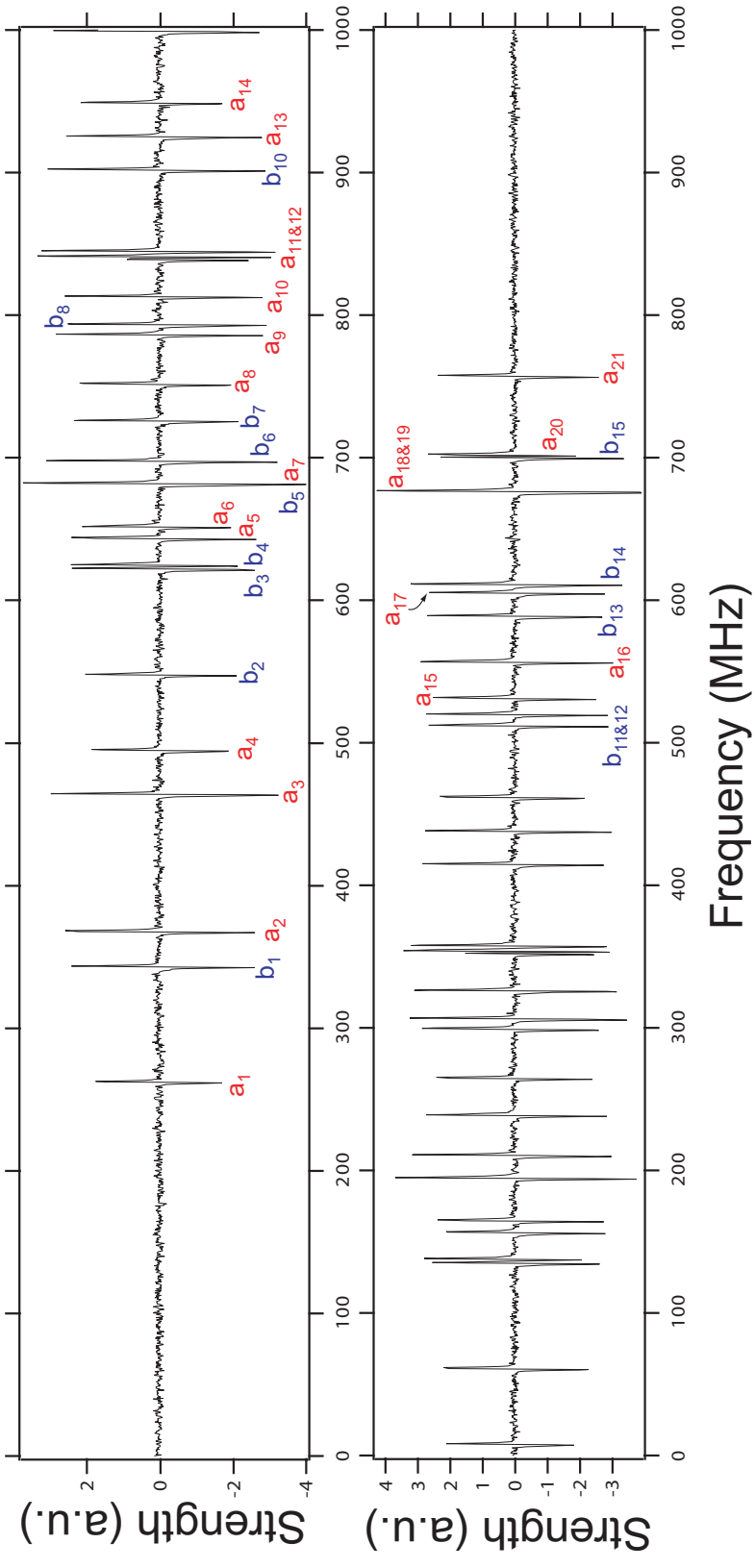

Figure B.2: Hyperfine spectrum recorded at P(17) 59-0 and R(18) 59-0. Hyperfine components a_1 - a_{21} belong to P(17) 59-0, b_1-b_{15} belong to R(18) 59-0.

B.48 R(18) 59-0

Table B.48: Hyperfine spectrum recorded at R(18) 59-0. Pump power: 6.3 - 6.7 mW, probe power: 0.36 mW, time constant of lock-in amplifier: 100 ms, cold-finger temperature: -2.28°C (vapor pressure: 3.3 Pa).

a	**F′**	Measurement (MHz)	Calculation (MHz)	Mea.-Cal. (MHz)
1	19	0	–	–
2	15	204.841	204.629	0.212
5*	16	338.729	338.843	−0.114
6	23	354.575	354.760	−0.185
7	17	382.732	382.974	−0.242
8	21	450.367	450.127	0.240
10	19	558.746	558.805	−0.059
11	17	655.972	656.080	−0.108
12	18	663.964	664.030	−0.067
13	20	732.906	732.819	0.086
14	21	755.079	754.957	0.122

Fitted hyperfine parameters for the excited state B

standard dev. (MHz)	0.20
eqQ_B (MHz)	$-564.99(44)^{\ddagger}$
C_B (MHz)	0.7332(14)
d_B (MHz)	−0.197(26)
δ_B (MHz)	0.030(37)

Hyperfine parameters for the ground state X used in th fit

eqQ_X (MHz)**	−2452.62
C_X (MHz)**	0.00315478
d_X (MHz)†	0.001524
δ_X (MHz)†	0.003705

* Not included in the fit.

** eqQ_X and C_X are determined by equations B.2 and B.3, respectively.

†d_X and δ_X are fixed in the fit to 1.524 and 3.705 kHz, respectively.

‡Quoted uncertainties (1σ) are estimated from the standard deviation of the fit.

B.49 P(27) 59-0

Table B.49: Hyperfine spectrum recorded at P(27) 59-0. Pump power: 2.5 - 2.7 mW, probe power: 0.27 mW, time constant of lock-in amplifier: 100 ms, cold-finger temperature: -2.28°C (vapor pressure: 3.3 Pa).

a	**F′**	Measurement (MHz)	Calculation (MHz)	Mea.-Cal. (MHz)
2	26	−491.743	−491.821	0.078
3*	31	−373.759	−374.299	0.540
4	22	−354.209	−354.168	−0.041
5	25	−220.600	−220.722	0.122
6	27	−203.946	−203.673	−0.273
8	24	−115.496	−115.654	0.159
12	29	0	–	–
13	26	66.577	66.632	−0.056
14	24	110.338	110.430	−0.092
17	27	235.758	235.808	−0.050
18	28	295.120	295.031	0.088
19	25	306.135	306.160	−0.025
20	26	340.070	340.107	−0.038
21	27	384.520	384.435	0.085

Fitted hyperfine parameters for the excited state B

standard dev. (MHz)	0.13
eqQ_B (MHz)	−573.49(28)‡
C_B (MHz)	0.71536(54)
d_B (MHz)	−0.569(14)
δ_B (MHz)	0.382(14)

Hyperfine parameters for the ground state X used in th fit

eqQ_X (MHz)**	−2452.69
C_X (MHz)**	0.00315478
d_X (MHz)†	0.001524
δ_X (MHz)†	0.003705

* Not included in the fit.

** eqQ_X and C_X are determined by equations B.2 and B.3, respectively.

†d_X and δ_X are fixed in the fit to 1.524 and 3.705 kHz, respectively.

‡Quoted uncertainties (1σ) are estimated from the standard deviation of the fit.

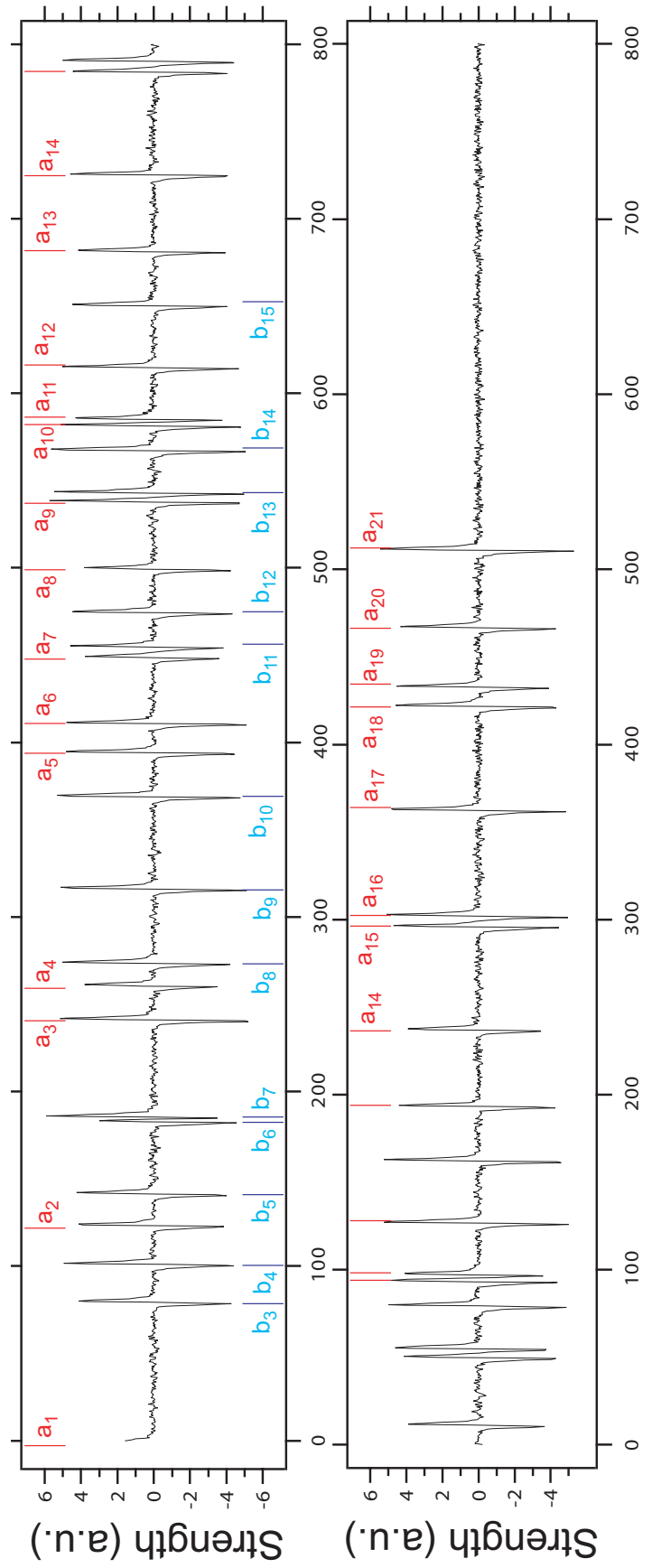

Figure B.3: Hyperfine spectrum recorded at P(27) 59-0 and R(28) 59-0. Hyperfine components a_1 - a_{21} belong to P(27) 59-0, b_3-b_{15} belong to R(28) 59-0. Vertical bars are fitting results using a four-term effective hyperfine Hamiltonian.

B.50 R(28) 59-0

Table B.50: Hyperfine spectrum recorded at R(28) 59-0. Pump power: 2.5 - 2.7 mW, probe power: 0.27 mW, time constant of lock-in amplifier: 100 ms, cold-finger temperature: -2.28°C (vapor pressure: 3.3 Pa).

a	**F′**	Measurement (MHz)	Calculation (MHz)	Mea.-Cal. (MHz)
3	28	0	–	–
4	30	21.725	21.876	−0.151
5	26	62.100	62.174	−0.074
8	31	194.318	194.381	−0.063
9	32	236.910	236.827	0.083
10	29	289.840	289.890	−0.049
12	28	395.205	395.176	0.029
14	31	488.189	488.164	0.026
15	29	571.196	571.211	−0.016

Fitted hyperfine parameters for the excited state B

standard dev. (MHz)	0.093
eqQ_B (MHz)	$-573.32(48)^{\ddagger}$
C_B (MHz)	0.72088(55)
d_B (MHz)	−0.476(24)
δ_B (MHz)	0.316(18)

Hyperfine parameters for the ground state X used in th fit

eqQ_X (MHz)*	−2452.7
C_X (MHz)*	0.00315478
d_X (MHz)†	0.001524
δ_X (MHz)†	0.003705

* eqQ_X and C_X are determined by equations B.2 and B.3, respectively.

†d_X and δ_X are fixed in the fit to 1.524 and 3.705 kHz, respectively.

‡Quoted uncertainties (1σ) are estimated from the standard deviation of the fit.

B.51 P(49) 59-1

Table B.51: Hyperfine spectrum recorded at P(49) 59-1. Pump power: 4.6 mW, probe power: 0.09 mW, time constant of lock-in amplifier: 100 ms, cold-finger temperature: -2.28°C (vapor pressure: 3.3 Pa).

a	**F′**	Measurement (MHz)	Calculation (MHz)	Mea.-Cal. (MHz)
2	48	−345.734	−345.723	−0.011
3	44	−247.286	−247.266	−0.019
4	53	−151.343	−151.327	−0.015
5	47	−95.746	−95.736	−0.010
6	45	−51.473	−51.469	−0.004
7	49	−34.934	−34.907	−0.027
8	46	0	−	−
9	45	81.782	81.797	−0.015
10	52	112.833	112.805	0.028
11	50	148.415	148.418	−0.003
12	51	194.168	194.163	0.005
13	48	214.852	214.879	−0.026
14	46	249.948	249.985	−0.037
15	47	309.851	309.890	−0.040
16	51	351.467	351.478	−0.010
17	49	397.873	397.877	−0.003
18	47	447.114	447.103	0.011
19	50	456.179	456.143	0.036
20	48	492.516	492.526	−0.010
21	49	542.739	542.738	0.000

Fitted hyperfine parameters for the excited state B

standard dev. (MHz)	0.022
eqQ_B (MHz)	$-571.695(39)^{\ddagger}$
C_B (MHz)	0.750322(35)
d_B (MHz)	−0.4326(26)
δ_B (MHz)	0.3335(20)

Hyperfine parameters for the ground state X used in th fit

eqQ_X (MHz)*	−2453.45
C_X (MHz)*	0.00318986
d_X (MHz)†	0.001524
δ_X (MHz)†	0.003705

* eqQ_X and C_X are determined by equations B.2 and B.3, respectively.

†d_X and δ_X are fixed in the fit to 1.524 and 3.705 kHz, respectively.

‡Quoted uncertainties (1σ) are estimated from the standard deviation of the fit.

B.52 R(81) 59-0

Table B.52: Hyperfine spectrum recorded at R(81) 59-0. Time constant of lock-in amplifier: 100 ms, cold-finger temperature: -2.28°C (vapor pressure: 3.3 Pa).

a	**F′**	Measurement (MHz)	Calculation (MHz)	Mea.-Cal. (MHz)
1	77	−636.036	−636.167	0.131
2	78	−299.459	−299.484	0.025
3	82	−281.279	−281.361	0.082
4	79	−77.525	−77.537	0.012
5	81	−66.353	−66.359	0.006
6	80	0	−	−
7	79	56.951	56.907	0.043
8	83	64.794	64.681	0.112
9	87	72.902	73.001	−0.099
10	80	261.676	261.686	−0.010
13	86	296.240	296.282	−0.041
14	81	345.647	345.634	0.013
15	85	354.050	353.981	0.069
16	81	483.678	483.669	0.008
17	83	493.246	493.187	0.059
18	85	503.852	503.829	0.022
19	82	558.535	558.525	0.010
20	84	575.676	575.655	0.020
21	83	636.260	636.202	0.058

Fitted hyperfine parameters for the excited state B

standard dev. (MHz)	0.065
eqQ_B (MHz)	$-572.12(11)^{\ddagger}$
C_B (MHz)	0.840592(60)
d_B (MHz)	−0.4355(78)
δ_B (MHz)	0.4337(59)

Hyperfine parameters for the ground state X used in th fit

eqQ_X (MHz)*	−2453.81
C_X (MHz)*	0.00315478
d_X (MHz)†	0.001524
δ_X (MHz)†	0.003705

* eqQ_X and C_X are determined by equations B.2 and B.3, respectively.

†d_X and δ_X are fixed in the fit to 1.524 and 3.705 kHz, respectively.

‡Quoted uncertainties (1σ) are estimated from the standard deviation of the fit.

B.53 P(87) 59-0

Table B.53: Hyperfine spectrum recorded at P(87) 59-0. Pump power: 5.7 - 6 mW, probe power: 0.19 mW, time constant of lock-in amplifier: 100 ms, cold-finger temperature: -2.28°C (vapor pressure: 3.3 Pa).

a	**F′**	Measurement (MHz)	Calculation (MHz)	Mea.-Cal. (MHz)
1	81	0	–	–
2	82	342.209	342.249	−0.041
3	86	377.556	377.573	−0.017
4	83	567.983	568.033	−0.050
5	85	587.498	587.547	−0.048
7	83	702.696	702.750	−0.054
8	87	728.626	728.568	0.058
9	91	754.889	754.993	−0.103
10	84	912.514	912.561	−0.047
13	90	972.537	972.536	0.000
14	85	1000.174	1000.183	−0.009
15	89	1026.670	1026.586	0.084
16	85	1138.301	1138.335	−0.033
17	87	1156.506	1156.469	0.036
18	89	1175.584	1175.566	0.017
19	86	1217.443	1217.430	0.013
20	88	1242.645	1242.583	0.062

Fitted hyperfine parameters for the excited state B

standard dev. (MHz)	0.055
eqQ_B (MHz)	$-572.555(90)^{\ddagger}$
C_B (MHz)	0.856503(46)
d_B (MHz)	−0.4360(65)
δ_B (MHz)	0.4444(55)

Hyperfine parameters for the ground state X used in th fit

eqQ_X (MHz)*	−2454.0
C_X (MHz)*	0.00315478
d_X (MHz)†	0.001524
δ_X (MHz)†	0.003705

* eqQ_X and C_X are determined by equations B.2 and B.3, respectively.
†d_X and δ_X are fixed in the fit to 1.524 and 3.705 kHz, respectively.
‡Quoted uncertainties (1σ) are estimated from the standard deviation of the fit.

B.54 P(21) 60-0

Table B.54: Hyperfine spectrum recorded at P(21) 60-0. Pump power: 4.7 - 5.3 mW, probe power: 0.32 mW, time constant of lock-in amplifier: 100 ms, cold-finger temperature: -2.28°C (vapor pressure: 3.3 Pa).

a	**F′**	Measurement (MHz)	Calculation (MHz)	Mea.-Cal. (MHz)
1	15	−536.534	−536.540	0.006
2	20	−420.233	−420.232	−0.001
3*	25	−308.604	−360.212	51.608
4	16	−288.380	−288.378	−0.002
7	17	−99.785	−99.787	0.002
8	18	−39.968	−39.961	−0.007
9	24	0	−	−
10	22	33.774	33.758	0.016
11	17	45.519	45.522	−0.003
12	23	67.340	67.331	0.009
13	20	138.500	138.503	−0.003
14	18	171.639	171.639	0.001
15	19	236.848	236.861	−0.013
16	23	254.163	254.181	−0.018
17	21	307.497	307.506	−0.009
20	20	407.927	407.915	0.012
21	21	458.147	458.132	0.015

Fitted hyperfine parameters for the excited state B

standard dev. (MHz)	0.011
eqQ_B (MHz)	−569.937(20)‡
C_B (MHz)	0.783323(37)
d_B (MHz)	−0.3773(13)
δ_B (MHz)	0.34612(86)

Hyperfine parameters for the ground state X used in th fit

eqQ_X (MHz)**	−2452.64
C_X (MHz)**	0.00315478
d_X (MHz)†	0.001524
δ_X (MHz)†	0.003705

* Not included in the fit.

** eqQ_X and C_X are determined by equations B.2 and B.3, respectively.

†d_X and δ_X are fixed in the fit to 1.524 and 3.705 kHz, respectively.

‡Quoted uncertainties (1σ) are estimated from the standard deviation of the fit.

B.55 R(34) 60-0

Table B.55: Hyperfine spectrum recorded at R(34) 60-0. Pump power: 6.6 - 6.8 mW, probe power: 0.4 mW, time constant of lock-in amplifier: 100 ms, cold-finger temperature: -2.28°C (vapor pressure: 3.3 Pa).

a	**F′**	Measurement (MHz)	Calculation (MHz)	Mea.-Cal. (MHz)
1	35	−403.333	−403.343	0.011
2	31	−245.273	−245.307	0.033
3	34	−142.603	−142.578	−0.025
4	36	−103.025	−103.027	0.002
5	32	−87.467	−87.463	−0.004
6	33	−42.678	−42.658	−0.020
7	39	0	–	–
8	37	75.354	75.321	0.033
9	38	121.291	121.277	0.014
10	35	157.115	157.126	−0.011
11	33	231.602	231.620	−0.018
12	34	258.132	258.144	−0.012
13	36	336.298	336.290	0.009
14	37	367.531	367.509	0.023
15	35	439.296	439.292	0.004

Fitted hyperfine parameters for the excited state B

standard dev. (MHz)	0.021
eqQ_B (MHz)	−569.964(45)‡
C_B (MHz)	0.799015(53)
d_B (MHz)	−0.3820(20)
δ_B (MHz)	0.3619(30)

Hyperfine parameters for the ground state X used in th fit

eqQ_X (MHz)*	−2452.78
C_X (MHz)*	0.00315478
d_X (MHz)†	0.001524
δ_X (MHz)†	0.003705

* eqQ_X and C_X are determined by equations B.2 and B.3, respectively.

†d_X and δ_X are fixed in the fit to 1.524 and 3.705 kHz, respectively.

‡Quoted uncertainties (1σ) are estimated from the standard deviation of the fit.

B.56 R(45) 60-1

Table B.56: Hyperfine spectrum recorded at R(45) 60-1. Pump power: 8 mW, probe power: 0.16 mW, time constant of lock-in amplifier: 100 ms, cold-finger temperature: -2.28°C (vapor pressure: 3.3 Pa).

a	**F′**	Measurement (MHz)	Calculation (MHz)	Mea.-Cal. (MHz)
3	42	−408.631	−408.684	0.053
4*	51	−293.039	−292.870	−0.168
5	45	−248.752	−248.673	−0.079
6	43	−209.932	−209.921	−0.011
7	47	−185.893	−185.853	−0.041
8	44	−155.234	−155.186	−0.049
9	43	−76.442	−76.448	0.006
10	50	−28.760	−28.690	−0.070
11	48	0.000	−	−
12	49	48.410	48.413	−0.004
13	46	63.019	63.041	−0.021
14	44	91.795	91.771	0.024
15	45	155.502	155.521	−0.019
16	49	207.805	207.866	−0.061
17	47	248.369	248.395	−0.026
18	45	292.724	292.745	−0.021
19	48	310.467	310.482	−0.015
20	46	340.319	340.289	0.029
21	47	393.809	393.795	0.013

Fitted hyperfine parameters for the excited state B

standard dev. (MHz)	0.043
eqQ_B (MHz)	−570.446(92)‡
C_B (MHz)	0.816760(82)
d_B (MHz)	−0.3800(0.0062)
δ_B (MHz)	0.3793(37)

Hyperfine parameters for the ground state X used in th fit

eqQ_X (MHz)**	−2453.38
C_X (MHz)**	0.00318986
d_X (MHz)†	0.001524
δ_X (MHz)†	0.003705

* Not included in the fit.

** eqQ_X and C_X are determined by equations B.2 and B.3, respectively.

†d_X and δ_X are fixed in the fit to 1.524 and 3.705 kHz, respectively.

‡Quoted uncertainties (1σ) are estimated from the standard deviation of the fit.

B.57 P(77) 60-0

Table B.57: Hyperfine spectrum recorded at P(77) 60-0. Pump power: 7.5 mW, probe power: 0.16 mW, time constant of lock-in amplifier: 100 ms, cold-finger temperature: -2.28°C (vapor pressure: 3.3 Pa).

a	F′	Measurement (MHz)	Fit 1: a_1-a_{10}, a_{13}-a_{21}		Fit 2: a_1-a_{10}, a_{13}	
			Calculation (MHz)	Mea.-Cal. (MHz)	Calculation (MHz)	Mea.-Cal. (MHz)
1	71	0.000	–	–	–	–
2	72	335.373	334.984	0.388	335.514	−0.141
3	76	353.666	352.257	1.408	354.035	−0.369
4	73	559.358	562.147	−2.789	559.578	−0.220
5	75	570.643	571.304	−0.661	570.609	0.034
6	74	637.558	639.582	−2.024	637.518	0.040
7	73	694.979	698.194	−3.216	695.096	−0.118
8	77	702.798	703.467	−0.669	702.235	0.563
9	81	714.630	718.434	−3.804	714.963	−0.334
10	74	897.526	898.396	−0.870	897.636	−0.110
13	80	937.374	939.232	−1.858	937.075	0.299
14	75	987.660	990.276	−2.616	984.829	2.831
15	79	1004.637	1001.267	3.370	995.625	9.012
16	75	1126.132	1127.383	−1.251	1123.250	2.882
17	77	1143.943	1140.909	3.034	1134.240	9.703
18	79	1152.239	1149.468	2.770	1145.480	6.759
19	76	1197.484	1197.532	−0.047	1196.070	1.414
20	78	1217.930	1216.899	1.031	1215.020	2.910
21	77	1283.635	1280.999	2.636	1276.850	6.785

Fitted hyperfine parameters for the excited state B

	Fit 1: a_1-a_{10}, a_{13}-a_{21}	Fit 2: a_1-a_{10}, a_{13}
standard dev. (MHz)	2.4	0.33
eqQ_B (MHz)	−550.7(3.8)‡	−563.68(89)‡
C_B (MHz)	0.9176(22)	0.91296(36)
d_B (MHz)	0.88(24)	0.119(64)
δ_B (MHz)	−0.30(18)	0.175(54)

Hyperfine parameters for the ground state X used in th fit

eqQ_X (MHz)*	−2453.69
C_X (MHz)*	0.00315478
d_X (MHz)†	0.001524
δ_X (MHz)†	0.003705

* eqQ_X and C_X are determined by equations B.2 and B.3, respectively.

†d_X and δ_X are fixed in the fit to 1.524 and 3.705 kHz, respectively.

‡Quoted uncertainties (1σ) are estimated from the standard deviation of the fit.

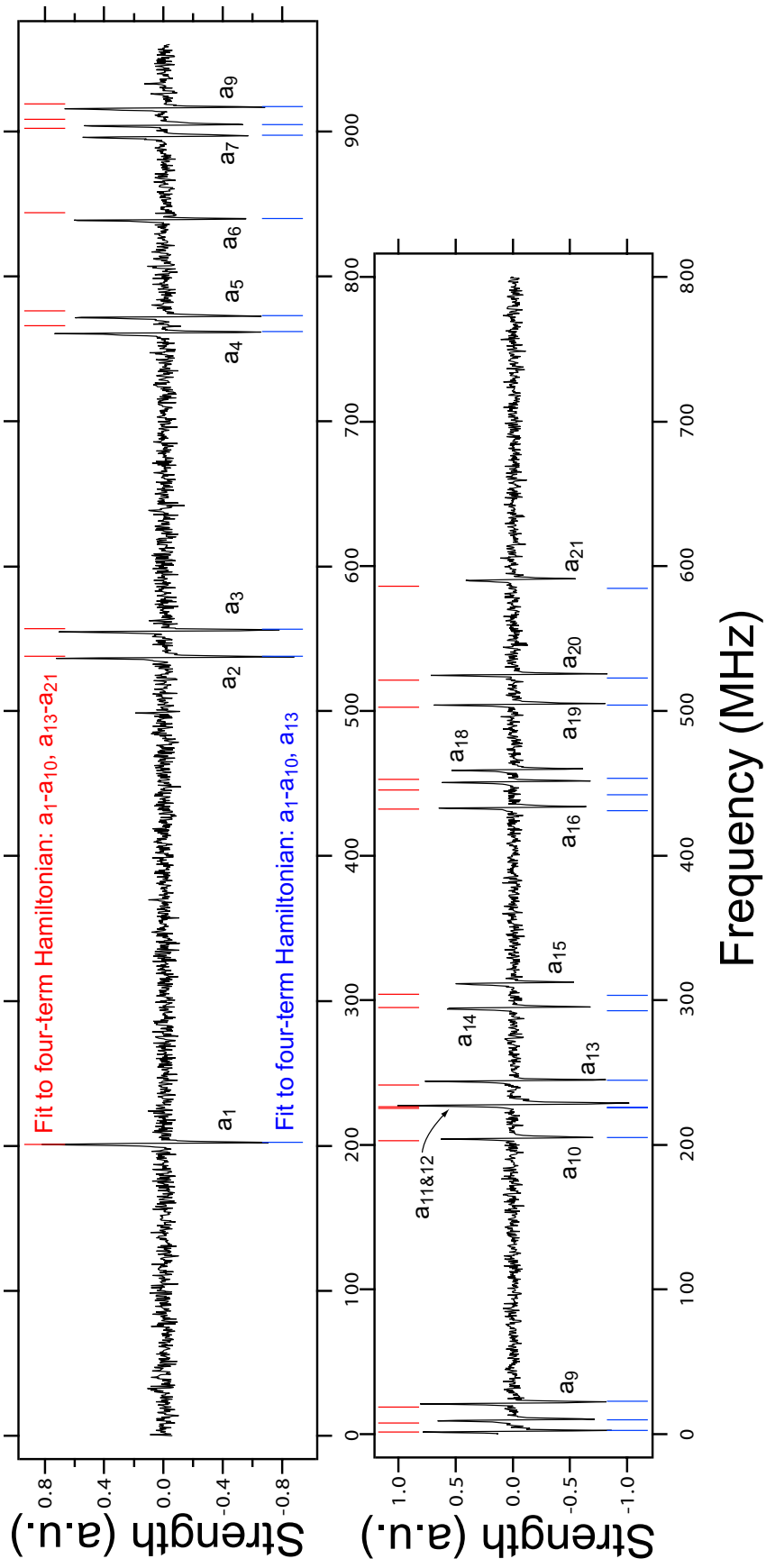

Figure B.4: Hyperfine spectrum recorded at P(77) 60-0.

B.58 P(84) 60-0

Table B.58: Hyperfine spectrum recorded at P(84) 60-0. Pump power: 6.4 - 6.6 mW, probe power: 0.19 mW, time constant of lock-in amplifier: 100 ms, cold-finger temperature: -2.28°C (vapor pressure: 3.3 Pa).

a	**F′**	Measurement (MHz)	Calculation (MHz)	Mea.-Cal. (MHz)
1	79	−383.291	−384.200	0.909
2*	83	–	−351.726	–
3	80	−170.299	−170.523	0.224
4	82	−145.383	−144.588	−0.795
5	81	−86.608	−86.104	−0.504
6	84	0	–	–
7	81	189.807	191.009	−1.202
8	83	207.952	207.792	0.160
9	85	219.298	218.693	0.605
10*	87	–	228.971	–
11	82	266.932	267.191	−0.258
12	86	297.494	299.535	−2.040
13	84	428.737	427.383	1.353
14	83	487.868	488.408	−0.540
15	85	504.357	503.047	1.309

Fitted hyperfine parameters for the excited state B

standard dev. (MHz)	1.1
eqQ_B (MHz)	−566.1(3.2)‡
C_B (MHz)	0.9093(21)
d_B (MHz)	−1.00(16)
δ_B (MHz)	0.25(17)

Hyperfine parameters for the ground state X used in th fit

eqQ_X (MHz)**	−2453.9
C_X (MHz)**	0.00315478
d_X (MHz)†	0.001524
δ_X (MHz)†	0.003705

* Not included in the fit.

** eqQ_X and C_X are determined by equations B.2 and B.3, respectively.

†d_X and δ_X are fixed in the fit to 1.524 and 3.705 kHz, respectively.

‡Quoted uncertainties (1σ) are estimated from the standard deviation of the fit.

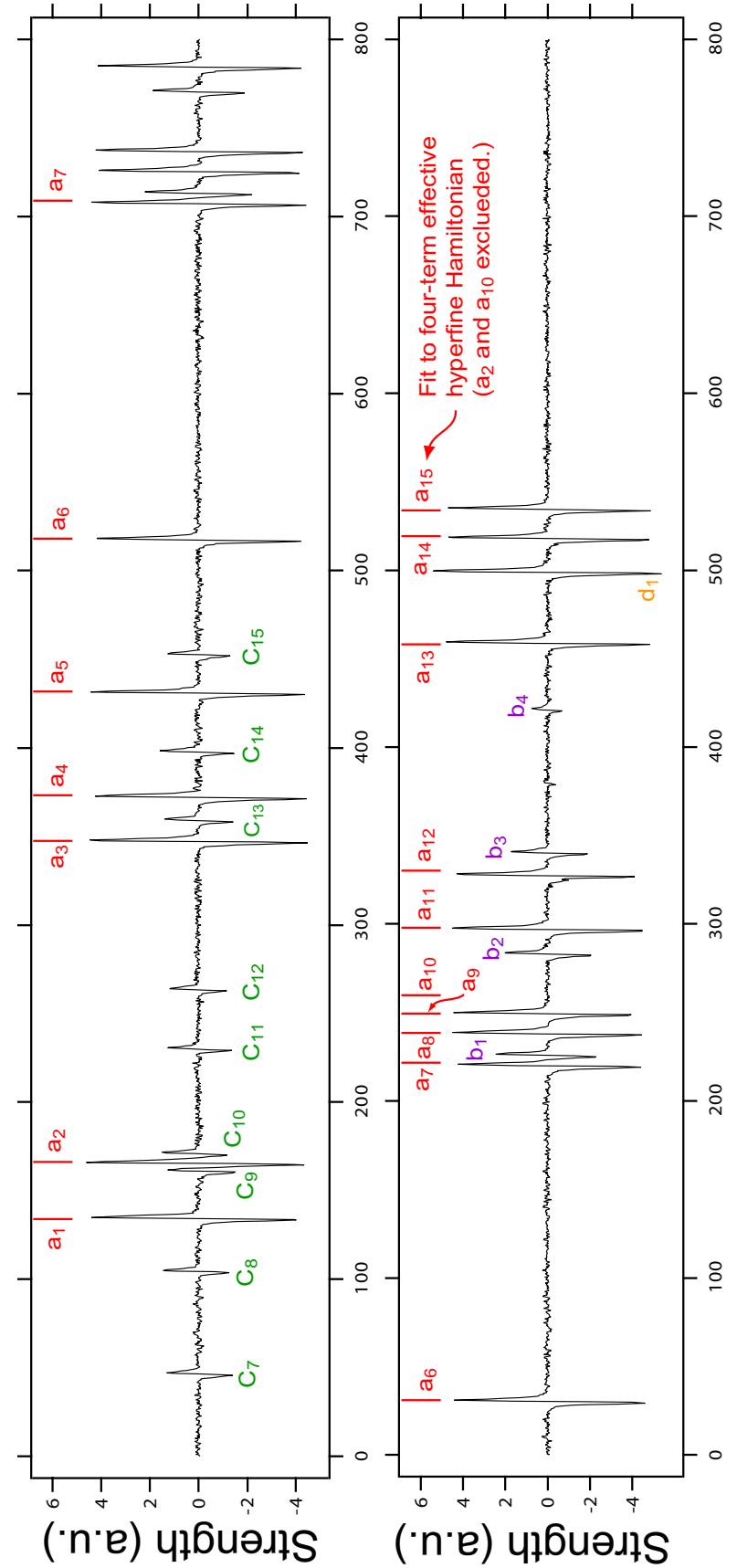

Figure B.5: Hyperfine spectrum recorded at P(84) 60-0. The vertical bars labeled a_1 - a_{15} are the fitted spectrum using a four-term effective Hamiltonian. Note that a_2 and a_{10} components are excluded from the fit. b_1 - b_4 arise from u - g mixing between the B and the $1_g(^1\Pi_g)$ states and b_2 is the crossover of b_1 and b_3. c_7 - c_{15} are identified as lines of a neighboring transition R(30) 64-1, and d_1 , left of a_{14} , belongs to another transition, P(81) 59-0.

B.59 R(99) 60-0

Table B.59: Hyperfine spectrum recorded at R(99) 60-0. Pump power: 5 - 5.7 mW, probe power: 0.2 mW, time constant of lock-in amplifier: 100 ms, cold-finger temperature: -2.28°C (vapor pressure: 3.3 Pa).

a	**F′**	Measurement (MHz)	Calculation (MHz)	Mea.-Cal. (MHz)
1	95	−702.474	−702.608	0.134
2	96	−329.889	−329.961	0.072
3	100	−179.831	−179.991	0.161
4	97	−76.598	−76.556	−0.042
5	99	0	−	−
6	98	33.094	33.144	−0.050
7	97	58.442	58.488	−0.046
8	101	201.312	201.105	0.206
9	98	298.417	298.442	−0.025
10	105	346.878	347.024	−0.146
11	100	380.897	380.837	0.060
12	99	413.600	413.599	0.001
13	102	448.910	448.698	0.212
14	104	533.008	533.022	−0.013
17	101	628.219	628.130	0.089
18	100	660.375	660.380	−0.005

Fitted hyperfine parameters for the excited state B

standard dev. (MHz)	0.12
eqQ_B (MHz)	−573.28(23)‡
C_B (MHz)	1.03267(11)
d_B (MHz)	−0.499(17)
δ_B (MHz)	0.688(14)

Hyperfine parameters for the ground state X used in th fit

eqQ_X (MHz)*	−2454.42
C_X (MHz)*	0.00315478
d_X (MHz)†	0.001524
δ_X (MHz)†	0.003705

* eqQ_X and C_X are determined by equations B.2 and B.3, respectively.

†d_X and δ_X are fixed in the fit to 1.524 and 3.705 kHz, respectively.

‡Quoted uncertainties (1σ) are estimated from the standard deviation of the fit.

B.60 P(17) 61-0

Table B.60: Hyperfine spectrum recorded at P(17) 61-0. Pump power: 7.7 - 8.7 mW, probe power: 0.33 mW, time constant of lock-in amplifier: 100 ms, cold-finger temperature: -2.28°C (vapor pressure: 3.3 Pa).

a	**F′**	Measurement (MHz)	Calculation (MHz)	Mea.-Cal. (MHz)
1	11	−797.493	−797.514	0.021
2	16	−683.672	−683.671	−0.001
3	21	−574.382	−574.358	−0.024
4	12	−562.972	−562.955	−0.017
7	13	−374.641	−374.647	0.005
8	14	−303.201	−303.189	−0.012
9	20	−254.512	−254.533	0.021
10	18	−233.833	−233.848	0.015
11	13	−218.245	−218.250	0.005
12	19	−199.944	−199.944	0.000
13	16	−126.262	−126.262	−0.001
14	14	−105.785	−105.774	−0.010
15	15	−34.674	−34.665	−0.008
16	19	0	−	−
17	17	42.708	42.711	−0.003
19	18	117.606	117.612	−0.006
20	16	138.459	138.455	0.004
21	17	195.324	195.324	0.001

Fitted hyperfine parameters for the excited state B

standard dev. (MHz)	0.013
eqQ_B (MHz)	$-569.550(24)^{\ddagger}$
C_B (MHz)	0.850067(59)
d_B (MHz)	−0.3944(14)
δ_B (MHz)	0.4414(10)

Hyperfine parameters for the ground state X used in th fit

eqQ_X (MHz)*	−2452.61
C_X (MHz)*	0.00315478
d_X (MHz)†	0.001524
δ_X (MHz)†	0.003705

* eqQ_X and C_X are determined by equations B.2 and B.3, respectively.

†d_X and δ_X are fixed in the fit to 1.524 and 3.705 kHz, respectively.

‡Quoted uncertainties (1σ) are estimated from the standard deviation of the fit.

B.61 R(36) 61-0

Table B.61: Hyperfine spectrum recorded at R(36) 61-0. Pump power: 6.2 - 6.9 mW, probe power: 0.38 mW, time constant of lock-in amplifier: 100 ms, cold-finger temperature: -2.28°C (vapor pressure: 3.3 Pa).

a	**F′**	Measurement (MHz)	Calculation (MHz)	Mea.-Cal. (MHz)
1	37	−421.236	−421.238	0.002
3	36	−165.277	−165.263	−0.015
6	35	−68.883	−68.892	0.009
7	41	0	−	−
8	39	66.597	66.575	0.022
9	40	116.201	116.175	0.026
10	37	139.458	139.473	−0.014
11	35	205.630	205.613	0.017
12	36	236.722	236.737	−0.015
13	38	322.588	322.595	−0.007
14	39	358.049	358.049	0.000
15	37	421.502	421.504	−0.002

Fitted hyperfine parameters for the excited state B

standard dev. (MHz)	0.016
eqQ_B (MHz)	−569.603(42)‡
C_B (MHz)	0.875111(89)
d_B (MHz)	−0.4056(19)
δ_B (MHz)	0.4638(27)

Hyperfine parameters for the ground state X used in th fit

eqQ_X (MHz)*	−2452.8
C_X (MHz)*	0.00315478
d_X (MHz)†	0.001524
δ_X (MHz)†	0.003705

* eqQ_X and C_X are determined by equations B.2 and B.3, respectively.

†d_X and δ_X are fixed in the fit to 1.524 and 3.705 kHz, respectively.

‡Quoted uncertainties (1σ) are estimated from the standard deviation of the fit.

B.62 P(53) 61-0

Table B.62: Hyperfine spectrum recorded at P(53) 61-0. Pump power: 3.6 - 3.8 mW, probe power: 0.27 mW, time constant of lock-in amplifier: 100 ms, cold-finger temperature: -2.28°C (vapor pressure: 3.3 Pa).

a	**F′**	Measurement (MHz)	Calculation (MHz)	Mea.-Cal. (MHz)
2	52	−397.073	−397.104	0.031
3	48	−338.646	−338.693	0.047
4	51	−158.392	−158.319	−0.073
5	57	−145.488	−145.453	−0.035
6	49	−133.464	−133.439	−0.025
9	49	0	−	−
10	56	105.502	105.498	0.004
11	54	120.218	120.142	0.076
12	52	164.111	164.133	−0.022
15	51	248.943	249.007	−0.064
16	55	332.913	332.925	−0.012
17	53	358.141	358.103	0.038
18	51	386.464	386.463	0.001
19	54	426.238	426.232	0.006
20	52	442.416	442.429	−0.013
21	53	502.797	502.773	0.023

Fitted hyperfine parameters for the excited state B

standard dev. (MHz)	0.044
eqQ_B (MHz)	$-570.037(79)^{\ddagger}$
C_B (MHz)	0.906087(75)
d_B (MHz)	−0.4162(42)
δ_B (MHz)	0.5154(42)

Hyperfine parameters for the ground state X used in th fit

eqQ_X (MHz)*	−2453.09
C_X (MHz)*	0.00315478
d_X (MHz)†	0.001524
δ_X (MHz)†	0.003705

* eqQ_X and C_X are determined by equations B.2 and B.3, respectively.

†d_X and δ_X are fixed in the fit to 1.524 and 3.705 kHz, respectively.

‡Quoted uncertainties (1σ) are estimated from the standard deviation of the fit.

B.63 P(83) 61-0

Table B.63: Hyperfine spectrum recorded at P(83) 61-0. Pump power: 2.9 - 3.3 mW, probe power: 0.3 mW, time constant of lock-in amplifier: 100 ms, cold-finger temperature: -2.28°C (vapor pressure: 3.3 Pa).

a	**F′**	Measurement (MHz)	Calculation (MHz)	Mea.-Cal. (MHz)
2	78	−507.178	−507.357	0.180
3	82	−431.730	−431.754	0.023
4	79	−271.267	−271.250	−0.017
5	81	−231.558	−231.441	−0.117
6	80	−179.580	−179.479	−0.101
7	79	−136.509	−136.511	0.002
8	83	−70.062	−70.123	0.061
9	87	0	–	–
10	80	83.070	83.116	−0.046
11	82	129.832	129.888	−0.055
12	84	159.110	158.999	0.110
13	81	181.304	181.364	−0.060
14	86	207.358	207.324	0.034
15	85	250.076	249.914	0.163
16	81	319.585	319.632	−0.048
17	83	358.725	358.686	0.040
18	85	399.644	399.588	0.057
19	82	409.168	409.229	−0.061
20	84	456.054	456.052	0.002
21	83	501.810	501.779	0.030

Fitted hyperfine parameters for the excited state B

standard dev. (MHz)	0.087
eqQ_B (MHz)	$-570.14(14)^{\ddagger}$
C_B (MHz)	1.02283(10)
d_B (MHz)	−0.422(10)
δ_B (MHz)	0.6224(83)

Hyperfine parameters for the ground state X used in th fit

eqQ_X (MHz)*	−2453.87
C_X (MHz)*	0.00315478
d_X (MHz)†	0.001524
δ_X (MHz)†	0.003705

* eqQ_X and C_X are determined by equations B.2 and B.3, respectively.

†d_X and δ_X are fixed in the fit to 1.524 and 3.705 kHz, respectively.

‡Quoted uncertainties (1σ) are estimated from the standard deviation of the fit.

B.64 P(23) 63-0

Table B.64: Hyperfine spectrum recorded at P(23) 63-0. Pump power: 10 - 12 mW, probe power: 0.56 mW, time constant of lock-in amplifier: 100 ms, cold-finger temperature: -2.28°C (vapor pressure: 3.3 Pa).

a	**F′**	Measurement (MHz)	Calculation (MHz)	Mea.-Cal. (MHz)
1	17	−512.525	−512.610	0.085
2	22	−369.072	−369.107	0.034
3	18	−254.068	−254.128	0.060
4	27	−222.042	−221.966	−0.076
5	21	−98.975	−99.008	0.033
6	23	−77.568	−77.621	0.053
7	19	−60.721	−60.721	0.000
8	20	0	–	–
11	24	99.857	99.808	0.048
12	25	139.832	139.812	0.021
13	22	190.842	190.843	−0.001
14	20	217.894	217.900	−0.006
15	21	285.940	285.922	0.018
16	25	322.664	322.668	−0.003
17	23	366.131	366.082	0.050
18	21	424.485	424.462	0.024
19	24	436.181	436.159	0.022
21	23	516.474	516.446	0.028

Fitted hyperfine parameters for the excited state B

standard dev. (MHz)	0.046
eqQ_B (MHz)	−568.464(78)‡
C_B (MHz)	1.01785(15)
d_B (MHz)	−0.4219(56)
δ_B (MHz)	0.6974(44)

Hyperfine parameters for the ground state X used in th fit

eqQ_X (MHz)*	−2452.66
C_X (MHz)*	0.00315478
d_X (MHz)†	0.001524
δ_X (MHz)†	0.003705

* eqQ_X and C_X are determined by equations B.2 and B.3, respectively.

†d_X and δ_X are fixed in the fit to 1.524 and 3.705 kHz, respectively.

‡Quoted uncertainties (1σ) are estimated from the standard deviation of the fit.

B.65 R(31) 63-0

Table B.65: Hyperfine spectrum recorded at R(31) 63-0. Pump power: 11.5 - 12 mW, probe power: 0.56 mW, time constant of lock-in amplifier: 100 ms, cold-finger temperature: -2.28°C (vapor pressure: 0.5 Pa).

a	**F′**	Measurement (MHz)	Calculation (MHz)	Mea.-Cal. (MHz)
1	27	−538.951	−539.091	0.140
2	32	−350.428	−350.513	0.084
3	28	−259.187	−259.239	0.052
4	37	−156.654	−156.523	−0.132
5	31	−93.728	−93.723	−0.005
6	29	−59.582	−59.596	0.014
7	33	−45.240	−45.294	0.054
8	30	0	−	−
9	29	75.889	75.861	0.028
10	36	120.878	120.887	−0.009
11	34	139.986	139.899	0.086
12	35	187.926	187.874	0.052
13	32	210.440	210.422	0.019
14	30	232.792	232.790	0.001
15	31	301.834	301.793	0.042
16	35	358.922	358.877	0.045
17	33	394.247	394.126	0.120
18	31	438.926	438.950	−0.024
19	34	464.144	464.176	−0.032
20	32	486.095	486.050	0.045
21	33	542.322	542.321	0.001

Fitted hyperfine parameters for the excited state B

standard dev. (MHz)	0.070
eqQ_B (MHz)	$-568.62(11)^{\ddagger}$
C_B (MHz)	1.03395(15)
d_B (MHz)	−0.4281(76)
δ_B (MHz)	0.7225(58)

Hyperfine parameters for the ground state X used in th fit

eqQ_X (MHz)*	−2452.74
C_X (MHz)*	0.00315478
d_X (MHz)†	0.001524
δ_X (MHz)†	0.003705

* eqQ_X and C_X are determined by equations B.2 and B.3, respectively.

†d_X and δ_X are fixed in the fit to 1.524 and 3.705 kHz, respectively.

‡Quoted uncertainties (1σ) are estimated from the standard deviation of the fit.

B.66 P(43) 63-0

Table B.66: Hyperfine spectrum recorded at P(43) 63-0. Pump power: 2.9 - 3.1 mW, probe power: 0.31 mW, time constant of lock-in amplifier: 100 ms, cold-finger temperature: -2.28°C (vapor pressure: 0.5 Pa).

a	**F′**	Measurement (MHz)	Calculation (MHz)	Mea.-Cal. (MHz)
2	42	−401.739	−401.728	−0.011
3	38	−338.308	−338.360	0.053
6	39	−133.354	−133.299	−0.055
7	43	−82.408	−82.434	0.026
8	40	−71.939	−71.892	−0.047
9	39	0	−	−
10	46	99.729	99.760	−0.030
11	44	111.260	111.201	0.059
15	41	245.329	245.376	−0.047
16	45	328.154	328.186	−0.032
17	43	352.523	352.516	0.007
18	41	382.527	382.535	−0.009
19	44	423.699	423.679	0.021
20	42	438.014	438.003	0.011
21	43	498.539	498.517	0.022

Fitted hyperfine parameters for the excited state B

standard dev. (MHz)	0.040
eqQ_B (MHz)	$-568.854(82)^{\ddagger}$
C_B (MHz)	1.05691(12)
d_B (MHz)	−0.4436(43)
δ_B (MHz)	0.7560(36)

Hyperfine parameters for the ground state X used in th fit

eqQ_X (MHz)*	−2452.91
C_X (MHz)*	0.00315478
d_X (MHz)†	0.001524
δ_X (MHz)†	0.003705

* eqQ_X and C_X are determined by equations B.2 and B.3, respectively.

†d_X and δ_X are fixed in the fit to 1.524 and 3.705 kHz, respectively.

‡Quoted uncertainties (1σ) are estimated from the standard deviation of the fit.

B.67 P(52) 63-0

Table B.67: Hyperfine spectrum recorded at P(52) 63-0. Pump power: 3.2 - 3.5 mW, probe power: 0.11 mW, time constant of lock-in amplifier: 100 ms, cold-finger temperature: -2.28°C (vapor pressure: 0.5 Pa).

a	**F′**	Measurement (MHz)	Calculation (MHz)	Mea.-Cal. (MHz)
1	51	−512.816	−512.839	0.024
2	47	−458.053	−458.122	0.069
3	50	−281.919	−281.865	−0.054
4	48	−269.828	−269.809	−0.019
5	49	−204.146	−204.071	−0.075
6	52	−181.445	−181.430	−0.014
7	55	0	–	–
8	53	21.992	21.889	0.103
9	51	48.952	48.935	0.017
10	49	72.012	72.006	0.006
11	54	89.917	89.869	0.048
12	50	126.788	126.805	−0.017
13	52	252.280	252.286	−0.007
14	53	309.774	309.762	0.011
15	51	330.435	330.441	−0.005

Fitted hyperfine parameters for the excited state B

standard dev. (MHz)	0.051
eqQ_B (MHz)	$-569.08(11)^{\ddagger}$
C_B (MHz)	1.084930(90)
d_B (MHz)	−0.4532(49)
δ_B (MHz)	0.7987(73)

Hyperfine parameters for the ground state X used in th fit

eqQ_X (MHz)*	−2453.07
C_X (MHz)*	0.00315478
d_X (MHz)†	0.001524
δ_X (MHz)†	0.003705

* eqQ_X and C_X are determined by equations B.2 and B.3, respectively.

†d_X and δ_X are fixed in the fit to 1.524 and 3.705 kHz, respectively.

‡Quoted uncertainties (1σ) are estimated from the standard deviation of the fit.

B.68 P(19) 65-0

Table B.68: Hyperfine spectrum recorded at P(19) 65-0. Pump power: 7 mW, time constant of lock-in amplifier: 100 ms, cold-finger temperature: -2.28°C (vapor pressure: 0.5 Pa).

a	**F′**	Measurement (MHz)	Calculation (MHz)	Mea.-Cal. (MHz)
1	13	−298.340	−298.408	0.068
2	18	−154.044	−154.039	−0.006
3	14	−50.181	−50.202	0.021
4	23	0	−	−
5	17	119.391	119.429	−0.039
6	19	134.999	134.980	0.019
7	15	144.428	144.432	−0.004
8	16	214.591	214.621	−0.030
9	15	292.968	292.977	−0.009
10	22	305.584	305.527	0.056
11	20	315.048	314.984	0.064
12	21	357.001	356.913	0.089
13	18	405.858	405.903	−0.045
14	16	421.004	421.060	−0.056
15	17	495.405	495.421	−0.016
16	21	551.325	551.292	0.033
17	19	582.592	582.572	0.019
18	17	635.772	635.800	−0.028
19	20	662.449	662.434	0.015
20	18	675.359	675.385	−0.026
21	19	735.217	735.206	0.011

Fitted hyperfine parameters for the excited state B

standard dev. (MHz)	0.043
eqQ_B (MHz)	−566.342(63)‡
C_B (MHz)	1.21056(14)
d_B (MHz)	−0.4648(37)
δ_B (MHz)	1.0373(32)

Hyperfine parameters for the ground state X used in th fit

eqQ_X (MHz)*	−2452.62
C_X (MHz)*	0.00315478
d_X (MHz)†	0.001524
δ_X (MHz)†	0.003705

* eqQ_X and C_X are determined by equations B.2 and B.3, respectively.

†d_X and δ_X are fixed in the fit to 1.524 and 3.705 kHz, respectively.

‡Quoted uncertainties (1σ) are estimated from the standard deviation of the fit.

B.69 P(33) 65-0

Table B.69: Hyperfine spectrum recorded at P(33) 65-0. Pump power: 11 - 12 mW, probe power: 0.57 mW, time constant of lock-in amplifier: 100 ms, cold-finger temperature: -2.28°C (vapor pressure: 3.3 Pa).

a	**F′**	Measurement (MHz)	Calculation (MHz)	Mea.-Cal. (MHz)
1	27	−626.827	−626.894	0.067
2	32	−410.684	−410.691	0.006
3	28	−338.119	−338.164	0.045
4	37	−181.026	−180.985	−0.041
5	31	−160.612	−160.577	−0.035
6	29	−134.159	−134.135	−0.024
7	33	−97.279	−97.328	0.049
8	30	−71.597	−71.544	−0.053
9	29	0	−	−
14	30	166.034	166.097	−0.063
15	31	238.347	238.358	−0.012
16	35	318.010	318.007	0.003
17	33	341.678	341.634	0.044
18	31	375.236	375.208	0.028
19*	34	417.943	417.154	0.789
20	32	429.299	429.294	0.004
21	33	489.868	489.808	0.060

Fitted hyperfine parameters for the excited state B

standard dev. (MHz)	0.046
eqQ_B (MHz)	$-566.504(73)^{\ddagger}$
C_B (MHz)	1.24010(14)
d_B (MHz)	−0.4893(33)
δ_B (MHz)	1.0966(34)

Hyperfine parameters for the ground state X used in th fit

eqQ_X (MHz)**	−2452.76
C_X (MHz)**	0.00315478
d_X (MHz)†	0.001524
δ_X (MHz)†	0.003705

* Not included in the fit.

** eqQ_X and C_X are determined by equations B.2 and B.3, respectively.

†d_X and δ_X are fixed in the fit to 1.524 and 3.705 kHz, respectively.

‡Quoted uncertainties (1σ) are estimated from the standard deviation of the fit.

B.70 R(43) 65-0

Table B.70: Hyperfine spectrum recorded at R(43) 65-0. Pump power: 10.5 mW, probe power: 0.41 mW, time constant of lock-in amplifier: 100 ms, cold-finger temperature: -2.28°C (vapor pressure: 0.5 Pa).

a	**F′**	Measurement (MHz)	Calculation (MHz)	Mea.-Cal. (MHz)
1	39	−661.109	−661.151	0.042
2	44	−367.446	−367.409	−0.037
3	40	−349.125	−349.143	0.017
8	45	−35.328	−35.373	0.045
9	41	0	–	–
10	46	171.306	171.284	0.022
14	47	240.460	240.486	−0.026
15	43	269.130	269.088	0.041
19	44	474.777	474.783	−0.007
20	46	485.587	485.660	−0.072
21	45	547.114	547.020	0.094

Fitted hyperfine parameters for the excited state B

standard dev. (MHz)	0.056
eqQ_B (MHz)	$-567.21(11)^{\ddagger}$
C_B (MHz)	1.28195(20)
d_B (MHz)	−0.4901(68)
δ_B (MHz)	1.1712(49)

Hyperfine parameters for the ground state X used in th fit

eqQ_X (MHz)*	−2452.91
C_X (MHz)*	0.00315478
d_X (MHz)†	0.001524
δ_X (MHz)†	0.003705

* eqQ_X and C_X are determined by equations B.2 and B.3, respectively.

†d_X and δ_X are fixed in the fit to 1.524 and 3.705 kHz, respectively.

‡Quoted uncertainties (1σ) are estimated from the standard deviation of the fit.

B.71 P(33) 69-0

Table B.71: Hyperfine spectrum recorded at P(33) 69-0. Pump power: 11 - 12.2 mW, probe power: 0.31 mW, time constant of lock-in amplifier: 100 ms, cold-finger temperature: -2.28°C (vapor pressure: 3.3 Pa).

a	**F′**	Measurement (MHz)	Calculation (MHz)	Mea.-Cal. (MHz)
1*	27	−606.777	−607.569	0.792
6	30	0	–	–
9	29	53.172	53.170	0.002
12	32	261.448	261.495	−0.047
13	36	284.401	284.446	−0.045
14	35	321.367	321.293	0.073
15	31	331.113	331.104	0.008
18	35	492.871	492.884	−0.013
19	32	544.099	544.090	0.009
20	34	572.866	572.835	0.031
21	33	622.070	622.099	−0.029

Fitted hyperfine parameters for the excited state B

standard dev. (MHz)	0.044
eqQ_B (MHz)	−558.63(12)‡
C_B (MHz)	1.85049(22)
d_B (MHz)	−0.6800(72)
δ_B (MHz)	2.3114(69)

Hyperfine parameters for the ground state X used in th fit

eqQ_X (MHz)**	−2452.76
C_X (MHz)**	0.00315478
d_X (MHz)†	0.001524
δ_X (MHz)†	0.003705

* Not included in the fit.

** eqQ_X and C_X are determined by equations B.2 and B.3, respectively.

†d_X and δ_X are fixed in the fit to 1.524 and 3.705 kHz, respectively.

‡Quoted uncertainties (1σ) are estimated from the standard deviation of the fit.

B.72 P(39) 69-0

Table B.72: Hyperfine spectrum recorded at P(39) 69-0. Pump power: 12.2 - 12.9 mW, probe power: 0.33 mW, time constant of lock-in amplifier: 100 ms, cold-finger temperature: -2.28°C (vapor pressure: 3.3 Pa).

a	**F′**	Measurement (MHz)	Calculation (MHz)	Mea.-Cal. (MHz)
1	33	−580.517	−580.629	0.112
2	34	−255.867	−255.896	0.029
3	38	−218.638	−218.820	0.183
4	35	−25.314	−25.316	0.003
5	37	0	−	−
6	36	61.368	61.432	−0.063
7	35	105.586	105.690	−0.104
8	39	131.165	130.987	0.178
9*	43	183.857	184.845	−0.988
10	36	309.903	309.936	−0.033
15	41	444.440	444.506	−0.066
16	37	542.312	542.239	0.073
17	39	570.913	570.758	0.155
18	41	610.643	610.788	−0.145
19	38	631.723	631.681	0.042
20	40	678.759	678.787	−0.028
21	39	718.777	718.641	0.135

Fitted hyperfine parameters for the excited state B

standard dev. (MHz)	0.12
eqQ_B (MHz)	$-560.05(23)^{\ddagger}$
C_B (MHz)	1.89425(41)
d_B (MHz)	−0.696(12)
δ_B (MHz)	2.422(10)

Hyperfine parameters for the ground state X used in th fit

eqQ_X (MHz)**	−2452.85
C_X (MHz)**	0.00315478
d_X (MHz)†	0.001524
δ_X (MHz)†	0.003705

* Not included in the fit.

** eqQ_X and C_X are determined by equations B.2 and B.3, respectively.

†d_X and δ_X are fixed in the fit to 1.524 and 3.705 kHz, respectively.

‡Quoted uncertainties (1σ) are estimated from the standard deviation of the fit.

B.73 R(44) 69-0

Table B.73: Hyperfine spectrum recorded at R(44) 69-0. Pump power: 16 - 17 mW, probe power: 0.5 mW, time constant of lock-in amplifier: 100 ms, cold-finger temperature: -2.28°C (vapor pressure: 3.3 Pa).

a	**F′**	Measurement (MHz)	Calculation (MHz)	Mea.-Cal. (MHz)
1	41	−589.777	−589.827	0.050
2	45	−520.813	−520.853	0.040
3	42	−370.917	−370.941	0.025
4	44	−319.268	−319.207	−0.062
5	43	−272.997	−272.970	−0.027
6	46	−154.066	−154.055	−0.011
7	43	0	−	−
8	45	45.463	45.436	0.027
11*	49	137.248	138.271	−1.023
13	46	285.342	285.334	0.007
14	45	324.711	324.551	0.160
15	47	374.804	374.868	−0.065

Fitted hyperfine parameters for the excited state B

standard dev. (MHz)	0.076
eqQ_B (MHz)	−561.17(27)‡
C_B (MHz)	1.96255(38)
d_B (MHz)	−0.732(12)
δ_B (MHz)	2.5258(96)

Hyperfine parameters for the ground state X used in th fit

eqQ_X (MHz)**	−2452.93
C_X (MHz)**	0.00315478
d_X (MHz)†	0.001524
δ_X (MHz)†	0.003705

* Not included in the fit.

** eqQ_X and C_X are determined by equations B.2 and B.3, respectively.

†d_X and δ_X are fixed in the fit to 1.524 and 3.705 kHz, respectively.

‡Quoted uncertainties (1σ) are estimated from the standard deviation of the fit.

B.74 R(49) 69-0

Table B.74: Hyperfine spectrum recorded at R(49) 69-0. Pump power: 14.3 - 15.2 mW, probe power: 0.36 mW, time constant of lock-in amplifier: 100 ms, cold-finger temperature: -2.28°C (vapor pressure: 3.3 Pa).

a	**F′**	Measurement (MHz)	Calculation (MHz)	Mea.-Cal. (MHz)
2	46	−523.882	−524.343	0.461
3	50	−380.255	−380.084	−0.171
4	47	−268.727	−268.742	0.016
5	49	−192.278	−191.887	−0.390
6	48	−157.767	−157.453	−0.313
7	47	−137.994	−137.931	−0.063
8	51	0	−	−
9	48	98.589	98.704	−0.115
10	55	165.183	165.481	−0.298
11	50	186.022	186.212	−0.190
12	49	218.982	219.150	−0.169
13	52	253.243	253.092	0.151
17	51	437.234	437.163	0.071
18	50	471.497	471.602	−0.105
19	53	529.132	528.992	0.139
20	52	569.054	569.047	0.008
21	51	583.396	583.252	0.144

Fitted hyperfine parameters for the excited state B

standard dev. (MHz)	0.24
eqQ_B (MHz)	$-560.28(43)^{\ddagger}$
C_B (MHz)	2.01971(48)
d_B (MHz)	−0.862(28)
δ_B (MHz)	2.597(25)

Hyperfine parameters for the ground state X used in th fit

eqQ_X (MHz)*	−2453.01
C_X (MHz)**	0.00315478
d_X (MHz)†	0.001524
δ_X (MHz)†	0.003705

* eqQ_X and C_X are determined by equations B.2 and B.3, respectively.

†d_X and δ_X are fixed in the fit to 1.524 and 3.705 kHz, respectively.

‡Quoted uncertainties (1σ) are estimated from the standard deviation of the fit.

B.75 P(53) 69-0

Table B.75: Hyperfine spectrum recorded at P(53) 69-0. Pump power: 11.8 - 12.3 mW, probe power: 0.32 mW, time constant of lock-in amplifier: 100 ms, cold-finger temperature: -2.28°C (vapor pressure: 0.5 Pa).

a	**F′**	Measurement (MHz)	Calculation (MHz)	Mea.-Cal. (MHz)
1	47	−739.507	−739.797	0.290
2	48	−373.953	−374.122	0.169
3	52	−211.757	−212.063	0.306
4	49	−114.853	−114.913	0.060
5	51	−29.775	−29.860	0.085
6	50	0	−	−
7	49	15.948	15.980	−0.032
8	53	174.497	174.231	0.267
9	50	259.066	258.936	0.130
12	51	382.908	382.701	0.207
13	54	432.661	432.598	0.062
14	51	518.257	518.003	0.254
17	53	610.770	610.520	0.250
18	52	640.376	640.188	0.188
19	55	711.531	711.985	−0.454
20	54	746.133	746.299	−0.167
21	53	756.360	756.079	0.281

Fitted hyperfine parameters for the excited state B

standard dev. (MHz)	0.25
eqQ_B (MHz)	$-562.09(50)^{\ddagger}$
C_B (MHz)	2.04973(57)
d_B (MHz)	−0.793(28)
δ_B (MHz)	2.691(22)

Hyperfine parameters for the ground state X used in th fit

eqQ_X (MHz)*	−2453.09
C_X (MHz)*	0.00315478
d_X (MHz)†	0.001524
δ_X (MHz)†	0.003705

* eqQ_X and C_X are determined by equations B.2 and B.3, respectively.
†d_X and δ_X are fixed in the fit to 1.524 and 3.705 kHz, respectively.
‡Quoted uncertainties (1σ) are estimated from the standard deviation of the fit.

B.76 P(35) 70-0

Table B.76: Hyperfine spectrum recorded at P(35) 70-0. Pump power: 8.7 - 9.6 mW, probe power: 0.24 mW, time constant of lock-in amplifier: 100 ms, cold-finger temperature: -2.28°C (vapor pressure: 0.5 Pa).

a	**F′**	Measurement (MHz)	Calculation (MHz)	Mea.-Cal. (MHz)
2	30	−563.491	−563.887	0.396
3	34	−528.460	−528.513	0.053
4	31	−332.665	−332.778	0.113
5	33	−307.378	−307.199	−0.179
6	32	−245.465	−245.315	−0.150
7	31	−202.640	−202.590	−0.050
8	35	−179.632	−179.715	0.083
9	39	−124.601	−124.337	−0.264
10	32	0	−	−
13	33	98.944	98.958	−0.015
14	38	109.664	109.668	−0.004
15	37	135.050	134.859	0.192
16	33	232.623	232.662	−0.039
17	35	262.622	262.528	0.094
18	37	305.238	305.131	0.106
19	34	323.973	323.973	−0.001
20	36	374.275	374.173	0.102
21	35	411.178	411.038	0.140

Fitted hyperfine parameters for the excited state B

standard dev. (MHz)	0.17
eqQ_B (MHz)	$-556.68(29)^{\ddagger}$
C_B (MHz)	2.08631(41)
d_B (MHz)	−0.832(17)
δ_B (MHz)	2.815(12)

Hyperfine parameters for the ground state X used in th fit

eqQ_X (MHz)*	−2452.79
C_X (MHz)*	0.00315478
d_X (MHz)†	0.001524
δ_X (MHz)†	0.003705

* eqQ_X and C_X are determined by equations B.2 and B.3, respectively.

†d_X and δ_X are fixed in the fit to 1.524 and 3.705 kHz, respectively.

‡Quoted uncertainties (1σ) are estimated from the standard deviation of the fit.

B.77 R(37) 70-0

Table B.77: Hyperfine spectrum recorded at R(37) 70-0. Pump power: 12 - 13.3 mW, probe power: 0.34 mW, time constant of lock-in amplifier: 100 ms, cold-finger temperature: -2.28°C (vapor pressure: 0.5 Pa).

a	**F′**	Measurement (MHz)	Calculation (MHz)	Mea.-Cal. (MHz)
1	33	−762.560	−762.987	0.427
2	34	−431.176	−431.304	0.128
3	38	−359.002	−358.823	−0.179
4	35	−191.524	−191.414	−0.111
5	37	−148.157	−147.762	−0.395
6	36	−95.586	−95.253	−0.333
7	35	−61.622	−61.405	−0.217
8	39	0	−	−
9	43	93.693	94.097	−0.404
10	36	151.684	151.817	−0.133
11	38	208.463	208.600	−0.137
12	40	235.942	235.782	0.160
13	37	259.070	259.161	−0.091
14	42	316.988	317.079	−0.091
15	41	333.885	333.699	0.186
16	37	392.762	392.834	−0.073
17	39	441.726	441.609	0.117
18	38	493.749	493.798	−0.049
19	41	502.559	502.427	0.132
20	40	562.065	561.969	0.096
21	39	589.733	589.542	0.191

Fitted hyperfine parameters for the excited state B

standard dev. (MHz)	0.23
eqQ_B (MHz)	$-557.55(32)^{\ddagger}$
C_B (MHz)	2.12504(50)
d_B (MHz)	−0.873(21)
δ_B (MHz)	2.884(18)

Hyperfine parameters for the ground state X used in th fit

eqQ_X (MHz)*	−2452.82
C_X (MHz)*	0.00315478
d_X (MHz)†	0.001524
δ_X (MHz)†	0.003705

* eqQ_X and C_X are determined by equations B.2 and B.3, respectively.

†d_X and δ_X are fixed in the fit to 1.524 and 3.705 kHz, respectively.

‡Quoted uncertainties (1σ) are estimated from the standard deviation of the fit.

B.78 R(45) 70-0

Table B.78: Hyperfine spectrum recorded at R(45) 70-0. Pump power: 14.5 - 15.5 mW, probe power: 0.37 mW, time constant of lock-in amplifier: 100 ms, cold-finger temperature: -2.28°C (vapor pressure: 0.5 Pa).

a	**F′**	Measurement (MHz)	Calculation (MHz)	Mea.-Cal. (MHz)
2	42	−531.974	−532.264	0.290
3	46	−382.131	−382.001	−0.130
4	43	−274.590	−274.577	−0.012
5	45	−194.590	−194.253	−0.337
6	44	−161.667	−161.372	−0.294
7	43	−145.104	−144.971	−0.133
8	47	0	–	–
9	44	93.215	93.227	−0.012
10*	51	176.439	178.041	−1.602
11*	46	185.292	185.372	−0.080
12	45	216.692	216.695	−0.003
13	48	256.183	256.205	−0.022
14	45	350.577	350.489	0.088
17	47	439.247	439.149	0.098
18	46	471.892	471.888	0.004
19	49	537.401	537.676	−0.275
20	48	576.083	576.190	−0.106
21	47	585.542	585.354	0.187

Fitted hyperfine parameters for the excited state B

standard dev. (MHz)	0.20
eqQ_B (MHz)	−558.80(44)‡
C_B (MHz)	2.22994(62)
d_B (MHz)	−0.937(24)
δ_B (MHz)	3.045(17)

Hyperfine parameters for the ground state X used in th fit

eqQ_X (MHz)**	−2452.94
C_X (MHz)**	0.00315478
d_X (MHz)†	0.001524
δ_X (MHz)†	0.003705

* Not included in the fit.

** eqQ_X and C_X are determined by equations B.2 and B.3, respectively.

†d_X and δ_X are fixed in the fit to 1.524 and 3.705 kHz, respectively.

‡Quoted uncertainties (1σ) are estimated from the standard deviation of the fit.

B.79 P(63) 70-0

Table B.79: Hyperfine spectrum recorded at P(63) 70-0. Pump power: 9.2 - 10.2 mW, probe power: 0.39 mW, time constant of lock-in amplifier: 100 ms, cold-finger temperature: -2.28°C (vapor pressure: 0.5 Pa).

a	**F′**	Measurement (MHz)	Calculation (MHz)	Mea.-Cal. (MHz)
1	57	−857.211	−857.998	0.787
2	58	−434.684	−434.920	0.235
3	59	−124.932	−124.817	−0.115
4	62	−51.349	−50.911	−0.437
5	59	0	−	−
6	60	42.332	42.589	−0.257
7	61	71.218	69.669	1.548
8	60	302.823	303.009	−0.186
9	63	383.840	384.297	−0.457
10	61	477.670	477.778	−0.108
11	62	503.611	503.878	−0.268
12	61	605.952	605.512	0.440
13	64	691.569	691.692	−0.123
16	63	811.490	811.286	0.204
17	65	863.653	863.537	0.116
18	66	913.131	913.468	−0.336
19	63	950.210	949.238	0.972

Fitted hyperfine parameters for the excited state B

standard dev. (MHz)	0.62
eqQ_B (MHz)	−584.3(1.2)‡
C_B (MHz)	2.5889(11)
d_B (MHz)	−2.408(50)
δ_B (MHz)	3.456(43)

Hyperfine parameters for the ground state X used in th fit

eqQ_X (MHz)*	−2453.31
C_X (MHz)*	0.00315478
d_X (MHz)†	0.001524
δ_X (MHz)†	0.003705

* eqQ_X and C_X are determined by equations B.2 and B.3, respectively.
†d_X and δ_X are fixed in the fit to 1.524 and 3.705 kHz, respectively.
‡Quoted uncertainties (1σ) are estimated from the standard deviation of the fit.

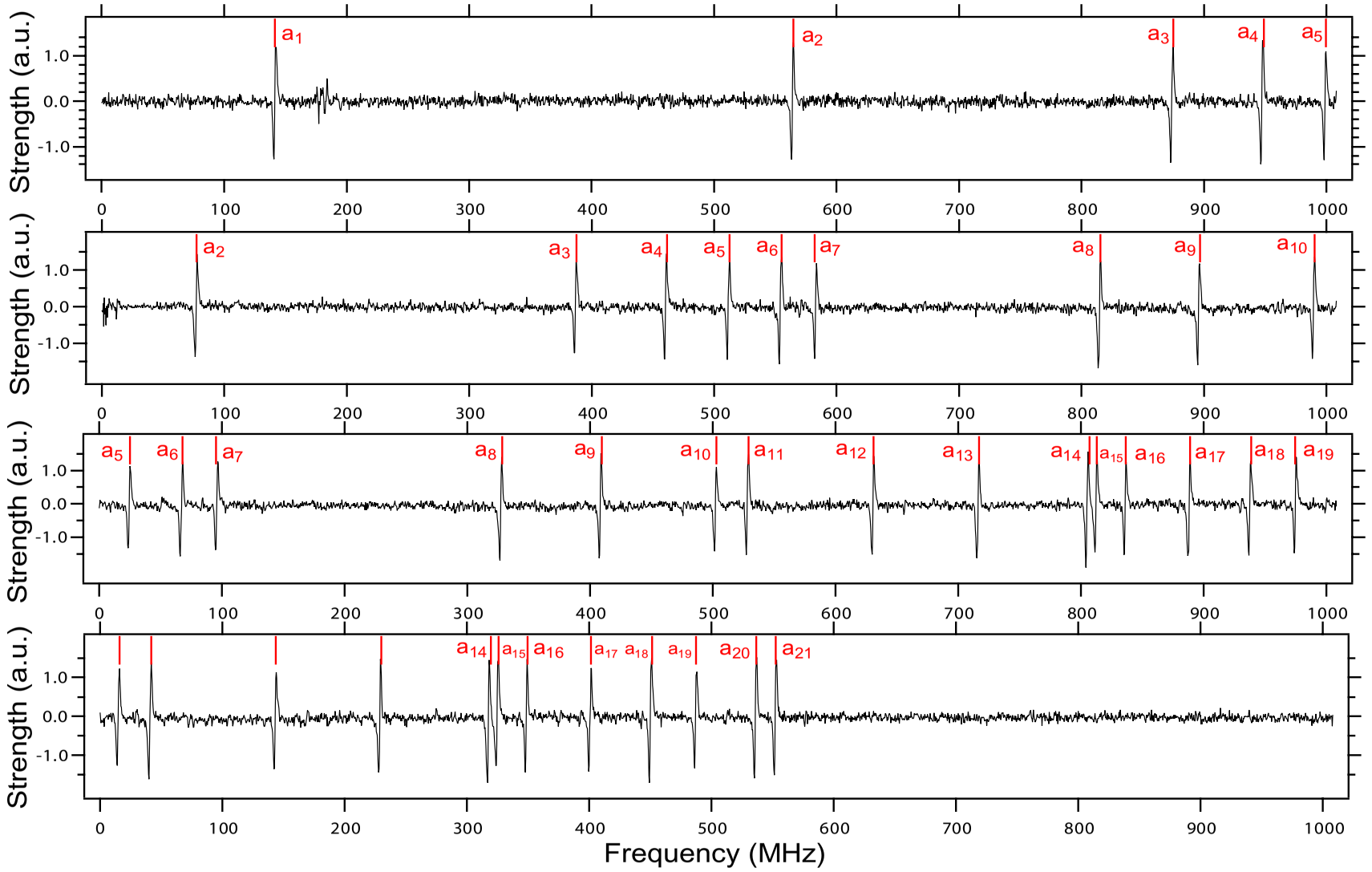

Figure B.6: Hyperfine spectrum recorded at P(63) 70-0. Vertical bars are fitting results using a four-term effective hyperfine Hamiltonian.